Multiscale thermo-hydro-mechanical-chemical coupling effects for fluid-infiltrating crystalline solids and geomaterials: theory, implementation, and validation

SeonHong Na

Submitted in partial fulfillment of the
requirements for the degree of
Doctor of Philosophy
in the Graduate School of Arts and Sciences

COLUMBIA UNIVERSITY

2018

ABSTRACT

Multiscale thermo-hydro-mechanical-chemical coupling effects for fluid-infiltrating crystalline solids and geomaterials: theory, implementation, and validation.

SeonHong Na

Extreme climate change and demanding energy resources have led to new geotechnical engineering challenges critical for sustainable development and resilient infrastructure of our society. Applications such as geological disposal of nuclear waste and carbon dioxide, artificial ground freezing, and hydraulic fractures all require an in-depth understanding of the thermo-hydro-mechanical coupling mechanisms of geomaterials subjected to various environmental impact. This dissertation presents a multiphysical computational framework dedicated to address the issues related to those unconventional applications.

Our objective is not only incorporating multiphysical coupling effects at the constitutive laws, but also taking into account the nonlocal effects originated from the flow of pore-fluid, thermal convection and diffusion among solid and fluid constituents, and crystallization and recrystallization of crystals in the pore space across length scales. By considering these coupling mechanisms, we introduce a single unified model capable of predicting complex thermo-hydro-mechanical responses of geological and porous media across wide spectra of temperature, confining pressure, and loading rate.

This modeling framework applies to two applications, i.e., the freezing and thawing of frozen soil and the anisotropic crystal plasticity/fracture response of rock salt. Highlights of the key ingredients of the models cover the stabilization procedure used for the multi-field finite element, the return mapping algorithm for crystal plasticity, the micromorphic regularization of the modified Cam-Clay model, and the strategy for enhancing computational efficiency of solvers, such as pre-conditioner, adaptive meshing, and internal variable mapping. By introducing the multiphysical coupling mechanisms explicitly, our computational geomechanics model is able to deliver more accurate and consistent results without introducing a significant amount of additional material parameters.

In a parallel effort, we analyze the impact of thermo-hydro-mechanical (THM) coupling effects on the dynamic wave propagation and strain localization in a fully saturated softening porous medium. The investigation starts with deriving the characteristic polynomial corresponding to the governing equations of the THM system. The theoretical analysis based on the Abel–Ruffini theorem reveals that the roots of the characteristic polynomial for the THM problem cannot be expressed algebraically. Our analysis concludes that the rate-dependence introduced by multiphysical coupling may not regularize the THM governing equations when softening occurs.

Contents

6   Closure   161

Bibliography   165

List of Figures

List of Tables

This page intentionally left blank.

Acknowledgements

During the last 4 years of my doctoral study at Columbia, I have learned the most essential knowledge and experienced the most valuable lessons, which I continue to live my life by. There are so many people who have made a significant impact that it would be simply impossible to thank them all here.

I would like first to express my most gratitude and appreciation to my advisor, Prof. Steve WaiChing Sun, for his enormous support and precious advice throughout the years. His dedication and effort to teaching, guiding, and mentoring inspire me to deepen my academic knowledge for research and broaden my insight as an independent scientist. Thank you very much for always believing in me, encouraging me, and disciplining me whenever I needed it.

I am so grateful to Dr. Moo Y. Lee and Dr. Hongkyu Yoon at Sandia National Laboratories for their consistent support. It was lucky for me to experience diverse research topics at Sandia and to have research collaborations with them. I thank again for taking their time to serve as my defense committee members. Their valuable comments and considerations are greatly appreciated.

I thank my other defense committee members: Prof. Hoe I. Ling, Prof. Ioannis A. Kougioumtzoglou, and Prof. Gerard A. Ateshian. I greatly appreciate their time and effort to provide constructive and insightful comments. I am also grateful to Prof. Jacob Fish and Prof. Jeffrey Kysar for serving as the members of my candidacy examination committee. My special thanks go to Prof. George Deodatis, the Chair of the Department of Civil En-

gineering and Engineering Mechanics, for his wholehearted encouragement and support during my last year at Columbia.

I want to extend my deep appreciation to my colleagues at Columbia. Jinwoo Jang, now at Florida Atlantic University, and Sung-Hwan Jang, at the University of Plymouth, have always supported me with encouragement and positive energy to overcome my tough time here in New York City. I am grateful to meet Juan, Miguel, and Ye during my first year at the TA office. I consider it a great privilege to have them during my doctoral study at Columbia.

I would like to thank my group members: Kun, Eric, Nikolaus, Yang, and Xinran; and other colleagues on the 7th floor Mudd: Sang-Guk, Jung Guen, and Lei. It was also a great pleasure to meet other postdocs at Columbia: Sujin Lee, Seungmin Lim, and Jinhyun Choo. I feel so happy and grateful for my friends, Changhwan, Jinyoung, Ina, and Sunil sharing great memories and moments together here in New York.

Lastly, JiYoung, you are my dearest. I will be indebted to you and love you forever. I am so blessed to have Yunha in our life together, that gives me one more reason to do my best in everything. I couldn't be more thankful to my parents and family for their devoted love and strong belief, which always give me the courage to overcome any difficulty.

To my beloved wife JiYoung

This page intentionally left blank.

Chapter 1

Introduction

1.1 Motivation and objective

Computer models of geological materials are nowadays indispensable for engineers and researchers to analyze engineering problems, validate designs, and make predictions for increasingly complex problems. In civil and environmental engineering applications, many commercial simulation packages such as ABAQUS, FLAC, or Plaxis, have become default tools for geotechnical engineering and geomechanics analysis. Along with this trend, a significant portion of research effort in geotechnical engineering has been dedicated on developing local constitutive models based on a critical state plasticity framework at the fully drained or undrained limits under the isothermal condition [1–5]. These models are then embedded in the finite element or finite difference solvers where the balance of linear momentum is solved in an incremental manner.

Emerging global issues associated with extreme climate events and demanding energy resources, however, require significant advancements in our knowledge and predictive capability of complex physical and chemical mechanisms across time and length scales. These complex processes are difficult to capture locally without considering the length scales. Furthermore, due to the multiphysical coupling effects, constitutive responses of a material point is not just influenced by the strain and strain history but is also affected

by the diffusion of pore-fluid, crystallization and re-crystallization of crystals in the pore space, and thermal convection and diffusion among solid and fluid constituents. Hence, proposing new phenomenological laws alone is no longer sufficient to meet the demand for the increasingly complex engineering applications, such as geological disposal of nuclear waste and carbon dioxide, unconventional hydrocarbon recovery, hydraulic fracture, thawing problems in permafrost region, artificial ground freezing for construction, and tunnel and underground facility detection.

This dissertation investigates the development of computational models that capture coupled thermo-hydro-mechanical-chemical behavior of geological materials across different length scales. To overcome the aforementioned limitations, our research approach focuses on not just the development of appropriate constitutive laws but also the derivation of field equations under the multiphysics aspect. The numerical issues and techniques in calculating the multifield problems are also explored associated with finite strain theory, implementation of solvers, preconditioners, and adaptive mesh refinement. The material parameter identification process inferred from experiments and the bridging-scale and homogenization techniques that replicate the interplay between microstructural attributes and macroscopic responses are also addressed.

1.2 Outline of dissertation

This dissertation explores the theoretical and computational modeling of the critical behavior of materials under the coupled multiphysics effects. In particular, the failure mechanism such as strain localization and fracture behavior are described associated with thermo-hydro-mechanical influence in geomaterials and crystalline solid. Firstly, we cover two topics, a multiphase frozen porous media and a geological repository for nuclear waste disposal, respectively. The derivation of governing equations indicates how we capture the characteristic behaviors such as phase transition and anisotropy. We further

address the failure mechanism in either macroscopic or microscopic aspects to properly incorporate physical and chemical phenomena. Next, we delve into the field equations for saturated porous media under the nonisothermal condition. Here the analytical investigation is performed to identify the influence of hydraulic and thermal diffusion on the regularization of the multiphase system under strain softening. We then cover numerical techniques and solution strategies associated with resolving multiphysics problems such as inf-sup condition, preconditioning, nonlocality, and adaptive finite element simulations. The following summarizes the outline of this thesis.

In Chapter 2, a stabilized thermo-hydro-mechanical (THM) finite element model is introduced to investigate the freeze–thaw action of frozen porous media in the finite deformation range. By applying the mixture theory, the frozen soil is idealized as a composite consisting of three phases, i.e., solid grain, unfrozen water and ice crystal. A generalized hardening rule at finite strain is incorporated to replicate how the elasto-plastic responses and critical state evolve under the influence of phase transitions and heat transfer. The enhanced particle interlocking and ice strengthening during the freezing processes and the thawing-induced consolidation at the geometrical nonlinear regimes are both replicated.

In Chapter 3, a combined multi-phase-field/crystal plasticity approach for crystalline solids is described based upon computational thermomechanics. The main objective of this topic is the computational modeling for crystalline rock salt, which is one of the major materials used for nuclear waste geological disposal. Conventionally, this microstructural effects of rock salt are often incorporated phenomenologically in macroscopic damage models. Nevertheless, the thermo-mechanical behavior of a crystalline material is dictated by the nature of the crystal lattice and micromechanics (i.e. the slip-system). Here we employ a crystal plasticity framework in which single-crystal halite is modeled as a face-centered cubic (FCC) structure with the secondary atoms in its octahedral holes, where a pair of Na^+ and Cl^- ions forms the bond basis. Utilizing the crystal plasticity framework, we capture the existence of an elastic region in the stress space and the sequence of slip

system activation of single-crystal halite under different temperature ranges. To capture the anisotropic nature of the intragranular fracture, we couple a crystal plasticity model with a multi-phase-field formulation that does not require high-order terms for the phase field.

In Chapter 4, the thermo-hydro-mechanical (THM) coupling effects on the dynamic wave propagation and strain localization in a fully saturated softening porous medium are analyzed. The characteristic polynomial corresponding to the governing equations of the THM system is derived, and the stability analysis is conducted to determine the necessary conditions for stability in both the non-isothermal and adiabatic cases. The result from the dispersion analysis based on the Abel–Ruffini theorem reveals that the roots of the characteristic polynomial for the THM problem cannot be expressed algebraically. Meanwhile, the dispersion analysis on the adiabatic case leads to a new analytical expression of the internal length scale. Our limit analysis on the phase velocity for the nonisothermal case indicates that the internal length scale for the nonisothermal THM system may vanish at the short wavelength limit. This result concludes that the rate-dependence introduced by multiphysical coupling may not regularize the THM governing equations when softening occurs. Numerical experiments are used to verify the results from the stability and dispersion analyses.

In Chapter 5, the numerical techniques and solution strategies for resolving multiphysics problems are investigated. The numerical system of phase-transiting frozen porous media in Chapter 2 has been solved in a monolithic way to simultaneously account for different physical and chemical mechanisms. The stabilized finite element formulation based upon the polynomial projection scheme is proposed, in which the inf–sup deficiency of equal-order finite element is counterbalanced using stabilization terms based on the weak two-fold inf–sup condition. Furthermore, the preconditioning strategy for the mixed finite element is introduced to resolve the calculation slow down the issue in direct solvers due to the ill-conditioned tangent matrix system. The operator-split

method to resolve a combined thermomechanics/multiphase damage problems in Chapter 3 is then addressed. For regularization of the numerical system under strain localization conditions, the micromorphic approach for nonlocal models is further covered associated with the adaptive mesh refinement techniques. The projection method for global updates of internal variables located in local quadrature points is further described.

Finally, in Chapter 6, the conclusions of this thesis, with a summary of the main contributions and a description of future work are presented.

This page intentionally left blank.

Chapter 2

Computational thermo-hydro-mechanics for phase transiting multiphase frozen soil in the finite deformation range

2.1   Introduction

In permafrost regions, soil underneath pavement and concrete structures may experience freeze-thaw action. During the freezing phase, the crystallization of ice leads to the expanding of voids and micro-cracks in the porous media. When temperature arises, ices near the heat source may thaw out and turn into meltwater, but this water may be trapped by the frozen region that remains nearly impermeable. This results in a thaw-weaken soil that is wet, loose and highly deformable [6–9]. The freeze-thaw action may repeat itself everyday due to the temperature difference between day and night near surface, and, in a larger spatial and time scale, between winter and spring. The accumulated damage and deterioration of roads, airfields and infrastructure due to freeze-thaw action are of ultimate importance for vehicle mobility and structural integrity of infrastructure in cold

region. This demand of understanding the freeze-thaw action of porous media undergoing large deformation is further intensified by the climate changes that bring in more extreme weather and heavier rains which are expected to accelerate the damages of infrastructure in alerting speed in the coming decades. For instance, the frost-free season in Fairbanks, Alaska has been lasted 50 percent longer between 1904 and 2008. The increase of permafrost temperature, which occurs throughout Alaska since the late 1970s, has caused land subsidence and put public infrastructure, such as roads, runways and sewer system, at risk [9, 10].

In this chapter we present a finite strain poromechanics theory that fully considers the thermo-hydro-mechanical coupling effect of the mass-exchanging, phase-transiting porous media. Previously, significant contributions have been made to derive thermal-sensitive or degree-of-saturation-sensitive constitutive laws for the frozen soil [11]. These constitutive laws are often incorporated in thermo-mechanical simulations in which the presence of unfrozen water is neglected. A notable exception is the work presented in Nishimura et al. [12] where the infinitesimal strain thermo-hydro-mechanical model is coupled with a modified Cam-clay model with generalized hardening rules. Unlike the previous modeling efforts in which the flow of unfrozen water, energy dissipation due to phase transition and geometrical nonlinearity are neglected (cf. Michalowowski and Zhu [11], Jessberger [13], and McKenzie, Voss, and Siegel [14]), we introduce a new comprehensive theory that incorporates all of these important thermo-hydro-mechanical mechanisms into the balance principles (linear momentum, mass, energy) in the finite deformation range. An implicit total Lagrangian finite element framework is formulated, while thermal and cryo-suction effects are explicitly captured by a generalized hardening rules that allow the yield surface to evolve based on the volume fraction of ices in the pore space and the temperature.

The organization of this chapter is as follows. We first provide the derivation of the balance principle for frozen soil in the geometrically nonlinear regime (Section 2.2). Then,

the finite strain elasto-plasticity model with the non-mechanical hardening rule and the finite strain suction-permeability theory is presented (Section 2.3). Following this is the total Lagrangian finite element formulation of the thermo-hydro-mechanical model (Section 2.4). Numerical examples are then provided (Section 2.5), followed by a conclusion.

2.2 Conservation laws

In this section, we present the balance principle (i.e. linear momentum, mass and energy) for frozen soil undergoing finite deformation. The soil is idealized as a continuum mixture that consists of three constituents, the liquid water and crystal ice, which occupy the pores inside the solid skeleton, and the solid constituent that forms the solid skeleton. Based on the classical thermo-hydro-mechanics theory as reported in the previous studies [7, 15–20], we present a new derivation that takes account of the heat generated from plastic dissipation and the thermal-convection to replicate the path-dependent thermo-hydro-mechanical effect of frozen porous media with infiltrating unfrozen water in the finite deformation range. The incorporation of geometrical nonlinearity effect is critical for modeling thawing materials in which the cryo-suction effect often leads to soft soil that develops large strain. The energy required for the phase transition between ice and water is incorporated into the balance of energy. Meanwhile we adopt the Taylor-Quinney coefficient to control the amount of mechanical dissipation converted into heat. We extend both the net stress theory in Gens [21] and the effective stress theory in Zhou and Meschke [17] for the finite strain problems. Consequently, the energy dissipation due to fluid diffusion, thermal convection, phase transition and outward heat flux are all formulated in the total Lagrangian framework. The implications of these modifications will be examined via numerical examples.

2.2.1 Kinematics of three-phase frozen porous media

We consider an idealized kinematics based on the theory of pre-melting dynamics which elucidates the mechanism of existence of unfrozen water at temperatures below the bulk freezing point [8, 22]. In addition, the behavior of crystal ice is captured through crystal ice pressure obtained by the Clausius-Clapeyron equation. This relation is based on thermodynamic requirements for equilibrium that needs to be satisfied by crystal ice pressure, liquid water pressure and temperature in non-isothermal condition [12, 23]. Within this framework, we adopt the passive air phase assumption. Hence, we neglect the existence of air in the pore space and consider a three-phase porous medium composed of solid skeleton, liquid water, and crystal ice [24, 25].

Based on the mixture theory, if the representative elementary volume exists, then the three-phase material can be idealized as a mixture continuum where each constituent occupies a fraction of volume at the same macroscopic material point [26–30]. Unlike solid composite in which one may assume that all constituents at a material point share the same trajectories until delamination or other forms of failure, the solid and pore-fluid constituents do not necessarily follow the same trajectory unless the porous medium is locally undrained. Therefore, the mappings for materials at a point $\boldsymbol{x}$ of the current configuration can be represented from the configuration of solid skeleton ($\boldsymbol{X}^{\mathrm{S}}$), liquid water ($\boldsymbol{X}^{\mathrm{L}}$) and crystal ice ($\boldsymbol{X}^{\mathrm{C}}$) counterparts:

$$\boldsymbol{x} = \varphi^{\alpha}\left(\boldsymbol{X}^{\alpha}, t\right), \quad \alpha = \mathrm{S, \ L, \ C}. \tag{2.1}$$

Because the path-dependent constitutive laws and the internal variables that represent the loading history of the solid skeleton are corresponding to the solid skeleton trajectory, our formulation will be derived in accordance with the motion of the solid skeleton (φ^{S}). As a result, the motion of liquid water and crystal ice in THM model at finite-strain is captured by their relative motion with respect to the solid skeleton. The frozen soil with

10

three constituents (solid skeleton (S), liquid water (L) and crystal ice(C)) is homogenized as a continuum. Therefore, the current density field of a porous medium can be written as,

$$\rho = \rho^S + \rho^L + \rho^C = \phi^S \rho_S + \phi^L \rho_L + \phi^C \rho_C, \tag{2.2}$$

where ρ^α ($\alpha = S, L, C$) is the partial mass density of constituent α given by $\rho^\alpha = \phi^\phi \rho_\alpha$; ϕ^α is the volume fraction of each constituent in the current configuration; ρ_α is the intrinsic mass density of each constituent α. By assuming that the pores inside the solid skeleton are fully saturated with either liquid water or crystal ice, the density of frozen soil mixture can be obtained by taking the freezing characteristic function. The freezing characteristic function (S_L) indicates the ratio between the volume of liquid water in the void to the total volume of the void, while the ratio of crystal ice in the total void space is $S_C = 1 - S_L$. The concept of freezing characteristic function is analogous to the water retention curve of unsaturated porous materials (in Section 2.3.2). Therefore, the total current density of (2.2) can be also rewritten as,

$$\rho = \phi^S \rho_S + \phi^L S_L \rho_L + \phi^L S_C \rho_C = (1 - \phi^L)\rho_S + \phi^L \left[S_L \rho_L + (1 - S_L)\rho_C \right]. \tag{2.3}$$

Note that this becomes the total current density of a fully saturated porous medium under unfrozen state when S_L becomes a unity (the pores are fully saturated only with liquid water).

2.2.2 Balance of linear momentum

To capture the stress status during thawing and freezing, we adopt the Bishop's effective stress theory for the frozen soil idealized as a three-phase continuum [31]. In other words, we assume that the total stress $\boldsymbol{\sigma}$ can be partitioned into the effective stress $\boldsymbol{\sigma}'$ which evolves due to the deformation and loading history of the solid skeleton, and a net pore pressure $\bar{p}$ build up in the void space due to the motion and interaction of the water and

ice crystal, that is,

$$\boldsymbol{\sigma} = \boldsymbol{\sigma}' - \bar{p}\boldsymbol{I}, \quad \text{with } \bar{p} = \chi p_\text{L} + (1 - \chi)p_\text{C}, \tag{2.4}$$

where the parameter χ is commonly assumed to be equal to the degree of liquid satura-tion ($\chi = S_\text{L}$) [32–34] where p_L and p_C indicate the liquid water and crystal ice pressures, respectively. Note that $\boldsymbol{I}$ is the second-order identity tensor. This treatment is a simpli-fication of the actual retention behavior in which the history or path dependence of the effective stress coefficient χ is neglected. In this formulation, the interaction between ice crystal and unfrozen water is characterized by a freezing retention curve in an anal-ogy of the characterization of the water-air interaction via the water retention curve (cf. O'Neill [35] and O'Neill and Miller [36]). As such, the pore space is assumed to be al-ways saturated by a combination of two constituents, the ice crystal and unfrozen water. Furthermore, we follows the treatment in Nishimura et al. [12] and Zhou [37] where the Bishop's effective stress principle originally proposed for unsaturated porous media is ap-plied to capture the interaction among the solid skeleton, ice crystal, and unfrozen water. It should be noted that while the usage of freezing retention curve and Bishop's effective stress theory does imply that the water-ice-skeleton and water-air-skeleton interactions share similarities, in particular, both of them are determined by pore size distribution and the water-solid interface tensional force [7, 12, 21, 32], the ice crystal is not considered as a fluid, and the influence of the presence of ice on the shear strength must be taken account properly. In this work, this influence is captured via a phenomenological ap-proach in the framework of finite strain critical state theory. More consistent approach may require more explicit modeling of the crystallization of ice phase at the pore scales and treating the ice and solid skeleton as a composite or effective medium composed of two solid phases [37]. These improvements are out of the scope of this study but will be considered in future extensions.

In this work, we adopt the total Lagrangian formulation and hence the model is formulated with respect to the reference configuration of the solid skeleton. Note that the total Lagrangian formulation is not the only feasible choice. For instance, Sanavia, Schrefler, and Steinmann [38] has successfully formulated the poromechanics problem in a spatial setting which results in an updated Lagrangian formulation. Due to the usage of total Lagrangian formulation in our current work, the balance of linear momentum is written in terms of the total Piola-Kirchhoff stress tensor, which is related to the first effective Piola-Kirchhoff stress tensor and the pull back of the contribution from the water and ice crystal constituents, i.e.,

$$\boldsymbol{P} = \boldsymbol{\tau} \cdot \boldsymbol{F}^{-\mathrm{T}} = \boldsymbol{\tau}' \cdot \boldsymbol{F}^{-\mathrm{T}} - J\bar{p}\boldsymbol{F}^{-\mathrm{T}}, \tag{2.5}$$

where $\boldsymbol{\tau} = J\boldsymbol{\sigma}$ is the symmetric total Kirchhoff stress tensor, $\boldsymbol{\tau}' = J\boldsymbol{\sigma}'$ is the effective Kirchhoff stress tensor (e.g. Diebels and Ehlers [39], Simo [40], Ehlers [41], Sanavia, Pesavento, and Schrefler [42], Sun, Ostien, and Salinger [43], and Song and Borja [44]). Therefore, by ignoring the inertia forces, the balance of linear momentum in Lagrangian form takes the following relation in the reference configuration:

$$\nabla^{\boldsymbol{X}} \cdot \boldsymbol{P} + \rho_0 \boldsymbol{G} = 0, \tag{2.6}$$

where $\rho_0 = J\rho$ is the pullback of the total mass density which can be determined via (2.3).

2.2.3 Balance of mass

We assume that the porous medium is fully saturated with three constituents, solid (S), liquid water (L), and crystal ice (C). The possibility of phase transition between liquid water and crystal ice is considered. The following derivation is formulated with our choice of primary variables (solid displacement, liquid phase pressure, and temperature) in mind. Since the frozen porous media we considered consist of three constituents, one may also

introduce additional primary variables, such as the degree of saturation or ice phase pressure. However, as we will discuss in Section 2.3, one may also exploit arguments from the Clausius-Clapeyron equation to eliminate the ice phase pressure from the prime variables by expressing it as a function of the liquid phase pressure and temperature. This approach allows us to derive a simplified system of equations with just three prime variables. The balance of mass for a three-phase solid-water-ice mixture, therefore, can be written as,

$$\frac{D\rho^{S}}{Dt} + \rho^{S} \, \nabla^{\boldsymbol{x}} \cdot \boldsymbol{v} = 0, \tag{2.7}$$

$$\frac{D\rho^{L}}{Dt} + \rho^{L} \, \nabla^{\boldsymbol{x}} \cdot \boldsymbol{v} + \nabla^{\boldsymbol{x}} \cdot \left(\rho^{L} \boldsymbol{v}_{LS}\right) = -\overset{\circ}{m}_{L \to C}, \tag{2.8}$$

$$\frac{D\rho^{C}}{Dt} + \rho^{C} \, \nabla^{\boldsymbol{x}} \cdot \boldsymbol{v} + \nabla^{\boldsymbol{x}} \cdot \left(\rho^{C} \boldsymbol{v}_{CS}\right) = \overset{\circ}{m}_{L \to C}. \tag{2.9}$$

Here $\overset{\circ}{m}_{L \to C}$ is the rate of liquid water mass changing into crystal ice. In general, the flow of ice with respect to soil skeleton ($\boldsymbol{v}_{CS}$) is much slower than the flow of liquid ice. Therefore, we can assume that $\boldsymbol{v}_{CS} \approx 0$. Combining (2.8) and (2.9) leads to the following equation,

$$\frac{D\rho^{L}}{Dt} + \frac{D\rho^{C}}{Dt} + (\rho^{L} + \rho^{C}) \, \nabla^{\boldsymbol{x}} \cdot \boldsymbol{v} + \nabla^{\boldsymbol{x}} \cdot \left(\rho^{L} \boldsymbol{v}_{LS}\right) = 0. \tag{2.10}$$

We can consider an equation of state for density/pressure relation through a barotropic flow assumption (e.g. Sun [19], Sun, Ostien, and Salinger [43], and Song and Borja [44]). Introducing a bulk modulus for each phase (solid, liquid water, and crystal ice), we expand the total time derivative of the partial density ρ^{π} as,

$$\frac{D\rho^{L}}{Dt} = \frac{D(\phi^{L}\rho_{L})}{Dt} = \rho_{L} \frac{D\phi^{L}}{Dt} + \phi^{L} \frac{D\rho_{L}}{Dt} = \rho_{L} \left(\frac{D\phi^{L}}{Dt} + \frac{\phi^{L}}{K_{L}} \frac{Dp_{L}}{Dt}\right), \tag{2.11}$$

likewise, $\qquad \frac{D\rho^{C}}{Dt} = \rho_{C} \left(\frac{D\phi^{C}}{Dt} + \frac{\phi^{C}}{K_{C}} \frac{Dp_{C}}{Dt}\right). \tag{2.12}$

Inserting these relationships into (2.7) and (2.10) gives,

$$\frac{D\phi^{\rm S}}{Dt} + \frac{\phi^{\rm S}}{K_{\rm S}}\frac{Dp_{\rm S}}{Dt} + \phi^{\rm S}\,\nabla^{\boldsymbol{x}}\!\cdot\boldsymbol{v} = 0, \tag{2.13}$$

$$\rho_{\rm L}\left(\frac{D\phi^{\rm L}}{Dt} + \frac{\phi^{\rm L}}{K_{\rm L}}\frac{Dp_{\rm L}}{Dt}\right) + \rho_{\rm C}\left(\frac{D\phi^{\rm C}}{Dt} + \frac{\phi^{\rm C}}{K_{\rm C}}\frac{Dp_{\rm C}}{Dt}\right) + (\rho^{\rm L} + \rho^{\rm C})\,\nabla^{\boldsymbol{x}}\!\cdot\boldsymbol{v}$$
$$+ \nabla^{\boldsymbol{x}}\!\cdot(\rho^{\rm L}\boldsymbol{v}_{\rm LS}) = 0. \tag{2.14}$$

Taking into account the saturation of liquid water and crystal ice, we use the following identity:

$$\begin{aligned}
\frac{D\phi^{\pi}}{Dt} &= \frac{D}{Dt}\left[S_{\pi}(1 - \phi^{\rm S})\right] \\
&= (1 - \phi^{\rm S})\frac{DS^{\pi}}{Dt} - S_{\pi}\frac{D\phi^{\rm S}}{Dt}, \qquad \pi = {\rm L,\ C,} \tag{2.15}
\end{aligned}$$

in which, $S_{\rm L}$ is the saturation of liquid water and $S_{\rm C}$ (= $1 - S_{\rm L}$) is the saturation of crystal ice. Combining the equations of (2.13), (2.14), and (2.15) leads to an expression for the mass balance equation of three-phase porous medium. Note the notation that $(\dot{\cdot}) = D(\cdot)/Dt$ is used.

$$\rho_{\rm L}\left[(1 - \phi^{\rm S})\dot{S}_{\rm L} + \frac{\phi^{\rm L}}{K_{\rm L}}\dot{p}_{\rm L} + \frac{S_{\rm L}\phi^{\rm S}}{K_{\rm S}}\dot{p}_{\rm S} + S_{\rm L}\,\nabla^{\boldsymbol{x}}\!\cdot\boldsymbol{v}\right] +$$
$$\rho_{\rm C}\left[(1 - \phi^{\rm S})\dot{S}_{\rm C} + \frac{\phi^{\rm C}}{K_{\rm C}}\dot{p}_{\rm C} + \frac{S_{\rm C}\phi^{\rm S}}{K_{\rm S}}\dot{p}_{\rm S} + S_{\rm C}\,\nabla^{\boldsymbol{x}}\!\cdot\boldsymbol{v}\right] + \nabla^{\boldsymbol{x}}\!\cdot\boldsymbol{w} = 0, \tag{2.16}$$

where $\boldsymbol{w} = \phi^{\rm L}\rho_{\rm L}\boldsymbol{v}_{\rm LS}$. The Piola transform of $\boldsymbol{w}$ is

$$\boldsymbol{W} = J\boldsymbol{F}^{-1}\cdot\boldsymbol{w}, \tag{2.17}$$

where $\boldsymbol{W}$ and $\boldsymbol{w}$ are the Lagrangian and Eulerian relative mass flow vectors with the following Piola identity (e.g. Diebels and Ehlers [39], Simo [40], Ehlers [41], Sanavia,

Pesavento, and Schrefler [42], Sun, Ostien, and Salinger [43], and Song and Borja [44]),

$$\nabla^{\boldsymbol{X}} \cdot \boldsymbol{W} = J \, \nabla^{\boldsymbol{x}} \cdot \boldsymbol{w}. \tag{2.18}$$

Furthermore, we note that (cf. Song and Borja [44]),

$$J\dot{p}_\pi = \overline{(J p_\pi)} - p_\pi \dot{J}, \quad \pi = \text{S, L, C}. \tag{2.19}$$

Substituting (2.17), (2.18) and (2.19) into (2.16) gives the mass balance equation in the reference configuration as,

$$
\begin{aligned}
&\rho_{\text{L}} \left[(1 - \phi^{\text{S}}) \dot{S}_{\text{L}} J + \frac{\phi^{\text{L}}}{K_{\text{L}}} \overline{\dot{p}_{\text{L}} J} + \frac{S_{\text{L}} \phi^{\text{S}}}{K_{\text{S}}} \overline{\dot{p}_{\text{S}} J} + \left(S_{\text{L}} - \frac{\phi^{\text{L}}}{K_{\text{L}}} p_{\text{L}} - \frac{S_{\text{L}} \phi^{\text{S}}}{K_{\text{S}}} p_{\text{S}} \right) \dot{J} \right] \\
&+ \rho_{\text{C}} \left[(1 - \phi^{\text{S}}) \dot{S}_{\text{C}} J + \frac{\phi^{\text{C}}}{K_{\text{C}}} \overline{\dot{p}_{\text{C}} J} + \frac{S_{\text{C}} \phi^{\text{S}}}{K_{\text{S}}} \overline{\dot{p}_{\text{S}} J} + \left(S_{\text{C}} - \frac{\phi^{\text{C}}}{K_{\text{C}}} p_{\text{C}} - \frac{S_{\text{C}} \phi^{\text{S}}}{K_{\text{S}}} p_{\text{S}} \right) \dot{J} \right] \\
&+ \nabla^{\boldsymbol{X}} \cdot \boldsymbol{W} = 0.
\end{aligned}
\tag{2.20}
$$

Assuming that the change of unfrozen fluid content due to the expansion and contraction of the constituents of porous medium is negligible compared to that due to changes of porosity and degree of saturation, mass conservation equation is simplified as,

$$(1 - \phi^{\text{S}})(\rho_{\text{L}} - \rho_{\text{C}}) \dot{S}_{\text{L}} J + [\rho_{\text{L}} S_{\text{L}} + \rho_{\text{C}} (1 - S_{\text{L}})] \dot{J} + \nabla^{\boldsymbol{X}} \cdot \boldsymbol{W} = 0. \tag{2.21}$$

Here the Lagrangian liquid water mass flux after a pull-back operation reads (cf. Sun [19] and Andrade and Borja [45]),

$$\boldsymbol{W} = \rho_{\text{L}} \boldsymbol{K}_{\text{L}} \cdot \left(-\nabla^{\boldsymbol{X}} p_{\text{L}} + \rho_{\text{L}} \boldsymbol{F}^{\text{T}} \cdot \boldsymbol{G} \right), \quad \text{where,} \quad \boldsymbol{K}_{\text{L}} = J \boldsymbol{F}^{-1} \cdot \boldsymbol{k} \cdot \boldsymbol{F}^{-\text{T}}. \tag{2.22}$$

The pull-back permeability tensor ($\boldsymbol{K}_{\text{L}}$) is obtained by pulling-back the Eulerian effective permeability tensor to the reference configuration [43]. The constitutive law for the Eule-

rian effective permeability tensor ($\boldsymbol{k}$) in (2.38), which depends on the degree of saturation of the ice crystal, porosity and temperature will be described in Section 2.3.2.

2.2.4 Balance of energy

For the sake of simplification, the previous efforts on frozen soil modeling often adopt a balance of energy equation that neglects the contribution of mechanical dissipation, heat convection, structural heating and the geometrical nonlinearity (cf. Michalowski and Zhu [11], Nishimura et al. [12], Zhou [37], and Michalowski [46]). This treatment is often a trade-off between convenience and rigorousness. A well-justified simplification may allow one to derive analytical solution or at the very least shorten the implementation time. Nevertheless, the additional assumptions also limit the application of the simplified thermo-hydro-mechanics theory to more general situation. For instead, dissipation due to the frictional shear of the frozen soil may generate heat that melts the portion of ice crystal in the pore space. Flow of unfrozen water that is significantly hotter or colder than the frozen soil may cause significant change in temperature of the frozen soil, and the thawing process may weaken the soil and cause the thaw-soil highly deformable. These mechanisms are important for modeling frozen soil that exhibits path dependent behaviors, especially when the hardening/softening mechanism of the frozen soil is sensitive to the temperature [12]. These reasons above motivate us to derive a version of the balance of energy that incorporates all the aforementioned mechanisms.

Our starting point is the balance of energy for three-phase frozen soil at finite strains expressed in the current configuration which reads (cf. Sun [19] and Simo and Miehe [47]):

$$Jc_{\boldsymbol{F}}\dot{T} = \left[-J\,\nabla^{\boldsymbol{x}}\!\cdot\boldsymbol{q} + \frac{\phi^{\mathrm{L}}S_{\mathrm{L}}c_{\boldsymbol{F}\mathrm{L}}}{\rho_{\mathrm{L}}}J\boldsymbol{w}\cdot\nabla^{\boldsymbol{x}}T\right] + [D_{\mathrm{mech}} + R_T]. \qquad (2.23)$$

Here we adopt an apparent heat capacity $c_{\boldsymbol{F}}$, which incorporates both the heat capacity

of frozen soil and latent heat [14, 48, 49], that is,

$$
\begin{aligned}
c_{\boldsymbol{F}} &= c_{\boldsymbol{F}\mathrm{S}}\phi^{\mathrm{S}} + c_{\boldsymbol{F}\mathrm{L}}(1-\phi^{\mathrm{S}})S_{\mathrm{L}} + c_{\boldsymbol{F}\mathrm{C}}(1-\phi^{\mathrm{S}})S_{\mathrm{C}} + \rho_{\mathrm{C}}(1-\phi^{\mathrm{S}})l\frac{\partial S_{\mathrm{L}}}{\partial T} \\
&= \rho_{\mathrm{S}}c_{\mathrm{S}}\phi^{\mathrm{S}} + \rho_{\mathrm{L}}c_{\mathrm{L}}(1-\phi^{\mathrm{S}})S_{\mathrm{L}} + \rho_{\mathrm{C}}c_{\mathrm{C}}(1-\phi^{\mathrm{S}})S_{\mathrm{C}} - \rho_{\mathrm{C}}(1-\phi^{\mathrm{S}})l\frac{\partial S_{\mathrm{C}}}{\partial T}, \quad (2.24)
\end{aligned}
$$

where c_{S}, c_{L} and c_{C} are the specific heats of each constituent, and l is the latent heat of fusion (liquid water and crystal ice). In (2.23), D_{mech} denotes the contribution to the dissipation due to pure mechanical load and R_T is the heat source term. Assuming that all constituents of frozen soil follow Fourier's law, the Cauchy heat flux may be expressed as the dot product of the gradient of temperature and the effective thermal conductivity of the multi-phase porous media (κ). In this work, we estimate the effective thermal conductivity as the geometric mean [50], i.e.,

$$
\boldsymbol{q} = -\kappa\,\nabla^{\boldsymbol{x}}\,T, \quad \kappa = \kappa_{\mathrm{S}}^{1-\phi^{\mathrm{S}}}\kappa_{\mathrm{L}}^{S_{\mathrm{L}}\phi^{\mathrm{S}}}\kappa_{\mathrm{C}}^{S_{\mathrm{C}}\phi^{\mathrm{S}}}, \tag{2.25}
$$

where κ_{S}, κ_{L} and κ_{C} indicate the isotropic thermal conductivities of solid, liquid water and crystal ice, respectively. It should be noted that the geometric mean is only one of the many possible ways to homogenize the thermal conductivity. Another valid choice can be, for instance, the estimate based on Eshelby equivalent inclusion method (cf. Sun [19]).

Applying the Piolar-Kirchhoff heat flux $\boldsymbol{Q}$ corresponding (2.25) reads,

$$
\boldsymbol{Q} = -\boldsymbol{K}_T \cdot \nabla^{\boldsymbol{X}}\,T, \tag{2.26}
$$

where $\boldsymbol{K}_T$ is the pull-back thermal conductivity tensor, that is,

$$
\boldsymbol{K}_T = J\boldsymbol{F}^{-1} \cdot \boldsymbol{\kappa} \cdot \boldsymbol{F}^{-T}, \quad \boldsymbol{\kappa} = \kappa\boldsymbol{I}. \tag{2.27}
$$

(2.23) can be recapitulated in the reference configuration as follows:

$$J c_{\boldsymbol{F}} \dot{T} = \left[-\nabla^{\boldsymbol{X}} \cdot \boldsymbol{Q} + \frac{\phi^{\mathrm{L}} S_{\mathrm{L}} c_{\boldsymbol{FL}}}{\rho_{\mathrm{L}}} \boldsymbol{W} \cdot \boldsymbol{F}^{-T} \cdot \nabla^{\boldsymbol{X}} T \right] + [D_{\mathrm{mech}} + R_{T}]. \qquad (2.28)$$

where $D_{\mathrm{mech}} = \beta \boldsymbol{S} : \boldsymbol{D}^{P}$ and β is the Taylor-Quinney coefficient (cf. Taylor and Quinney [51], Stainier and Ortiz [52], and Arriaga, McAuliffe, and Waisman [53]). Here we assume that the mechanical dissipation of the solid skeleton is primary driven by plastic work. A more comprehensive study would require the consideration of other dissipative mechanisms, such as creeping and fracture. Furthermore, it is also possible that the Taylor-Quinney coefficient of frozen soil can be temperature and strain-rate dependent. Nevertheless, the identification of the relation among the Taylor-Quinney coefficient and the temperature and strain-rate requires suitable design of experiments to generate sufficient experimental data. These generalizations of the proposed model will be considered in the future studies.

2.3 Constitutive model

The balance principle presented in Section 2.2 provides a general description for the three-phase frozen porous media undergoing large deformation. In this section, we introduce specific constitutive models to replicate the thermo-hydro-mechanical responses of a soil undergoing deformation in geometrical nonlinear regime. In particular, we assume that the soil in the unfrozen and isothermal states may exhibit constitutive responses adequately described by a finite strain Cam-Clay model with an associative hardening rule (e.g. Borja and Tamagnini [54] and Callari, Auricchio, and Sacco [55]). We then introduce an additional hardening/softening mechanism which allows the yield surface changes according to the degree of saturation of ice crystal to mimic the tensile and enhanced shear strength due to the presence of ice crystal in the void space. This solid constitutive law is coupled with the freezing retention model, which relates the degree of saturation of ice

crystal with temperature and the difference between the ice and pore water pressure.

2.3.1 Constitutive law for skeleton with ice crystals

The finite strain solid constitutive law is derived based on the the infinitesimal-strain generalized hardening model firstly introduced in Nishimura et al. [12] and further explained in Gens [21]. This constitutive law has ties to the basic Barcelona model [56] and the generalized hardening rule [57, 58] in the sense that yield function is expressed not only as a function of the effective stress invariants and preconsolidation pressure, but also depends on suction (and indirectly the degree of saturation). As a result, the hardening/softening of the material can be triggered by a change of the (mechanical) effective stress state as well as a change on the (non-mechanical) material state (e.g. frozen/unfrozen, chemical weathering). Here our goal is to extend this model to the finite deformation range, within the framework of multiplicative plasticity.

As explained in Cuitino and Ortiz [59], one of the key difficulties in introducing constitutive law in the finite deformation range is the cumbersome derivation and implementation requiring proper linearization of the multiplicative kinematics. One attractive way to overcome this obstacle is to establish a formal connection between the infinitesimal-strain constitutive law and the finite-strain counterpart. This idea is not new. For instance, Simo [40] has shown that in the case of isotropic plasticity, infinitesimal constitutive law can be extended to a finite strain counterpart by adopting suitable energy conjugated measure. Borja and Tamagnini [54] introduces an algorithmic design that employs exponential/logarithmic mapping and spectral decomposition to derive the analytical consistent tangent for the Cam-Clay model. Meanwhile, Cuitino and Ortiz [59] introduces a general algorithmic design where one may create a finite-strain version of any constitutive law by embedding a infinitesimal-strain constitutive law within a three-step framework [54, 59, 60].

This simple and yet efficient approach is used in this study. In the implementation

process, we first implement an infinitesimal-strain constitutive law with a generalized hardening rule that depends on the degree of saturation of ice crystal. Following this step, we introduce additional pre and post-processing steps. In particular, the pre-processing step allows one to employ logarithmic mapping to project finite strain measures to the infinitesimal strain counterparts such that infinitesimal-strain constitutive law is used to generate an incremental stress update. Following this step, the first effective Piola-Kirchhoff stress tensor can be obtained via the Piola transformation (cf. Cuitino and Ortiz [59] and Souza Neto, Peric, and Owen [60]). For completeness, this procedure is outlined below.

(i) *Pre-processing.* Given incremental displacement $\Delta \boldsymbol{u}$, update the deformation gradient and compute elastic trial state as,

$$\boldsymbol{F}_\Delta := \boldsymbol{I} + \nabla^{\boldsymbol{X}}(\Delta \boldsymbol{u}), \quad \boldsymbol{F}_{n+1} := \boldsymbol{F}_\Delta \cdot \boldsymbol{F}_n, \quad \boldsymbol{B}_b^e := \exp\left[2\boldsymbol{\varepsilon}_n^e\right]$$

$$\boldsymbol{B}_{n+1}^{e\,\text{trial}} := \boldsymbol{F}_\Delta \cdot \boldsymbol{B}_n^e \cdot (\boldsymbol{F}_\Delta)^{\text{T}}, \quad \boldsymbol{\varepsilon}_{n+1}^{e\,\text{trial}} := \frac{1}{2}\ln\left[\boldsymbol{B}_{n+1}^{e\,\text{trial}}\right].$$

(ii) *infinitesimal-strain update.* The general elastic predictor/return mapping algorithm using the relationship between $\boldsymbol{\tau}'$ and $\boldsymbol{\varepsilon}$.

(iii) *Post-processing.* Update the first effective Piola-Kirchhoff stress tensor ($\boldsymbol{P}'$),

$$\boldsymbol{P}'_{n+1} = \boldsymbol{\tau}'_{n+1} \cdot \boldsymbol{F}_{n+1}^{-\text{T}}.$$

Note that the relationship between $\boldsymbol{\tau}'$ and $\boldsymbol{\varepsilon}$ requires the exact calculation of derivative of logarithmic tensor or consideration of higher order terms in Taylor expansion while deriving the consistent tangent stiffness matrix (in Section 2.4.2).

In the infinitesimal-strain algorithm, we employ a two-invariant isotropic hyper-elasto-plasticity model based on the modified Cam-Clay model with associative flow rule for the reference unfrozen state [54, 61]. We then extend it to capture the mechanical be-

havior of the frozen state by introducing the cryo-suction effects (cf. Nishimura et al. [12], Gens [21], and Zhou [37]). Presumably, it is possible to extend this framework for the non-associative plasticity models, which may capture the constitutive responses more closely than the associative counterpart. However, in such cases, the restriction imposed by the principle of maximum plastic dissipation must be carefully considered before incorporating non-associative flow rule into the balance of energy equation [62]. This extension is out of the scope of this study, but will be considered in the near future.

Our starting point is to consider the frozen soil as a three-phase porous medium that consists of two constituents that can be viewed as the same two-phase media in two different phase regions (i.e. liquid vs. crystalline solid). An important implication is that one may use the corresponding thermodynamically-consistent Clausius–Clapeyron equation to establish relation among crystal ice pressure (p_C), liquid water pressure (p_L) and temperature (T) [12] at the thermodynamics equilibrium, i.e.,

$$p_C = \frac{\rho_C}{\rho_L} p_L - \rho_C l \ln \left(\frac{T}{273.15} \right), \tag{2.29}$$

where the unit of temperature is in Kelvin and l is the specific latent heat of fusion. Notice that, in (2.29), the ice pressure is a function of pore water pressure, temperature and the densities of both ice crystal and the unfrozen water. Due to the usage of the exponential/logarithmic mapping, both the ice and pore water pressure described above and the constitutive relation is described in the infinitesimal strain setting. The elastic responses of the frozen soil are replicated by an isotropic hyperelasticity model (cf. Borja [61] and Borja, Tamagnini, and Amorosi [63]), with a modification such that the volumetric constitutive law depends on the amount of cryo-suction pressure, i.e.,

$$p' = k s_{\text{cryo}} + (p_0 - k s_{\text{cryo}}) \exp \left(\frac{\varepsilon_{v0} - \varepsilon_v^e}{c_r} \right), \quad q = 3\mu \varepsilon_s^e, \tag{2.30}$$

where p_0 is the reference pressure; s_{cryo} is the cyo-suction given by $s_{\text{cryo}} = \max(p_C - p_L, 0)$;

k is the parameter describing the increase in cohesion with suction (cf. Alonso, Gens, and Josa [64]); ε_{v0} is the reference volumetric strain; c_r is the elastic compressibility parameter (or recompression index); ε_v^e and ε_s^e are the volumetric and deviatoric strain invariants of the elastic logarithmic strain, respectively; and μ is the elastic shear modulus. Note that the freezing and thawing processes should influence both the stiffness and strength of the three-phase frozen porous media. In this work, our focus is mainly on the latter, following the treatment of [12]. Nevertheless, a more comprehensive treatment can be also made by considering that the change of degree of ice saturation affects the elastic stiffness. This can be done via a purely phenomenological approach if sufficient experimental data are available or based on a theoretical approach, such as Eshelby's equivalent inclusion method (e.g. Zhou and Meschke [17] and Zhou [37]). The yield surface of the frozen soil that incorporates the cryo-suction effect is represented as follows,

$$f = \left[p' - \left(\frac{p_c + ks_{\text{cryo}}}{2}\right)\right]^2 + \frac{q^2}{M^2} - \left(\frac{p_c - ks_{\text{cryo}}}{2}\right)^2, \tag{2.31}$$

where p_c is the preconsolidation stress; M is the slope of critical state line; and p' and q are the mean normal and deviatoric stresses as defined below,

$$p' = \frac{1}{3}\operatorname{tr}(\boldsymbol{\tau}'), \quad q = \sqrt{\frac{3}{2}}\,\|\,\boldsymbol{\xi}\,\|, \quad \boldsymbol{\xi} = \boldsymbol{\tau}' - p'\boldsymbol{I}. \tag{2.32}$$

Figure 2.1 indicates how the yield surface and critical state line change from unfrozen to frozen state. We can identify that frozen soil holds stable without the confining pressure due to the apparent cohesion by cryo-suction. We note that the preconsolidation stress (p_c) is assumed to be independent upon temperature (cf. Nishimura et al. [12]).

In the return mapping algorithm for the two-invariant plasticity model, we adopt the hardening law proposed in Borja and Tamagnini [54], Borja [61], Butterfield [65], and
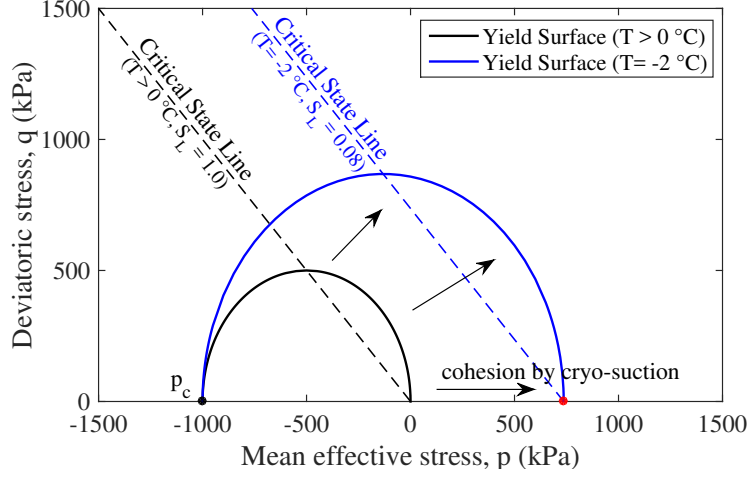
Figure 2.1: Change of the yield surface from unfrozen ($T > 0$ °C) to frozen state ($T = -2$ °C) – tension is positive

Hashiguchi [66, 67] which takes the following form,

$$\frac{\dot{\nu}}{\nu} = -c_c \frac{\dot{p}_c}{p_c}, \tag{2.33}$$

where ν is the specific volume of the soil; c_c is a compressibility index (or compression index). This hardening law allows the hardening parameter p_c to be expressed exactly as a known function of the plastic volumetric strain ε_v^p as,

$$\dot{p}_c = -\frac{\dot{\varepsilon}_v^p}{c_c - c_r} p_c, \tag{2.34}$$

under the condition of $0 < c_r < c_c$ [54, 61]. Therefore, we employ the residual vector ($\boldsymbol{r}$) and unknown vector ($\boldsymbol{x}$) for a local Newton's iteration as follows:

$$\boldsymbol{r} = \begin{Bmatrix} \varepsilon_v^e - \varepsilon_v^{e\ \text{trial}} + \Delta\lambda\partial_{p'}f \\ \varepsilon_s^e - \varepsilon_s^{e\ \text{trial}} + \Delta\lambda\partial_{q'}f \\ f \end{Bmatrix}; \quad \boldsymbol{x} = \begin{Bmatrix} \varepsilon_v^e \\ \varepsilon_s^e \\ \Delta\lambda \end{Bmatrix}; \quad \boldsymbol{a} = \boldsymbol{r'}\left(\boldsymbol{x}\right), \tag{2.35}$$

where $\Delta\lambda$ is the incremental plastic multiplier; f is the yield function in (2.31), while $\partial_{p'}f$ and $\partial_q f$ indicate the derivative of f with respect to p' and q, respectively; $\boldsymbol{a}$ is the local

24

consistent tangent operator. More details regarding the process of the return mapping algorithm presented herein can be found in Borja and Tamagnini [54]. Note that the cryo-suction pressure (s_{cryo}) in the local Newton mapping algorithm adopts the global variables of liquid water pressure p_{L} and temperature T (for p_{C}). As the thermal and hydraulic convection-diffusion takes place in the porous media, these two physical quantities are determined not solely from a local material state, but also dependent on the material state of the neighborhood. Through the thermo-hydro-mechanical coupling effect, these non-local effects may affect the path-dependent responses [20].

2.3.2 Freezing characteristic function for frozen soil

In the unsaturated soil mechanics, the water retention curve or the soil-water character-istic function can be derived from the liquid-air interface energy between gas and liquid phases coexisting in the pores. This concept can be expanded to a three-phase frozen soil in which the frozen soil is idealized as a solid-ice-water mixture. In this case, one relates the difference between the pressure of the ice crystal and the unfrozen water with the degree of saturation of liquid or ice crystal while neglecting the presence of water or vapor in the pores (e.g. O'Neill [35] and O'Neill and Miller [36]). The similarity of the soil retention characteristic to the soil moisture characteristic has been studied in a number of previous studies such as Koopmans and Miller [68] and Spaans and Baker [69]. Assume that pre-melting theory is valid such that thin water film exists in between the ice crystal and solid skeleton, one important mechanism that leads to this similarity is the relative small water-ice interfacial force compared to the water-solid interfacial force. This allows the absorptive forces dominate. Since adsorptive forces only act on the liquid phase, whether ice or air is present at the other side of the water-solid interface does not affect the retention significantly. Consequently, the ice-water interfacial energy can be neglected.

Mimicking the air-water-suction relation in the van Genuchten retention model (cf.

Van Genuchten [70]) and neglecting the hysteresis due to the dissipation during the freeze-thaw cycles, one may introduce a non-hysteretic phenomenological characteristic function to relate the liquid water saturation with the pressure difference between the crystal ice and the liquid water ($p_C - p_L > 0$), which is cryo-suction [12, 37], i.e.,

$$S_L = \left[1 + \left(\frac{s_{cryo}}{P}\right)^n\right]^{-m}, \quad s_{cryo} = \max(p_C - p_L, 0), \tag{2.36}$$

in which P, n and m are material parameters. P is a scaling parameter, and n and m are empirical constants defining the shape of the freezing characteristic curve ($m = \frac{n-1}{n}$). We note that the capillary suction pressure in the water retention curve by Van Genuchten [70] for unsaturated soil is replaced by the cryo-suction for saturated frozen soil [12]. We remark that other models for freezing characteristic function can be used (e.g. O'Neill and Miller [36] - using a given value of water content and the porosity; Zhou [37] - a simplified temperature only model). Finally, one may substitute (2.29), the Clausius–Clapeyron equation, into (2.36) to express the freezing characteristic function of (2.36) as a relation among the degree of saturation of liquid water (S_L), pore water pressure (p_L) and the temperature (T) when $s_{cryo} > 0$, that is,

$$S_L = \left[1 + \left[\frac{-(1 - \rho_C/\rho_L)p_L - \rho_C l \ln(T/273.15)}{P}\right]^n\right]^{-m}, \tag{2.37}$$

where the unit of temperature T is Kelvin; l stands for the latent heat of fusion. In the numerical examples shown in Section 2.5, we adopted the parameter $n = 2.0$, the reference pressure $P = 200$ kPa and the latent heat of fusion $l = 334$ kJ/kg (cf. Nishimura et al. [12]). The freezing characteristic function becomes a unity when $T > 0\,°C$, which leads to unfrozen state fully saturated only with liquid water ($S_L = 1.0$). Figure 2.3.2 (a) shows how the freezing characteristic function varies by temperature (T) and liquid water pressure (p_L). It should be noted that the pore pressure dependence of the freezing characteristic function remains important near the phase transition temperature but exhibits

relatively minor impact on the degree of saturation of water once the phase transition completes [12].

The constitutive law for the flow of the unfrozen water is assumed to be Darcian. We adopt the saturation-dependent relative permeability (e.g. Luckner, Van Genuchten, and Nielsen [71]) and the temperature-dependent viscosity (e.g. Grant [72]). As a result, for the unfrozen water, the evolution of hydraulic conductivity tensor ($\boldsymbol{k}$) is formulated using the relation below,

$$\boldsymbol{k} = \frac{k_r}{\mu_r}\boldsymbol{k}_{\mathrm{L}}, \tag{2.38}$$

where k_r and μ_r are the relative permeability and the temperature-dependent viscosity, respectively. $\boldsymbol{k}_{\mathrm{L}}$ is the isotropic hydraulic conductivity tensor at the reference temperature. Meanwhile, the relative permeability and the temperature-dependent viscosity are empirical relations that read,

$$k_r = \sqrt{S_{\mathrm{L}}}\left[1 - \left(1 - S_{\mathrm{L}}^{1/m}\right)^m\right]^2, \; \mu_r = 1.5963 \times 10^{-2}\exp\left(\frac{509.53}{T - 150}\right). \tag{2.39}$$

Here m is a material parameter described above ($m = \frac{n-1}{n}$), T is the temperature in Kelvin and S_{L} is the saturation of liquid water described by freezing characteristic function [17, 72]. Figure 2.3.2 (b) presents how the relative permeability (k_r) changes under various liquid water pressure and temperature conditions. The relative permeability is highly sensitive to the change of liquid water pressure and temperature. Nevertheless, the relative permeability and hence the hydraulic conductivity approach to zero once the temperature is lower than approximately $-2\,^{\circ}\mathrm{C}$ regardless of the liquid water pressure. Meanwhile, a decrease in temperature will also reduce the viscosity. These two mechanisms make it difficult for the supercooled water to flow as the temperature drops.
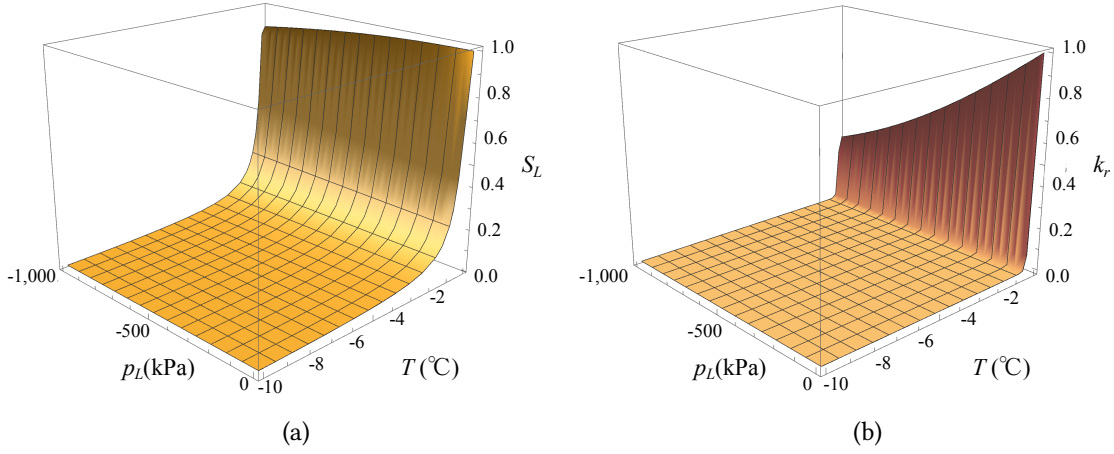
Figure 2.2: (a) Freezing characteristic function (S_{L}, degree of saturation) and (b) Relative permeability (k_r) under different liquid water pressure (p_{L}) and temperature (T) conditions

2.4 Variational formulation

In this section, we introduce the variational form, the corresponding equal-order displacement-liquid water pressure-temperature finite element implementation, and the corresponding stabilization procedure of the thermo-hydro-mechanical model for frozen soil undergoing finite deformation range. We first define the standard weak form of the poromechanics problem based on the conservation laws derived in Section 2.2.

2.4.1 Galerkin form

We proceed the numerical implementation by deriving a weighted residual statement suitable for a total Lagrangian formulation. Firstly, we can consider a reference domain $\mathcal{B}$ whose boundary $\partial\mathcal{B}$ is composed of the Dirichlet and von Neumann boundaries as,

$$\partial\mathcal{B} = \overline{\partial\mathcal{B}_{\boldsymbol{u}} \cup \partial\mathcal{B}_{\boldsymbol{t}}} = \overline{\partial\mathcal{B}_{p_{\mathrm{L}}} \cup \partial\mathcal{B}_{Q_{p_{\mathrm{L}}}}} = \overline{\partial\mathcal{B}_T \cup \partial\mathcal{B}_{Q_T}}, \tag{2.40}$$

$$\emptyset = \overline{\partial\mathcal{B}_{\boldsymbol{u}} \cap \partial\mathcal{B}_{\boldsymbol{t}}} = \overline{\partial\mathcal{B}_{p_{\mathrm{L}}} \cap \partial\mathcal{B}_{Q_{p_{\mathrm{L}}}}} = \overline{\partial\mathcal{B}_T \cap \partial\mathcal{B}_{Q_T}}, \tag{2.41}$$

where $\partial\mathcal{B}_{\boldsymbol{u}}$ is the solid displacement boundary; $\partial\mathcal{B}_{\boldsymbol{t}}$ is the solid traction boundary; $\partial\mathcal{B}_{p_{\mathrm{L}}}$ is the liquid water pressure boundary; $\partial\mathcal{B}_{Q_{p_{\mathrm{L}}}}$ is the liquid water fluid flux boundary; $\partial\mathcal{B}_{T}$ is the temperature boundary; $\partial\mathcal{B}_{Q_{T}}$ is the heat flux boundary. Dirichlet boundary conditions of the thermo-hydro-mechanical (THM) problem for frozen soil read,

$$
\begin{cases}
\boldsymbol{u} = \overline{\boldsymbol{u}} \ \text{ on } \ \partial\mathcal{B}_{\boldsymbol{u}}, \\[2mm]
p_{\mathrm{L}} = \overline{p_{\mathrm{L}}} \ \text{ on } \ \partial\mathcal{B}_{p_{\mathrm{L}}}, \\[2mm]
T = \overline{T} \ \text{ on } \ \partial\mathcal{B}_{T}.
\end{cases}
\tag{2.42}
$$

Meanwhile, the von Neumann boundary conditions that describe the traction and fluxes read,

$$
\begin{cases}
\boldsymbol{P} \cdot \boldsymbol{N} = \overline{\boldsymbol{t}} \ \text{ on } \ \partial\mathcal{B}_{\boldsymbol{t}}, \\[2mm]
-\boldsymbol{N} \cdot \boldsymbol{Q}_{p_{\mathrm{L}}} = \overline{Q}_{p_{\mathrm{L}}} \ \text{ on } \ \partial\mathcal{B}_{Q_{p_{\mathrm{L}}}}, \\[2mm]
-\boldsymbol{N} \cdot \boldsymbol{Q}_{T} = \overline{Q}_{T} \ \text{ on } \ \partial\mathcal{B}_{Q_{T}},
\end{cases}
\tag{2.43}
$$

where $\boldsymbol{N}$ is the outward normal vector on the reference configuration $\partial\mathcal{B}$. In addition, we consider the trial space for the weak form that reads,

$$
V_{\boldsymbol{u}} = \left\{ \boldsymbol{u} : \mathcal{B} \to \mathbb{R}^{3} | \boldsymbol{u} \in [H^{1}(\mathcal{B})]^{3}, \ \boldsymbol{u}|_{\partial\mathcal{B}_{\boldsymbol{u}}} = \overline{\boldsymbol{u}} \right\},
\tag{2.44}
$$

$$
V_{p_{\mathrm{L}}} = \left\{ p_{\mathrm{L}} : \mathcal{B} \to \mathbb{R} | p_{\mathrm{L}} \in H^{1}(\mathcal{B}), \ p_{\mathrm{L}}|_{\partial\mathcal{B}_{p_{\mathrm{L}}}} = \overline{p_{\mathrm{L}}} \right\},
\tag{2.45}
$$

$$
V_{T} = \left\{ T : \mathcal{B} \to \mathbb{R} | T \in H^{1}(\mathcal{B}), \ T|_{\partial\mathcal{B}_{T}} = \overline{T} \right\}.
\tag{2.46}
$$

Here, H^{1} denotes the Sobolev space of degree one. The admissible variations of the displacement $\boldsymbol{\eta}$, liquid water pressure ψ and temperature θ read,

$$
V_{\boldsymbol{\eta}} = \left\{ \boldsymbol{\eta} : \mathcal{B} \to \mathbb{R}^{3} | \boldsymbol{\eta} \in [H^{1}(\mathcal{B})]^{3}, \ \boldsymbol{\eta}|_{\partial\mathcal{B}_{\boldsymbol{u}}} = \boldsymbol{0} \right\},
\tag{2.47}
$$

$$
V_{\psi} = \left\{ \psi : \mathcal{B} \to \mathbb{R} | \psi \in H^{1}(\mathcal{B}), \ \psi|_{\partial\mathcal{B}_{p_{\mathrm{L}}}} = 0 \right\},
\tag{2.48}
$$

$$V_\theta = \left\{ \theta : \mathcal{B} \to \mathbb{R} | \theta \in H^1(\mathcal{B}), \; \theta|_{\partial \mathcal{B}_T} = 0 \right\}. \tag{2.49}$$

Therefore, the weighted residual statement of the balance of linear momentum, mass and energy are: find $u \in V_u$, $p_L \in V_{p_L}$ and $T \in V_T$ such that for all $\eta \in V_\eta$, $\psi \in V_\psi$ and $\theta \in V_\theta$,

$$G\left(u, p_L, T, \eta\right) = H\left(u, p_L, T, \psi\right) = L\left(u, p_L, T, \theta\right) = 0, \tag{2.50}$$

where $G : V_u \times V_{p_L} \times V_T \times V_\eta \to \mathbb{R}$ is the weak statement of the balance of linear momentum, that is,

$$G\left(u, p_L, T, \eta\right) = \int_{\mathcal{B}} \left(\nabla^X \eta : P - J\rho\eta \cdot G\right) dV - \int_{\partial \mathcal{B}_t} \eta \cdot \bar{t} d\Gamma. \tag{2.51}$$

$H : V_u \times V_{p_L} \times V_T \times V_\psi \to \mathbb{R}$ is the weak statement of the balance of mass, that is,

$$\begin{aligned} H\left(u, p_L, T, \psi\right) \quad &= \int_{\mathcal{B}} \psi \left[(1 - \phi^S)(\rho_L - \rho_C)\dot{S}_L\right] J dV + \int_{\mathcal{B}} \psi \left[\rho_L S_L + \rho_C(1 - S_L)\right] \dot{J} dV \\ &- \int_{\mathcal{B}} \nabla^X \psi \cdot W dV - \int_{\partial \mathcal{B}_{Q_p}} \psi \overline{Q}_p d\Gamma. \end{aligned} \tag{2.52}$$

And $L : V_u \times V_{p_L} \times V_T \times V_\theta \to \mathbb{R}$ is the weak statement of the balance of energy, that is,

$$\begin{aligned} L\left(u, p_L, T, \theta\right) \quad &= \int_{\mathcal{B}} \theta \left(Jc_F\right) \dot{T} dV + \int_{\mathcal{B}} \nabla^X \theta \cdot K_T \cdot \nabla^X T dV \\ &- \int_{\mathcal{B}} \theta \left(\frac{\phi^L S_L c_{FL}}{\rho_L} W \cdot F^{-T} \cdot \nabla^X T\right) dV - \int_{\partial \mathcal{B}_{Q_T}} \theta \overline{Q}_T d\Gamma. \end{aligned} \tag{2.53}$$

2.4.2 Consistent linearization

Since we use an implicit time integration scheme to solve the system of equations, it is essential to either approximate or obtain the exact expression of the consistent tangent such that the solution fields of u, p_L, and T can be updated in an incremental fashion.

Here we perform the consistent linearization of the weak form (2.51), (2.52) and (2.53) with respect to variation of displacement, pore pressure and temperature. We first focus on the linearization of momentum balance equation which adopts the infinitesimal strain algorithm including the pre and post– processing steps. This can be represented as:

$$\delta G\left(\boldsymbol{u}, p_{\mathrm{L}}, T, \boldsymbol{\eta}\right) \quad = \int_{\mathcal{B}} \nabla^{\boldsymbol{X}} \boldsymbol{\eta} : \boldsymbol{A} : \delta \boldsymbol{F} dV - \int_{\mathcal{B}} \nabla^{\boldsymbol{X}} \boldsymbol{\eta} : \delta(J \boldsymbol{F}^{-\mathrm{T}} \bar{p}) dV$$
$$- \int_{\mathcal{B}} \boldsymbol{\eta} \cdot \delta\left(J \rho \boldsymbol{G}\right) - \int_{\partial \mathcal{B}_t} \boldsymbol{\eta} \cdot \delta \bar{\boldsymbol{t}} d\Gamma = 0, \tag{2.54}$$

where $\boldsymbol{A}$ in the first term is defined as in (2.55) below. The partial derivative of the effective first Piola-Kirchhoff stress with respect to the deformation gradient or other tangential stiffness tensor stemmed from other energy-conjugate pair must be sought, that is,

$$\boldsymbol{A} \equiv \frac{\partial \boldsymbol{P}'}{\partial \boldsymbol{F}}, \quad \boldsymbol{P}' = J\boldsymbol{\sigma}' \cdot \boldsymbol{F}^{-\mathrm{T}} = \boldsymbol{\tau}' \cdot \boldsymbol{F}^{-\mathrm{T}}. \tag{2.55}$$

Expressing $\boldsymbol{A}$ in terms of index notation using the effective Kirchhoff stress $\boldsymbol{\tau}'$ and considering two point tensors $\boldsymbol{F}$ and $\boldsymbol{P}'$ yield,

$$A_{iMkN} = \frac{\partial P'_{iM}}{\partial F_{kN}} = \frac{\partial \tau'_{ip}}{\partial F_{kN}} F^{-1}_{Mp} + \tau'_{ip} \frac{\partial F^{-1}_{Mp}}{\partial F_{kN}}. \tag{2.56}$$

Note that the difference of $\boldsymbol{F}^{-1}$ and $\boldsymbol{F}^{-\mathrm{T}}$ should be considered in tensor and index notations,

$$\boldsymbol{F}^{-1} = F^{-1}_{Ji} \boldsymbol{G}_J \otimes \boldsymbol{g}_i, \quad \boldsymbol{F}^{-\mathrm{T}} = F^{-1}_{Ji} \boldsymbol{g}_i \otimes \boldsymbol{G}_J, \tag{2.57}$$

where $\boldsymbol{g}_i$ and $\boldsymbol{G}_J$ stand for the basis vectors of current and reference configurations, respectively. An logarithmic/exponential mapping is employed to allow infinitesimal strain constitutive law extended into the geometrical nonlinear regime [40, 59]. As a result, the Kirchhoff stress in the first term of (2.56) can be updated by means of the incremental

constitutive function of small strain algorithm ($\tilde{\boldsymbol{\tau}}$)

$$\frac{\partial \boldsymbol{\tau}'}{\partial \boldsymbol{F}} = \frac{\partial \tilde{\boldsymbol{\tau}}}{\partial \boldsymbol{\epsilon}^{e \text{ trial}}} : \frac{\partial \boldsymbol{\epsilon}^{e \text{ trial}}}{\partial \boldsymbol{B}^{e \text{ trial}}} : \frac{\partial \boldsymbol{B}^{e \text{ trial}}}{\partial \boldsymbol{F}}, \tag{2.58}$$

where,

$$\frac{\partial \tilde{\boldsymbol{\tau}}}{\partial \boldsymbol{\epsilon}^{e \text{ trial}}} = \text{D} = \text{the infinitesimal elastoplastic consistent tangent modulus,} \tag{2.59}$$

$$\frac{\partial \boldsymbol{\epsilon}^{e \text{ trial}}}{\partial \boldsymbol{B}^{e \text{ trial}}} = \text{L} = \frac{\partial \ln \boldsymbol{B}^{e \text{ trial}}}{\partial \boldsymbol{B}^{e \text{ trial}}}, \tag{2.60}$$

$$\frac{\partial \boldsymbol{B}^{e \text{ trial}}}{\partial \boldsymbol{F}} = \text{B}, \quad \text{B}_{ipkN} = \delta_{ik} \left(\boldsymbol{F}^{e \text{ trial}} \right)_{pN} + \delta_{pk} \left(\boldsymbol{F}^{e \text{ trial}} \right)_{iN}, \tag{2.61}$$

by the definition of the left Cauchy-Green tensor $\boldsymbol{B}$.

As stated, D can be obtained from the infinitesimal-strain constitutive model in Section 2.3.1. More details regarding the process of deriving the consistent tangent operator D can be found in Borja and Tamagnini [54]. In the second term of (2.56), the tensor derivative of the inverse of deformation gradient can be derived using the derivative of the second order identity tensor, which gives:

$$\frac{\partial F_{Mp}^{-1}}{\partial F_{kN}} = -F_{Ml}^{-1} \delta_{lk} \delta_{MN} F_{Mp}^{-1} = -F_{Mk}^{-1} F_{Np}^{-1}. \tag{2.62}$$

Note that the linearization for update of the effective first Piola-Kirchhoff stress ($\boldsymbol{P}'$) in (2.55) includes not only the consistent tangent operator from the infinitesimal-strain constitutive model (2.59) but other terms as in (2.56) to (2.62) to be represented in the total Lagrangian framework considering the geometrical nonlinearity at finite deformation regime. As stated, the associative flow rule is used and the general elastic predictor/return-mapping algorithm is adopted through the relationship between the Kirchhoff stress ($\boldsymbol{\tau}'$) and the elastic logarithmic strain ($\boldsymbol{\varepsilon} = \frac{1}{2} \ln \boldsymbol{B}$), from the left Cauchy-Green tensor $\boldsymbol{B}$. Note again that this relation requires the exact calculation of derivative of logarithmic tensor

32

or consideration of higher order terms in Taylor expansion while deriving the consistent tangent stiffness matrix. The following relations can be used for linearization [44]:

$$\delta \boldsymbol{F} = \nabla^{\boldsymbol{X}}\left(\delta \boldsymbol{u}\right), \quad \delta \boldsymbol{F}^{-1} = -\boldsymbol{F} \cdot \nabla^{\boldsymbol{x}}\left(\delta \boldsymbol{u}\right), \quad \delta J = J \, \nabla^{\boldsymbol{x}} \cdot \left(\delta \boldsymbol{u}\right), \qquad (2.63)$$

where we recall the following identities [73, 74]: $\nabla^{\boldsymbol{x}}(\delta \boldsymbol{u}) = \nabla^{\boldsymbol{X}}(\delta \boldsymbol{u}) \cdot \boldsymbol{F}^{-1}$ and $\nabla^{\boldsymbol{x}} \cdot (\delta \boldsymbol{u}) = \nabla^{\boldsymbol{X}}(\delta \boldsymbol{u}) : \boldsymbol{F}^{-\mathrm{T}}$. Next the linearization of the mass balance equation reads:

$$
\begin{aligned}
\delta H\left(\boldsymbol{u}, p_{\mathrm{L}}, T, \psi\right) \quad &= \delta\left(\int_{\mathcal{B}} \psi\left[(1 - \phi^{\mathrm{S}})(\rho_{\mathrm{L}} - \rho_{\mathrm{C}})\dot{S}_{\mathrm{L}}\right] J dV\right) \\
&+ \delta\left(\int_{\mathcal{B}} \psi\left[\rho_{\mathrm{L}} S_{\mathrm{L}} + \rho_{\mathrm{C}}(1 - S_{\mathrm{L}})\right]\dot{J} dV\right) \\
&- \int_{\mathcal{B}} \nabla^{\boldsymbol{X}} \psi \cdot \delta \boldsymbol{W} dV - \int_{\partial \mathcal{B}_{Qp}} \psi \delta \overline{Q}_{p} d\Gamma, \qquad (2.64)
\end{aligned}
$$

where the linearization of S_{L} can be conducted by considering a function of p_{L} and T as in (2.37). In addition, we can use the relation $\dot{J} = J \, \nabla^{\boldsymbol{x}} \cdot \dot{\boldsymbol{u}}$ and $\nabla^{\boldsymbol{x}} \cdot \dot{\boldsymbol{u}} = \nabla^{\boldsymbol{X}} \dot{\boldsymbol{u}} : \boldsymbol{F}^{-\mathrm{T}}$ [74]. The linearization of the Lagragian relative liquid water mass flux, $\boldsymbol{W}$, requires the linearization of the pull-back permeability tensor $\boldsymbol{K}_{L}$, which is represented based on $\boldsymbol{k}$ in (2.38), that is,

$$
\begin{aligned}
\delta \boldsymbol{K}_{L} = \delta\left(J \boldsymbol{F}^{-1} \cdot \boldsymbol{k} \cdot \boldsymbol{F}^{-\mathrm{T}}\right) \quad &= \delta\left(J\right) \boldsymbol{F}^{-1} \cdot \boldsymbol{k} \cdot \boldsymbol{F}^{-\mathrm{T}} + J \delta\left(\boldsymbol{F}^{-1}\right) \cdot \boldsymbol{k} \cdot \boldsymbol{F}^{-\mathrm{T}} \\
&+ J \boldsymbol{F}^{-1} \cdot \delta\left(\boldsymbol{k}\right) \cdot \boldsymbol{F}^{-\mathrm{T}} + J \boldsymbol{F}^{-1} \cdot \boldsymbol{k} \cdot \delta\left(\boldsymbol{F}^{-\mathrm{T}}\right), \qquad (2.65)
\end{aligned}
$$

$$
\begin{aligned}
\text{with } \delta(\boldsymbol{k}) \quad &= \frac{\partial \boldsymbol{k}}{\partial k_{r}}\delta k_{r} + \frac{\partial \boldsymbol{k}}{\partial \mu_{r}}\delta \mu_{r} = \frac{\boldsymbol{k}_{\mathrm{L}}}{\mu_{r}}\frac{\partial k_{r}}{\partial S_{\mathrm{L}}}\delta S_{\mathrm{L}} + \left(-\frac{k_{r}}{\mu_{r}^{2}}\boldsymbol{k}_{\mathrm{L}}\right)\frac{\partial \mu_{r}}{\partial T}\delta T \\
&= \frac{\boldsymbol{k}_{\mathrm{L}}}{\mu_{r}}\frac{\partial k_{r}}{\partial S_{\mathrm{L}}}\frac{\partial S_{\mathrm{L}}}{\partial p_{\mathrm{L}}}\delta p_{\mathrm{L}} \\
&+ \left[\frac{\boldsymbol{k}_{\mathrm{L}}}{\mu_{r}}\frac{\partial k_{r}}{\partial S_{\mathrm{L}}}\frac{\partial S_{\mathrm{L}}}{\partial T} + \left(-\frac{k_{r}}{\mu_{r}^{2}}\boldsymbol{k}_{\mathrm{L}}\right)\frac{\partial \mu_{r}}{\partial T}\right]\delta T. \qquad (2.66)
\end{aligned}
$$

Finally the linearization of energy balance equation can be performed as the same

procedure for momentum and mass balance equations, that is,

$$
\begin{aligned}
\delta L\left(\boldsymbol{u}, p_{\mathrm{L}}, T, \theta\right) \quad &= \int_{\mathcal{B}} \theta \delta\left(J c_{\boldsymbol{F}} \dot{T}\right) dV + \int_{\mathcal{B}} \nabla^{\boldsymbol{X}} \theta \cdot \delta\left(\boldsymbol{K}_T \cdot \nabla^{\boldsymbol{X}} T\right) dV \qquad (2.67) \\
&- \int_{\mathcal{B}} \theta \delta\left(\frac{\phi^{\mathrm{L}} S_{\mathrm{L}} c_{\boldsymbol{F}\mathrm{L}}}{\rho_{\mathrm{L}}} \boldsymbol{W} \cdot \boldsymbol{F}^{-T} \cdot \nabla^{\boldsymbol{X}} T\right) dV - \int_{\partial \mathcal{B}_{Q_T}} \theta \delta \overline{Q}_T d\Gamma.
\end{aligned}
$$

Note that the linearization of $\boldsymbol{K}_T$ can be sought considering (2.25) and (2.27) following the procedure for the pull-back permeability tensor in (2.65).

2.4.3 Time discretization

In order to solve the transient boundary value problem, the weak statement in (2.50) is discretized in time. In this implementation, the solution is incrementally advanced via the backward Euler scheme following Sun, Ostien, and Salinger [43] and Sun [19]. The time-discretized weighted-residual form reads,

$$
\hat{G}\left(\boldsymbol{u}_{n+1}, p_{\mathrm{L}n+1}, T_{n+1}, \boldsymbol{\eta}\right) = \hat{H}\left(\boldsymbol{u}_{n+1}, p_{\mathrm{L}n+1}, T_{n+1}, \psi\right) = \hat{L}\left(\boldsymbol{u}_{n+1}, p_{\mathrm{L}n+1}, T_{n+1}, \theta\right) = 0 \quad (2.68)
$$

where the discrete weak form of the balance of linear momentum now reads

$$
\begin{aligned}
G\left(\boldsymbol{u}_{n+1}, p_{\mathrm{L}n+1}, T_{n+1}, \boldsymbol{\eta}\right) = \quad &\int_{\mathcal{B}}\left[\nabla^{\boldsymbol{X}} \boldsymbol{\eta} : \boldsymbol{P}_{n+1} - \left(J_{n+1} \rho_{n+1}\right) \boldsymbol{\eta} \cdot \boldsymbol{G}\right] dV \\
&- \int_{\partial \mathcal{B}_{\boldsymbol{t}}} \boldsymbol{\eta} \cdot \bar{\boldsymbol{t}}_{n+1} d\Gamma. \qquad (2.69)
\end{aligned}
$$

Similarly, the discrete weak from of the mass and energy balance equations can be represented as

$$
\begin{aligned}
H\left(\boldsymbol{u}_{n+1}, p_{\mathrm{L}n+1}, T_{n+1}, \psi\right) \quad &= \int_{\mathcal{B}} \psi\left[(1 - \phi_{n+1}^{\mathrm{S}})(\rho_{\mathrm{L}} - \rho_{\mathrm{C}}) \frac{(S_{\mathrm{L}})_{n+1} - (S_{\mathrm{L}})_n}{\Delta t}\right] J_{n+1} dV \\
&+ \int_{\mathcal{B}} \psi\left[\rho_{\mathrm{L}} S_{\mathrm{L}} + \rho_{\mathrm{C}}(1 - S_{\mathrm{L}})\right]_{n+1} J_{n+1} \frac{\nabla^{\boldsymbol{X}}\left(\boldsymbol{u}_{n+1} - \boldsymbol{u}_n\right)}{\Delta t} : \boldsymbol{F}_{n+1}^{-\mathrm{T}} dV
\end{aligned}
$$

$$-\int_{\mathcal{B}} \nabla^{\boldsymbol{X}} \psi \cdot \boldsymbol{W}_{n+1} dV - \int_{\partial \mathcal{B}_{Q_p}} \psi \overline{Q}_{p_{n+1}} d\Gamma, \tag{2.70}$$

$$\begin{aligned}
L\left(\boldsymbol{u}_{n+1}, p_{\mathrm{L}n+1}, T_{n+1}, \theta\right) \quad &= \int_{\mathcal{B}} \theta \left(J_{n+1} c_{\boldsymbol{F}n+1}\right) \frac{T_{n+1} - T_n}{\Delta t} dV \\
&+ \int_{\mathcal{B}} \nabla^{\boldsymbol{X}} \theta \cdot \boldsymbol{K}_{Tn+1} \cdot \nabla^{\boldsymbol{X}} T_{n+1} dV \\
&- \int_{\mathcal{B}} \theta \left[\left(\frac{\phi^{\mathrm{L}} S_{\mathrm{L}} c_{\boldsymbol{F}\mathrm{L}}}{\rho_{\mathrm{L}}}\right)_{n+1} \boldsymbol{W}_{n+1} \cdot \boldsymbol{F}_{n+1}^{-T} \cdot \nabla^{\boldsymbol{X}} T_{n+1} \right] dV \\
&- \int_{\partial \mathcal{B}_{Q_T}} \theta \overline{Q}_{Tn+1} d\Gamma.
\end{aligned} \tag{2.71}$$

2.4.4 Spatial discretization

In this study, we introduce the standard shape functions of equal-order interpolation (linear) to the testing functions and field variables. Therefore, the following approximations are adopted:

$$\begin{cases}
\boldsymbol{u} \approx \boldsymbol{u}^h = \sum_{a=1}^{n} \boldsymbol{N}_a \boldsymbol{u}_a, \\
p_{\mathrm{L}} \approx p_{\mathrm{L}}^h = \sum_{a=1}^{n} N_a p_{\mathrm{L}a}, \\
T \approx T^h = \sum_{a=1}^{n} N_a T_a,
\end{cases}
\qquad
\begin{cases}
\boldsymbol{\eta} \approx \boldsymbol{\eta}^h = \sum_{a=1}^{n} \boldsymbol{N}_a \boldsymbol{\eta}_a, \\
\psi \approx \psi^h = \sum_{a=1}^{n} N_a \psi_a, \\
\theta \approx \theta^h = \sum_{a=1}^{n} N_a \theta_a.
\end{cases} \tag{2.72}$$

Here the superscript h indicates a spatially discretized function; N_a is the shape function matrix; $\boldsymbol{u}_a$, $p_{\mathrm{L}a}$ and T_a are the nodal values of displacement, liquid water pressure, and temperature; $\boldsymbol{\eta}_a$, ψ_a and θ_a denotes the nodal values of corresponding test functions; n indicates the number of node per element. We can substitute the approximations of (2.72) into (2.68) and take $\hat{G}$, $\hat{H}$ and $\hat{L}$ as residuals of the full discrete system of equations for THM problems. This leads to three-field mixed finite element formulations of the thermo-hydro-mechanical model for frozen soil in which the Jacobian system in each Newton

update has a following form:

$$
\begin{bmatrix} \mathbf{A} & \mathbf{B}_1 & \mathbf{D}_1 \\ \mathbf{B}_2 & \mathbf{C} & \mathbf{E}_1 \\ \mathbf{D}_2 & \mathbf{E}_2 & \mathbf{F} \end{bmatrix} \begin{bmatrix} \delta\boldsymbol{u} \\ \delta p_{\mathrm{L}} \\ \delta\boldsymbol{T} \end{bmatrix} = - \begin{bmatrix} \mathbf{R}_{\mathrm{mom.}} \\ \mathbf{R}_{\mathrm{mas.}} \\ \mathbf{R}_{\mathrm{ene.}} \end{bmatrix}. \tag{2.73}
$$

Note that the Jacobian has a three by three block structure; $\delta\boldsymbol{u}$, δp_{L}, δT are the nodal incrementals over given time interval for displacement, liquid water pressure and temperature fields; $\mathbf{R}_{\mathrm{mom.}}$, $\mathbf{R}_{\mathrm{mas.}}$, $\mathbf{R}_{\mathrm{ene.}}$ are residuals expressed by the balance of linear momentum, mass and energy as in (2.68) to (2.71). For a detailed expression of 3×3 Jacobian, please refer to [75].

2.5 Numerical examples

We conducted four numerical simulations to test the applicability and robustness of the proposed thermo-hydro-mechanical model for frozen soil. Through these models, we analyze the geometrical effect during thawing by comparing results from infinitesimal and finite strain simulations. We demonstrate how the plastic dissipation influences the three-phase frozen porous medium at finite deformation range, and validate our predictions with experimental results. The first two examples are selected to analyze and validate the simulated phase-transition effect during the freezing and thawing processes. In the first example, we idealize the frozen soil deposit as a one dimensional domain subjected to an increased temperature at the top of the surface with drained boundary condition. Due to the temperature difference, heat flux developing on the top of the deposit leads to the thawing and therefore the ground consolidates until the steady state is reached. In another related example, we decrease the temperature at the top surface of a unfrozen soil deposit so that the outflow heat flux may instead lead to the freezing process starting at the top and developing through depth of the domain. The third example is adopted

a well injection problem. We formulate the frozen ground with a well at the center and apply both pore flux and temperature gradient to mimic the injection of hot water. In the last example, we examine the formation of shear band and the influence of plastic dissipation in a biaxial compression test. We vary the Taylor-Quinney coefficient and re-run the simulations to obtain the axial stress-displacement curve of the sample and analyze the effect of plastic dissipation. In addition, we obtain the shear band under different combinations of thermal conductivity and permeability to see how thermal and hydraulic couplings influence the regularization of THM formulation for frozen porous media.

2.5.1   Thawing consolidation of frozen ground

In this numerical example, we simulate a thawing consolidation process of frozen ground by a raised temperature prescribed at the top surface. The purpose of this example is to validate the numerical model and demonstrate the performance of numerical formulation when phase transition from crystal ice to liquid water occurs. It should be noted that other experimental data such as those reported in Zhang et al. [76] can also be used for validation purpose. We discretize the three-dimensional domain and fix the displacement at the bottom and radial surfaces to simulate an 1-D consolidation induced by thawing. The domain of frozen soil sample has a height of 10 cm and a cross-section of 0.3×0.3 cm^2 following the previous experimental set up by Yao, Qi, and Wu [77].

Figure 2.3 (a) shows the schematic diagram and test conditions. The initial temperature of the domain except the top surface is -1 °C and the surcharge load of 50 kPa is applied. Meanwhile, the temperature at the top surface is prescribed to be 20 °C with a drained condition by imposing zero pore pressure. The bottom end is kept at -1 °C and the radial surfaces are insulated and assumed to be undrained to consolidate only through the top surface. As a result of this setup, thawing consolidation progresses in time until a new isothermal status is reached. The material properties of solid, liquid water and crystal ice used in the simulations including the hydraulic conductivity of 7.0×10^{-9} m/s can be

found in detail from Yao, Qi, and Wu [77].

Figure 2.3 (b) shows the thawing settlement results obtained from both infinitesimal and finite strain simulations. In addition, the experimental results along with the previous numerical analyses performed by Yao, Qi, and Wu [77] are also presented in the same figure. This simulation is performed under the elastic range and we obtained the settlement at the top surface along with time. Both current infinitesimal and finite strain model show good agreement with the previous experiment data. Furthermore, we can identify that the infinitesimal strain model predicts larger vertical settlement compared to the corresponding finite strain model due to geometrical non-linearity effect (e.g., Li, Borja, and Regueiro [78]).

(a) Schematic diagram   (b) Thawing settlement
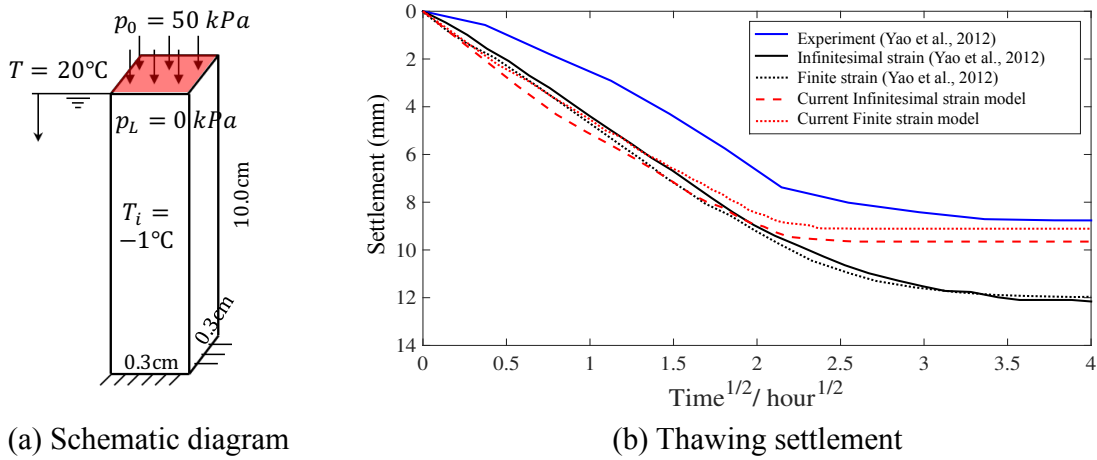
Figure 2.3: Schematic diagram of thawing simulation with boundary conditions (a) and the comparison of thawing settlement results (b) with the previous research [77]

2.5.2   Soil freezing from unfrozen state

In addition to the thawing simulation, the soil freezing test under 1-D heat flux condition is also conducted to check the numerical implementation regarding phase transition from unfrozen to frozen states. This example can be considered as an opposite situation of the previous numerical experiment of which the concept is adopted from the previous study

38

Table 2.1: Reference input parameters of homogeneous numerical model for material sensitivity test

Parameter	Description	Value	Unit
ρ_S	Mass density of solid	2.7	Mg/m^3
ρ_L	Mass density of liquid water	1.0	Mg/m^3
ρ_C	Mass density of crystal ice	0.9	Mg/m^3
c_S	Specific heat of solid	900	kJ/Mg/K
c_L	Specific heat of liquid water	4,180	kJ/Mg/K
c_C	Specific heat of crystal ice	2,100	kJ/Mg/K
κ_S	Thermal conductivity of solid	3.0×10^{-3}	kW/m/K
κ_L	Thermal conductivity of water	0.6×10^{-3}	kW/m/K
κ_C	Thermal conductivity of crystal ice	2.2×10^{-3}	kW/m/K
ϕ	Initial porosity	0.3	-
k	Intrinsic permeability	1.0×10^{-12}	m^2
μ_0	Viscosity (at 0 °C)	1.8×10^{-6}	kPa·s
c_r	Recompression index	0.035	-
c_c	Compression index	0.30	-

by Zhou [37]. Likewise in the schematic in Figure 2.3, we formulated three dimensional domain and fixed the bottom and radial surface displacement. With the initially unfrozen condition with temperature of 2 °C, we lower the temperature at the top to −2 °C so that the freezing process mobilizes to downward. The temperature at the bottom surface is fixed with 2 °C and the radial surfaces are insulated. Table 2.1 describes the input parameters used in this numerical simulation. We prescribed the impermeable boundary conditions except the bottom surface with drained condition ($p_L = 0$) to allow water supply.

The first column in Figure 2.4 shows the temperature profile along the depth in different times. We can see that the temperature reaches the steady state after 20 hours. The second column shows the suction pressure profile with different times in depth. It is observed that cryo-suction due to freezing is developed and progressed downward along the time. In addition, frost heaving or volume expansion due to freezing in frozen porous medium is captured through the change of porosity in the third column. The last column shows how the freezing fringe changes along with time through the ice saturation profile.
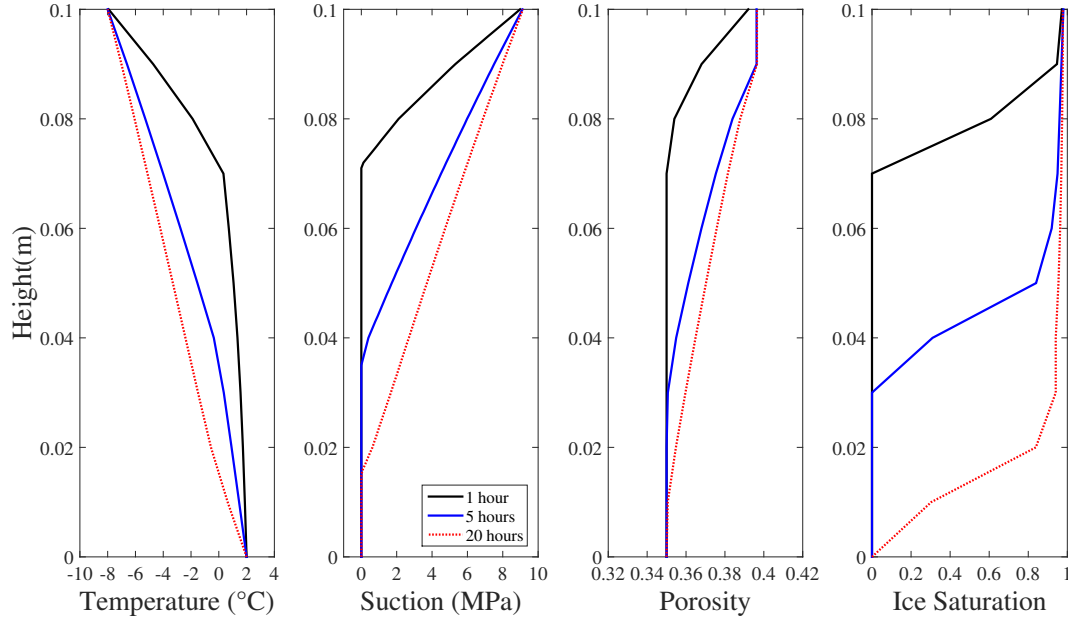
Figure 2.4: Transient responses of the freezing soil - changes of temperature, cryo-suction, porosity and ice saturation

2.5.3 Injecting unfrozen fluid in frozen ground

To demonstrate the forward-prediction capacity of the proposed model, an injection well problem is replicated numerically. Figure 2.5 shows the schematics of the current problem. Due to rotational symmetry, only a quarter of the domain is considered. The domain is defined by the length (L) of 0.38 m and the injection well radius (R) of 0.03 m. The initial temperature condition was set to -2 °C. The outer boundaries are assumed to be impermeable and insulated and mechanically confined with the pressure (p_0) of 100 kPa. We assumed the type of frozen soil as a lightly overconsolidated clay (OCR = 1.5), and the mechanical, hydraulic and thermal properties are described in Table 2.2.

We conducted the preliminary test prescribing the fluid flux without temperature change, and the constant mass flux of 0.001 cm^2/sec. was selected which had little influence (no equivalent plastic strain) on the domain during the given time (up to 10 hours from the initial state). Then we prescribed the fluid mass flux with temperature increase around the well surface to induce the inelastic behavior vicinity of the well causing the
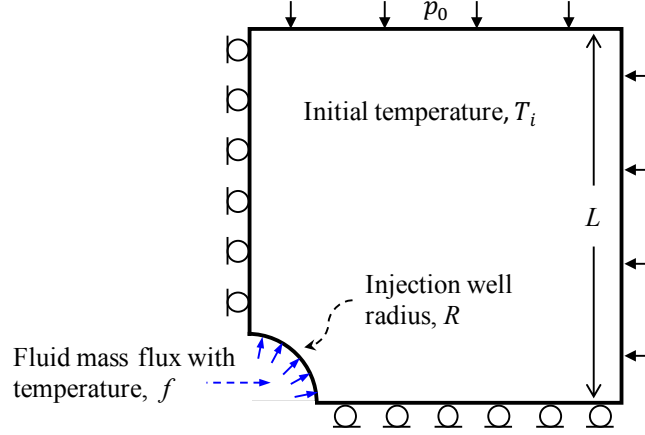
Figure 2.5: Schematics of injection well simulation: a quarter of the domain (the domain length, L = 0.38 m; the radius of injection well, R = 0.03 m; the confining pressure, p_0 = 100 kPa) was simulated from the initial temperature (T_i) of $-2\,°C$. The temperature of the fluid mass flux (f = 0.001 cm^2/sec.) was increased to $1\,°C$

plastic deformation. First of all, we compare the numerical results from infinitesimal and finite strain models. Figure 2.6 presents the thermo-hydro-mechanical behavior of injection well at different time for each model. As can be expected, phase transition zones expand after 10 hours from the initial state due to heat transfer. The increase of temper-

Table 2.2: Mechanical, hydraulic and thermal input parameters for injection well problem

Parameter	Description	Value	Unit
ρ_S	Mass density of solid	2.7	Mg/m^3
ρ_L	Mass density of liquid water	1.0	Mg/m^3
ρ_C	Mass density of crystal ice	0.9	Mg/m^3
c_S	Specific heat of solid	900	kJ/Mg/K
c_L	Specific heat of liquid water	4,190	kJ/Mg/K
c_C	Specific heat of crystal ice	2,095	kJ/Mg/K
κ_S	Thermal conductivity of solid	1.27×10^{-3}	kW/m/K
κ_L	Thermal conductivity of water	5.80×10^{-3}	kW/m/K
κ_C	Thermal conductivity of crystal ice	2.20×10^{-3}	kW/m/K
ϕ	Initial porosity	0.3	-
k	Intrinsic permeability	1.0×10^{-15}	m^2
μ_0	Viscosity (at 0 °C)	1.8×10^{-6}	kPa·s
c_r	Recompression index	0.03	-
c_c	Compression index	0.13	-
p_c	Preconsolidation stress	150	kPa

ature makes the crystal ice into liquid water through the freezing characteristic function (2.37), which leads to the change of liquid water pressure reflected on stream line configuration. Therefore, we can see the different phases from both the temperature contour and the hydraulic stream line induced by injecting unfrozen water around the well surface. With respect to the comparison of infinitesimal and finite strain model, we can see the little difference in heat transfer from temperature contours. However, the expansion of liquid water stream line is delayed in finite strain model compared to that from the infinitesimal model. This can be explained by the effect of geometrical nonlinearity, as we observed in Section 2.5.1 that the finite strain model estimates less settlement due to geometrical nonlinear effect [77, 78]. The more distinct difference between the infinitesimal and finite strain models is observed as the time progresses (Figure 2.6).

Next we analyze the effect of latent heat reflected on apparent heat capacity. In the concept of apparent heat capacity, the freezing characteristic function is introduced into heat capacity to incorporate the phase transition effect in the energy balance equation (2.23). Therefore, the effective specific heat of the frozen soil system changes along the temperature change. When the temperature ranges around 0.0 to -2.0 where the freezing characteristic function shows significant changes, the increase of effective specific heat of the system delays the heat transfer to account for the latent heat effect in phase transition. We note that the effect of latent heat due to phase transition is evaluated qualitatively. This consideration may play an important role in changes of temperature profile with time diffuse and related pore pressure distributions, elastic and inelastic behaviors for the frozen soil [79, 80]. Figure 2.7 shows how the apparent heat capacity influences the heat transfer and the frozen soil system. At the same time step, the heat transfer develops much faster when the latent heat effect is not considered. These are depicted both on temperature contour line and liquid water stream line. Moreover, as the phase transition zone further expands under the no latent heat effect model, the higher equivalent plastic strain is concentrated around the well surface. This can be further explained from
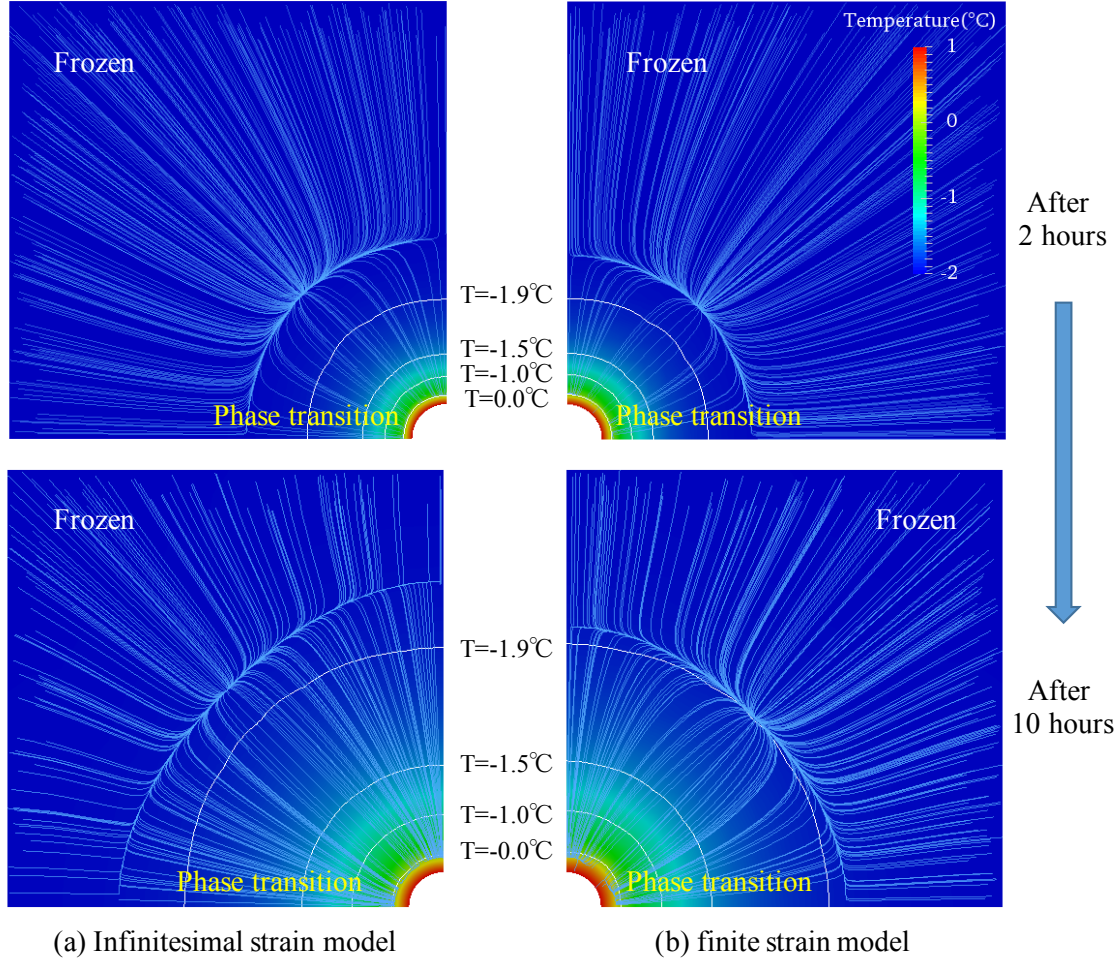
Figure 2.6: Thermo-hydro-mechanical behavior of frozen soil in the injection well problem - different phase zones indicated by the temperature contour and liquid water stream line under (a) infinitesimal and (b) finite strain models

the constitutive model (2.31), which includes the temperature change upon the yield surface size due to the cryo-suction. In other words, the increase of temperature accelerates the plastic behavior by shrinking the yield surface as an recursive process. We further present the influence of latent heat effect on the mechanical behavior along the time in Figure 2.8. Along with the prescribed temperature boundary condition, the changes of temperature around 0.03 m away from the well surface with time are described in Figure 2.8 (a) to evaluate the consideration of latent heat. While the region around the well surface becomes unfrozen state in 1 hour when the latent heat is ignored, the heat transfer is

delayed and the well surface region stays below $0\,^{\circ}$C until around 5 hours after the initial state when the latent heat is considered. This is also reflected on cryo-suction pressure changes in Figure 2.8 (b). The displacement and equivalent plastic strain results in Figure 2.8 (c) and (d) further identify the recursive process between the temperature increase and yield surface change. In other words, the more inelastic behavior around the well surface is observed in a shorter time when latent heat effect is not considered. However, the heat transfer delay due to latent heat effect causes less concentration of equivalent plastic strain by procrastinating the change of yield surface against temperature change.

(a) No latent heat effect

(b) Considering latent heat effect
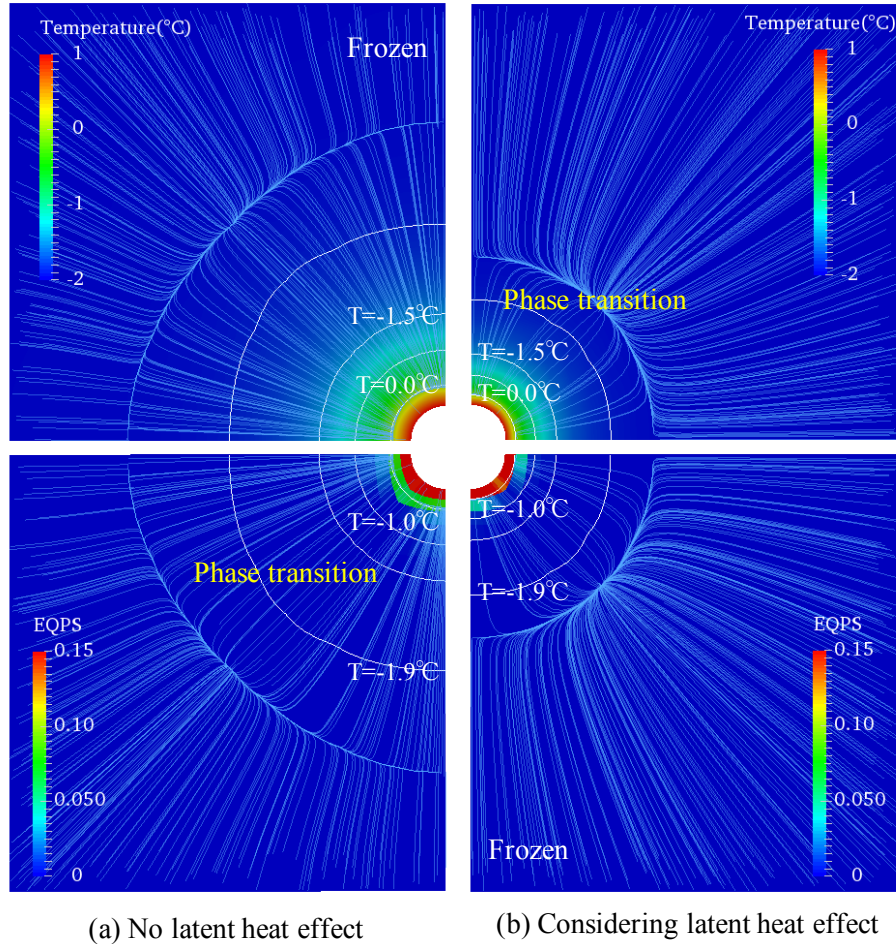
Figure 2.7: The effect of considering latent heat in apparent specific heat on thermo-hydro-mechanical behavior of frozen soil. Temperature and equivalent plastic strain distribution with fluid flow stream line is compared at the same time (after 2 hours from the initial state)
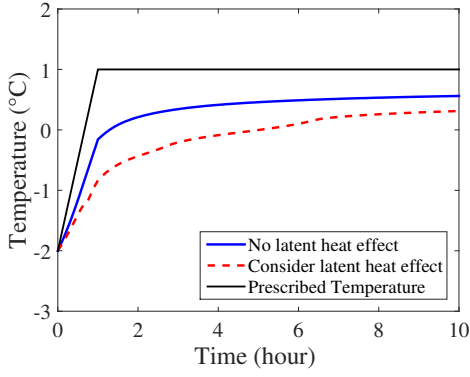
(a) Temperature vs. time around the injection well (0.03 m away from the well surface)
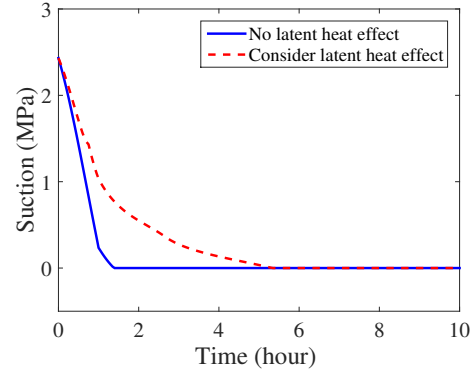
(b) cryo-suction pressure vs. time around the injection well (0.03 m away from the well surface)
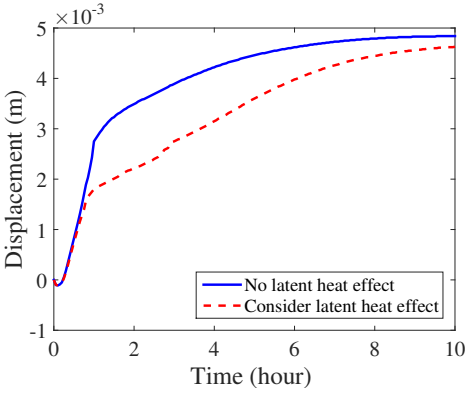
(c) Displacement vs. time at the injection well surface
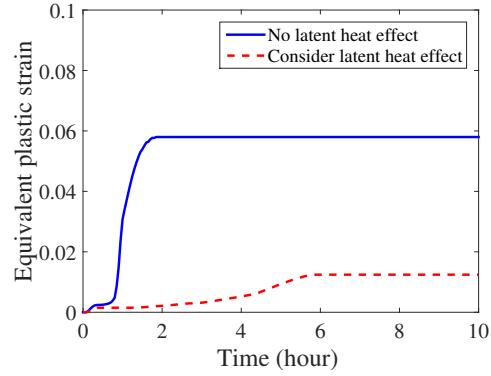
(d) Equivalent plastic strain vs. time around the injection well

Figure 2.8: The effect of considering latent heat in apparent specific heat on thermo-hydro-mechanical behavior of frozen soil: displacement vs. time at the well surface, cry-suction, temperature and equivalent plastic strain vs. time around the injection well (0.03 m away from the well surface)

2.5.4 Thermal softening by plastic dissipation in 2D biaxial test

In this section, we analyze how the plastic dissipation in frozen soil influences the mechanical behavior using numerical experiments. The plastic dissipation can be considered as heat generation due to frictional movement of soils in the shear band. We set up the numerical simulation based on 2D biaxial test (Figure 2.9). The top boundary moves downwards uniformly with the rate of 0.0002 m/sec., while a constant confining pressure of $\sigma_c = 1,000$ kPa is applied on the right side of the specimen. The bottom of the specimen is fixed, and the left side is fixed along the lateral direction for shear band

initiation. The gravity is neglected for this small specimen to simplify the problem. The specimen is globally undrained and thus no-fluid-flux boundary conditions are prescribed. All four surfaces are thermally insulated with no-thermal-flux condition. In other words, no Dirichlet boundary condition is adopted for both liquid water pressure and temperature fields. The mechanical, hydraulic and thermal properties of frozen soil were used based on the injection well problem (Table. 2.2), but the preconsolidation stress (p_c) of $3,000$ kPa was adopted.
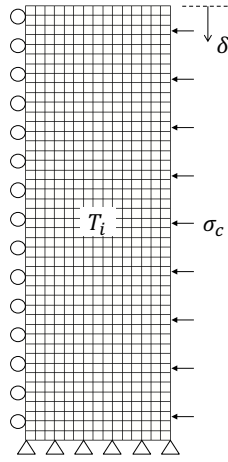
Figure 2.9: The schematic of the 2D biaxial test with the dimensions of 0.1 m $\times$ 0.3 m deforming in plane strain: the vertical displacement (δ) is applied on the top surface of the specimen, while the bottom of the specimen is fixed; the left side is fixed in the lateral direction; the confining pressure (σ_c) of 1000 kPa is applied on the right side of the specimen. The initial temperature (T_i) was set to -1 °C

In general, the loading rate needs to be fast enough so that we can see the effect of heat generation due to mechanical dissipation. Otherwise, the heat generated would reach the steady state condition before it acts. Figure 2.10 indicates how the shear band is formed using the equivalent plastic strain (at 80 sec.) and related temperature distributions to identify the effect of plastic dissipation, which leads to heat generation. We use the Taylor-Quinney coefficient β to control the plastic dissipation in the energy balance equation (2.28). When the plastic dissipation is considered ($\beta = 1.0$, Figure 2.10 (b)), the increase of temperature and heat transfer are observed around the shear band, while no

heat generation occurs when the plastic dissipation is totally ignored ($\beta = 0.0$, Figure 2.10 (c)). Considering the freezing characteristic function and mechanical constitutive model we used in this study, it can be expected that the increase of temperature leads to shrink the size of the yield surface. Figure 2.11 (a) shows how the local yield surface changes due to heat generation including the local stress path at two indicated points. Initially at Point 1, the stress path moves upward vertically (Path 1) due to the location of element and globally undrained boundary conditions with low permeability of the specimen. When the stress path reaches the yield surface, the shrink of yield surface because of heat generation enforces the stress path to follow the trajectory described in Path 1 of Figure 2.11 (a). At Point 2, the similar behavior is observed but its stress path changes before hitting the yield surface (Path 2). Due to the location of the element, the local liquid water pressure changes in the elastic regime even though the boundary conditions are globally undrained. We can further analyze the local behavior in Figure 2.11 (b). In the selected elements, the local deviatoric stress-strain behaviors are observed along with the volume changes. The thermal softening comes from the change of yield surface due to temperature increase along the shear band. The deviatoric stress-strain curves on Point 1 and 2 give the similar behavior. However, due to the mean effective stress changes in Point 2 with Path 2, the volume expansion shows different in Point 2 compared to Point 1. The specific volume changes including temperature changes are depicted in Figure 2.11 (c). Both curves of the specific volume-logarithm of $-p'$ do not encounter the critical state line of $-1.0°C$ which changes with the temperature. The higher increase of temperature at Point 1 compared to Point 2 is also identified.

We can further evaluate the effect of plastic dissipation in terms of the stress-strain behavior of frozen soil specimen. The vertical stress and axial strain obtained at the top of the specimen are presented in Figure 2.12 (a). Here we include additional test results with slow loading rate of 2.0×10^{-7} m/s. When the dissipation effect is ignored ($\beta = 0$), the hardening behavior is captured in the given range of axial strain ($< 5\%$). However,
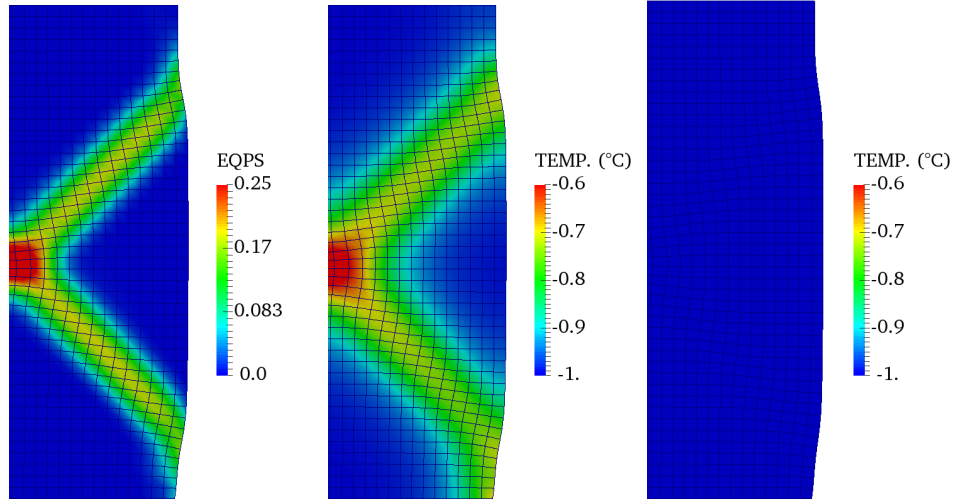
(a) Equivalent plastic strain   (b) Temperature ($\beta = 1.0$)   (c) Temperature ($\beta = 0.0$)

Figure 2.10: The effect of plastic dissipation in 2D biaxial test: Equivalent plastic strain forming shear band (a) at 80 seconds and the temperature distribution with different Taylor-Quinney coefficients ((b) $\beta = 1.0$, (c) $\beta = 0.0$ – no dissipation) in a deformed shape (scale=1.0)

the fast loading case (2.0×10^{-4} m/s) with plastic dissipation effects leads to the strain softening behavior after the axial strain increases more than 3%. Considering the local element behavior (in Figure 2.12), the thermal softening due to shrink of yield surfaces with temperature increase is reflected on the specimen behavior. When the slow loading rate is adopted (2.0×10^{-7} m/s), however, the vertical stress of the specimen follows the no dissipation case ($\beta = 0$) with slight decrease of stress values. In other words, the decrease of loading rate allows the heat to transfer fast enough which leads to the minor increase of temperature around the shear band. The increase of temperature with the slow loading rate was less than $0.05\,^{\circ}$C. Note that the mechanical constitutive model is rate independent. However, the proposed framework captures the effect of loading rate by including the mechanical dissipation as well as coupled governing equations for thermo-hydro-mechanical interactions. In addition, we present the volume change in the specimen using the porosity distribution (Figure 2.12 (b)). Note that the porosity distribution of slow loading rate shows little difference compared to the no dissipation

case. As can be seen, the strain localization and increase of porosity are concentrated around the shear band when the loading rate is slow (or when thermal dissipation is ignored). However, the increase of porosity from other parts as well as shear band in the specimen are observed when the plastic dissipation is considered. This indicates that the contribution of heat transfer from the temperature increase along the shear band leads to thermal softening by affecting the yield surface change.

2.5.5 Coupled THM effects of frozen soil system on shear band

The frozen soil system formulated in this study is not in an isothermal condition and the phase transition between the liquid water and crystal ice is considered. Thus, solid response is affected by both thermal and hydraulic couplings. As studied in the previous researches [19, 20, 81], shear band width is influenced by the thermal diffusivity as well as diffusivity of the pore fluid. To identify how thermal and hydraulic diffusivities influence the thermo-hydro-mechanical responses of frozen soil which include phase transition, we conducted a parametric study by changing the permeability and thermal conductivity.

The numerical experiment is set up based on the 2D biaxial test conducted in the previous section (Section 2.5.4). Likewise, Figure 2.9 shows the schematics of the test while the confining stress (σ_c) of 500 kPa was used. The same rate of moving boundary condition (0.0002 m/sec) was used on the top of the specimen. Note that the drained condition was applied on the top and bottom surfaces of the specimen to allow liquid water flow. Table 2.3 presents a set of intrinsic permeability and thermal conductivity of frozen soil. First we hold the permeability as the reference value and evaluate the effect of thermal conductivity by comparing the low and high values. Next we fix the thermal conductivity with the reference value and analyze shear band with low and high permeability.

Figure 2.13 demonstrates equivalent plastic strain, temperature distribution and the pore pressure at 150 sec. after the loading. The equivalent plastic strain results in the

49
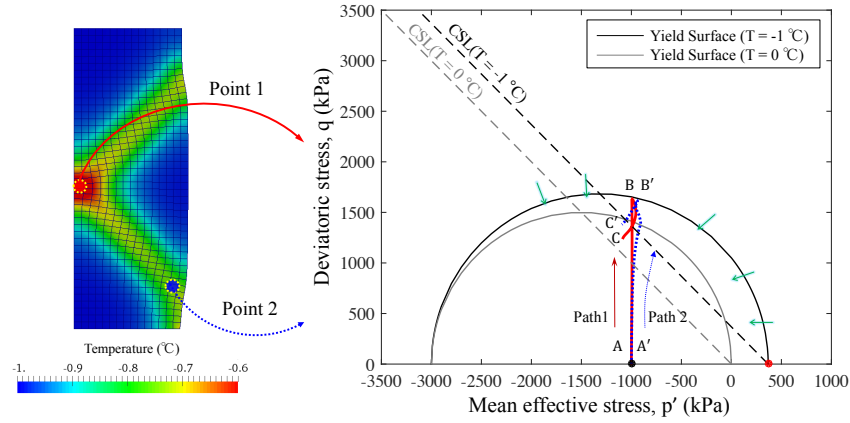
(a) The change of yield surface and stress paths at two different local elements due to increase of temperature by plastic dissipation (Point 1 with Path 1: A–B–C, and Point 2 with Path 2: A′–B′–C′)
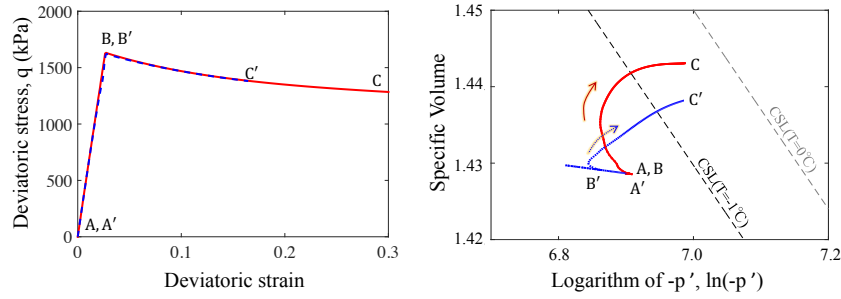
(b) The deviatoric stress vs. deviatoric strain curve and specific volume vs. logarithm of means effective stress $(\ln(-p'))$ curves at the two local elements (Path 1: A–B–C and Path 2: A′–B′–C′)
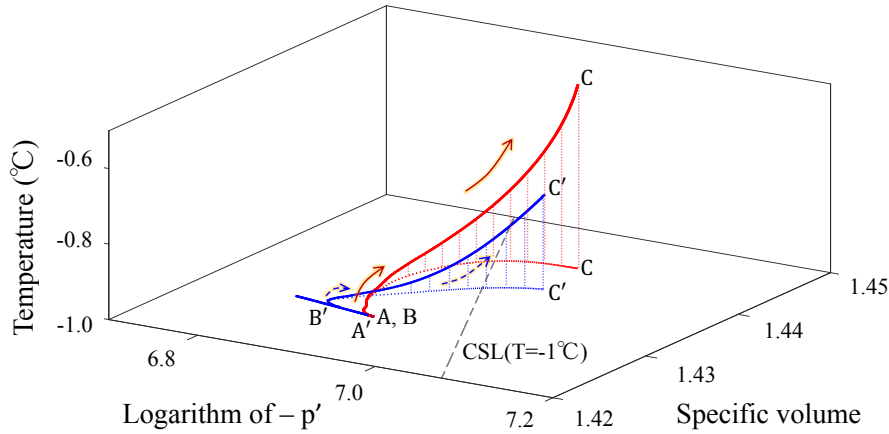
(c) The behavior of specific volumes with respect to logarithm of means effective stress $(\ln(-p'))$ including temperature change (following the trajectory of A–B–C and A′–B′–C′)

Figure 2.11: The effect of plastic dissipation in 2D biaxial test: the change of yield surface, stress path, deviatoric stress vs. strain and specific volume vs. logarithm of mean effective stress at two different local elements

50

(a) Vertical stress vs. strain obtained at the top surface of the specimen

(b) Comparison of porosity showing volume change in the specimen
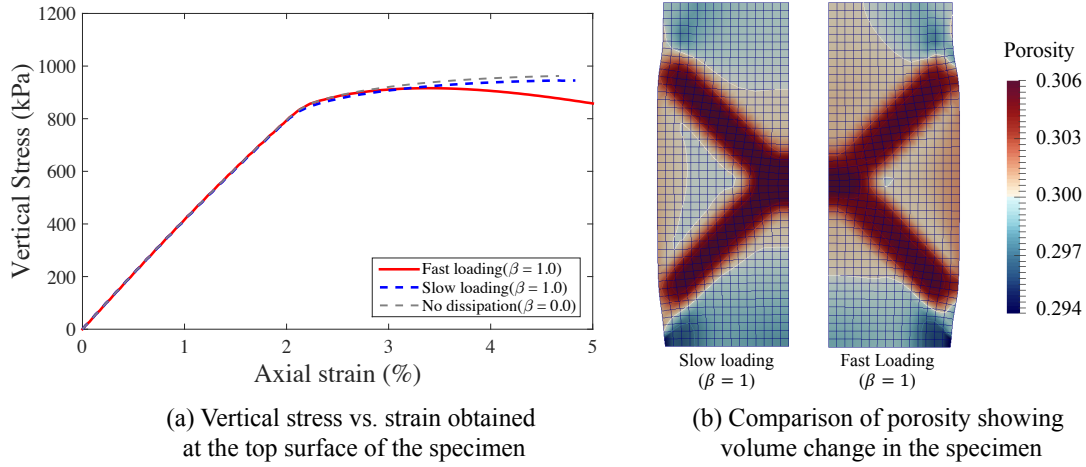
Figure 2.12: The effect of plastic dissipation reflected on the specimen. Fast and slow loading indicates 2.0×10^{-4} m/s and 2.0×10^{-7} m/s, respectively

formation of shear band under the high (left) and low (high) thermal conductivities. The onset of shear bands locates slightly different in both cases, but the concentration of equivalent plastic strain and shape of shear bands show little difference. The temperature distribution due to generation of heat by plastic dissipation on shear bands differs, however, because of thermal conductivity difference. As can be expected, the high thermal conductivity leads heat transfer much faster as in Figure 2.13 (b). The pore pressure increase shows little difference while the stream line of liquid fluid follows the onset of shear band (Figure 2.13 (c)). In this numerical experiment, the change of thermal diffusivity may affect the location of shear band due to heat transfer difference.

Next we fix the thermal conductivity and change the permeability. Figure 2.14 demonstrates equivalent plastic strain, temperature distribution and the liquid water pressure at

Table 2.3: Mechanical, hydraulic and thermal input parameters for thermo-hydro-mechanical coupling effects of frozen soil on shear band

Parameter	Low	Reference	High
Thermal conductivity (kW/m/K)	3.0×10^{-6}	3.0×10^{-3}	3.0×10^{0}
Intrinsic permeability (m^2)	1.0×10^{-20}	1.0×10^{-15}	1.0×10^{-10}

(a) Equivalent plastic strain

(b) Temperature
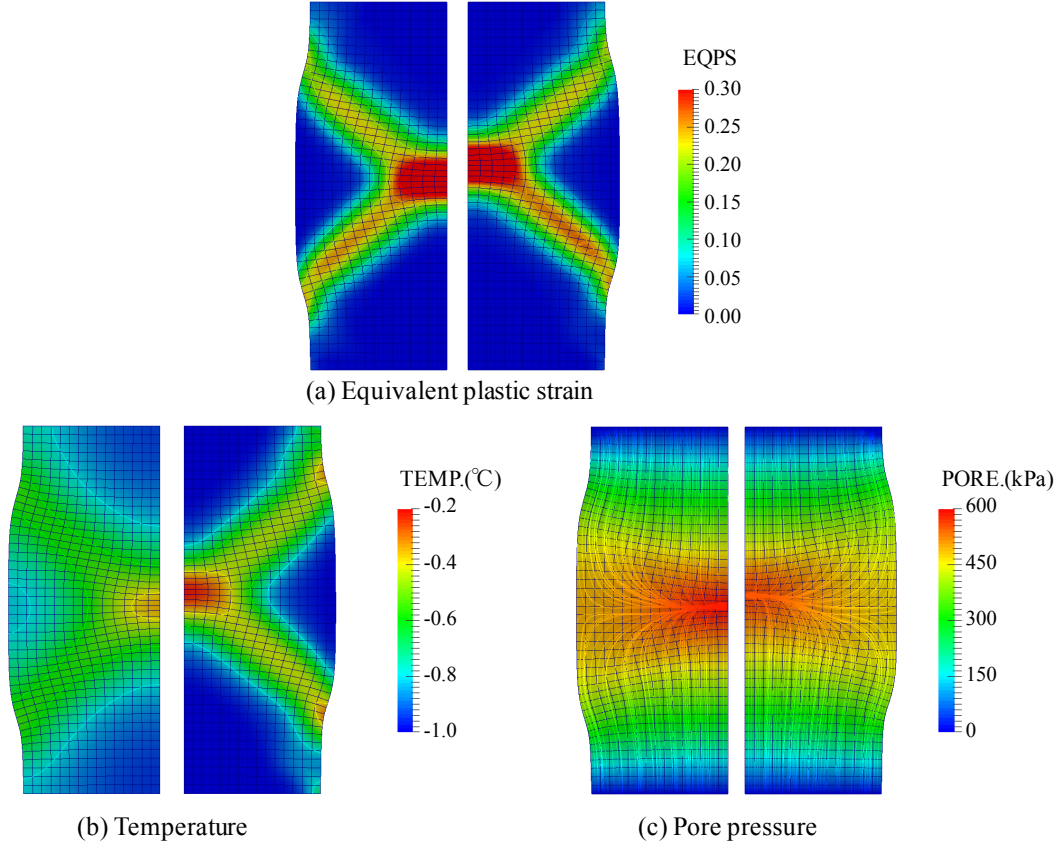
(c) Pore pressure

Figure 2.13: The effect of different thermal conductivities on shear band (equivalent plastic strain, temperature and pore pressure distributions): the left and right figures in (a), (b) and (c) present the results under high and low thermal conductivities, respectively

150 sec. after the loading with different permeability conditions. The little difference in initiation and formation of the shear band is observed. However, a marginally thicker shear banding and lower concentration of equivalent plastic strain is identified under the high permeability condition (Figure 2.14 (a)). In addition, slightly faster heat transfer is captured, which can be considered as convection effect in energy balance equation (Figure 2.14 (b)). By considering the temperature increase and yield surface change reflected on the solid constitutive model of this framework, the heat transfer accelerated by convection effects may contribute the size of shear band. The difference in permeability is identified from the results of pore pressure in Figure 2.14 (c), where the most excess pore pressure generated by loading is dissipated.

(a) Equivalent plastic strain

(b) Temperature
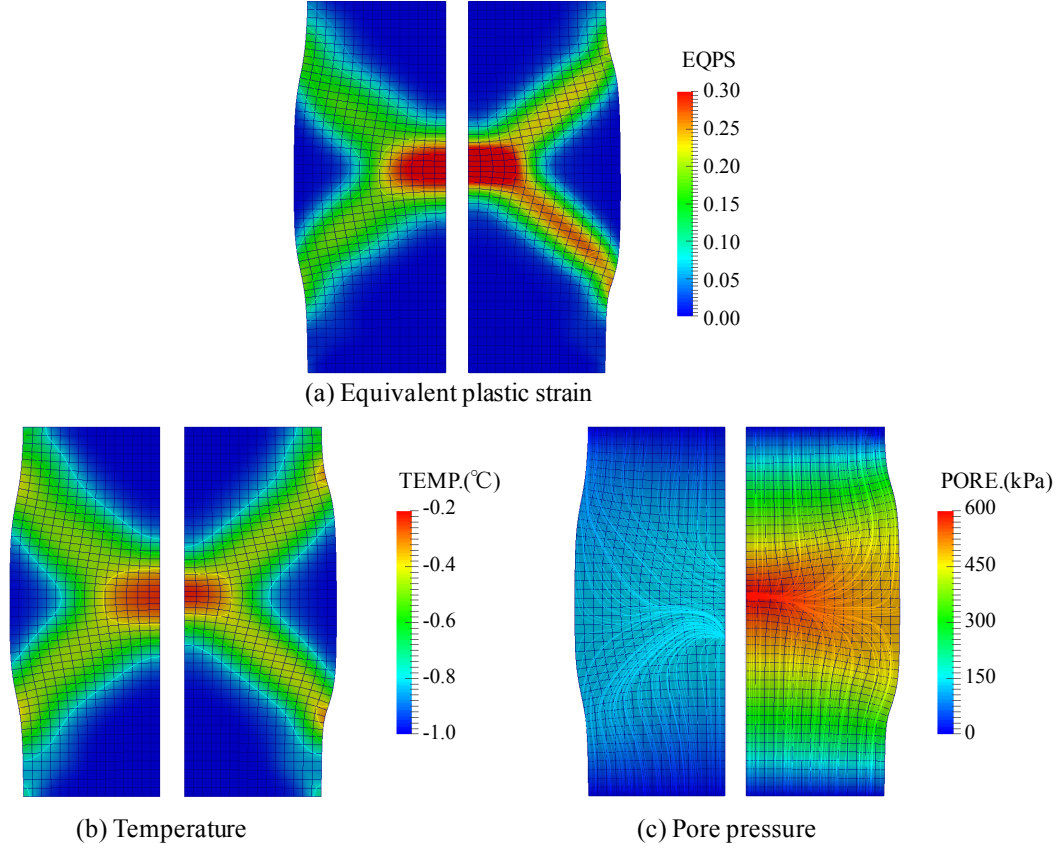
(c) Pore pressure

Figure 2.14: The effect of different permeability on the development shear band (equivalent plastic strain, temperature and pore pressure distributions): the left and right figures in (a), (b) and (c) present the results under high and low effective permeabilities, respectively

2.6 Conclusions

In this chapter, we present a computational framework that simulates the thermo-hydro-mechanical responses of freezing and thawing porous media at the finite deformation range. Our starting point is the mixture and pre-melting theory, which enables one to derive finite strain constitutive laws for both the path-dependent solid, hydraulic and thermal constitutive responses. On the theoretical side, we analyze how the degree of saturation of ice, determined from the unfrozen pore water pressure and temperature, introduces nonlocality and rate dependence to the non-mechanical hardening/softening mechanism. Unlike the single-physics solid mechanics problem in which strain and strain

history alone are sufficient to predict stress, the incorporation of non-mechanical harden-ing makes the solid skeleton constitutive responses to be highly sensitive to the evolution of the pore water pressure, temperature and the corresponding gradients. As a result, any simplification made on the balance principles, such as eliminating the heat generated by the plastic dissipation in the balance of energy and neglecting the heat convection terms, may have profound impacts on the quality of predictions on the solid mechanical behavior. In summary, this work provides a feasible approach to model frozen porous media with unfrozen water constituents and addresses some key theoretical and computational issues for capturing the essence of the path-dependent thermo-hydro-mechanical responses of porous media.

Chapter 3

Computational plasticity and damage mechanics for crystalline solids under the nonisothermal condition

3.1   Introduction

The demands for safe and permanent disposal of nuclear waste in geologic formations date back over decades. Natural rock salt, found in domal and bedded formations and the reconsolidated counterpart formed in a high-pressure and high-temperature environment, has been used for geological repositories of nuclear waste disposal in the United States and Germany [82]. Two operating facilities include the Waste Isolation Pilot Plant (WIPP) in Carlsbad (New Mexico, USA), and the Endlager für radioaktive Abfälle Morsleben (ERAM) site in Morsleben, Germany [83].

The decision to use salt formation for storage and disposal of radioactive wastes is attributed to its desirable thermo-hydro-mechanical-chemical characteristics, i.e., (1) high thermal conductivity, (2) low permeability, (3) self-healing mechanism and, (4) biolog-

ically inactivity of rock salt (as compared with clay). Firstly, the heat generated from nuclear wastes can be dissipated to the surrounding area much faster in salt than in other materials since the host salt rock exhibits high thermal conductivity [84]. In addition, the permeability of rock salt is sufficiently low that it is often idealized as impermeable. Therefore, it may function as a secured barrier for radioactive wastes [85]. Finally, the creeping property of salt enables microcracks or damage under mechanical load to be self-sealed, which may also naturally guarantee the necessary geological barrier function (e.g. Berlepsch and Haverkamp [83] and Chan, Bodner, and Munson [86]).

Figure 3.1: Disposal operations for Transuranic (TRU) waste at the Waste Isolation Pilot Plant (WIPP) – reproduced from Hansen and Leigh [87]

Decades of experimental investigations for rock salt provided insight on its mechanisms of brine migration, vapor transport, and related solution-precipitation creeps under nonisothermal conditions [82, 88–92]. However, the numerical modeling of crystalline rock salt remains an active research area. Analysis of complex multi-physical responses of the natural and reconsolidated salt, therefore, is an integral component of the design of short- and long-term life cycle of a salt repository. In the repository, the facility may have various phases of operation cycles that involve plugging, sealing, testing, and reconsolidation of the saline materials [87]. Under such conditions, the reconsolidated salt is

influenced by moisture content, brine inclusions inside halite crystals, and other materials, such as clay or impurity, that might present in the grain boundary. Within certain temperature and confining pressure ranges (between $250°C$ to $790°C$ and between 0.15 MPa and 12 MPa), the responses of salt may become even more complicated due to re-crystallization and grain boundary migration. This generally leads to precipitation creeping [93]. A number of previous studies, therefore, investigate the phenomenology and micro-mechanisms associated with the mechanical behavior of salt [94–100]. These studies have explored the dislocation, dissolution-precipitation creep, healing behavior, and flow transport properties of natural or reconsolidated salt under a wide range of load and temperature conditions in a phenomenological setting where microstructural attributes of the rock salt are not explicitly modeled.

Since salt formations found in nature often contain varying amounts of impurities, minerals, and brine inclusion, how to capture these spatial heterogeneous effects without explicitly model its microstructure remains a major challenge. Various phenomenological constitutive models have been proposed to capture the macroscopic responses of salt [86, 98, 101–109]. For instance, Olivella et al. [110] proposed a general formulation for nonisothermal multiphase flow of gas and brine in saline media, which was further extended into a series of works for coupled thermo-hydro-mechanical analysis of saline materials [111–113]. Although they did not explicitly incorporate the grain boundary, damage and healing, and the microstructural information, the complicated history- and rate-dependent behaviors of saline media as well as the multiphase interactions among constituents including gas, liquid, and solid were addressed by linking fluid flow, permeability change, thermal gradient, and phenomenological constitutive law for the solid skeleton.

While these phenomenological approaches inspired by micromechanics of crystals have achieved a level of success in the past, more physically consistent forward prediction may require stronger physical underpinnings such that the interaction between the

impurity, the precipitated brine and the anisotropy of crystalline constitutive responses can be captured properly [87]. Yet, bridging the multiscale coupling effects from the grain scale to the field applications remains a challenging task due to the complexity of the physical nature of rock salt. Our ultimate goal is to create a multiscale polycrystalline material model suitable for field-scale applications. As a first step toward this goal, this article will focus on modeling the thermo-mechanical response of single-crystal halite.

In this chapter, our objective is to derive, implement, and validate an elastoplastic model for single-crystal halite subjected to different thermal and mechanical loadings relevant to nuclear disposal applications. We will incorporate other important multiphysics and multiscale polycrystalline mechanisms such as the interactions across grain boundaries, the intra-crystalline and inter-crystalline brine inclusion, and the role of the impurity and additive on the precipitating and pressure solution of the grain boundaries in future contributions.

We present a unified mathematical framework that enables us to capture the anisotropic inelastic brittle and ductile behaviors of single-crystal halite. We achieve this by combining 1) a thermal-sensitive rate-dependent crystal plasticity formulation that captures the anisotropic plastic deformation caused by the slip of crystallographic planes and 2) a multi-phase-field regularized fracture model that captures interactions of the anisotropic intragranular and transgranular fractures of single-crystal halite under the temperature range relevant to nuclear waste disposal applications (e.g. the WIPP). The intrinsic anisotropy of halite stemming from the microstructure is incorporated into the crystal plasticity theory. This theory is a micromechanics-based constitutive law where the anisotropic plastic flow is associated with activation(s) of the slip systems oriented according to the lattice structure of the crystalline materials [60, 114–117]. In this work, we use the strain energy equivalence theory such that the crystal plasticity framework can be integrated into a phase field model capturing the evolution of damage. Because the creeping mechanisms, such as grain boundary diffusion, dislocation creep, and thermal

activated glide, are highly sensitive to temperature, the temperature-dependent energy dissipation due to creeping is incorporated into the crystal plasticity model [118–123]. The damage and crack growth of single-crystal materials are captured via the phase field approach, which is a sub-class of the smeared crack approach. This method allows us to capture complicated crack patterns without introducing an embedded discontinuity [124–128]. It should be noted that incorporation of the phase field model is not the only feasible way to model cleavage fractures. Other methods, such as the introduction of pseudo-slip in crystalline materials, [129, 130] have been used to model the coupled effect of single crystal plasticity and damage.

We use a sub-class of the phase field model that employs multiple phase fields to capture damage accumulated in different directions. The multi-phase-field approach has been very popular to model a wide spectrum of material behaviors including anisotropic responses of regularized interfaces for planar dislocation [131], re-crystallization [132] and anisotropic fracture [133–135]. See also Steinbach [136] for a comprehensive review. In the content of anisotropic phase field models, one obvious advantage of the multi-phase-field approach is the lack of higher-order terms that are typically required for the single-phase-field counterpart to capture non-convex anisotropic fracture energies [137, 138]. As a result, the multi-phase-field model does not require specific finite element spaces spanned by piece-wise smooth and globally C^1-continuous basis functions. Instead, a simple low-order finite element can be used. This simplicity, although offset by the additional computational cost due to the additional degrees of freedom, motivates us to use the multi-phase-field model in this work. The number of independent phase fields and their directional features are assumed to be consistent with the slip planes of halite. Finally, the crystal plasticity theory and the multi-phase-field approach are incorporated into a set of multi-physical field equations. The formulations include the balance of linear momentum, the micro-force equations for plastic slip and multiple phase-fields, and the balance of energy.

The organization of this chapter is as follows. In Section 3.2, we first describe the kinematics of a halite grain with multiple slip systems. Then, the application of effective stress equivalence theory on the multi-phase-field model is discussed with respect to anisotropic fracture for crystalline materials. Within this mathematical framework, the general governing equations including the balance of linear momentum, microforce equations, and balance of energy are derived. The specific choice of a free energy function that combines the crystal plasticity and the multi-phase-field approaches is provided. Subsequently, in Section 3.3, the stress update algorithm in effective stress space is described followed by the description of both rate-dependent and rate-independent settings. In Section 3.4, the finite element formulation, are presented. Numerical simulations are then provided in Section 3.5, followed by a conclusion.

3.2 Governing equations

In this section, we present the field equations that capture the thermo-mechanical coupling effect of single-crystal halite. We begin by reviewing kinematics of deformation of a crystalline solid with multiple slip systems. To capture the brittle-ductile transition and the brittle fractures that might occur under low confining pressure, a multi-phase-field model is used. Adopting the ideas originated from Nguyen et al. [135], we introduce multiple phase fields to model anisotropic damage such that each phase field represents the damage along a particular preferential direction. Finally, the coupled anisotropic damage-plasticity behavior of single-crystal halite is captured via the effective stress [139, 140]. The total stress in damaged configuration is then recovered based on the effective stress and the anisotropic gradient damage computed from the phase fields. Meanwhile, the field theory for balances of linear momentum and energy are discussed.

3.2.1 Strain energy equivalence for coupling phase field and plasticity

In this work, an anisotropic phase field fracture framework is coupled with a crystal plasticity model to simulate the anisotropic path-dependent behavior of single-crystal halite. Here we adopt the strain energy equivalence principle used previously in isotropic and anisotropic damage mechanics [140–142]. This principle hypothesizes that there exists a fictitious undamaged counterpart of the damaged halite such that a body composed of the fictitious undamaged material will experience an effective stress $\hat{\boldsymbol{\sigma}}$ while the actual body will experience a stress $\boldsymbol{\sigma}$. Furthermore, we assume that despite the damage characterized by the multiple phase fields is anisotropic, the effective stress and the total stress are co-axial. Consequentially, the degradation function $g(\underline{d})$ becomes a scalar function of the collection of phase fields $\underline{d}$. The relationship between the total and effective stresses when both the fictitious and the real material exhibit the same infinitesimal strain (i.e., $\epsilon = \hat{\epsilon}$) are,

$$\boldsymbol{\sigma} = g(\underline{d})\hat{\boldsymbol{\sigma}}, \tag{3.1}$$

and the corresponding infinitesimal stress rate is,

$$\dot{\boldsymbol{\sigma}} = \sum_{i=1}^{N} \frac{\partial g(\underline{d})}{\partial d_i} \, \dot{d}_i \hat{\boldsymbol{\sigma}} + g(\underline{d})\dot{\hat{\boldsymbol{\sigma}}}, \tag{3.2}$$

where $d_i, (i = 1, 2, ..., N)$, is the phase field for each preferential direction and N is the total number of phase fields. An important implication of (3.1) is that while damage and plastic processes remain coupled, the plasticity model can be associated with the fictitious undamaged body. Hence one may use a decoupled plasticity algorithm to first obtain the effective stress from the strain field then update the total stress using the degradation function from each material point.

3.2.2 Kinematics for crystal deformation of the damaged halite

For completeness, we briefly review the kinematics of crystal deformation and restrict the formulation within the infinitesimal range. More comprehensive treatment of this subject can be found in [61, 119, 121, 143]. Recall that we adopt the approach in Simo and Ju [142] in which we assume that the actual (damaged) crystal and the fictitious counterpart undertake the same strain and strain history.

The elastoplastic deformation of a single-crystal grain is attributed to the interactions between crystal blocks along the predefined crystallographic planes in the slip system. A *slip-system* is defined by a combination of crystallographic planes (i.e. *slip planes*) and the corresponding sliding directions (i.e. *slip directions*). The atomic arrangement of the slip system of crystalline materials leads to a preferential direction of the plastic flow, hence the overall constitutive responses of a single crystal is anisotropic. In Face Cubic Centered (FCC) crystals, for example, the slip-systems are defined by the densest packing planes in terms of atomic arrangement as the slip-plane $\{111\}$ and slip-direction $\langle 110 \rangle$. This dense packing causes FCC materials, such as aluminum, copper, gold, and silver to exhibit higher ductility than the Body Cubic Center (BCC) crystals such as, iron and chromium (although packing alone is not the only factor that influences ductility) [61]. One may view the halite structure as a FCC with secondary atoms in its octahedral holes (cf. Williams [144]). As a result, a set of the slip-planes is known to be $\{110\}$ (rather than $\{111\}$ for FCC), and the corresponding slip directions are $\langle 1\bar{1}0 \rangle$. This set of planes is electrically neutral, and the motion on these planes avoids charged layers gliding over one another (cf. Hansen [100] and Carter and Norton [145]).

We consider a continuum body ($\mathcal{B}$) with material points identified by the position vectors $\boldsymbol{x} \in \mathcal{B}$. The displacement of a material point with time t can be denoted by $\boldsymbol{u}(\boldsymbol{x}, t)$, and we define the strain measure ($\boldsymbol{\epsilon}$) as the symmetric part of the displacement gradient, i.e.,

$$\boldsymbol{\epsilon} := \nabla^{\text{sym}} \boldsymbol{u} = \frac{1}{2}(\nabla \boldsymbol{u} + (\nabla \boldsymbol{u})^{\text{T}}). \tag{3.3}$$
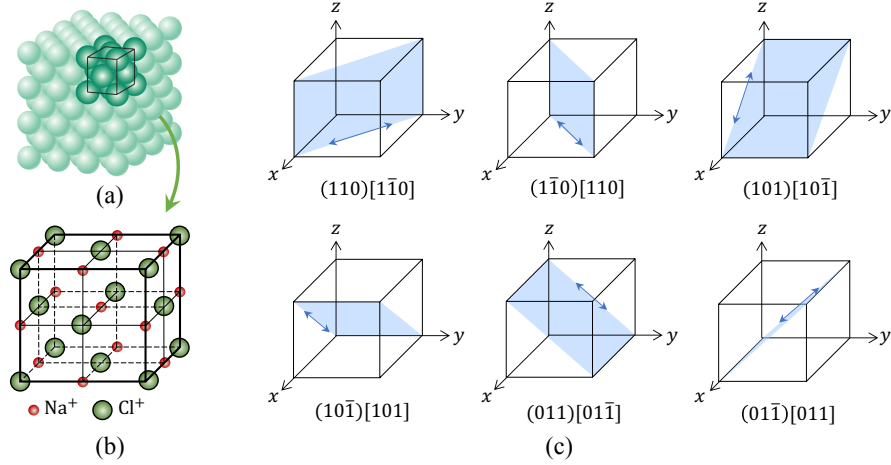
Figure 3.2: The description of the slip-system of single-crystal halite, (a) an aggregate of many atoms for the face centered cubic crystal structure (reproduced from Callister Jr and Rethwisch [146] – adapted from the original Moffat, Pearsall, and Wulff [147]), (b) a unit cell for the sodium chloride (NaCl) crystal structure (reproduced from Callister Jr and Rethwisch [146]), and (c) the slip-system $\{110\}\langle 1\bar{1}0\rangle$

The additive decomposition of the infinitesimal total strain leads to,

$$\boldsymbol{\epsilon} = \boldsymbol{\epsilon}^e + \boldsymbol{\epsilon}^p + \boldsymbol{\epsilon}^\theta, \tag{3.4}$$

where $\boldsymbol{\epsilon}^e$ and $\boldsymbol{\epsilon}^p$ indicate the elastic and plastic components, respectively. Meanwhile, the thermal component is assumed to be isotropic and defined as a function of the thermal expansion coefficient, i.e., $\boldsymbol{\epsilon}^\theta = \alpha(\theta - \theta_0)\boldsymbol{I}$, where α is the thermal expansion coefficient; θ_0 is a reference temperature at which the thermal strain $\boldsymbol{\epsilon}^\theta = \boldsymbol{0}$ (cf. Clayton [130], Aldakheel [148], and Miehe et al. [149]). In crystalline materials, the elastic strain describes distortion of the lattice structure which vanishes when the applied stress is released. On the other hand, the plastic strain is irreversible and evolves due to the slip on crystallographic planes. In this work, we assume the thermal expansion as an elastic response and consider it in the elastic part of free energy functional in (3.41) followed by Anand and Gurtin [150].

The α-slip system is composed of: 1) $\boldsymbol{m}^\alpha$, the unit normal to a crystallographic plane, and 2) $\boldsymbol{s}^\alpha$, the direction of plastic slip on that plane. Therefore, the slip-system α is defined by orthonormal vectors $(\boldsymbol{m}^\alpha, \boldsymbol{s}^\alpha)$ based on the crystallographic features of crystals. We then obtain the plastic strain by summing over all crystallographic slips,

$$\boldsymbol{\epsilon}^p = \sum_\alpha \gamma^\alpha \boldsymbol{S}^\alpha, \tag{3.5}$$

where γ^α indicates the plastic slip corresponding to the slip-system α. $\boldsymbol{S}^\alpha$ denotes the symmetric part of the Schmid tensor (i.e. $\boldsymbol{m}^\alpha \otimes \boldsymbol{s}^\alpha$), which can be expressed as follows,

$$\boldsymbol{S}^\alpha = \frac{1}{2} \left(\boldsymbol{m}^\alpha \otimes \boldsymbol{s}^\alpha + \boldsymbol{s}^\alpha \otimes \boldsymbol{m}^\alpha \right). \tag{3.6}$$

Note that the summation convention is not employed in respect of indices relating to the slip systems. Furthermore, the thermal expansion and structural heating are included by using a thermal-sensitive elastic stored energy function for thermoelastic coupling in (3.40). For crystals with cubic symmetry crystals, the second-order material tensors such as thermal expansion and conductivity are all symmetric with one independent component [151]. For other types of crystals, the anisotropy of any symmetric second-order material tensors can be introduced via spectral decomposition. In this case, one may assume that the principal crystallographic directions are parallel to the eigenvectors of the material tensors (cf. Meissonnier, Busso, and O'Dowd [152]). The thermal effect on the inelastic behavior of single-crystal halite is incorporated via the temperature-dependent flow rule for the plastic slips (Section 3.2).

3.2.3 Multi-phase-field approximation for anisotropic fracture

The phase field fracture modeling can be considered as a regularized smeared approach. In this approach the cracks are not explicitly captured via embedded discontinuities but approximated by an implicit indicator function obtained from regularizing the strong dis-

continuities with a characteristic length [153–155]. Here we assume that this characteristic length is sufficiently smaller than the grain size but larger than the finite element mesh size used for numerical simulations. In those cases, the strongly anisotropic damage and fracture behaviors can be captured either via a single phase field within a higher-order Cahn-Hilliard framework [127, 137, 138] or via multiple phase fields, each constrained by governing equation without the forth-order terms [134, 135]. Due to the simplicity of the latter approach, we adopt it to capture the damage and fracture behavior in single-crystal halite.

In a regularized framework where the sharp crack topology is approximated by a diffusive representation, the phase-field variable, $d(\boldsymbol{x}, t) \in [0, 1]$, is an implicit function whose value indicates the location of the smeared crack(s). Let $\mathcal{T}$ denote a set of discontinuous fractures inside a body $\mathcal{B}$. Then the total area of the crack surfaces can be described by an area integral over $\mathcal{T}$. By introducing a crack density function $\Gamma_l(d, \nabla d)$ the total crack area can be described by the volume integral as,

$$\Gamma = \int_{\mathcal{T}} dA \approx \int_{\mathcal{B}} \Gamma_l(d, \nabla d) \, dV \quad \text{where} \quad \Gamma_l(d, \nabla d) := \frac{1}{2l}d^2 + \frac{l}{2}|\nabla d|^2. \qquad (3.7)$$

Here l indicates a length scale that controls the width of the smooth approximation of the crack. The assigned scalar phase-field values 0 and 1 represent the intact and completely damaged region, respectively. The phase-field value between $0 < d < 1$ indicates a partially damaged material state at the corresponding material point. The regularized crack surface can be further extended to the anisotropic case as,

$$\Gamma_l(d, \nabla d, \boldsymbol{w}) := \frac{1}{2l}d^2 + \frac{l}{2}\boldsymbol{\omega} : (\nabla d \otimes \nabla d), \qquad (3.8)$$

where $\boldsymbol{\omega}$ is a second-order structural tensor, which is invariant with respect to rotations

for characterizing the material anisotropy [127]. This tensor can be defined as,

$$\boldsymbol{\omega} = \boldsymbol{I} + \beta(\boldsymbol{I} - \boldsymbol{m} \otimes \boldsymbol{m}), \tag{3.9}$$

where $\boldsymbol{I}$ denotes the second-order identity tensor; m indicates the unit normal vector to the potentially preferred cleavage plane; $\beta \gg 1$ is the parameter penalizing fracture on planes not normal to the unit vector $\boldsymbol{m}$. The isotropic crack surface energy function in (3.7) can be recovered by setting $\beta = 0$.

To capture the anisotropy inherent in the crystalline materials, we associate the orientations of each slip plane as a potential cleavage plane. Adopting the multi-phase-field technique first introduced by Oshima, Takaki, and Muramatsu [133] and further developed in [134, 135], we assign multiple phase fields $\underline{d} = \{d_1, d_2, ..., d_n\}$ to quantify the damage accumulation on each slip plane normal to the unit vector $\boldsymbol{m}^i$. Therefore, the total crack length can be defined by the summation of each anisotropic crack density function which is rewritten as [134, 135],

$$\Gamma_l(\underline{d}, \nabla \underline{d}, \boldsymbol{\omega}) = \sum_i \left[\frac{1}{2l}(d_i)^2 + \frac{l}{2}\boldsymbol{\omega}_i : (\nabla d_i \otimes \nabla d_i) \right],$$

$$\text{where } \boldsymbol{\omega}_i = \boldsymbol{I} + \beta(\boldsymbol{I} - \boldsymbol{m}^i \otimes \boldsymbol{m}^i). \tag{3.10}$$

For convenience we use the underline to denote a set of variables. In analogy to (3.6), $\boldsymbol{m}^i$ corresponds to $\boldsymbol{m}^\alpha$ – the unit normal vector of each crystallographic slip plane. The length scale l and penalizing parameter β are assumed to be the same for each slip system. These parameters may further differentiate for each slip system based on the microscopic information of crystalline materials.

3.2.4 Balance of linear momentum and microforce

In this section, we derive the balance of linear momentum and microforce for single crystals with damage via the principle of virtual power. The virtual-power formulation of the single crystal using microforce balance is well established and has been described in the literature [117]. Based on this standard theory, De Lorenzis, McBride, and Reddy [156] extended the virtual power formulation by introducing an additional microforce balance associated with a crack phase-field. In this, our new contribution is to extend this work for the multi-phase-field formulation coupled with crystal plasticity. We postulate the existence of multiple microforces, each microforce conjugates to a phase field for anisotropic damage in a single crystal. Furthermore, we extend this framework to incorporate thermal diffusion such that non-isothermal condition can be simulated. For simplicity, we limit our analysis within the small deformation range and the small temperature difference assumption [150]. As described in Section 3.2.2, therefore, the thermal expansion effect is included in the elastic stored energy function (3.40) based on the standard virtual power formulation [150]. This treatment may be sufficient for a geological disposal under the limited temperature change condition for low-level radioactive waste materials, for example, generated by military activities (e.g. the Waste Isolation Pilot Plant, WIPP) [87, 157].

The standard derivation procedure using the principle of virtual power for phase-field modeling of fracture in a single-crystal are described in great detail in Gurtin, Fried, and Anand [117] and De Lorenzis, McBride, and Reddy [156]. Here we briefly outline the expression of virtual power formulations including macroforce (i.e. the total Cauchy stress), microforce for a single crystal, and additional microforces for multiple phase fields associated with the resultant balance equations. In a domain $\mathcal{B}$, the internal power ($\mathcal{I}$) over a subregion $\mathcal{P} \subset \mathcal{B}$ may take the form of,

$$\mathcal{I}(\mathcal{P}) = \int_{\mathcal{P}} \boldsymbol{\sigma} : \dot{\boldsymbol{\epsilon}}^e \, dV + \sum_{\alpha} \int_{\mathcal{P}} \pi^{\alpha} \dot{\gamma}^{\alpha} \, dV + \sum_{i} \left(\int_{\mathcal{P}} \boldsymbol{\xi}_i \cdot \nabla \dot{d}_i \, dV + \int_{\mathcal{P}} \pi_i \, \dot{d}_i \, dV \right), \quad (3.11)$$

where $\boldsymbol{\sigma}$ indicates the Cauchy stress with the power-conjugate to $\dot{\boldsymbol{\epsilon}}^e$; π^α denotes the microscopic force associated with the slip rate $\dot{\gamma}^\alpha$; $\boldsymbol{\xi}_i$ is the microscopic stress power-conjugate to $\nabla \dot{d}_i$; and π_i is the microscopic internal body force (power conjugate to $\dot{d}_i$). Note that the summation convention is not employed regarding indices related to multiple phase-fields. Each phase-field variable corresponds to the direction of a crystalline slip system. As mentioned in Section 3.2.1, $\boldsymbol{\sigma}$ is a total stress considering damage to the material obtained by (3.1). The calculation of the total stress and a stress update algorithm will be explained in a later section. Now we assume that the external power ($\mathcal{W}$) acting upon $\mathcal{P} \subset \mathcal{B}$ has the form as,

$$\mathcal{W}(\mathcal{P}) = \int_{\partial \mathcal{P}} \boldsymbol{t}(\boldsymbol{n}) \cdot \dot{\boldsymbol{u}} \, dA + \int_{\mathcal{P}} \boldsymbol{b} \cdot \dot{\boldsymbol{u}} \, dV + \sum_i \left(\int_{\partial \mathcal{P}} \chi_i(\boldsymbol{n}) \cdot \dot{d}_i \, dA + \int_{\mathcal{P}} \lambda_i \, \dot{d}_i \, dA \right), \quad (3.12)$$

where $\boldsymbol{t}$ is the traction vector with outward unit normal $\boldsymbol{n}$; $\boldsymbol{b}$ is the macroscopic body force; χ_i and λ_i are the microscopic external traction and body force, respectively, both power-conjugate to $\dot{d}_i$. Note that a scalar external virtual microscopic force power conjugate to $\dot{\gamma}^\alpha$ is not considered [117]. An additional assumption is made such that each field, that is $\dot{\boldsymbol{u}}$, $\dot{\boldsymbol{\epsilon}}^e$, $\dot{\gamma}^\alpha$, and $\dot{d}_i$, is known at some arbitrary known but at fixed time and can be independently specified within the kinematic constraints, (3.3) to (3.5), as

$$\nabla^{\mathrm{sym}} \tilde{\boldsymbol{u}} = \tilde{\boldsymbol{\epsilon}}^e + \sum_\alpha \tilde{\gamma}^\alpha \boldsymbol{S}^\alpha. \quad (3.13)$$

By denoting each virtual field by $\tilde{\boldsymbol{u}}$, $\tilde{\boldsymbol{\epsilon}}^e$, $\tilde{\gamma}^\alpha$, and $\tilde{d}_i$, a generalized virtual velocity $\mathcal{V}$ can be defined by [117, 150, 156],

$$\mathcal{V} = (\tilde{\boldsymbol{u}}, \tilde{\boldsymbol{\epsilon}}^e, \underline{\tilde{\gamma}}, \underline{\tilde{d}}). \quad (3.14)$$

Then the principle of virtual power is the requirement that, $\mathcal{I}(\mathcal{P}, \mathcal{V}) = \mathcal{W}(\mathcal{P}, \mathcal{V})$, that is,

$$\int_{\mathcal{P}} \boldsymbol{\sigma} : \tilde{\boldsymbol{\epsilon}}^e \, dV + \sum_\alpha \int_{\mathcal{P}} \pi^\alpha \tilde{\gamma}^\alpha \, dV + \sum_i \left(\int_{\mathcal{P}} \boldsymbol{\xi}_i \cdot \nabla \tilde{d}_i \, dV + \int_{\mathcal{P}} \pi_i \, \tilde{d}_i \, dV \right)$$

$$= \int_{\partial \mathcal{P}} \boldsymbol{t}(\boldsymbol{n}) \cdot \tilde{\boldsymbol{u}} \, dA + \int_{\mathcal{P}} \boldsymbol{b} \cdot \tilde{\boldsymbol{u}} \, dV + \sum_i \left(\int_{\partial \mathcal{P}} \chi_i(\boldsymbol{n}) \cdot \tilde{d}_i \, dA + \int_{\mathcal{P}} \lambda_i \tilde{d}_i \, dA \right), \quad (3.15)$$

for all virtual velocities $\mathcal{V}$. Again, the derivation of balance equations is straightforward [117, 150, 156], thus resulting in the following final expressions:

$$\nabla \cdot \boldsymbol{\sigma} + \boldsymbol{b} = \boldsymbol{0}, \quad \text{(Linear momentum)} \tag{3.16}$$

$$\boldsymbol{t}(\boldsymbol{n}) = \boldsymbol{\sigma} \cdot \boldsymbol{n}, \quad \text{(Macroscopic traction)} \tag{3.17}$$

$$\pi^\alpha = \tau^\alpha \text{ with } \tau^\alpha = \boldsymbol{S}^\alpha : \boldsymbol{\sigma}, \quad \text{(Microscopic force balance for each slip system)} \tag{3.18}$$

$$\nabla \cdot \boldsymbol{\xi}_i - \pi_i + \lambda_i = 0, \quad \text{(Microscopic force balance for each phase field)} \tag{3.19}$$

$$\chi_i(\boldsymbol{n}) = \boldsymbol{\xi}_i \cdot \boldsymbol{n}. \quad \text{(Phase-field microscopic traction)} \tag{3.20}$$

Here τ^α indicates the Schmid stress or the resolved shear stress, which represents the macroscopic stress $\boldsymbol{\sigma}$ resolved on the slip system α. In addition, the number of (3.19) and (3.20) is consistent with the number of each phase-field corresponding to the slip system of single-crystal halite. We further note that the macro and microforces are related based on (3.18) such that τ^α represents the force applied on the lattice of a single crystal for dislocations on the slip system α while π^α constitutes internal forces on the slip system α [117]. The multiple phase-field variables, however, do not show clear relations associated with the macroforce and the microforce on the slip systems. This interaction is established based on our choice of a free energy functional, which will be covered in a later section.

3.2.5   Energy balance equation and dissipation inequality

To capture the thermo-mechanical behavior of a single crystal, we present an energy balance equation which includes contributions of heat conduction, mechanical dissipation, and structural heating. The first law (energy balance) can be expressed in a local form,

$$\dot{e} = \boldsymbol{\sigma} : \dot{\boldsymbol{\epsilon}} - \nabla \cdot \boldsymbol{q} + r_\theta, \tag{3.21}$$

where e is internal energy per unit volume; $\boldsymbol{q}$ is the heat flux vector; r_θ is the heat source term. This equation can be rewritten in greater detail by including the dissipation of the plastic slip and the work done by the growth of phase field (3.15). Recall that the rate of the phase-field change is power conjugate to the microforce [158, 159]. The balance of energy, therefore, reads,

$$\dot{e} = \boldsymbol{\sigma} : \dot{\boldsymbol{\epsilon}}^e + \sum_\alpha \pi^\alpha \dot{\gamma}^\alpha + \sum_i \left(\boldsymbol{\xi}_i \cdot \nabla \dot{d}_i + \pi_i \, \dot{d}_i \right) - \nabla \cdot \boldsymbol{q} + r_\theta. \tag{3.22}$$

Then the second law of thermodynamics (Clausius-Duhem inequality) is,

$$\mathscr{D}_{\text{int}} = \dot{\eta} + \nabla \cdot \left(\frac{\boldsymbol{q}}{\theta} \right) - \frac{r_\theta}{\theta} \geq 0, \tag{3.23}$$

in which η is an entropy term, and θ is absolute temperature. Here the the flux vector $(\boldsymbol{q})$ can be expressed using Fourier's law for heat conduction,

$$\boldsymbol{q} = -\boldsymbol{\kappa} \cdot \nabla \theta, \tag{3.24}$$

where $\boldsymbol{\kappa}$ is the thermal conductivity tensor. In addition, we may recall the Helmholtz free energy (ψ) which shows the relation between the internal energy (e) and entropy (η) as,

$$\psi = e - \theta \eta. \tag{3.25}$$

Therefore, the dissipation inequality $(\mathscr{D}_{\text{int}})$ can be rewritten as,

$$\mathscr{D}_{\text{int}} = \boldsymbol{\sigma} : \dot{\boldsymbol{\epsilon}}^e + \sum_\alpha \pi^\alpha \dot{\gamma}^\alpha + \sum_i \left(\boldsymbol{\xi}_i \cdot \nabla \dot{d}_i + \pi_i \, \dot{d}_i \right) - \left(\eta \dot{\theta} + \dot{\psi} \right) - \frac{1}{\theta} \boldsymbol{q} \cdot \nabla \theta \geq 0. \tag{3.26}$$

Now we consider the Helmholtz free energy function for thermo-elasto-plastic crystal materials of the following form,

$$\psi = \hat{\psi}(\boldsymbol{\epsilon}^e, \underline{s}, \theta, \underline{d}, \nabla \underline{d}), \tag{3.27}$$

where $\boldsymbol{\epsilon}^e$ is the elastic strain ; θ the temperature; $\underline{d}$ a set of crack phase-fields and its gradient $\nabla \underline{d}$; $\underline{s}$ a set of a local scalar measure related to the plastic slip accumulation for each slip system defined by,

$$\dot{s}^\alpha := \dot{\gamma}^\alpha \geq 0 \quad \text{where} \quad s^\alpha(t) = \int_0^t \dot{\gamma}^\alpha d\tau. \tag{3.28}$$

The substitution of (3.27) into (3.26) induces the dissipation inequality as the following form,

$$\left(\boldsymbol{\sigma} - \frac{\partial \hat{\psi}}{\partial \boldsymbol{\epsilon}^e} \right) : \dot{\boldsymbol{\epsilon}}^e + \sum_\alpha \pi^\alpha \dot{\gamma}^\alpha - \sum_\alpha \frac{\partial \hat{\psi}}{\partial s^\alpha} \dot{s}^\alpha + \sum_i \left(\pi_i - \frac{\partial \hat{\psi}}{\partial d_i} \right) \dot{d}_i$$
$$+ \sum_i \left(\boldsymbol{\xi}_i - \frac{\partial \hat{\psi}}{\partial \nabla d_i} \right) \cdot \nabla \dot{d}_i - \left(\eta + \frac{\partial \hat{\psi}}{\partial \theta} \right) \dot{\theta} - \frac{1}{\theta} \boldsymbol{q} \cdot \nabla \theta \geq 0. \tag{3.29}$$

Well-known arguments (e.g. Standard Coleman–Noll arguments) lead to the constitutive relations for the Cauchy stress and entropy, respectively,

$$\boldsymbol{\sigma} = \frac{\partial \hat{\psi}}{\partial \boldsymbol{\epsilon}^e}, \ \eta = -\frac{\partial \hat{\psi}}{\partial \theta}. \tag{3.30}$$

We then further derive the dissipation inequality by following the individual group terms. The inequality related the each phase-field variable can be expressed as,

$$\sum_i \left(\pi_i - \frac{\partial \hat{\psi}}{\partial d} \right) \dot{d}_i + \sum_i \left(\boldsymbol{\xi}_i - \frac{\partial \hat{\psi}}{\partial \nabla d_i} \right) \cdot \nabla \dot{d}_i \geq 0, \tag{3.31}$$

which leads to the phase-field microscopic constitutive equations as,

$$\pi_i = \frac{\partial \hat{\psi}}{\partial d_i} \quad \text{and} \quad \boldsymbol{\xi}_i = \frac{\partial \hat{\psi}}{\partial \nabla d_i}. \tag{3.32}$$

Substitution of (3.32) into (3.19) with the assumptions of no microscopic body force ($\lambda_i = 0$) leads to the multi-phase-field equations as,

$$\nabla \cdot \left(\frac{\partial \hat{\psi}}{\partial \nabla d_i} \right) - \frac{\partial \hat{\psi}}{\partial d_i} = 0. \tag{3.33}$$

Note that previous phase field fracture models, such as the time-regularized viscous crack propagation mode in Miehe, Welschinger, and Hofacker [124], often introduce dissipation function that depends on rate of phase field and that of the phase field gradient. Such an extension is out of the scope of this study but will be considered in the future. Interested readers are referred to previous works such as Stainier and Ortiz [52], Miehe, Welschinger, and Hofacker [124], Mota et al. [160], and Yang, Stainier, and Ortiz [161], for a variational consistent way to introduce rate-dependence for path-dependent materials. Based on (3.30) and (3.32), the reduced dissipation inequality becomes,

$$\underbrace{\sum_\alpha \pi^\alpha \dot{\gamma}^\alpha - \sum_\alpha \frac{\partial \hat{\psi}}{\partial s^\alpha} \dot{s}^\alpha}_{D_p} - \frac{1}{\theta} \boldsymbol{q} \cdot \nabla \theta \geq 0, \tag{3.34}$$

where D_p denotes the plastic dissipation rate. Considering the definition of g^α, the inequality (3.34) can be further reduced to,

$$\sum_\alpha \left(\pi^\alpha \dot{\gamma}^\alpha + g^\alpha \dot{s}^\alpha \right) - \frac{1}{\theta} \boldsymbol{q} \cdot \nabla \theta \geq 0, \quad \text{where} \quad g^\alpha = -\frac{\partial \hat{\psi}}{\partial s^\alpha}, \tag{3.35}$$

in which the thermodynamic force g^α power-conjugate to $\dot{s}^\alpha$ is introduced. Finally, the balance of energy is obtained by substituting the free energy (3.25) into (3.22):

$$\dot{\psi} + \dot{\eta}\theta + \eta\dot{\theta} - \boldsymbol{\sigma} : \dot{\boldsymbol{\epsilon}}^e - \sum_\alpha \pi^\alpha \dot{\gamma}^\alpha - \sum_i \left(\boldsymbol{\xi}_i \cdot \nabla \dot{d}_i + \pi_i \, \dot{d}_i \right) + \nabla \cdot \boldsymbol{q} - r_\theta = 0. \quad (3.36)$$

This equation can be rewritten by combining the constitutive relations of (3.30) and (3.32) as,

$$-\theta \frac{\partial^2 \hat{\psi}}{\partial \theta^2} \dot{\theta} = \sum_\alpha \left(\pi^\alpha \dot{\gamma}^\alpha + g^\alpha \dot{s}^\alpha \right) + \sum_\alpha \left(\theta \frac{\partial^2 \hat{\psi}}{\partial \theta \partial s^\alpha} \dot{s}^\alpha \right) + \sum_i \left(\frac{\partial^2 \hat{\psi}}{\partial \theta \partial d_i} \dot{d}_i + \frac{\partial^2 \hat{\psi}}{\partial \theta \partial \nabla d_i} \cdot \nabla \dot{d}_i \right) \theta$$
$$+ \theta \left(\frac{\partial^2 \hat{\psi}}{\partial \theta \partial \boldsymbol{\epsilon}^e} : \dot{\boldsymbol{\epsilon}}^e \right) - \nabla \cdot \boldsymbol{q} + r_\theta. \quad (3.37)$$

Considering a choice of a free energy function in (3.40), we may reduce the equation as,

$$\underbrace{-\theta \frac{\partial^2 \hat{\psi}}{\partial \theta^2}}_{c_v} \dot{\theta} = \underbrace{\sum_\alpha \left(\pi^\alpha \dot{\gamma}^\alpha + g^\alpha \dot{s}^\alpha \right) + \theta \left(\frac{\partial^2 \hat{\psi}}{\partial \theta \partial \boldsymbol{\epsilon}^e} : \dot{\boldsymbol{\epsilon}}^e \right)}_{D_{\text{mech}} - H_\theta} - \nabla \cdot \boldsymbol{q} + r_\theta, \quad (3.38)$$

which can be written in a simplified expression by Simo and Miehe [47],

$$c_v \dot{\theta} = [D_{\text{mech}} - H_\theta] - \nabla \cdot \boldsymbol{q} + r_\theta. \quad (3.39)$$

Here c_v is the specific heat per unit volume at constant deformation; D_{mech} denotes the contribution to the dissipation due to pure mechanical load and/or thermal flow, which may be consistent in the form of $\beta\boldsymbol{\sigma} : \dot{\boldsymbol{\epsilon}}^p$ with β the Taylor-Quinney coefficient; H_θ is the non-dissipative (latent) thermoelastic structural heat or cooling.

3.2.6 A specific free energy functional

We derive the explicit expressions for the balance equations by choosing the following stored free energy functional:

$$\psi = \hat{\psi}^e(\boldsymbol{\epsilon}^e, \theta, \underline{d}) + \hat{\psi}^p(\underline{s}, \underline{d}\,; \theta) + \hat{\psi}^c(\underline{d}, \nabla\underline{d}, \underline{\omega}) + \hat{\psi}^\theta(\theta). \tag{3.40}$$

The elastic part $\hat{\psi}^e$ is composed of the thermoelastic strain energy (w^e) considering the thermal expansion [149, 150, 161–164], which is multiplied by the degradation function $g(\underline{d})$ for damage evolution:

$$\hat{\psi}^e = g(\underline{d})w^e(\boldsymbol{\epsilon}^e, \theta) \quad \text{with} \quad w^e(\boldsymbol{\epsilon}^e, \theta) = \frac{1}{2}\boldsymbol{\epsilon}^e : \mathbb{C}^e : \boldsymbol{\epsilon}^e - 3\alpha K(\theta - \theta_0)\,\text{tr}\,\boldsymbol{\epsilon}^e, \tag{3.41}$$

Firstly, the degradation function $g(\underline{d})$ for multiple phase-field can be assumed to have a simple form [134, 135] as,

$$g(\underline{d}) = (1 - k)\prod_i (1 - d_i)^2 + k. \tag{3.42}$$

This function has been chosen such that $g'(d_i = 1) = 0$ to guarantee that the strain energy density function takes a finite value as the domain is locally cracked. The small parameter $k \ll 1$ is introduced for maintaining the well-posedness of the problem for partially broken part of the domain [134, 135, 165]. Next $\mathbb{C}^e$ denotes the fourth-order elasticity tensor, which may constitute the isotropic or cubic symmetry for crystalline materials. α is the thermal expansion coefficient for isotropic behavior, K is the bulk modulus, and θ_0 denotes a fixed reference temperature. To avoid crack propagation under compression, the elastic strain can be further decomposed into a positive part w^e_+ and negative part w^e_- by the spectral decomposition or the volumetric and deviatoric split [135, 149, 166, 167].

$$\hat{\psi}^e = g(\underline{d})w^e_+ + w^e_-, \tag{3.43}$$

where the description of w_+^e and w_-^e for crystalline materials will be revisited in the following section.

We then take the contribution of plastic work for crack growth into account to simulate ductile fracture behavior. The simple equation for the plastic work may have the form:

$$\hat{\psi}^p = g(\underline{d})^p \langle w^p - w_0^p \rangle, \text{ where } g(\underline{d})^p = g(\underline{d}) \text{ and } w^p = \frac{1}{2} \sum_\alpha h(s^\alpha)^2. \tag{3.44}$$

In our formulation, the plastic work is temperature-dependence due to the incorporation of temperature-dependent creep motion (see the viscoplastic flow rule in (3.60)). Nevertheless, we follow the treatment in Simo and Miehe [47] and assume that the free energy function is temperature-independent for simplicity. As such, the thermoelastic heating contains no latent plastic terms and is in fact identical to the Gough-Joule effect, as explained in Simo and Miehe [47]. A more comprehensive treatment that considers the plastic contribution in thermo-plastic solids can be found in recent work by Aldakheel [148]. Here the degradation function for plastic work is assumed to be identical to that of the elastic work, and a plastic work threshold w_0^p may be introduced for controlling the plastic deformation in ductile fracture [149, 167]. The angle bracket operator is defined as,

$$\langle x \rangle = \begin{cases} 0 & \text{if } x < 0 \\ x & \text{if } x \geq 0 \end{cases}. \tag{3.45}$$

The plastic work ω^p comes from the hardening contribution, which is consistent with the Taylor hardening in (3.58). Therefore, the thermodynamic force g^α power-conjugate to $\dot{s}^\alpha$ in (3.35) can be explicitly described as,

$$g^\alpha = -\sum_\alpha h s^\alpha. \tag{3.46}$$

The stored energy function $\hat{\psi}^c(\underline{d}, \nabla\underline{d}, \underline{\omega})$ describes the total anisotropic crack surface energy. The total crack density formulation is previously defined by (3.10) based on the diffusive crack topology using the multi-phase-field approximation (Section 3.2.3). By assuming the same fracture energy for each slip direction (or the same energy release rate, G_c), the total crack energy function can be expressed as,

$$\hat{\psi}^c = G_c \sum_i \left[\frac{1}{2l}(d_i)^2 + \frac{l}{2}\boldsymbol{\omega}_i : (\nabla d_i \otimes \nabla d_i) \right]. \tag{3.47}$$

The purely thermal contribution on the stored energy function $\hat{\psi}^\theta$ constitutes the heat transfer, in which the equation of $\hat{\psi}^\theta$ may have a simple form as [149, 161–164, 168, 169],

$$\hat{\psi}^\theta = c_v \left[(\theta - \theta_0) - \theta \log(\theta/\theta_0) \right], \tag{3.48}$$

where c_v is the specific heat defined in (3.37). The specific heat is assumed to be a constant for single-crystal halite based on Urquhart and Bauer [84]. In addition, we simplify the thermal-mechanical-fracture coupling problems by assuming that the stored thermal energy is not affected by fracture [149].

Finally, the microscopic multiple phase-field evolution equation for each phase of (3.33) now becomes,

$$2(1 - d_i)\mathcal{H}_i + \frac{G_c}{l}d_i + G_c l \nabla \cdot (\boldsymbol{\omega}_i \cdot \nabla d_i) = 0, \tag{3.49}$$

where $\mathcal{H}_i$ is the strain-history functional that governs the evolution of the irreversible crack propagation (cf. Nguyen, Réthoré, and Baietto [134] and Nguyen et al. [135]). This functional may takes the following form,

$$\mathcal{H}_i = \max_{\tau \in [0,t]} \left\{ \prod_{j \neq i}(1 - d_j)^2 \left[w_+^e + \langle w^p - w_0^p \rangle \right] \right\}. \tag{3.50}$$

3.3 Constitutive law

In this section, we present the constitutive law to capture the anisotropic behavior of crystalline materials. We combine the multi-phase-field method and the single-crystal plasticity theory to replicate the damage-elasto-plastic behavior via the effective stress theory [170–173]. The effective stress theory hypothesizes that there exists an effective stress space where local stresses are redistributed to the effective area such as the undamaged skeleton of the body, undamaged material micro-bonds, the vicinity of growing voids. In addition, we also employ the hypothesis of strain equivalence. This assumption states that the strain caused by applying the total stress on the actual damaged material is the same as the strain caused by applying the effective stress on the fictitious undamaged material. As a result, the local elastoplastic constitutive responses and the evolution of internal variables can be resolved in a decoupled manner. While this technique is often employed for coupling damage and plasticity models (e.g. Borst and Verhoosel [140]), Choo and Sun [174] have used this technique to couple a pressure-dependent plasticity model and the phase-field fracture framework.

Recalling the specific free energy function, (3.40) and (3.41), with the constitutive relation (3.30) reaches that the Cauchy stress, or total stress, can be resolved as,

$$\boldsymbol{\sigma} = \frac{\partial \hat{\psi}}{\partial \boldsymbol{\epsilon}^e} = g(\underline{d})\hat{\boldsymbol{\sigma}} \quad \text{with} \quad \hat{\boldsymbol{\sigma}} = \mathbb{C}^e : \boldsymbol{\epsilon}^e - 3\alpha K(\theta - \theta_0)\boldsymbol{I}, \tag{3.51}$$

where $\hat{\boldsymbol{\sigma}}$ denotes the effective stress or damage effective stress. It should be noted that the term effective stress of this study is different from that of porous media, in which the effective stress indicates the stress of the solid skeleton when saturated or partially saturated with fluid [19, 20, 28, 43, 175–179]. The stress update algorithm for the multi-phase-field approach coupled to crystal plasticity is described in Algorithm 1.

3.3.1 Single crystal elasticity

In this study, the elastic response of single-crystal halite is described by the fourth-order elasticity tensor $\mathbb{C}^e$ as in (3.41) and (3.51). As a crystal structure having cubic symmetry, single-crystal halite can be represented by three elastic constant, C_{11}, C_{12}, and C_{44}, where the x, y, and z axes are aligned with the crystallographic axes (e.g. Hirth and Lothe [180] and Wachtman, Cannon, and Matthewson [181]). Apart from the anisotropic features originated from the microstructure, the elastic behavior of halite depends on temperature, pressure, and loading conditions [182, 183]. Therefore, the experimental set-up including sample preparation process is an integral part to estimate the elastic parameters. There have been many efforts to measure the elastic constants of natural rock salt. According to Birch [184], the ultrasonics, one of the dynamical methods, may be the best technique to estimate the elastic properties of halite including its aggregates. One of the pioneering works was proposed by Oliver and Pharr [185], in which the load-displacement data from indentation experiments is used for determining elastic modulus of materials. Here we assume that the effect of elastic anisotropy is minor compared to the effect of plastic and damage anisotropy, following the standard assumption in crystal plasticity [186]. A more accurate model may apply the Zener anisotropy factor (cf. Clayton [151] p. 559) to estimate how severe the assumption of elastic isotropy is for halite. The optimal estimation of material parameters via inverse problems or optimization procedure, and the calculation of Zener anisotropy factor for halite are out of the scope but will be considered in future work. The average bulk modulus (K) and Poisson's ratio (ν), obtained from single-crystal data in Carter and Norton [145], are presented in Table 3.1.

The thermoelastic strain energy (w^e) in (3.41) can be rewritten in terms of volumetric and deviatoric strain as,

$$w^e = \frac{1}{2}K(\epsilon_v^e)^2 + \mu\left(\boldsymbol{\epsilon}_d^e : \boldsymbol{\epsilon}_d^e\right) - 3\alpha K(\theta - \theta_0)\epsilon_v^e, \quad \text{with} \quad \boldsymbol{\epsilon}^e = \frac{1}{3}\epsilon_v^e\boldsymbol{I} + \boldsymbol{\epsilon}_d^e, \qquad (3.52)$$

where K and μ are the elastic bulk and shear moduli, respectively, $\epsilon_v^e = \text{tr}\,\epsilon^e$ is the volumetric strain, and ϵ_d^e is the deviatoric strain tensor. By decomposing the elastic strain into volumetric and deviatoric contributions, we can further separate the thermoelastic strain energy as follows to prevent unrealistic crack propagation under compression:

$$\begin{cases} w_+^e := \dfrac{1}{2}K\langle\epsilon_v^e\rangle_+^2 + \mu\left(\epsilon_d^e : \epsilon_d^e\right) - 3\alpha K(\theta - \theta_0)\langle\epsilon_v^e\rangle_+ \\ w_-^e := \dfrac{1}{2}K\langle\epsilon_v^e\rangle_-^2 - 3\alpha K(\theta - \theta_0)\langle\epsilon_v^e\rangle_- \end{cases}. \tag{3.53}$$

This additive volumetric-deviatoric split is proposed by Amor, Marigo, and Maurini [187], while the split of the compressive and tensile components via spectral decomposition can be found in Miehe, Hofacker, and Welschinger [125].

3.3.2 Single crystal plasticity

This section presents the stress update algorithm for single-crystal plasticity on effective stress space. The unified fully implicit return algorithm for both rate-independent and rate-dependent settings are implemented based on Miehe and Schröder [121]. Within this framework, a multisurface-type model with the elastic domain is used as in Cuitino and Ortiz [118], and the power low-type viscoplastic slip-rate is introduced for single-crystal halite. This slip-rate equation takes temperature and rate-dependent effects into account to describe dislocation creep. For the rate independent limit, the pseudo-inverse method based on the singular value decomposition (SVD) is used for the inverse of the Jacobian matrix in the constitutive equations [120, 121].

Followed by (3.3), we first denote by the homogeneous strain rate $\dot{\epsilon}$ in a crystal and consider its additive decomposition into elastic ($\dot{\epsilon}^e$), plastic ($\dot{\epsilon}^p$), and thermal ($\dot{\epsilon}^\theta$) parts, respectively.

$$\dot{\epsilon} = \dot{\epsilon}^e + \dot{\epsilon}^p + \dot{\epsilon}^\theta. \tag{3.54}$$

The plastic component coming from the slips on crystallographic planes results in the

following expression (cf. (3.5)) :

$$\dot{\boldsymbol{\epsilon}}^p = \sum_{\alpha} \dot{\gamma}^\alpha \boldsymbol{S}^\alpha. \tag{3.55}$$

Again, $\dot{\gamma}^\alpha$ and $\boldsymbol{S}^\alpha$ denote the plastic slip rate and the symmetric part of the Schmid tensor on α-slip system, respectively.

Now we present the stress update algorithm for a crystal with $2N$ potentially active slip systems, $\mathcal{J} := \{1, 2, ..., 2N\}$. Considering the microforce balance equation (3.18) for the slip system and crystal plasticity theory [60, 121, 122], the yield condition can be expressed as a function of the Schmid resolved shear stress (τ^α) and the critical resolved shear stress (τ_Y^α) for each slip system. Here we set up the yield condition based on the effective stress and critical resolved shear stress [139, 188],

$$f^\alpha = \tau^\alpha - \tau_Y^\alpha, \quad \text{where} \quad \tau^\alpha = \hat{\boldsymbol{\sigma}} : \boldsymbol{S}^\alpha. \tag{3.56}$$

Then a non-smooth convex elastic domain in the stress space can be defined as,

$$\mathbb{E} = \left\{ (\hat{\boldsymbol{\sigma}}, \tau_Y^\alpha) \mid f^\alpha \leq 0 \ \text{for} \ \alpha = 1, 2, ..., 2N \right\}. \tag{3.57}$$

The evolution of these resistances within a multislip deformation process is governed by the hardening equations,

$$\dot{\tau}_Y^\alpha = h \sum_{\beta=1}^{2N} \dot{\gamma}^\beta. \tag{3.58}$$

The hardening of the yield surface is characterized by the simple Taylor hardening law that introduces only one additional material parameter, i.e., the plastic modulus (h). Here we rewrite the plastic strain rate in Koiters's form for rate-dependent single-crystal plasticity as,

$$\dot{\boldsymbol{\epsilon}}^p = \sum_{\alpha=1}^{2N} \dot{\gamma}^\alpha \frac{\partial f^\alpha}{\partial \hat{\boldsymbol{\sigma}}} = \sum_{\alpha=1}^{2N} \dot{\gamma}^\alpha \boldsymbol{S}^\alpha, \tag{3.59}$$

80

where the slip rate $\dot{\gamma}^\alpha$ satisfies a constitutive viscoplastic form under loading conditions to incorporate plastic flow by the dislocation creep motion in single-crystal halite as (cf. Hansen [100], Miehe and Schröder [121], and Wawersik and Zeuch [189]):

$$\dot{\gamma}^\alpha = C_0 \exp\left(-\frac{Q}{R\theta}\right)\left[\left(\frac{f^{\alpha+}}{\tau_Y^\alpha} + 1\right)^p - 1\right]. \tag{3.60}$$

Here C_0 represents a fitting parameter; Q is the activation energy; R is the universal gas constant; θ is the absolute temperature; p is a strain-rate-sensitivity exponent. The overstress function $f^{\alpha+}$ is defined by,

$$f^{\alpha+} := \begin{cases} f^\alpha & \text{if } f^\alpha > 0 \\ 0 & \text{otherwise} \end{cases}. \tag{3.61}$$

The slip rate $\dot{\gamma}^\alpha$ takes the form of (3.60) such that the rate-dependence can be introduced into the plastic constitutive responses [150]. Note that the dislocation creep equation obtained from the experiments [189] is not originally intended for describing a microscopic slip-system response. Instead, it was first used to describe the macroscopic response of a specimen. Nevertheless, we hypothesize that the creeping equation of the slip system takes a similar form. To minimize the discrepancy between simulated results and experimental data, we calibrate the material parameters by solving the inverse problems [190, 191].

The unified stress update algorithm on effective stress space is outlined for both rate-independent and rate-dependent crystal plasticity frameworks. Algorithm 1 describes the elastic predictor phase on effective space, while the plastic corrector and determination of active slip systems are performed in Algorithm 2. In the rate-dependent case, the viscoplastic regularization of single-crystal plasticity for halite (3.60) is used. At the rate-independent limit, the slip rate $\dot{\gamma}^\alpha$ satisfies the classical Kuhn-Tucker conditions [121, 122,

143, 192]:

$$\dot{\gamma}^\alpha \geq 0, \quad f^\alpha \leq 0, \quad \dot{\gamma}^\alpha f^\alpha = 0, \tag{3.62}$$

for all α. Furthermore, the inverse of the Jacobian ($\mathbf{D}$) can be obtained directly if it is non-singular. If the loading rate is sufficiently low such that the response is approaching the rate-independent regime, the Jacobian ($\mathbf{D}$) may become singular. In this case, the Moore-Penrose pseudo-inverse, which can be determined via the singular value decomposition (SVD), is used to compute the incremental plastic slip [120]. For brevity, we drop the subscript $n + 1$ for variables pertaining to the time t_{n+1}.

Algorithm 1 Elastic predictor phase on effective stress space

---

1: At integration point compute strain increments $\Delta\boldsymbol{\epsilon}$
2: Compute the effective trial stress $\hat{\boldsymbol{\sigma}}^{\mathrm{tr}} = \hat{\boldsymbol{\sigma}}_n + \mathbb{C}^e : \Delta\boldsymbol{\epsilon}$
3: Assemble trial active set $\mathscr{A}^{\mathrm{tr}} = \{\alpha \in \mathcal{J} \mid \hat{\boldsymbol{\sigma}}^{\mathrm{tr}} : \boldsymbol{S}^\alpha - \tau_{Y,n}^\alpha > 0\}$
4: **if** $\mathscr{A}^{\mathrm{tr}} =$ **then**
  Elastic response: set $\hat{\boldsymbol{\sigma}} = \hat{\boldsymbol{\sigma}}^{\mathrm{tr}}$, $\tau_Y^\alpha = \tau_{Y,n}^\alpha$, $\mathscr{A} =$,
  $\mathbb{C} = \mathbb{C}^e$, and exit
5: **else**
  Plastic response: call Algorithm 2
  Update $\hat{\boldsymbol{\sigma}}$, τ_Y^α, and $\mathscr{A}$
  $\mathbb{C} \leftarrow \mathbb{C}^{ep}$, and exit
6: **end if**
7: Resolve the total stress $\boldsymbol{\sigma} = g(\underline{d})\hat{\boldsymbol{\sigma}}$

In Algorithm 1 we assemble the trial active set by checking the yield conditions for each slip system (3.56) under the given temperature θ. When the trial active set is empty, the material is in the purely elastic regime. If the trial active set contains any element, Algorithm 2 is triggered and the Newton iteration for the plastic response is performed. In this iteration step, the active slip system is successively checked and reassembled followed by two constraints. Firstly, we check γ^α in the trial active set whether each parameter violates the discrete loading conditions, (3.60) and (3.62), in the sense $\gamma^\alpha \leq 0$. If this is the case, we drop the slip system from the active set $\mathscr{A}$ and restart the local Newton iteration. Secondly, we check the yield conditions again for the slip systems, not in the current trial active set. We then reassemble the active set and restart the local Newton iteration by

Algorithm 2 Plastic integrator and determination of active slip systems

1: Initialize the active set $\mathscr{A} = \mathscr{A}_n$
2: Set initial values for plastic slip iteration: $\gamma^\alpha = 0 \quad \forall \alpha \in \mathscr{J}$
3: Get the current effective stress: $\hat{\boldsymbol{\sigma}} = \hat{\boldsymbol{\sigma}}^{\text{tr}} - \mathbb{C}^e : \left(\sum_{\alpha=1}^{2N} \gamma^\alpha \boldsymbol{S}^\alpha \right)$
4: Compute the residuals for active slips systems ($\alpha, \beta \in \mathscr{A}$) and construct the Jacobian (**D**)

$$r^\alpha = \hat{\boldsymbol{\sigma}} : \boldsymbol{S}^\alpha - \tau_Y^\alpha \sqrt[p]{\frac{\eta}{\Delta t}\gamma^\alpha + 1}$$

$$\mathrm{D}^{\alpha\beta} = \boldsymbol{S}^\alpha : \mathbb{C}^e : \boldsymbol{S}^\beta + h\left(\frac{\eta}{\Delta t}\gamma^\alpha + 1\right)^{1/p} + \tau_Y^\alpha \delta^{\alpha\beta}\frac{\eta}{p\Delta t}\left(\frac{\eta}{\Delta t}\gamma^\alpha + 1\right)^{1/p-1}$$

$$\text{with } \tau_Y^\alpha = \tau_{Y,n}^\alpha + \sum_{\alpha \in \mathscr{A}} h\gamma^\alpha; \quad \eta = 1/\left[C_0 \exp\left(-\frac{Q}{R\theta}\right)\right]$$

5: **if D** is singular **then**
Perform singular value decomposition on **D** and obtain the Moore-Penrose pseudo inverse from SVD:

$$\bar{\mathbf{D}}^{-1} = \mathbf{V}\bar{\boxtimes}^{-1}\mathbf{U}^{\mathrm{T}}$$

6: **else** Compute $\mathbf{D}^{-1}$ by inversing **D**, then set $\bar{\mathbf{D}}^{-1} = \mathbf{D}^{-1}$ based on standard inversion
7: **end if**
8: Update incremental plastic slip: $\gamma^\alpha \leftarrow \gamma^\alpha + \sum_{\alpha \in \mathscr{A}}(\bar{\mathbf{D}}^{-1})^{\alpha\beta}r^\beta$
9: If $\left(\sqrt{\sum_{\alpha \in \mathscr{A}}[r^\alpha]^2} > \text{tol}\right)$ go to 3
10: Check the minimum loaded system (I) :
11: **if** $\gamma^\alpha \leq 0$ for some $\alpha \in \mathscr{A}$ **then** $\mathscr{A} \leftarrow \{\mathscr{A} \setminus \alpha^*\}$ and go to 2
where $\gamma^{\alpha^*} = \min[\gamma^\alpha] \, \forall \alpha \in \mathscr{A}$
12: **else** go to 15
13: **end if**
14: Check the maximum loaded system (II):
15: **if** $f^\alpha > 0$ for some $\alpha \in \mathscr{J} \setminus \mathscr{A}$ **then** $\mathscr{A} \leftarrow \{\mathscr{A} \cup \alpha^*\}$ and go to 2
where $f^{\alpha^*} = \max[f^\alpha] \, \forall \alpha \in \mathscr{J} \setminus \mathscr{A}$
16: **else** Construct the consistent tangent-moduli:

$$\mathbb{C}^{ep} := \mathbb{C}^e - \sum_{\alpha \in \mathscr{A}} \sum_{\beta \in \mathscr{A}} (\bar{\mathbf{D}}^{-1})^{\alpha\beta}(\mathbb{C}^e : \boldsymbol{S}^\alpha) \otimes (\boldsymbol{S}^\beta : \mathbb{C}^e)$$

17: **end if**
18: Return to Algorithm 1

initializing $\gamma^\alpha = 0$ for all $\alpha \in \mathscr{A}$. Otherwise, Algorithm 2 is terminated, and the updated parameters are forwarded to Algorithm 1 for the total stress calculation.

3.4 Variational formulation

This section describes a finite element formulation that combines the multi-phase-field and the crystal plasticity for modeling thermo-mechanical behaviors of single-crystal halite. We first derive the variational form of thermo-mechanical problems with multiple phase fields representing damage along preferential directions. This is followed by the description of a staggered scheme for solving the equilibrium (momentum and energy balances) and multiple phase-field equations in Section 5.2.3.

3.4.1 Galerkin form

We consider a domain $\mathcal{B}$ with its boundary $\partial\mathcal{B}$ composed of Dirichlet boundaries (solid displacement $\partial\mathcal{B}_u$, temperature $\partial\mathcal{B}_\theta$) and von Neumann boundaries (solid traction $\partial\mathcal{B}_t$, heat flux $\partial\mathcal{B}_q$) satisfying,

$$\begin{cases} \partial\mathcal{B} = \overline{\partial\mathcal{B}_u \cup \partial\mathcal{B}_t} = \overline{\partial\mathcal{B}_\theta \cup \partial\mathcal{B}_q} \\ \emptyset = \partial\mathcal{B}_u \cap \partial\mathcal{B}_t = \partial\mathcal{B}_\theta \cap \partial\mathcal{B}_q. \end{cases} \tag{3.63}$$

The prescribed boundary conditions (Dirichlet and von Neumann boundary conditions) read,

$$\begin{cases} \boldsymbol{u} = \overline{\boldsymbol{u}} \quad \text{on} \quad \partial\mathcal{B}_u, \\ \boldsymbol{\sigma} \cdot \boldsymbol{n} = \overline{\boldsymbol{t}} \quad \text{on} \quad \partial\mathcal{B}_t, \\ \theta = \overline{\theta} \quad \text{on} \quad \partial\mathcal{B}_\theta, \\ -\boldsymbol{n} \cdot \boldsymbol{q} = \overline{q} \quad \text{on} \quad \partial\mathcal{B}_q, \\ \nabla\underline{d} \cdot \boldsymbol{n} = 0 \quad \text{on} \quad \partial\mathcal{B}, \end{cases} \tag{3.64}$$

where $\boldsymbol{n}$ is outward unit normal on surface $\partial\mathcal{B}$. For model closure, the initial conditions are imposed as,

$$\boldsymbol{u} = \boldsymbol{u}_0, \quad \theta = \theta_0 \ \text{ at } \ t = t_0. \tag{3.65}$$

In addition, we consider the trial space for the weak form that reads,

$$V_{\boldsymbol{u}} = \left\{\boldsymbol{u} : \mathcal{B} \to \mathbb{R}^3 | \boldsymbol{u} \in [H^1(\mathcal{B})], \boldsymbol{u}|_{\partial\mathcal{B}_{\boldsymbol{u}}} = \overline{\boldsymbol{u}}\right\}, \tag{3.66}$$

$$V_{\theta} = \left\{\theta : \mathcal{B} \to \mathbb{R}|_{\theta} \in H^1(\mathcal{B}), \theta|_{\partial\mathcal{B}_{\theta}} = \overline{\theta}\right\}, \tag{3.67}$$

$$\underline{V_d} = \left\{\underline{d} : \mathcal{B} \to \mathbb{R}|\underline{d} \in H^1(\mathcal{B})\right\}, \quad \text{i.e., } \ V_{d_i} = \left\{d_i : \mathcal{B} \to \mathbb{R}|d_i \in H^1(\mathcal{B})\right\}. \tag{3.68}$$

Here H^1 denotes the Sobolev space of degree one. The number of d_i depends on how we define preferential directions, which is consistent with the slip systems for single-crystal halite. The corresponding admissible spaces of variations are defined as,

$$V_{\boldsymbol{\eta}} = \left\{\boldsymbol{\eta} : \mathcal{B} \to \mathbb{R}^3 | \boldsymbol{\eta} \in [H^1(\mathcal{B})], \boldsymbol{\eta}|_{\partial\mathcal{B}_{\boldsymbol{u}}} = \boldsymbol{0}\right\}, \tag{3.69}$$

$$V_{\psi} = \left\{\psi : \mathcal{B} \to \mathbb{R}|_{\psi} \in H^1(\mathcal{B}), \psi|_{\partial\mathcal{B}_{\theta}} = 0\right\}, \tag{3.70}$$

$$\underline{V_{\phi}} = \left\{\underline{\phi} : \mathcal{B} \to \mathbb{R}|\underline{\phi} \in H^1(\mathcal{B})\right\} \quad \text{i.e., } \ V_{\phi_i} = \left\{\phi_i : \mathcal{B} \to \mathbb{R}|\phi_i \in H^1(\mathcal{B})\right\}. \tag{3.71}$$

Therefore, the weighted residual statements of the balance of linear momentum, energy, and phase-field are: Find $\boldsymbol{u} \in V_{\boldsymbol{u}}$, $\theta \in V_{\theta}$, and $\underline{d} \in \underline{V_{\phi}}$ such that all $\boldsymbol{\eta} \in V_{\boldsymbol{\eta}}$, $\psi \in V_{\psi}$, and $\underline{\phi} \in \underline{V_{\phi}}$,

$$G(\boldsymbol{u}, \theta, \underline{d}, \boldsymbol{\eta}) = H(\boldsymbol{u}, \theta, \underline{d}, \psi) = \underline{L}(\boldsymbol{u}, \theta, \underline{d}, \underline{\phi}) = 0. \tag{3.72}$$

Consider the governing equations given by (3.16), (3.37), and (3.49). Through the standard weighted residual procedure, we obtain the variational equations as,

$$G : V_{\boldsymbol{u}} \times V_{\theta} \times \underline{V_d} \times V_{\boldsymbol{\eta}} \to \mathbb{R},$$

$$G(\boldsymbol{u}, \theta, \underline{d}, \boldsymbol{\eta}) = \int_{\mathcal{B}} \nabla\boldsymbol{\eta} : \boldsymbol{\sigma}\, dV - \int_{\partial\mathcal{B}} \boldsymbol{\eta} \cdot \overline{\boldsymbol{t}}\, d\Gamma = 0, \tag{3.73}$$

$$H : V_{\boldsymbol{u}} \times V_\theta \times \underline{V_d} \times V_\psi \to \mathbb{R},$$

$$H(\boldsymbol{u}, \theta, \underline{d}, \psi) = \int_{\mathcal{B}} \psi c_v \dot{\theta} dV - \int_{\mathcal{B}} \psi \left[\sum_\alpha (\pi^\alpha \dot{\gamma}^\alpha + g^\alpha \dot{s}^\alpha) \right] dV - \int_{\mathcal{B}} \psi \left(3\alpha K \boldsymbol{I} : \dot{\boldsymbol{\epsilon}}^e \right) \theta dV \qquad (3.74)$$

$$+ \int_{\mathcal{B}} \nabla \psi \cdot \kappa \nabla \theta dV - \int_{\partial \mathcal{B}} \psi \bar{q} d\Gamma = 0,$$

$$\underline{L} : V_{\boldsymbol{u}} \times V_\theta \times \underline{V_d} \times \underline{V_\phi} \to \mathbb{R},$$

$$L_i(\boldsymbol{u}, \theta, d_i, \phi_i) = \int_{\mathcal{B}} \phi_i \left[2(1 - d_i)\mathcal{H}_i \right] dV + \int_{\mathcal{B}} \frac{G_c}{l} \left[\phi_i d_i + l^2 \nabla \phi_i \cdot \boldsymbol{\omega}_i \cdot \nabla d_i \right] dV, \quad (3.75)$$

where $\mathcal{H}_i$ is previously defined by (3.50).

3.4.2 Linearization for the staggered algorithm

Due to nonlinearity and path-dependence nature of the proposed model, linearizing the system of equations is necessary if an implicit solver is used. In this work, the system of equations is multi-physical. As a result, this system of equations can be solved either in a monolithic or operator-split manner [193, 194]. As previously numerical experiments with single phase-field problems show that the operator splitting approach may potentially be more robust [125, 165], we propose a semi-split iterative strategy that is covered in the later chapter 5. In this procedure, the multiple phase fields are advanced followed by the thermo-mechanical solver, which updates the displacement and temperature fields together. The solution strategies are described in the later chapter.

To obtain the numerical solution of the thermo-mechanical problems iteratively, the linearization of residuals of the governing equations is required. Due to the usage of the iterative sequential solver, the operator-split residual will only update one set of unknowns within one split iterative step. Hence the linearization is only consistent numerically for the staggered solver but not for the monolithic counterpart. With this in mind, we first describe the linearization of the balance of linear momentum with respect to the displace-

ment and temperature as follows:

$$\delta G(\boldsymbol{u}, \theta, \underline{d}, \boldsymbol{\eta}) = \int_{\mathcal{B}} \nabla \boldsymbol{\eta} : \mathbb{C} : \delta \boldsymbol{u} dV - \int_{\mathcal{B}} \nabla \cdot \boldsymbol{\eta} \left[g(\underline{d}) 3\alpha K \right] \delta\theta dV, \qquad (3.76)$$

in which $\mathbb{C} = g(\underline{d})\mathbb{C}^{ep}$ can be obtained from the constitutive laws based on the effective stress concept (Algorithms 1 and 2). Likewise, the linearization of energy balance equation can be derived as follows:

$$\delta H(\boldsymbol{u}, \theta, \underline{d}, \psi) = \int_{\mathcal{B}} \psi c_v \delta\theta dV - \int_{\mathcal{B}} \psi \delta \left[\sum_\alpha (\pi^\alpha \dot{\gamma}^\alpha + g^\alpha \dot{s}^\alpha) \right] dV - \int_{\mathcal{B}} \psi \delta \left(3\alpha K \boldsymbol{I} : \dot{\boldsymbol{\epsilon}}^e \right) \theta dV$$
$$- \int_{\mathcal{B}} \psi \left(3\alpha K \boldsymbol{I} : \dot{\boldsymbol{\epsilon}}^e \right) \delta\theta dV + \int_{\mathcal{B}} \nabla\psi \cdot \kappa \delta(\nabla\theta) dV. \qquad (3.77)$$

We note that the plastic dissipation and structure heating terms in the energy balance equation (3.38) can be considered as a source term due to internal mechanical work. The consistent linearization of these terms for full implicit calculations requires complicated computations unless we employ automatic differentiation tools (e.g. Albany [195–197]). We, therefore, adopt the semi-implicit scheme for the energy balance equations by combining the backward Euler and forward Euler schemes (5.9). This procedure leads to the following tangent for the energy balance equation,

$$\delta H(\boldsymbol{u}, \theta, \underline{d}, \psi) = \int_{\mathcal{B}} \psi c_v \delta\theta dV - \int_{\mathcal{B}} \psi \left(3\alpha K \boldsymbol{I} : \dot{\boldsymbol{\epsilon}}^e \right) \delta\theta dV + \int_{\mathcal{B}} \nabla\psi \cdot \kappa \delta(\nabla\theta) dV. \quad (3.78)$$

For completeness, we include the linearization of the multiple phase-field equations as follows:

$$\delta L_i(\boldsymbol{u}, \theta, d_i, \phi_i) = \int_{\mathcal{B}} -2\phi_i \mathcal{H}_i \delta d_i dV + \int_{\mathcal{B}} \frac{G_c}{l} \left[\phi_i \delta d_i + l^2 \nabla\phi_i \cdot \boldsymbol{\omega}_i \cdot \delta(\nabla d_i) \right] dV. \quad (3.79)$$

Note again that this equation is for phase-field variable d_i, and other phase-field variables exhibit identical expressions.

3.5 Numerical examples

We present numerical examples to validate and evaluate the applicability of the proposed combined multi-phase-field crystal plasticity model for single-crystal halite. Firstly, plane strain (2D) tests are used to investigate influence of different orientations of the slip system on anisotropic behavior of halite. In particular, we compare the stress-strain curves, plastic slips, and crack phase fields obtained from multiple simulations with different relative angles between the slip-system and the loading direction. Then, we conduct additional tests with different mechanical and thermal boundary and initial conditions to evaluate the thermo-mechanical coupling effects of halite. A two-dimensional tension test with an existing crack is set up to examine how rate-dependence affects the onset and propagation of anisotropic fracture. Finally, to provide an insight on how grain boundary toughness affects the macroscopic mechanical behaviors, we conduct three tensile loading simulations on bicrystals with the same crystal properties but with grain boundary exhibiting different critical energy release rates.

The material properties, such as stiffness, strength, thermal parameters, activation energy, of halite depend significantly on the environmental and loading conditions. In an idealized case in which experimental data are sufficient, a subset of material parameters can be determined from the first principle, while the rest of the material parameters are then inferred by solving inverse problems [190, 191, 198]. However, due to the complexity of the inverse problems that involve both crystal plasticity and anisotropic fracture, such an approach is not used but will consider in the future study. As an alternative, the material parameters used in this study are obtained from the various sources in the literature. Firstly, the elastic moduli and fracture energy of single-crystal halite are obtained from the previous study by Tromans and Meech [199]. The length scale l in Table 3.1 is on the order of mesh size and is used as a regularization parameter [135, 187, 200]. Meanwhile, the critical resolved stress, hardening parameter, and creep parameters are obtained from Wawersik and Zeuch [189] and Wenk et al. [201]. The thermal parame-

Table 3.1: Material properties of the specimens for the numerical simulations

Parameters	Description	Value	Unit
K	Bulk modulus	25.0	GPa
ν	Poisson's ratio	0.25	-
τ	Critical resolved shear stress	5.0×10^{-3}	GPa
h	hardening parameter	1.0×10^{-1}	GPa
G_c	Fracture energy	1.15	J/m^2
l	Length scale	1.0×10^{-5}	m
β	Anisotropy factor	40.0	-
Q	Activation energy	14.0	kcal/mol
R	Gas constant	1.986×10^{-3}	kcal/mol/K
C_0	Shape factor	1.0	-
p	exponent parameter	10.0	-
α	Thermal expansion coefficient	11.0×10^{-6}	1/K
c_v	Specific heat	2.0×10^6	J/m^3/K
κ	Thermal conductivity	2.0	W/m/K

ters including the specific heat, thermal conductivity, and thermal expansion coefficients of halite were studied by Urquhart and Bauer [84]. The material properties used in this study are summarized in Table 3.1. Note that the some of these material parameters, such as such as thermal conductivity, heat capacity, hardening parameter, and activation energy are strictly speaking temperature dependence [148]. For instance, experimental data in Urquhart and Bauer [84], Birch and Clark [202], and Smith [203] have shown that the thermal conductivity of single-crystal halite may be reduced by half from $-75\ ^\circ$C to $100\ ^\circ$C whereas the the specific heat remains close to 2.0 MJ/m^3/K. Nevertheless, these measurements are highly dependent on the experimental settings and the discrepancies among different data sets are large compared to the statistical noise. As a result, due to the fact that the geological disposal for nuclear waste is expected to operate in a higher temperature range [82], and the lack of sufficient experimental data to incorporating the temperature dependence of all the aforementioned material parameters, the temperature dependence of these material parameters are not considered in this work.

The implementation of the numerical model leverages *Geocentric*, a massively parallel finite element code for geomechanics, which is built on the open-source finite element

library *deal.II* [204, 205] interfaced with the *p4est* mesh handling library [206], and the *Trilinos* project [207]. This code base has been widely used in previous studies including multiphysics problems [128, 177, 178, 194, 208–210].

3.5.1 Effect of crystal orientations

In this section, numerical examples are presented to investigate the anisotropic mechanical behavior of single-crystal halite when subjected to loadings under different orientations of the slip system. Figure 3.3 depicts the boundary conditions and the definition of Euler angles for rotating the slip system. For boundary conditions, the horizontal directions are constrained on both top and bottom surfaces of the sample. The bottom surface is further constraint along the vertical direction, and the displacement boundary condition is applied at the top surface to compress the sample. Note that the influence of confining pressure is not considered, but its effect considering the grain boundary simulation will be covered in future study. As can be seen from Figures 3.2 and 3.3, two cleavage planes (or slip planes) projected onto the 2D plane are used for directional information of multi-phase-field calculations. To be specific, unless changing orientations of the slip systems, each cleavage plane aligns to $45°$ and $135°$ directions onto 2D (x-horizontal, y-vertical) plane, respectively. While such a simplified treatment can be physically reasonable in a plane strain idealized setting, a more comprehensive modeling effort should consider the non-coaxial cases. For instance, fracture planes that are more likely to fail, such as $\{100\}$ [201], can be associated with one of the phase fields. This improvement will be considered in future studies. We note that the full set of $\{110\}\langle1\bar{1}0\rangle$ slip systems are considered for dislocation slip in crystal plasticity calculations, while the two slip planes are assumed to be aligned with the fracture planes.

For halite or other FCC crystals undergoing plane deformation, it is not essential to consider the whole set of the slip systems in the crystal plasticity model if the planar double-slip model is used [60, 211]. This simplified model has been introduced in the

pioneering study reported in Rashid and Nemat-Nasser [211] where only two "effective" slip systems whose slip and normal directions lies on the plane of loading. In this work, we follow the notation in Borja [61], Borja and Wren [119], and Borja and Rahmani [122] and use two Euler angles (ϕ, ψ) to describe the orientation of the crystal axes relative to the fixed reference system. We firstly use the default orientation (i.e. the slip orientations as in Figure 3.2), and then set ϕ to $10°$ and $30°$, respectively, to rotate the slip system on the x-y plane. Due to the constraint at the top and bottom surfaces, we obtain the localized plastic and damage zones without adding other conditions (e.g. geometric or material defects).
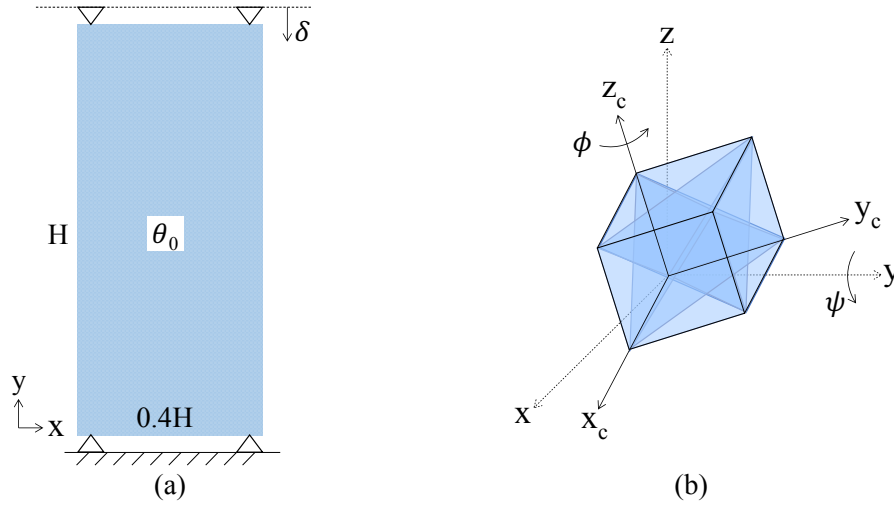
Figure 3.3: Analysis of material anisotropy by changing the orientation of the slip system, (a) the set-up for plane strain compression test, (b) the definition of Euler angles (ϕ, ψ) in the three-dimensional plane (reproduced from Borja [61]) including the slip system of single-crystal halite (see each slip system in Figure 3.2)

Four thousand bilinear quadrilateral finite elements are used to discretize the domain with the height H = 1.0 mm. The displacement, temperature, and multiple phase fields are interpolated by the same basis functions. As a result, there are 12,423 displacement degree of freedoms (DOFs), 41,141 temperature DOFs and 8,282 phase-field DOFs (4,141 for each phase-field) before applying the essential boundary conditions. Under three differ-

ent orientations, (ψ is fixed at 0 °; with ϕ = 0°, 10°, and 30°, respectively), we observe the significant influence of material anisotropy on the mechanical responses without introducing any defects or inhomogeneity. The constraint boundary condition with material anisotropy facilitates the different responses and patterns of plastic and damage behaviors. In these simulations, the reference temperature, or the initial temperature condition is set to 25 °C for all three test cases. The top boundary is moving downward during the simulation with the strain rate of 1.0×10^{-5}/sec.
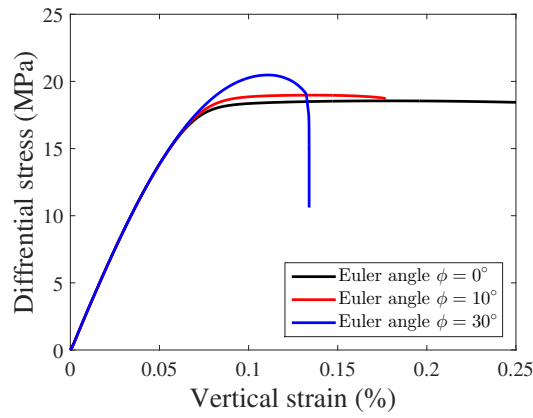
Figure 3.4: Stress-strain curve of single-crystal halite with different orientations of the slip-system (the Euler angle ψ is fixed 0° while changing ϕ = 0°, 10°, and 30°, respectively)

To analyze the mechanical responses under plane strain tests, the differential stress (the difference between the most and least compressive principal stresses) vs. axial strain curve obtained from specimens of different orientations are presented in Figure 3.4. Although little difference is observed in the stress-strain curves obtained from the ϕ = 0° and ϕ = 10° cases, the resultant plastic slip patterns in Figure 3.5 clearly show the anisotropy of the plastic and damage responses. When Euler angle ϕ is within the range from 0° to around 10 °, the damage is localized at the boundaries. In the case of ϕ = 30°, however, we observe the localized damage zone in the center of the domain, not the edges. Furthermore, the plastic slip is also concentrated in accordance with the damaged zone. These patterns are consistent with the stress-strain curve in Figure 3.4, which suggests

the brittle fracture behavior. The temperature field for the effect of energy dissipation converging to heat is not presented, which has a minor role to influence the mechanical behavior of halite.
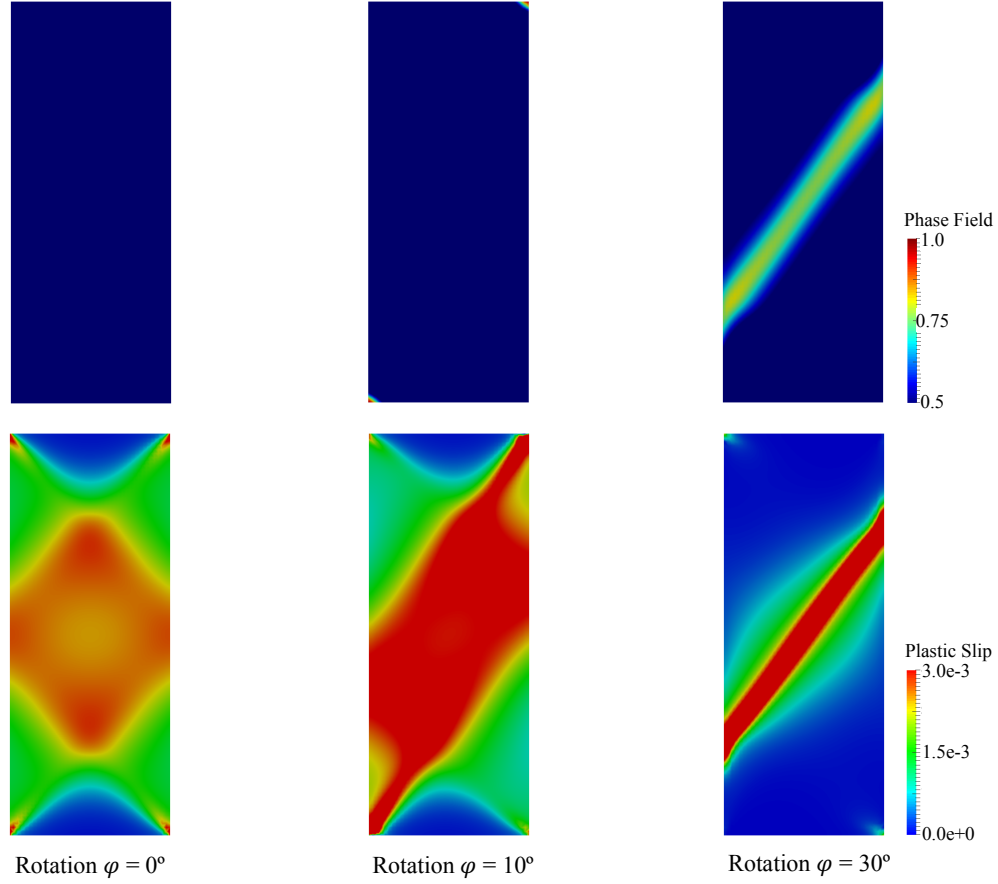
Figure 3.5: Phase-field values (top) and plastic slip results patterns (bottom) with different orientations of the slip-system to investigate the material anisotropy under plane strain compression test condition. The patterns are captured at the last numerical step of each case. Euler angle $\theta = 0°$ is fixed while ϕ varies $0°$, $10°$, and $30°$, respectively

3.5.2 Thermal effect on anisotropic creeping

We conduct the plane strain compression tests with different boundary conditions to analyze the thermal effect on halite. Firstly we designed the boundary conditions as depicted

in Figure 3.6. The left boundary is fixed along the horizontal direction, and the bottom surface is fixed against the vertical direction. The moving boundary with a constant strain late (1.0×10^{-5}/sec.) applies the loading on the top surface as in the previous numerical example. Under the same mechanical loading condition, we set three different initial reference temperatures on the sample domain: 25 °C, 50 °C, and 90 °C, respectively. In these cases the same Euler angles $\psi = 0°$ and $\phi = 70°$ are used. Under different equilibrium temperature conditions, the mechanical responses including fracture and plastic behavior are evaluated.

(a) Test set-up   (b) Stress-strain curve
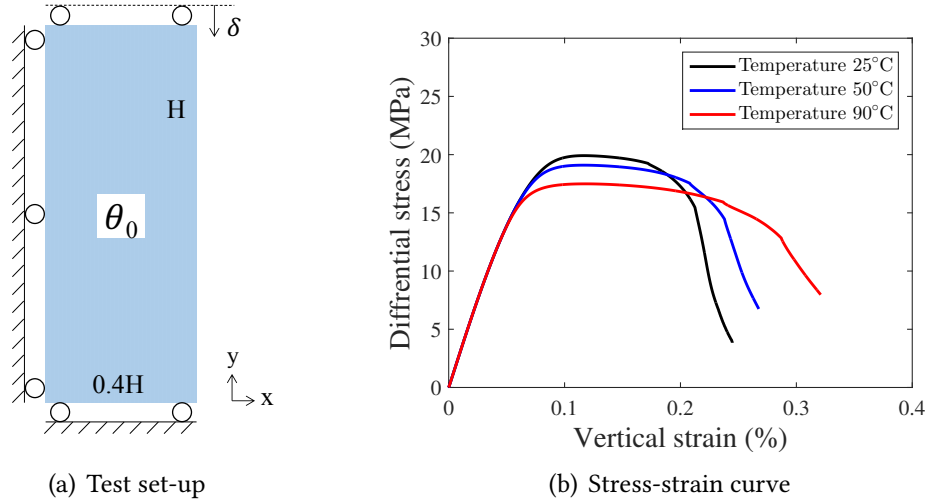
Figure 3.6: Analysis of temperature effect on mechanical responses, (a) the set-up for plane strain compression test, (b) stress-strain curves for each temperature condition (θ_0 = 25 °C, 50 °C, and 90 °C, respectively)

First of all, we compare the mechanical responses under different temperature conditions using the differential stress and vertical strain curves in Figure 3.6. In these cases the ductile fracture behaviors are observed while the plastic behaviors differ due to the difference in initial temperatures. Our crystal plasticity model adopts the creep behavior of halite that constitutes the temperature, which is essential in analyzing salt problems. Although the calibration has not been completed for temperature dependence and the fracture initiated on the sample, the influence of temperature on the mechanical behavior

of halite is clearly identified. Furthermore, we present the damage and plastic patterns at the same vertical strain, 0.23 % in Figure 3.7. Followed by the stress-strain curves in Figure 3.6, the clear fracture initiated from the top left edge is observed when the temperature is 25 °C. The plastic zones including the localized region can be further identified. As the initial temperature increases, the less damage is observed at the same displacement, which can be easily expected from the stress-strain curves. Interestingly, the more plastic slip is concentrated at the right bottom area of the domain as the temperature increases. This indicates that the temperature may further influence the patterns of plastic zones under the same mechanical loading condition.

3.5.3 Loading rate effect

In this section, we conduct a simple tensile test on a halite specimen with a pre-existing crack. By changing the prescribed loading rates, we examine how the loading rate affects the interplays between the plastic deformation and the crack growth. The size of the square domain L is 1mm $\times$ 1mm, and the initial crack length is 0.5 mm. The bottom surface of the specimen is constrained along both horizontal and vertical directions while the top surface is stretched vertically under a constant loading rate in each simulation. As demonstrated in Figure 3.8 (b), the ductile-brittle transition of halite under different loading rate is captured. Increasing the loading rate leads to higher peak differential stress and the material also behaves more ductile in the softening regime. This is consistent with the behavior of crystalline rock [212]. A closer look at the crack pattern and the distribution of the plastic strain also reveals that the loading rate affect the macroscopic responses as well as the anisotropic fracture and plastic deformation.

In particular, when the loading rate is slow ($\dot{\epsilon} = 1.0 \times 10^{-7}$/sec.), the main crack tends to follow the cleavage plane directions (see the right figure in Figure 3.9). As the strain rate is increased to $\dot{\epsilon} = 1.0 \times 10^{-6}$/sec, (the $10\dot{\epsilon}$ case in Figure 3.9), a slight zig-zag pattern is observed. It appears that initially the crack follows the cleave plane but diverts the propa-
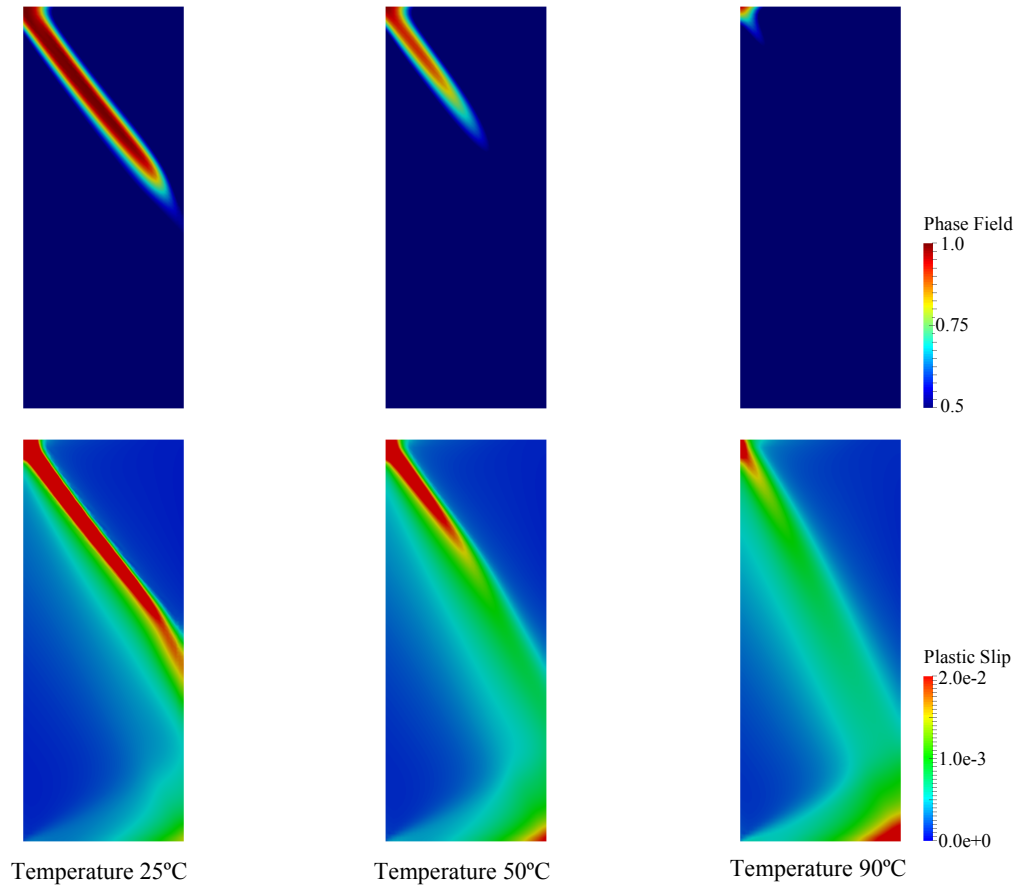
Figure 3.7: Phase-field values (top) and plastic slip results (bottom) patterns with different initial temperature conditions at the same vertical strain, 0.23 %. The constant displacement loading is applied at the top, and the Euler angles are fixed with $\psi = 0°$ and $\phi = 70°$
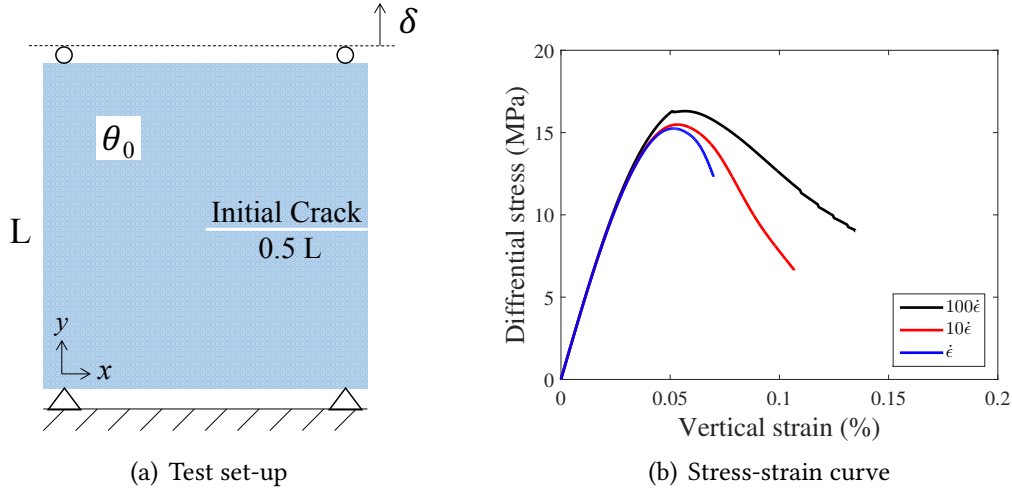
Figure 3.8: Analysis of the loading rate effect under two-dimensional tension test, (a) the set-up for boundary value problem, (b) stress-strain curve with different loading rates ($\dot{\epsilon} = 1.0\mathrm{e}^{-7}$/sec.). The initial temperature θ_0 is set to 25 °C, and the Euler angles are set to $\psi = 0°$ and $\phi = 0°$

gation direction due to loading conditions. This crack then follows another cleavage plane at the left edge of the domain. Finally, when the loading rate further increases (see the left figure in Figure 3.9), the crack propagation appears to be straight and the damaged zone is also more diffusive than the low-strain-rate counterpart. This result is perhaps attributed to the different amount of energy dissipation due to creeping deformation. As the plastic flow of each slip system is highly sensitive to the loading rate (3.60), the changes of loading rate may affect the magnitude and direction of the overall plastic flow. In the low strain rate case where the results resemble closely to the rate-independent crystal plasticity, the plastic flow is likely to be dominated by the fewer slip system, which causes plastic deformation appears to be more anisotropic. This in return changes the distribution of the driving force for each multiple phase field system in (3.50). As the multiple phase fields and plastic slip both evolve differently under different loading rates, this leads to the crack pattern appears to be more anisotropic in the low-strain-rate case.
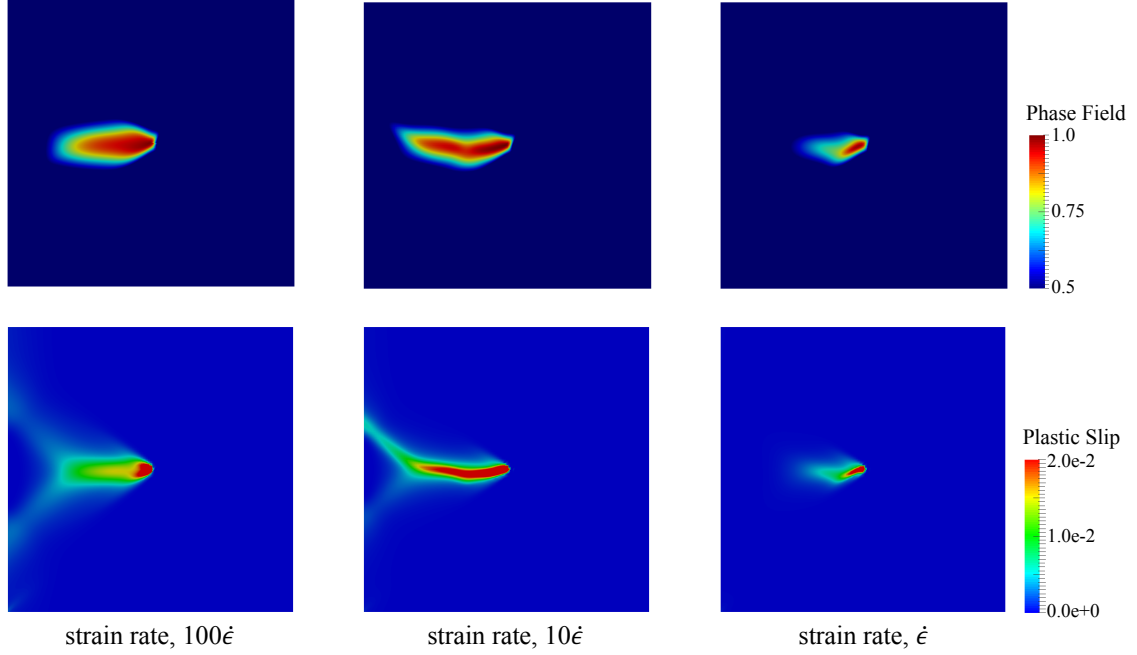
Figure 3.9: Phase-field values (top) and plastic slip results (bottom) patterns with different loading rates are illustrated. The results are captured at the last numerical step of each simulation with the loading rate $\dot{\epsilon} = 1.0e^{-7}$/sec

3.5.4   Crack propagation in a bicrystal halite

In this final example, we simulate a tensile test conducted on a bicrystal domain to investigate the interaction between grain and grain boundary. Similar boundary value problems have been used previously in Oshima, Takaki, and Muramatsu [133] and Nguyen et al. [135] to model intragrain and grain boundary fractures. In this study, our major point of departure is 1) the introduction of crystal plasticity model to capture the plastic flow of the slip system inside the crystal and 2) the modeling of plastic slip of the grain boundary. To simplify the modeling effort, the grain boundary is approximated using a crystalline material with a finite thickness that has a single-cleavage plane of which the slip direction is aligned to the longitudinal direction of the grain boundary. The upshot of this treatment on grain boundary leads to a much simpler numerical model in which there is

no need to capture the embedded discontinuities via the cohesive element or enrichment function. However, as explained previously in Wei and Anand [213], one must be cautious that representing strong discontinuities with regularized interfaces might lead to an unrealistic large volume of a fraction of grain-boundary regions if the thickness of the regularized interface is too large. The setup of the boundary value problem is depicted in Figure 3.10, the grain boundary locates on the diagonal of the domain, which is separated into two grains having different orientations (30 and 60 degrees). This pre-existing crack is purposely put inside the gain such that the intragrain crack may propagate toward the grain boundary.

We adopt the fracture energies reported by Tromans and Meech [199], which estimates ideal fracture energies of both grain and grain boundary of a variety of minerals including halite. In this chapter, the grain boundary fracture energy was estimated to 86% of the grain fracture energy: 1.155 J/m^2 for the grain, and 0.993 J/m^2 for the grain boundary, respectively. We further assume the critical resolved stress $\tau_Y = 7.5$ MPa, hardening parameter ($h = 5$ GPa), and activation energy $Q = 10.0$ kcal/mol/K). To analyze the relationship between the crack patterns and the grain boundary fracture energy, we conduct multiple simulations where the fracture energy of the grain boundary is assumed to be 86%, 75%, and 50% of the intra-grain counterpart. Other material properties of the grain boundary, that may differ from the grain due to diverse reasons, such as impurity, solid mass exchange, precipitation creep, etc., are out of the scope in this study but will be considered in the future. The material parameters used in the simulations can be found in Table 3.1. We note that the material parameters of halite are highly sensitive to thermal and mechanical conditions. The well-designed experiments, therefore, need to be conducted to calibrate the numerical models for particular engineering application purposes.

The simulated crack patterns of a bicrystal with three different grain-boundary fracture energies (86%, 75%, and 50% of intragrain fracture energy), are shown in Figure 3.11.
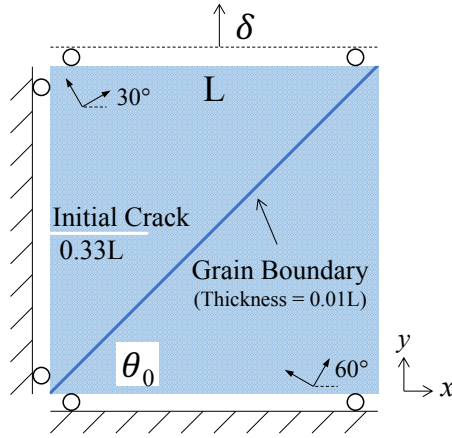
Figure 3.10: The numerical set-up for a bicrystal is depicted to analyze the impact of the grain boundary fracture energy on crack propagations (reproduced from Oshima, Takaki, and Muramatsu [133]). The Euler angles ϕ are set to 30° and 60°, respectively to left and right side grains. The single cleavage plane is assumed to the grain boundary with the direction of 45° along the diagonal. The initial temperature is set to 25 °C, and the fracture energies of the grain boundary are adopted 86%, 75%, and 50% of the grain fracture energy, respectively

In particular, The damage represented by the combined phase field (the left figures) and the magnitude of the plastic slip (the right figures) for the cases where the grain-boundary fracture energy is 86%, 75% and 50% are (a) and (b), (c) and (d), and (e) and (f) accordingly. In the 86% case, the crack initiates from the pre-existing crack tip and propagates through the grain boundary until reaching the right end of the domain. In other words, the grain boundary causes the refraction of the crack, a phenomenon commonly observed in materials with inter-layer(s) [214].

When the grain-boundary fracture energy is reduced to 70% of the grain fracture energy, as shown in Figure 3.11(c) and (d), the main fracture behavior is similar to the previous case before reaching the grain boundary. However, when the crack reaches the grain boundary, it grows along the grain boundary before the crack refraction occurs. In the last case where the grain-boundary fracture energy is further reduced to 50% of the grain fracture energy, the crack simply propagates along the grain boundary once reaching it.

One interesting implication of this result is that the assumption that cracks only occur along the grain boundary may only be valid when the interface is sufficiently weak. Otherwise, it is possible that the grain boundary may lead to crack refraction, which may in return leads to damage and even fragmentation of crystal grains. Although this example is significantly simplified set-up, this result is an indicator that the intragrain fractures could be significant in polycrystalline materials in certain circumstance. In those cases, the phase field approach may provide a convenient mean to capture the interactions of intragrain and grain-boundary fractures.
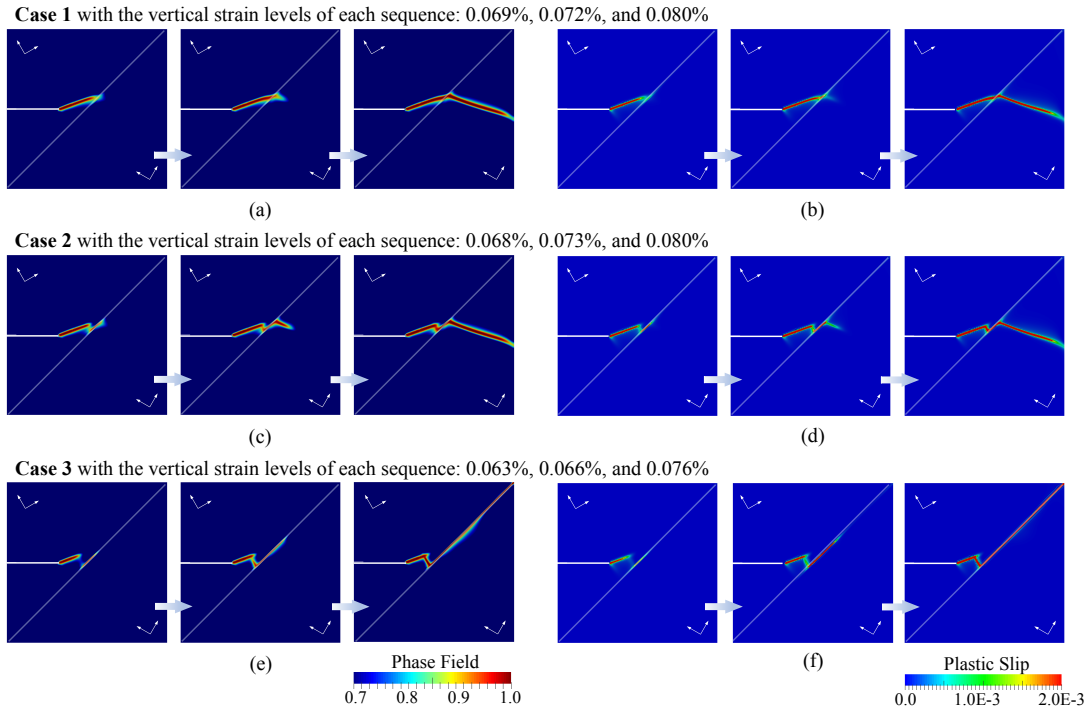
Figure 3.11: Phase-field values (left) and plastic slip results (right) patterns with different fracture energies of the grain boundary are illustrated. Case 1 (a) and (b) assumes the fracture energy of the grain boundary with 86% of grain fracture energy; Case 2 (c) and (d) with 75%; Case 3 (e) and (f) with 50% of the grain fracture energy, respectively

3.6   Conclusions

In this work, we developed a framework that combines the multi-phase-field method and the crystal plasticity theory under non-isothermal conditions for modeling single-crystal halite. This work is a starting point for modeling coupled thermo-hydro-mechanical behavior of polycrystalline rock salt. Under the postulation of microforces associated with plastic and fracture behaviors, the microstructure information coming from its slip system is incorporated into the governing equations. Both rate-dependent and rate-independent features are captured via the crystal plasticity stress update algorithm. Besides, the multi-phase-field method presents anisotropic damage of which each directional crack phase-field is associated with the slip planes. The energy balance equation is further encapsulated into the numerical framework to address the heat conduction, plastic dissipation, and thermoelastic structural heating. The numerical examples for single crystals demonstrate that, under the mechanical loading, the proposed numerical framework well captures the material anisotropy by rotating the slip-system orientations and the variation of inelastic to fracture behavior under different temperature conditions. Furthermore, the thermal loading by heat flux in a single crystal exhibits the anisotropic deformation, or distortion due to temperature increase. The tension test by changing the loading rate indicates the brittle-to-ductile transition along with the change of fracture patterns. Finally, the numerical example using a bicrystal presents the impact of fracture energy of the grain boundary on the inter- and intra-granular fracture, in which the grain boundary is simplified using a single cleavage crystal material. Although this framework for single-crystal halite is a starting point to be utilized as field scale simulations for polycrystalline rock salt, the results suggested here clearly indicate that this contribution provides quantitatively compatible physical behaviors of halite and potential applicability for practical engineering applications, e.g., a geologic repository for heating generating nuclear waste.

Chapter 4

Thermo-hydro-mechanical (THM) coupling effects on the dynamic wave propagation and strain localization in a softening porous media

4.1 Introduction

Localization of deformation in solids occurs in many natural processes and engineering applications. Examples of localization of deformation include the formation of Lüder and Portevin-Le Chatelier (PLC) bands [215, 216] in metals and alloys, crack bands in concrete [217], and shear, compaction and dilation bands in sand, clay, ice and rocks [43, 218–222]. For single-phase porous media under the static condition, the onset of strain localization is related to the loss of ellipticity, while the dynamics counterpart is due to the wave speed becoming imaginary [223–226]. These cases have been studied via stability and perturbation analyses in Hill [224] and Hill [227], which prove that perturbation grows instead of

decays in unstable materials due to the ill-posedness of the governing equation. This ill-posedness of the governing equation, which can be triggered by strain softening and/or lack of normality [218], can lead to tremendous difficulty to replicate strain localization in computer simulations. One undesirable consequence is that the numerically simulated localization zones exhibit pathological dependence on the mesh size [226, 228–233]. As a result of this inherent mesh dependency, the size of mesh may affect the simulated post-bifurcation local and global responses, which do not converge upon mesh refinement [19, 234].

To circumvent this mesh dependency, a material length scale must be introduced in the governing equation. Belytschko et al. [235] summarized a number of ways to introduce length scale and coined them localization limiters. These methods include introducing nonlocal or gradient based internal variables [216, 236], or higher-order continuum [237–239], and incorporating rate dependence in constitutive model [226, 240] to regularize the simulated responses after the onset of strain localization. This rate-dependent localization limiter is relevant to many deformation-diffusion coupling processes in multiphase materials, as the transient diffusion process is likely to introduce rate dependence to the mechanical responses due to the coupling effect. The previous works [81, 239, 241, 242] analyze the rate-dependent effect in fluid-infiltrating porous solid via stability and dispersion analyses, and derive the inherent length scale as a function of permeability and viscosity of the fluid among other material parameters. Zhang and Schrefler [239], Benallal and Comi [243], and Abellan and Borst [244] argue that while disperse effects are indeed observed in two-phase porous media, the physical length scale introduced via hydro-mechanical coupling effect vanishes at short wavelength limit.

Nevertheless, the aforementioned stability and dispersion analyses are based on the assumptions that the porous media is under the isothermal condition, and the thermal effect is negligible and decoupled from the hydro-mechanical processes. These assumptions are reasonable for numerous engineering applications in which thermal effect plays little

role on the safety or efficiency of the operations. However, thermo-hydro-mechanical coupling effect is critical for various applications, such as geothermal energy piles [245], geological disposal of carbon dioxide and nuclear wastes [246], freezing-thawing of pavement systems [6], and landslide triggered by thermal induced creeping [247].

To the best knowledge of the authors, there is no study concerning the thermo-hydro-mechanical coupling effect on the inherent length scale of porous media under non-isothermal condition. The purpose of this article is to fill this important knowledge gap. In particular, we apply the Routh-Hurwitz stability theorem to the THM governing equations and determine whether small perturbation can grow into localized instability and whether dispersive wave can propagate at finite wave speed in a thermal-sensitive softening porous media under the general non-isothermal condition and at the adiabatic limit. Our analysis indicates that the characteristic polynomial for the porous media under the general non-isothermal condition is of the fourth-order in the stability analysis, and of the sixth-order in the dispersion analysis. According to the Abel-Ruffini theorem (Abel's impossibility theorem), a polynomial higher than the fifth-order has no general algebraic solution. As a result, we prove that it is impossible to express the internal length scale algebraically for the general non-isothermal case. On the other hand, under the adiabatic condition, we prove that the characteristic polynomial is reduced to the third-order for the dispersion analysis. Therefore, we derive the algebraic expression of length scale for this limit case and compare both new results with the previous works on isothermal porous media [81, 244, 248].

The rest of this chapter is organized as follows. We first perform the stability analysis for both general non-isothermal and adiabatic cases, and determine the onset of instability in Section 4.2.2. We then investigate the dispersive wave propagation in Section 4.2.3. In particular, we derive the phase velocity for the non-isothermal case at the long wavelength limit, and the vanishing of the physical internal length scale is observed at the short wavelength limit. For many thermo-hydro-mechanical coupling processes at very

small time scale, the thermal conductivity of the porous media is negligible. For those adiabatic cases, we derive the simplified expression of the internal length scales and analyze the wave propagation speed during strain softening. In section 4.3, we conduct numerical experiments using an 1D dynamic THM finite element code to compare and validate the analytical derivation in Sections 4.2.2 and 4.2.3. Furthermore, the influences of hydraulic properties (permeability) and thermal parameters (thermal conductivity and specific heat) on internal length scale and wave propagation behavior are evaluated for both non-isothermal and adiabatic cases, respectively. Finally, concluding remarks are given in Section 4.4.

4.2 Stability and dispersion analyses

In this section, the governing equations for the wave propagation of a one-dimensional softening bar composed of fully saturated porous media under the general non-isothermal and adiabatic conditions are introduced. We perform stability and dispersion analyses on both cases and obtain the corresponding characteristic polynomials. Then, we derive the explicit expression of phase velocity and determine the vanishing length scale under long and short wavelength limits for the non-isothermal condition. In the adiabatic condition, analytical derivations of the cutoff wavenumber and internal length scale are investigated for dynamic wave propagation in a two-phase porous medium. These new results are compared with the stability and dispersion analyses for isothermal porous media.

4.2.1 Model assumptions and governing equations

The thermo-hydro-mechanical response of fluid infiltrating porous solids is governed by the balance principles, i.e., the balance of linear momentum, mass and energy. Biot [249] formulated a general thermodynamics theory for non-isothermal porous media. McTigue [250] derived a field theory for the linear thermo-elastic response of fully saturated porous

media. This model is extended in Coussy [175] to incorporate the structural heating effect. Belotserkovets and Prévost [16] derived analytical solutions of an elastic fluid-saturated porous sphere subjected to boundary heating, prescribed pore pressure and flux. Selvadurai and Suvorov [251] analyzed the same thermo-hydro-mechanical problem of a spherical domain. By neglecting the heat generated and dissipated due to deformation of the solid skeleton and the flow convection of the porous spheres, the analytical solution of THM responses of the sphere composed of a fluid-saturated elasto-plastic material was derived and compared with finite element solution.

In this study, we adopt the governing equations of Coussy [175] and Belotserkovets and Prévost [16]. We assume that the strain is infinitesimal and that there is no mass exchange between the solid and fluid constituents. The gravitational body force and heat convection of among the constituents are neglected. Furthermore, we ignored the difference between the acceleration of the fluid and solid skeleton in (4.1) and (4.2) to simplify the analysis as previously done in Zienkiewicz et al. [24] and Zhang, Sanavia, and Schrefler [81]. As a result, the governing equations of the linear momentum, the fluid mass balance and the energy balance read,

$$\nabla \cdot (\sigma' - bp - \beta T) - \rho \ddot{u} = 0, \tag{4.1}$$

$$b\nabla \cdot \dot{u} - k\nabla^2 p + \frac{1}{M}\dot{p} - 3\alpha_m \dot{T} = 0, \tag{4.2}$$

$$\rho c \dot{T} - \kappa \nabla^2 T + T_0 \beta \nabla \cdot \dot{u} - 3\alpha_m T_0 \dot{p} = 0, \tag{4.3}$$

where σ' is effective stress (nominal effective stress in Liu et al. [252]), p is pore pressure, T is temperature, u is displacement of solid skeleton, and b is the Biot's coefficient. The mobility, k, is defined as $k = k_s/\mu_f = k_{perm}/\rho_f g$, in which k_s is the intrinsic permeability, μ_f is the fluid viscosity, k_{perm} is the permeability or hydraulic conductivity and g is the gravity acceleration. Furthermore, T_0 is the reference temperature as defined in [16]. β is calculated as $\beta = 3\alpha_s K$, in which α_s is the linear thermal expansion coefficient of

solid, and K is the bulk modulus. Also, α_m is described as, $\alpha_m = (b-n)\alpha_s + b\alpha_f$, including porosity n and the linear thermal expansion coefficient of fluid α_f. Here, $\rho = (1-n)\rho_s + n\rho_f$, in which ρ_s and ρ_f are solid and fluid mass densities, κ is the thermal conductivity, and c_s, c_f are the specific heats of solid and fluid. The Biot's modulus is denoted as M, which is a function of the Biot's coefficient b, porosity n, the bulk modulus of the solid grain K_s and that of the fluid constituent K_f, i.e.,

$$\frac{1}{M} = \frac{b-n}{K_s} + \frac{n}{K_f}. \tag{4.4}$$

In this study, the volume-averaged specific heat of the constituents, $\rho c = (1-n)\rho_s c_s + n\rho_f c_f$, is considered to be specific heat of two-phase fluid-solid mixture. In addition, we assume that the temperature is at equilibrium locally and hence there is no temperature difference between the two constituents at the same material point. To simplify the stability and dispersion analyses, we limit our attention to a one-dimensional dynamic thermo-hydro-mechanics boundary value problem.

4.2.2 Stability analysis

In this section, we analyze stability of a one-dimensional wave propagation in a thermal-sensitive fluid-saturated porous media. Our goal here is to determine the necessary and sufficient conditions to maintain stability of the thermo-hydro-mechanical system in the generalized non-isothermal case and at the adiabatic limit. Our results are compared with the previous analyses on isothermal porous media. In particular, we apply the Routh-Hurwitz stability theorem to the characteristic equations of the general non-isothermal and adiabatic THM systems. The Routh-Hurwitz criterion enables us to determine whether it is possible that the solution of characteristic equation can have a real and positive part, which in return implies that homogeneous state is unstable and a small perturbation may grow [216].

Non-isothermal case

To investigate the stability of an equilibrium state, we apply a harmonic perturbation with respect to an incremental axial displacement, pore pressure and temperature. For an infinite one-dimensional thermo-sensitive porous medium initially in a homogeneous state, the solution of displacement, pore pressure and temperature in space-time (x, t) may take the following form,

$$
\begin{bmatrix} du \\ dp \\ dT \end{bmatrix} = \begin{bmatrix} A_u \\ A_p \\ A_T \end{bmatrix} e^{i(k_w x - \omega t)} = A e^{ik_w x + \lambda t}, \ \lambda = -i\omega,
\tag{4.5}
$$

where k_w is the wavenumber, ω the angular frequency, and λ eigenvalue. A_u, A_p and A_T are the amplitudes of the displacement, pore pressure and temperature perturbations, respectively. Following the approach in Zhang, Sanavia, and Schrefler [81] and Abellan and Borst [244], we use an incremental linear constitutive model to relate the infinitesimal change of the nominal effective stress and that of the total strain for the one-dimensional THM problem, i.e.,

$$
\dot{\sigma}' = E_t \frac{\partial \dot{u}}{\partial x} = E_t \dot{\epsilon},
\tag{4.6}
$$

where E_t is the tangential stiffness modulus of the solid (cf. Abellan and Borst [244]). The relations among the one-dimensional total stress σ, Biot's effective stress σ'' and the nominal effective stress σ' are [252],

$$
\dot{\sigma} = \dot{\sigma}'' - b\dot{p} = \dot{\sigma}' - \beta\dot{T} - b\dot{p}.
\tag{4.7}
$$

The spatial derivative of the incremental nominal effective stress equation (4.6) gives,

$$
\frac{\partial \dot{\sigma}'}{\partial x} = -E_t A_u k_w^2 \exp(ik_w x + \lambda t).
\tag{4.8}
$$

The substitution of (4.5) into (4.1) to (4.3) therefore gives,

$$-E_t k_w^2 A_u - i(bk_w)A_p - i(\beta k_w)A_T - \rho\lambda^2 A_u = 0, \tag{4.9}$$

$$i(bk_w\lambda)A_u + kk_w^2 A_p + M^{-1}\lambda A_p - 3\alpha_m \lambda A_T = 0, \tag{4.10}$$

$$\rho c\lambda A_T + \kappa k_w^2 A_T + i(T_0\beta k_w\lambda)A_u - 3\alpha_m T_0 \lambda A_p = 0. \tag{4.11}$$

A non-trivial solution to this set of homogeneous equations exists if and only if the following relation holds,

$$\begin{vmatrix} -E_t k_w^2 - \rho\lambda^2 & -i(bk_w) & -i(\beta k_w) \\ i(bk_w\lambda) & kk_w^2 + M^{-1}\lambda & -3\alpha_m\lambda \\ i(T_0\beta k_w\lambda) & -3\alpha_m T_0\lambda & \rho c\lambda + \kappa k_w^2 \end{vmatrix} = 0, \tag{4.12}$$

which can be rewritten as shown below,

$$(-E_t k_w^2 - \rho\lambda^2)\left[(kk_w^2 + M^{-1}\lambda)(\rho c\lambda + \kappa k_w^2) - (-3\alpha_m\lambda)(-3\alpha_m T_0\lambda)\right]$$

$$+i(bk_w)\left[i(bk_w\lambda)(\rho c\lambda + \kappa k_w^2) - (-3\alpha_m\lambda)(i(T_0\beta k_w\lambda))\right]$$

$$-i(\beta k_w)\left[i(bk_w\lambda)(-3\alpha_m T_0\lambda) - (kk_w^2 + M^{-1}\lambda)(i(T_0\beta k_w\lambda))\right] = 0. \tag{4.13}$$

Expanding (4.13) yields,

$$-\frac{1}{M}\rho^2 c\lambda^4 + 9\alpha_m^2 \rho T_0\lambda^4 - \frac{1}{M}\rho\kappa k_w^2\lambda^3 - \rho^2 ckk_w^2\lambda^3$$

$$-\frac{1}{M}\rho c E_t k_w^2\lambda^2 - \rho cb^2 k_w^2\lambda^2 - \rho\kappa kk_w^4\lambda^2$$

$$-\frac{1}{M}\beta^2 T_0 k_w^2\lambda^2 - 6\alpha_m\beta bT_0 k_w^2\lambda^2 + 9E_t\alpha_m^2 T_0 k_w^2\lambda^2$$

$$-\frac{1}{M}E_t\kappa k_w^4\lambda - b^2\kappa k_w^4\lambda - \rho c E_t kk_w^4\lambda - \beta^2 kT_0 k_w^4\lambda - E_t k\kappa k_w^6 = 0, \tag{4.14}$$

After rearranging (4.14), the characteristic equation is a forth-order polynomial that reads,

$$a_4\lambda^4 + a_3\lambda^3 + a_2\lambda^2 + a_1\lambda + a_0 = 0, \tag{4.15}$$

with the following real coefficients,

$$a_4 = \rho(\rho c - 9\alpha_m^2 T_0 M), \tag{4.16}$$

$$a_3 = \rho(\kappa + \rho ckM)k_w^2, \tag{4.17}$$

$$a_2 = (\rho cE_t + \rho cb^2 M + \rho\kappa kMk_w^2 + \beta^2 T_0 + 6\alpha_m\beta bT_0 M - 9E_t\alpha_m^2 T_0 M)k_w^2, \tag{4.18}$$

$$a_1 = (E_t\kappa + b^2\kappa M + \rho cE_t kM + \beta^2 kT_0 M)k_w^4, \tag{4.19}$$

$$a_0 = E_t k\kappa Mk_w^6. \tag{4.20}$$

According to the Routh-Hurwitz stability criterion, the stability of the governing equations is maintained if and only if all the solutions of characteristic polynomial have negative real part [253, 254]. For the fourth-order polynomial shown in (4.15), the necessary condition to satisfy the Routh-Hurwitz stability criterion is to have the coefficients listed in (4.16) to (4.20) hold the following properties,

$$a_n > 0, \; a_3a_2 > a_4a_1, \text{ and } a_3a_2a_1 > a_4a_1^2 + a_3^2a_0 \text{ , where } n = 0, 1, 2, 3, 4. \tag{4.21}$$

We first examine $(4.21)_1$, which requires all coefficients $a_i, i = 0, 1, 2, 3, 4$, to be strictly positive. Notice that these coefficients are all the functions of the material parameters that characterize the mechanical, hydraulic and thermal responses of porous media. As a result, one may deduce the necessary condition to satisfy $(4.21)_1$ by examining the physical meaning and the possible ranges of the material parameters. Here we categorize the material parameters into three groups – strictly positive, non-negative, and real number (which can be negative, zero or positive). Among these three groups, we first assume that the total density ρ, specific heat c, Biot's modulus M and Biot's coefficient b are all strictly

Table 4.1: Assumptions on range of the material properties of thermo-sensitive porous media

Parameter	Description	Range
ρ	Total Density	$\mathbb{R}^+$
c	Specific Heat	$\mathbb{R}^+$
M	Biot's Modulus	$\mathbb{R}^+$
b	Biot's Coefficient	$(0,1]$
k	Mobility	$[0,\infty)$
κ	Thermal Conductivity	$[0,\infty)$
α	Thermal Expansion Coefficient	$[0,\infty)$
T_0	Reference Temperature	$[0,\infty)$
E_t	Tangential Modulus	$\mathbb{R}$

positive and hence greater than zero. Meanwhile, the mobility k, thermal conductivity κ, thermal expansion coefficient α_m and the reference temperature T_0 are assumed to be non-negative (if the temperature unit is Kelvin). Finally, the tangential stiffness E_t can be both positive, negative or zero, as summarized in Table 4.1.

With the aforementioned assumptions in mind, we notice that a_0, a_1 and a_3 may all become non-positive when both thermal conductivity and permeability of the material become zero. This result indicates that the wave propagating in non-isothermal porous medium may lose stability at the undrained limit even though there is no softening. At the adiabatic limit, we found that one of the roots of the characteristic polynomial is zero and at least one of the root may have a positive real part if at least one of the four conditions listed at the end of section 4.2.2 is met. On the other hand, a_4 is greater than zero if both solid and fluid constituents do not exhibit thermal expansion such that $\alpha_m = 0$. However, to maintain stability, the specific heat must be large enough such that $c > 9\alpha_m^2 T_0 M/\rho$. In other words, from a theoretical standpoint, it is possible for the THM governing equations to lose stability if the fluid and solid constituents are both nearly incompressible but the porous medium is vulnerable to significant thermal expansion (e.g. marine clay). This indicates that material softening is not the only indicator that detects the loss of stability in the THM problem. Furthermore, a necessary and sufficient condition for $a_0 > 0, a_1 > 0$

and $a_2 > 0$ is to have $E_t > 0$, i.e., no softening occurring. A few algebraic operations reveal that,

$$a_2 > 0 \text{ implies that } E_t > \frac{-\rho c b^2 M - \rho \kappa k M k_w^2 - \beta^2 T_0 - 6\alpha_m \beta b T_0 M}{\rho c - 9\alpha_m^2 T_0 M}, \tag{4.22}$$

$$a_1 > 0 \text{ implies that } E_t > \frac{-b^2 \kappa M - \beta^2 k T_0 M}{\kappa + \rho c k M}. \tag{4.23}$$

Since the stability condition also requires $a_4 > 0$ and hence $\rho c - 9\alpha_m^2 T_0 M > 0$, both (4.22) and (4.23) would not be violated unless softening occurs (i.e. $E_t < 0$). Meanwhile, the explicit expression of $a_3 a_2 > a_4 a_1$ reads,

$$k\kappa^2 M \rho^2 k_w^6 + b^2 c^2 k M^2 \rho^3 k_w^4 + ck^2 \kappa M^2 \rho^3 k_w^6 + \beta^2 \kappa \rho T_0 k_w^4 + 6\alpha_m b \beta \kappa M \rho T_0 k_w^4$$

$$+ 9\alpha_m^2 b^2 \kappa M^2 \rho T_0 k_w^4 + 6\alpha_m b \beta ck M^2 \rho^2 T_0 k_w^4 + 9\alpha_m^2 \beta^2 k M^2 \rho T_0^2 k_w^4 > 0,$$

$$\tag{4.24}$$

which can be expressed as below,

$$\rho k_w^4 \left[\rho^2 ck^2 \kappa M^2 k_w^2 + \kappa T_0 (\beta + 3b\alpha_m M)^2 + kM(\rho \kappa^2 k_w^2 + M(b\rho c + 3\beta \alpha_m T_0)^2) \right] > 0. \tag{4.25}$$

Condition (4.25) always holds if the wavenumber is real, either the permeability or the thermal conductivity is non-zero and the rest of the material parameters are strictly positive. Finally, $a_3 a_2 a_1 > a_4 a_1^2 + a_3^2 a_0$ can be expanded as,

$$b^2 k\kappa^3 M^2 \rho^2 k_w^{10} + b^2 c^2 E_t k\kappa M^2 \rho^3 k_w^8 + b^4 c^2 k\kappa M^3 \rho^3 k_w^8 + b^2 ck^2 \kappa^2 M^3 \rho^3 k_w^{10}$$

$$+ b^2 c^3 E_t k^2 M^3 \rho^4 k_w^8 + \beta^2 E_t \kappa^2 T_0 \rho k_w^8 + b^2 \beta^2 \kappa^2 M T_0 \rho k_w^8 + 6\alpha_m b \beta E_t \kappa^2 M T_0 \rho k_w^8$$

$$+ 6\alpha_m b^3 \beta \kappa^2 M^2 T_0 \rho k_w^8 + 9\alpha_m^2 b^2 E_t \kappa^2 M^2 T_0 \rho k_w^8 + 9\alpha_m^2 b^4 \kappa^2 M^3 T_0 \rho k_w^8 + \beta^2 c E_t k\kappa M T_0 \rho^2 k_w^8$$

$$+ 12\alpha_m b \beta c E_t k M^2 T_0 \kappa \rho^2 k_w^8 + \beta^2 k^2 \kappa^2 M^2 T_0 \rho^2 k_w^{10} + 6\alpha_m b^3 \beta ck\kappa M^3 T_0 \rho^2 k_w^8$$

$$+ 9\alpha_m^2 b^2 c E_t k\kappa M^3 T_0 \rho^2 k_w^8 + b^2 \beta^2 c^2 k^2 M^3 T_0 \rho^3 k_w^8 + 6\alpha_m b \beta c^2 E_t k^2 M^3 T_0 \rho^3 k_w^8$$

$$+ \beta^2 c k^3 \kappa M^3 T_0 \rho^3 k_w^{10} + \beta^4 k \kappa M T_0^2 \rho k_w^8 + 6 \alpha_m b \beta^3 k \kappa M^2 T_0^2 \rho k_w^8$$

$$+ 9 \alpha_m^2 \beta^2 E_t k \kappa M^2 T_0^2 \rho k_w^8 + 18 \alpha_m^2 b^2 \beta^2 k \kappa M^3 T_0^2 \rho k_w^8 + 6 \alpha_m b \beta^3 c k^2 M^3 T_0^2 \rho^2 k_w^8$$

$$+ 9 \alpha_m^2 \beta^2 c E_t k^2 M^3 T_0^2 \rho^2 k_w^8 + 9 \alpha_m^2 \beta^4 k^2 M^3 T_0^3 \rho k_w^8 > 0, \tag{4.26}$$

which can be further simplified as,

$$E_t \rho k_w^8 (\kappa + \rho c k M) \left[6 \alpha_m b \beta M T_0 (\kappa + \rho c k M) + b^2 M^2 (\rho^2 c^2 k + 9 \alpha_m^2 \kappa T_0) \right.$$

$$\left. + \beta^2 T_0 (\kappa + 9 \alpha_m^2 k M^2 T_0) \right] + \rho k_w^8 M (b^2 \kappa + \beta^2 k T_0) \left[\rho^2 c k^2 \kappa M^2 k_w^2 + \kappa T_0 (\beta + 3 \alpha_m b M)^2 \right.$$

$$\left. + k M (\kappa^2 \rho k_w^2 + M (\rho c b + 3 \alpha_m \beta T_0)^2) \right] > 0. \tag{4.27}$$

In other words, $a_3 a_2 a_1 > a_4 a_1^2 + a_3^2 a_0$ implies that,

$$E_t > \frac{-M (b^2 \kappa + \beta^2 k T_0) \left[\rho^2 c k^2 \kappa M^2 k_w^2 + \kappa T_0 (\beta + 3 \alpha_m b M)^2 + k M (\kappa^2 \rho k_w^2 + M (\rho c b + 3 \alpha_m \beta T_0)^2) \right]}{(\kappa + \rho c k M) \left[6 \alpha_m b \beta M T_0 (\kappa + \rho c k M) + b^2 M^2 (\rho^2 c^2 k + 9 \alpha_m^2 \kappa T_0) + \beta^2 T_0 (\kappa + 9 \alpha_m^2 k M^2 T_0) \right]}, \tag{4.28}$$

which would not be violated unless softening occurs (i.e. $E_t < 0$) as the above (4.22) and (4.23).

As a result, the THM governing equations may fail the Routh-Hurwitz criterion if at least one of the following situations happens:

1. Softening occurs such that $E_t < 0$.

2. Both permeability and thermal conductivity of the porous media become zero.

3. Specific heat $c \leq 9 \alpha_m^2 T_0 M / \rho$.

Adiabatic case

The stability analysis conducted in the previous section can be significantly simplified by assuming that the entire one-dimensional bar is in the adiabatic or isothermal condi-

tion. While the latter case has been extensively studied in the past [81, 239, 244, 248], the stability analysis of adiabatic porous media has not yet been established. For many engineering applications in which high-rate and shock responses are of interest, it is reasonable to assume that the thermal conductivity is negligible. In those cases, we may derive the characteristic equation for the adiabatic condition by assuming the thermal conductivity to be zero, $\kappa \approx 0$. As a result, the characteristic equation of the adiabatic THM system reads,

$$\begin{vmatrix} -E_t k_w^2 - \rho\lambda^2 & -i(bk_w) & -i(\beta k_w) \\ i(bk_w\lambda) & kk_w^2 + M^{-1}\lambda & -3\alpha_m\lambda \\ i(T_0\beta k_w\lambda) & -3\alpha_m T_0\lambda & \rho c\lambda \end{vmatrix} = 0, \tag{4.29}$$

which can be rewritten as shown below,

$$(-E_t k_w^2 - \rho\lambda^2)\left[(kk_w^2 + M^{-1}\lambda)\rho c\lambda - (-3\alpha_m\lambda)(-3\alpha_m T_0\lambda)\right]$$

$$+i(bk_w)\left[i(bk_w\lambda)\rho c\lambda - (-3\alpha_m\lambda)(i(T_0\beta k_w\lambda))\right]$$

$$-i(\beta k_w)\left[i(bk_w\lambda)(-3\alpha_m T_0\lambda) - (kk_w^2 + M^{-1}\lambda)(i(T_0\beta k_w\lambda))\right] = 0. \tag{4.30}$$

Expanding (4.30) yields,

$$-\frac{1}{M}\rho^2 c\lambda^4 + 9\rho\alpha_m^2 T_0\lambda^4 - \rho^2 ck k_w^2\lambda^3$$

$$-\frac{1}{M}\rho c E_t k_w^2\lambda^2 - \rho cb^2 k_w^2\lambda^2 - \frac{1}{M}\beta^2 T_0 k_w^2\lambda^2 - 6\alpha_m\beta bT_0 k_w^2\lambda^2 + 9E_t\alpha_m^2 T_0 k_w^2\lambda^2$$

$$-\rho c E_t kk_w^4\lambda - \beta^2 kT_0 k_w^4\lambda = 0, \tag{4.31}$$

which can be rewritten as,

$$-\frac{1}{M}\lambda\left[\rho(\rho c - 9\alpha_m^2 T_0 M)\lambda^3 + \rho^2 ckM k_w^2\lambda^2\right.$$

115

$$+(\rho c E_t + \rho c b^2 M + \beta^2 T_0 + 6\alpha_m \beta b T_0 M - 9 E_t \alpha_m^2 T_0 M)k_w^2\lambda$$

$$+(\rho c E_t + \beta^2 T_0)k M k_w^4 \big] = 0. \qquad (4.32)$$

This equation can be expressed into a more compacted form that reads ($M \neq 0$),

$$b_3\lambda^4 + b_2\lambda^3 + b_1\lambda^2 + b_0\lambda = 0 \ \text{ or } \ (b_3\lambda^3 + b_2\lambda^2 + b_1\lambda + b_0)\lambda = 0, \qquad (4.33)$$

where the expressions of the coefficients are,

$$b_3 = \rho(\rho c - 9\alpha_m^2 T_0 M), \qquad (4.34)$$

$$b_2 = \rho^2 c k M k_w^2, \qquad (4.35)$$

$$b_1 = (\rho c E_t + \rho c b^2 M + \beta^2 T_0 + 6\alpha_m \beta b T_0 M - 9\alpha_m^2 E_t T_0 M)k_w^2, \qquad (4.36)$$

$$b_0 = (\rho c E_t + \beta^2 T_0)k M k_w^4. \qquad (4.37)$$

At the adiabatic limit, the vanishing of the Laplacian term in the balance of energy equation leads to a fourth-order characteristic polynomial (4.33) of which one of the roots is obviously zero ($\lambda = 0$). This root represents a neutrally stable condition in which perturbation neither grows (which requires a positive real part) or decay (which requires a negative real part) [216]. To determine whether perturbation may grow, we examine the rest of the roots corresponding to (4.33) and analyze the ranges of material parameters that lead to at least one root having a positive real part (and hence causes a perturbation to grow). Note that the coefficients $b_i, i = 0, 1, 2, 3$ in (4.33) are either functions of an exponentiation of the wavenumber of a particular order, i.e., k_w^2, k_w^4, or independent of k_w. Furthermore, each coefficient does not depend on the exponentiation of the wavenumber with multiple orders as a_2 in (4.18). This feature allows one to derive the cutoff wavenumber, which provides the range of wavenumbers where wave propagation is possible in the adiabatic porous media.

Now apply the Routh-Hurwitz stability criterion to the polynomial corresponding to the non-zero roots, i.e., $b_3\lambda^3 + b_2\lambda^2 + b_1\lambda + b_0 = 0$. The necessary condition to satisfy the Routh-Hurwitz stability criterion reads,

$$b_n > 0 \text{ and } b_2 b_1 > b_3 b_0 \text{ , where } n = 0, 1, 2, 3, \tag{4.38}$$

where $b_2 b_1 - b_3 b_0 > 0$ can be written as,

$$\rho k M^2 \left(\rho c b + 3\alpha_m \beta T_0\right)^2 k_w^4 > 0. \tag{4.39}$$

This condition holds when the mobility k is positive. In analogy to the general non-isothermal case, we can identify the necessary condition that leads to instability. The loss of stability may appear if one of the following criteria is met:

1. Mobility $k = 0$, in which case b_0 and b_2 are both equal to 0.

2. Tangential modulus $E_t \leq -(\beta^2 T_0/\rho c)$ leads to $b_0 \leq 0$.

3. Tangential modulus $E_t \leq -(\rho c b^2 M + \beta^2 T_0 + 6\alpha_m \beta b T_0 M)/(\rho c - 9\alpha_m^2 T_0 M)$ leads to $b_1 \leq 0$.

4. Specific heat $c \leq 9\alpha_m^2 T_0 M/\rho$ so that $b_3 \leq 0$.

Remark 1

Notice that in many THM formulations, such as Selvadurai and Suvorov [251] and Selvadurai and Suvorov [255], the work done or energy dissipation of the fluid and solid constituents are assumed to be negligible in the balance of energy equation. In this case, the energy balance equation (4.3) may be simplified as,

$$\dot{T} - \frac{\kappa}{\rho c}\frac{\partial^2 T}{\partial x^2} = 0. \tag{4.40}$$

Hence, the mechanical and hydraulic responses are only one-way coupled with the heat transfer process. While the temperature changes may still cause deformation and/or flow, (4.40) indicates that neither deformation of the solid skeleton or the pore-fluid flow may impose any influence on the temperature due to the simplified assumptions. In this special case, the characteristic equation reads,

$$
\begin{vmatrix}
-E_t k_w^2 - \rho\lambda^2 & -i(bk_w) & -i(\beta k_w) \\
i(bk_w\lambda) & kk_w^2 + M^{-1}\lambda & -3\alpha_m\lambda \\
0 & 0 & \rho c\lambda + \kappa k_w^2
\end{vmatrix} = 0. \tag{4.41}
$$

In the one-way coupling THM formulations, the characteristic equation will have two roots identical with those in the fully saturated isothermal condition [81, 244, 248], while the additional root is $\lambda = -\kappa k_w^2/(\rho c)$ which is either equal to zero (when $\kappa = 0$) or negative (when κ is positive). In other words, if the thermal conductivity is non-zero, then the governing equations of the one-way coupling THM system and the isothermal THM system share the same necessary and sufficient conditions for stability.

4.2.3 Dispersion analysis

Even if stability is lost, numerical simulations may still continue and give meaningful results as pointed out by Abellan and Borst [244]. However, when the THM problem becomes ill-posed, the physical length scale inferred from the physical properties vanishes and a numerical length scale, which is often the mesh size, may influence the numerical solutions and cause mesh dependency.

The dispersion analysis provides a tool to predict the vanishing of finite non-zero physical wavelength by checking whether the associated cutoff wavenumber or damping factor can be identified. Recall that a wave is considered dispersive if the phase velocity (or wave velocity, v_p) depends on the wavenumber [81, 239, 243, 244, 248, 256–259]. In this case, the waves of different wavelengths travel at different phase velocities and hence the

shape of a dispersive wave may change as it propagates [260]. To capture localization of deformation properly, governing equation must be able to change the shape of an arbitrary loading wave into a stationary wave in a localization zone [231, 244]. It is well known that wave propagation in the standard single-phase continuum upon the occurrence of strain softening is not dispersive, and hence the mesh dependency is observed [216, 244].

In this section, our objectives are to (1) investigate whether a dispersive wave can propagate at the long and short wavelength limits in the non-isothermal case, and (2) examine the cutoff wavenumber and internal length scale when strain softening at the adiabatic limit.

Non-isothermal case

We assume that the solution of the governing equations of a damped, harmonic wave propagating in a thermo-sensitive fully saturated two-phase porous media takes the following form:

$$
\begin{bmatrix} du \\ dp \\ dT \end{bmatrix} = \begin{bmatrix} A_u \\ A_p \\ A_T \end{bmatrix} e^{i(k_w x - \omega t)} = A e^{\lambda_r t + i(k_w x - \omega t)}, \tag{4.42}
$$

where A_u, A_p and A_T are the amplitudes of the displacement, pore pressure and temperature accordingly. In the dispersion analysis, we split the possible complex eigenvalue into real part (λ_r) and imaginary party (ω or λ_i) as $\lambda = \lambda_r - i\omega$. According to Zhang, Sanavia, and Schrefler [81] and the dispersion analysis of adiabatic case below, the cutoff wavenumber can be derived using the discriminant of cubic polynomial of eigenvalue when the same order of wavenumber term exists in each coefficient of the characteristic equation (e.g. (4.33)). However, in the characteristic equation of non-isothermal condition (4.15), the coefficient a_2 has two different orders of wavenumber (k_w^2 and k_w^4) and the derivation of discriminant of quartic polynomial cannot give the explicit expression of wavenumber having the complex conjugate roots. Nevertheless, we may still determine

119

the relation between the phase velocity and the real and imaginary parts of the eigenvalue by substituting $\lambda = \lambda_r - i\omega$ into (4.15). This process, based on Abellan and Borst [244], decomposes the characteristic equation into real and imaginary parts as follows,

$$a_4\lambda_r^4 + a_3\lambda_r^3 + a_2\lambda_r^2 + a_1\lambda_r + a_0 - a_2\omega^2 - 3a_3\lambda_r\omega^2 - 6a_4\lambda_r^2\omega^2 + a_4\omega^4$$

$$+i(-a_1\omega - 2a_2\lambda_r\omega - 3a_3\lambda_r^2\omega - 4a_4\lambda_r^3\omega + a_3\omega^3 + 4a_4\lambda_r\omega^3) = 0. \quad (4.43)$$

The imaginary part of (4.43) vanishes if the following condition holds,

$$\omega = 0 \ \text{ or } \ \omega^2 = \frac{4a_4\lambda_r^3 + 3a_3\lambda_r^2 + 2a_2\lambda_r + a_1}{4a_4\lambda_r + a_3}. \quad (4.44)$$

For the dispersion analysis of dynamic governing equations, we can assume $\omega \neq 0$ and take the condition of $(4.44)_2$. By considering the coefficients $a_i, i = 0, 1, 2, 3, 4$ of (4.16) to (4.20), we know that ω is expressed in terms of wavenumber (k_w), and the relation of phase velocity $(v_p = \omega/k_w)$ and wavenumber can be derived. Since the phase velocity is dependent on the wavenumber, we can find out that the wave propagation is dispersive. Furthermore, by substituting $(4.44)_2$ into (4.43), the equation of real part of eigenvalue λ_r can be expressed as shown below,

$$\big[64a_4^3\lambda_r^6 + 96a_3a_4^2\lambda_r^5 + (48a_3^2a_4 + 32a_2a_4^2)\lambda_r^4 + (8a_3^3 + 32a_2a_3a_4)\lambda_r^3$$

$$+(8a_2a_3^2 + 4a_2^2a_4 + 4a_1a_3a_4 - 16a_0a_4^2)\lambda_r^2 + (2a_2^2a_3 + 2a_1a_3^2 - 8a_0a_3a_4)\lambda_r$$

$$+a_1a_2a_3 - a_0a_3^2 - a_1^2a_4\big]/(16a_4^2\lambda_r^2 + 8a_4a_3\lambda_r + a_3^2) = 0. \quad (4.45)$$

Unfortunately, as proven by the Abel-Ruffini theorem (also referred as the Abel's impossibility theorem [261]), there exists no **general** algebraic solution in radicals to polynomials of degree five or higher with arbitrary coefficients. In other words, there is no general formula that allows the real part of eigenvalue λ_r to be expressed algebraically, even though it is still possible to solve (4.45) numerically. However, we can estimate λ_r

by taking long and short wavelength limits considering the coefficients $a_i, i = 0, 1, 2, 3, 4$ and (4.44) to (4.45).

Firstly, we found that taking the long wavelength limit, i.e. $k_w \to 0$, yields the eigenvalue $\lambda_r \to 0$ in (4.45). As demonstrated in Abellan and Borst [244], this result leads to the relation of phase velocity and wavenumber according to $(4.44)_2$. Therefore, we can explicitly derive the phase velocity for the long wavelength limit as shown below.

$$v_p = \sqrt{\frac{E_t\kappa + b^2\kappa M + \rho c E_t kM + \beta^2 kT_0 M}{\rho(\kappa + \rho ckM)}} = \sqrt{\frac{E_t}{\rho} + \frac{b^2\kappa M}{\rho(\kappa + \rho ckM)} + \frac{\beta^2 T_0 kM}{\rho(\kappa + \rho ckM)}}. \tag{4.46}$$

We can further observe that the phase velocity o f (4.46) is reduced to the classical bar velocity, $v_p = \sqrt{E_t/\rho}$, when thermal effects are ignored and the fluid is removed (or simply, when κ and k are ignored). Figure 4.1 shows how the phase velocity changes depending on the thermal conductivity and permeability (or mobility k), where the material properties are selected from the previous studies [19, 81]. When the thermal conductivity is given, for example $\kappa = 2.5 \times 10^{-3}$kW/m/°C, the phase velocity does not change until the permeability decreases below $k_{perm} \approx 1.0 \times 10^{-6}$ m/s. Besides, when the permeability is further decreased and beyond the range, $1.0 \times 10^{-8} < k_{perm} < 1.0 \times 10^{-6}$ (m/s), additional response from the phase velocity is not observed. In other words, the phase velocity of the THM system can be influenced by how the permeability and thermal conductivity are combined, but the effect is limited.

For the short wavelength limit, i.e. $k_w \to \infty$, we can estimate that $\lambda_r \sim k_w^{10}$ from (4.45) and the wave velocity becomes proportional to the wavenumber, $v_p \sim k_w$, from (4.44). By adopting the relation of the internal length scale and damping coefficient from a single-phase rate-dependent medium [260], the internal length scale (l) is defined as follows:

$$l = \lim_{k_w \to \infty} \left(-\frac{v_p}{\lambda_r} \right) \sim \lim_{k_w \to \infty} k_w^{-9} = 0. \tag{4.47}$$

This means that the internal length scale vanishes at the short wavelength limit. The loss
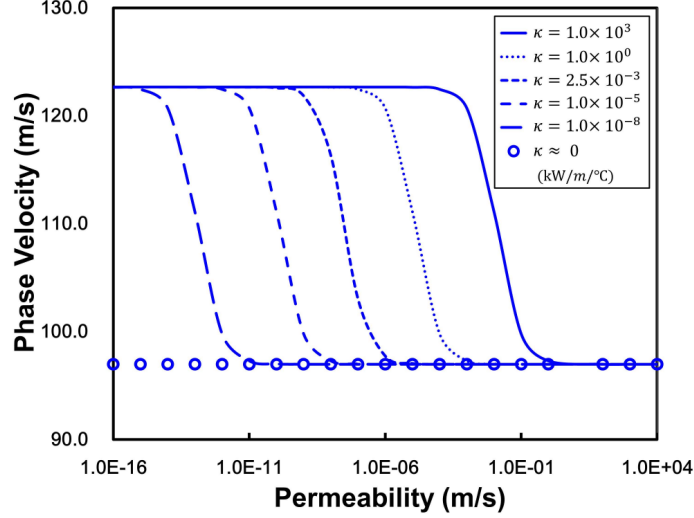
Figure 4.1: Phase velocity vs. permeability with different thermal conductivities (With $E_t = 30$ MPa, $\rho c = 4.5$ kJ/m^3/°C, M = 200 MPa and $T_0 = 20$ °C)

of physical internal length scale also suggests that any grid-based numerical model that solves the THM governing equations may exhibit mesh dependency, as any regularization effect induced by multi-physical coupling may vanish if the physical length scale vanished.

In other words, the rate-dependence introduced through multiphysical coupling may not regularize the THM governing equations when softening occurs. This conclusion echoes the previous dispersion analysis of isothermal two-phase porous media by Abellan and Borst [244], which also indicates that the internal length scale vanishes at the short wavelength limit. The wave propagation behavior of non-isothermal condition when strain softening occurs is further evaluated by numerical experiments in Section 4.3.2.

For the adiabatic case, we derived the internal length scale of the adiabatic THM system within a limited range of wavenumbers by expanding the derivation for isothermal porous system in Zhang, Sanavia, and Schrefler [81]. In addition, we conducted parametric studies to analyze how the specific heat and permeability may affect the cutoff wavenumber and the corresponding internal length scale.

Adiabatic Case

By assuming that the thermal conductivity is approximately zero, we obtained the characteristic equation of a damped harmonic wave propagating in a porous medium at the adiabatic limit. Based on the derivations in Section 4.2.2, we conducted a dispersion analysis and derive the expression of the internal length scale when the porous medium remains at the adiabatic limit. Our starting point is the third-order characteristic polynomial, which takes the following form,

$$D(\lambda) = \lambda^3 + a\lambda^2 + b\lambda + c = 0, \tag{4.48}$$

where,

$$a = a^0 y, \quad a^0 = \frac{\rho c k M}{\rho c - 9\alpha_m^2 T_0 M}, \tag{4.49}$$

$$b = b^0 y, \quad b^0 = \frac{\rho c E_t + \rho c b^2 M + \beta^2 T_0 + 6\alpha_m \beta b T_0 M - 9\alpha_m^2 E_t T_0 M}{\rho(\rho c - 9\alpha_m^2 T_0 M)}, \tag{4.50}$$

$$c = c^0 y^2, \quad c^0 = \frac{(\rho c E_t + \beta^2 T_0) k M}{\rho(\rho c - 9\alpha_m^2 T_0 M)}, \tag{4.51}$$

$$y = k_w^2. \tag{4.52}$$

When strain softening occurs, the tangential modulus E_t becomes negative. In this case, waves propagating in the porous medium can be either dispersive or non-dispersive, depending on the wavenumber k_w.

Our objective here is to determine whether it is possible to propagate waves with finite speed when stability of the THM system has already been lost. Recall that the stability analysis in Section 4.2.2 indicates loss of stability when either one of the following conditions holds , i.e., (1) $E_t < -(\beta^2 T_0/\rho c)$, (2) $c > 9\alpha_m^2 T_0 M/\rho$, (3) $k = \kappa = 0$. Here, we assume that the permeability is non-zero and focus our attention only on the cases in which condition (1) and (2) hold. Furthermore, we assume that the softening tangential

modulus $E_t > -b^2 M$ always holds [81, 227]. In other words, our objective is to determine whether the roots of the characteristic polynomial contain positive real part for the special case where the following condition holds,

$$-b^2 M < E_t < -\beta^2 T_0/\rho c \ , \ \ c > 9\alpha_m^2 T_0 M/\rho \ , \ \ k > 0. \tag{4.53}$$

Given the condition expressed above, we conclude that at least one of the roots has a positive real part. This is due to the fact that $E_t < -\beta^2 T_0/\rho c$ implies that $\rho c E_t + \beta^2 T_0 < 0$, which in return leads to $D(0) < 0$. Meanwhile, $\lim_{x\to\infty} D(x) > 0$, as the characteristic polynomial of (4.48) is monic. According to the intermediate value theorem (or more specifically Bolzano's theorem, cf. Morales [262]), the two aforementioned conditions combining the fact that the polynomial with real coefficients is continuous imply that (4.48) has at least one root with positive real part. Thus, there are two possible sets of solutions of $D(\lambda)$: (1) one positive real root and a pair of complex conjugate roots, (2) three real roots in which at least one is positive. As discussed in Zhang, Sanavia, and Schrefler [81], the first case enables waves to propagate by remaining the governing equations to be hyperbolic under strain softening condition. In the second case, however, the wave speed becomes imaginary which leads the dynamic governing equations to be elliptic: the finite element analysis will show mesh dependency [81]. Therefore, we evaluate the cubic polynomial of (4.48) to have one real root and a pair of complex conjugate roots by considering that the discriminant (denoted as, $\triangle$) should be less than zero. According to (4.48) to (4.52), the discriminant of cubic function can be expressed as,

$$\triangle = -4b^{0^3}y^3 + a^{0^2}b^{0^2}y^4 + 18a^0 b^0 c^0 y^4 - 27c^{0^2}y^4 - 4a^{0^3}c^0 y^5. \tag{4.54}$$

This expression can be rewritten in terms of coefficients, w, r and s, i.e.,

$$\triangle = -y^3(wy^2 + ry + s), \tag{4.55}$$

where,

$$w = 4a^{0^3}c^0, \tag{4.56}$$

$$r = 27c^{0^2} - a^{0^2}b^{0^2} - 18a^0b^0c^0, \tag{4.57}$$

$$s = 4b^{0^3}. \tag{4.58}$$

To keep the discriminant ($\triangle$) negative, we note that the quadratic polynomial of $wy^2 + ry + s$ in (4.55) should be always positive. Under the given condition in (4.53), we know that the coefficient w becomes negative since c^0 is negative and a^0 is positive. Besides, we can find out that s becomes positive since b^0 is come to be positive. Therefore, we can derive the only positive root of $wy^2 + ry + s = 0$ in the form of $(-r - \sqrt{r^2 - 4ws})/2w$ based on the fact that $w < 0$ and $s > 0$. In other words, this makes (4.55) be always negative ($\triangle < 0$) when the square of the wavenumber y ($= k_w^2$) is within the range described as follows:

$$0 < y < \frac{-r - \sqrt{r^2 - 4ws}}{2w} (= k_{w,cut}^2). \tag{4.59}$$

The cutoff wavenumber ($k_{w,cut}$) as a function of the permeability or mobility (k), specific heat (ρc), tangential modulus (E_t), reference temperature (T_0) and other material properties of porous media has also been sought in this study. Meanwhile, the influences of the permeability and specific heat on the cutoff wavenumber are depicted in Figure 4.2. The reciprocal of permeability shows a linear relation to the cutoff wavenumber in log-log plane, however, the specific heat shows limited effect until it reaches to 1.0. In this regard, we can find out that the permeability is closely related to the cutoff wavenumber while the specific heat has little influence on it.

Within the range of cutoff wavenumber, three roots (one real and two complex conjugate roots) of the third-order characteristic equation can be determined by Cardano's
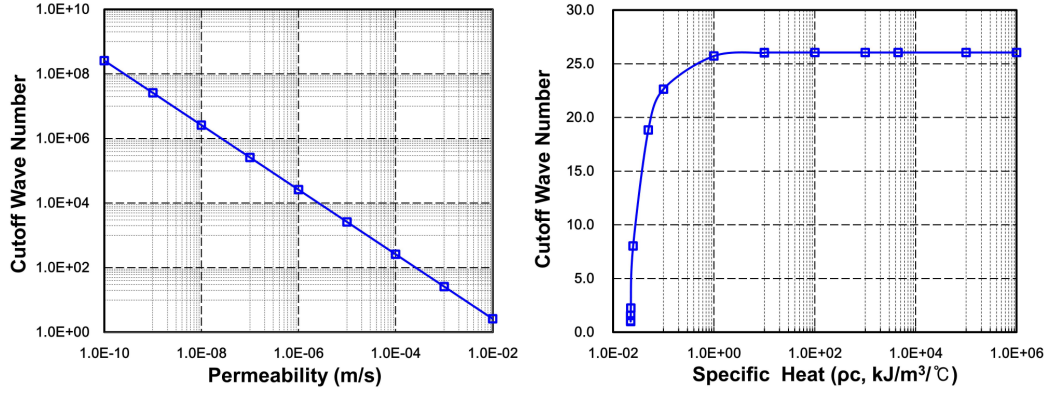
(a) Cutoff wavenumber vs. Permeability ($\rho c = 4.5 kJ/m^3/°C$)

(b) Cutoff wavenumber vs. Specific Heat ($k_{perm} = 1.0 \times 10^{-3}$ m/s)

Figure 4.2: Relationship of the cutoff wavenumber with permeability and specific heat under adiabatic condition

formula. By letting $\lambda = z - \frac{a}{3}$, the third-order polynomial (4.48) can be rewritten as,

$$z^3 + pz + q = 0, \tag{4.60}$$

where,

$$p = \frac{1}{3}(3b - a^2), \quad q = \frac{1}{27}(2a^3 - 9ab + 27c). \tag{4.61}$$

This equation has three roots that take the following forms,

$$z_1 = A + B, \quad z_{2,3} = -\frac{A+B}{2} \pm \frac{i\sqrt{3}}{2}(A - B), \tag{4.62}$$

where,

$$A = \sqrt[3]{-\frac{q}{2} + \sqrt{\frac{q^2}{4} + \frac{p^3}{27}}}, \quad B = \sqrt[3]{-\frac{q}{2} - \sqrt{\frac{q^2}{4} + \frac{p^3}{27}}}. \tag{4.63}$$

Therefore, we can rewrite the solution λ as follows,

$$\lambda_1 = (A + B) - \frac{a}{3}, \quad \lambda_{2,3} = -\frac{A+B}{2} + \frac{i\sqrt{3}}{2}(A - B) - \frac{a}{3}, \tag{4.64}$$

126

and distinguish the real part and imaginary part in the roots:

$$\lambda_r = -\frac{1}{2}(A+B) - \frac{a}{3}, \ \lambda_i = \frac{\sqrt{3}}{2}(A-B). \tag{4.65}$$

By substituting the complex root into the damped harmonic equation like we did before in (4.42), we have (note that $\lambda_i = \omega$):

$$v(x,t) = Ae^{ik_w x}e^{\lambda_r t - i\omega t} = Ae^{ik_w x}e^{\lambda_r t - i\lambda_i t}, \ \ v = [u,p,T]^T. \tag{4.66}$$

Recall the relation between the phase velocity v_p and the wavenumber k_w,

$$v_p = \frac{|\lambda_i|}{k_w}. \tag{4.67}$$

By means of $t = x/v_p$, the damping term $e^{(\lambda_r)t}$ changes into $e^{k_w((\lambda_r)/|\lambda_i|)x} = e^{-\alpha x}$, where α is the damping coefficient [81]. Notice that the thermo-hydro-mechanical coupling introduces rate dependence to the mechanical response, even if the solid phase continuum does not exhibit any viscous behavior. As a result of this rate dependence, the internal length scale l is introduced, i.e.,

$$l = \alpha^{-1}, \quad \alpha = -\frac{\lambda_r}{|\lambda_i|}k_w, \tag{4.68}$$

in which λ_r and λ_i are obtained from (4.65). It is obvious that the definition of internal length scale holds only for dynamic analysis. The damping coefficient α and the internal length scale l can be expressed as below:

$$\alpha = \frac{\left|A+B+\frac{2}{3}a\right|k_w}{\sqrt{3}(A-B)}, \quad l = \frac{\sqrt{3}(A-B)}{\left|A+B+\frac{2}{3}a\right|k_w}. \tag{4.69}$$

Therefore, we can identify the internal length scale as a function of the mobility (k), specific heat (ρc), wavenumber (k_w), reference temperature (T_0), tangential modulus under

strain softening (E_t) and other material properties as:

$$l = f\left(k, \rho c, k_w, E_t, M, \beta, \alpha_m, T_0\right).$$ (4.70)

Remark 2

In the adiabatic condition, we derived the cutoff wavenumber which guarantees the wave propagation is possible. Within this range, we can analyze how the damping coefficient changes along the wavenumber by normalizing it with the cutoff wavenumber in Figure 4.3.
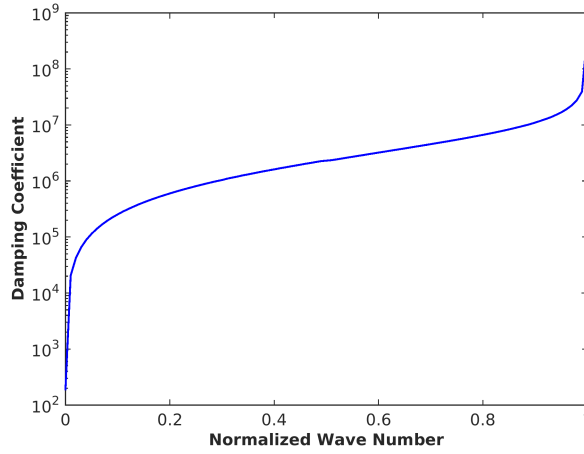
Figure 4.3: Damping coefficient (α) vs. Normalized wavenumber

In this figure, we can see that the damping coefficient (α) approaches zero when the wavenumber decreases, which is natural phenomenon considering the definition of α. On the other hand, the damping coefficient approaches to infinity when the wavenumber converges to the cutoff value, which states that the internal length scale, a reciprocal of α, vanishes. This fact is also analogous to the case of long wavelength limit under the non-isothermal condition (4.47). The effect of permeability (or mobility, k) and specific heat (ρc) of porous media on the internal length scale is compared in Figure 4.4. We can see that the permeability has proportional relation to the internal length scale while the
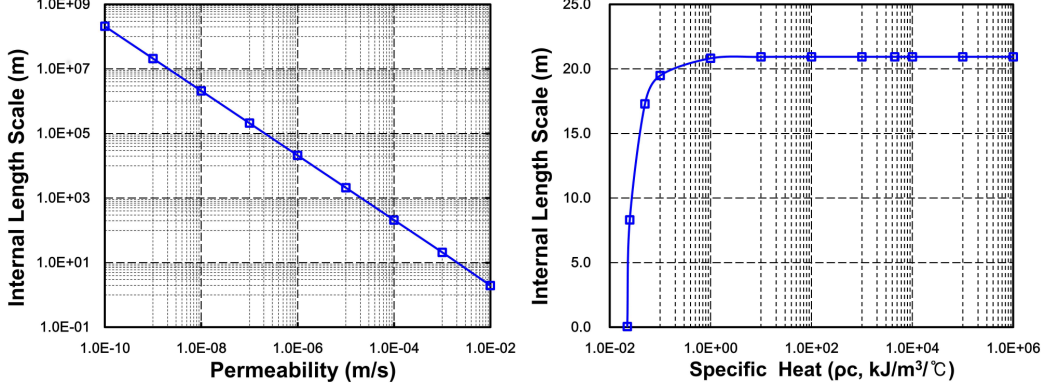
(a) Internal length scale vs. Permeability ($\rho c = 4.5 kJ/m^3/°C$)

(b) Internal length scale vs. Specific Heat ($k_{perm} = 1.0 \times 10^{-3}$ m/s)

Figure 4.4: Relationship of the internal length scale with the permeability and specific heat under the adiabatic condition

specific heat has limited effect.

4.3 Numerical experiments

To illustrate the influences of thermo-hydro-mechanical coupling on the width of localization zone, we use an implicit dynamic finite element code to simulate one-dimensional wave propagation in a thermo-sensitive fully saturated porous bar with different set of material parameters. Our objective here is to use the numerical experiments to (1) verify the theoretical analysis on the phase velocity and internal length scales in Section 4.2.2 and (2) confirm whether mesh dependency occurs when the physical internal length scale is predicted to be vanished according to (4.47) and (4.70).

As mentioned previously in Section 4.2.3, we did not obtain the expression of internal length scale for the non-isothermal condition, as the general algebraic expression of the internal length scale does not exist according to the Abel-Ruffini theorem [261]. As a result, we first limit our focus on the adiabatic condition and performed numerical experiments to validate the analytical expression of the internal length scale. We then analyze the simulated wave propagation behavior of the non-isothermal condition with a series

of numerical simulations under the different thermal conductivities. The changes of wave propagation behaviors observed in the numerical simulations due to changes of the thermal conductivity are also compared. We found that the observed behavior is consistent with the phase velocity expressed in (4.46).
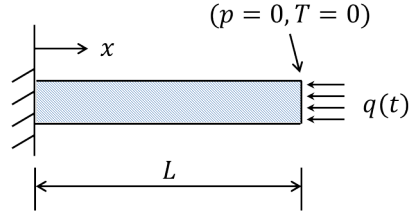
Figure 4.5: One dimensional soil bar in axial compression
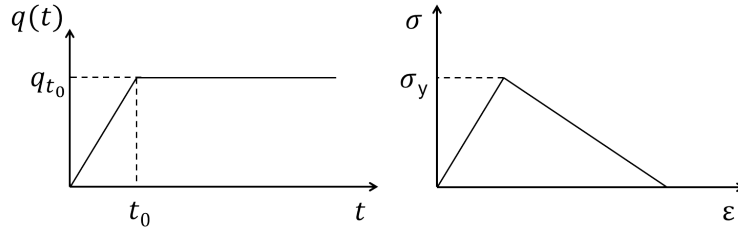
Figure 4.6: Applied stress and local stress-strain diagram

The numerical model consists of a softening bar constrained to move in only one direction. In addition, heat transfer and pore-fluid diffusion are also confined to be one-dimensional. The length of the bar is 10 m. At $x = 0$ m, the bar is fixed and has zero displacement, while a perturbation of force is applied at $x = 10$ m. Both pore pressure and temperature are prescribed as zero at $x = 10$ m. A constant time step $\triangle t = 1.0 \times 10^{-2}$ sec. is used to all the numerical simulations. The absolute mass densities of soil and fluid are selected as $\rho_s = 2,700$ kg/m^3 and $\rho_f = 1,000$ kg/m^3. The elastic and tangential moduli under strain softening are assumed to be 30 MPa and -20 MPa, respectively, and the Biot's modulus (M) is considered to be 200 MPa. The reference temperature T_0 is set to be 20 $^\circ C$, and the numerical condition of applied stress and local stress-strain diagram are depicted with boundary conditions in Figures 4.5 and 4.6. Here, t_0 is set to be 0.1 sec., q_{t_0} is applied as 500 kPa, and σ_y values are indicated in the figures for each simulation.

Table 4.2: The internal length scale under the different conditions (Adiabatic case)

k_{perm}(m/s)	ρc(kJ/m^3/°C)	l(m)($k_w = 1.0$)	Comparison
5.0×10^{-3}	4.5	4.10	the reference
2.5×10^{-2}	4.5	0.19	permeability change
5.0×10^{-3}	2.4×10^{-2}	0.94	specific heat change

4.3.1 Adiabatic case

The reference case of internal length scale under the adiabatic condition is calculated with the permeability (k_{perm}) of 5.0×10^{-3} m/s and the specific heat (ρc) of 4.5 kJ/m^3/°C. The internal length of each case is described in the following Table 4.2 when the wavenumber is assumed to be unity. The numerical simulations are investigated with the element size of 0.4 m.

The reference case gives the internal length scale of 4.10 m and the plastic wave is able to propagate. We can verify this from the numerical simulation results depicted in Figure 4.7. Nevertheless, in another two numerical experiments, one with increased permeability and the other with lowered specific heat, the harmonic wave ceases to propagate and the plastic zone seizes at a certain depth as shown in Figure 4.8. This fixed plastic zone with time indicates that the wave is unable to propagate. This observation is consistent with (4.69) and the relationship among the internal length scale, permeability and specific heat showcased in Figure 4.4. Similar plastic strain patterns were noticed by Zhang, Sanavia, and Schrefler [81] in dynamic wave propagation simulations under the isothermal condition.

4.3.2 Non-isothermal case

With the results shown in Figure 4.7 as the reference, we vary the thermal conductivity and determine how the thermal conductivity affects wave propagation. We assumed that the thermal conductivities of fluid and solid are the same and selected the value from the previous study by Sun [19], $\kappa = 2.5 \times 10^{-3}$ kW/m/°C. According to our previous

Figure 4.7: Development of the localization zone under possible wave propagation - the plastic strain moves towards the depth along the time (the reference condition, permeability $= 5.0 \times 10^{-3}$ m/s, $\rho c = 4.5$ kJ/m^3/°C, $\sigma_y =$30 MPa)

(a) Permeability change ($k_{perm} = 2.5 \times 10^{-2}$m/s, $\sigma_y = 34$ MPa)

(b) Specific heat change ($\rho c = 2.2 \times 10^{-2} kJ/m^3$/°C, $\sigma_y = 30$ MPa)

Figure 4.8: Development of the localization zone under no wave propagation - the plastic strain stays at the same depth along the time

analysis, both thermal conductivity and permeability can influence on the behavior of the THM system (Figure 4.1). In order to analyze this effect, we conducted parametric study of thermal conductivity under two permeability conditions: (1) 5.0×10^{-3} m/s from the reference case in Section 4.3.1, and (2) 1.0×10^{-10} m/s as low permeability case. A series of numerical simulations are performed by varying the thermal conductivities provided that the specific heat (ρc) is assumed to be 4.5 kW/m/°C.

Firstly, we introduced the thermal conductivity into the reference case and conducted the numerical simulation. When $\kappa = 2.5 \times 10^{-3}$ kW/m/°C was adopted, the numerical simulation showed little change in the plastic strain compared to the adiabatic condition in Figure 4.7. However, when the thermal conductivity is increased to 1.0 kW/m/°C, we found the wave propagation behavior started to change. These results are depicted in Figure 4.9. The plastic strain is increased compared to the adiabatic case, and the plastic wave is still able to propagate along time. Considering the initial and boundary conditions of temperature field, we expect that the prescribed zero temperature at the surface (10 m) contributes additional compression to the one-dimensional bar.
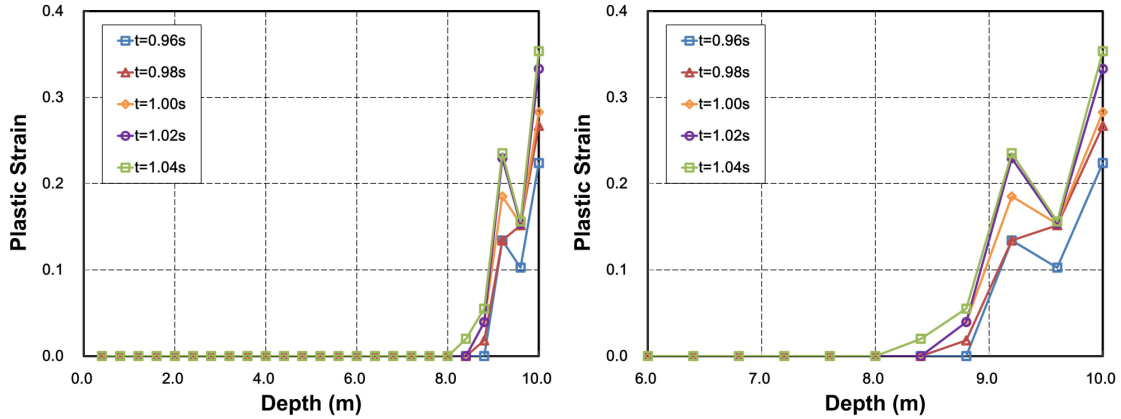
Figure 4.9: Developement of the localization zone (non-isothermal condition with $\kappa = 1.0$ kW/m/°C, $\sigma_y = 30$ MPa)

Next, we started from the numerical set up of adiabatic limit with the permeability equal to 1.0×10^{-10} m/s. When the thermal conductivity of 2.5×10^{-3} kW/m/°C was applied, the response of plastic strain gave little effects compared to the adiabatic condition.

(a) $\kappa = 2.5 \times 10^{-3}$ kW/m/°C   (b) $\kappa = 1.0$ kW/m/°C
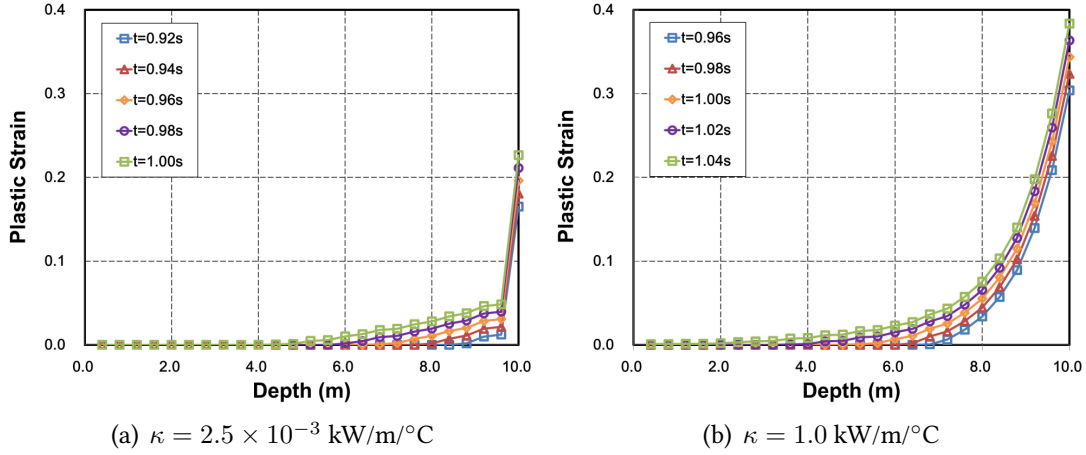
Figure 4.10: Developement of the localization zone of non-isothermal condition with different thermal conductivities - plastic zone moves toward the depth along the time ($k_{perm} = 1.0 \times 10^{-10}$ m/s, $\rho c = 3.5$ kW/m/°C, $\sigma_y = 3.8$ MPa)

When κ became larger than 1.0×10^{-1} kW/m/°C, however, we found the changes of plastic localization zone. Figure 4.10 depicts the changes of wave propagation with different thermal conductivities under the low permeability condition. We can identify that both permeability and thermal conductivity influence on the behavior of wave propagation under strain softening from Figures 4.9 and 4.10.

Furthermore, we took two cases in Section 4.3.1, in which the wave was not able to propagate, and re-analyzed the simulations by introducing the thermal conductivity. Again, the thermal conductivity of 2.5×10^{-3} kW/m/°C showed little effect on both cases. Figure 4.11 shows when $\kappa = 1.0$ kW/m/°C was applied. We can see the width of localization zones and the plastic strains are increased compared to adiabatic case in Figure 4.8. However, the plastic wave does not propagate along time. This indicates that the thermal conductivity appears limited effect on regularization.

Remark 3

We conducted additional numerical simulations for the non-isothermal case to analyze the influence of mesh size on shear band width. The permeability of 1.0×10^{-10} m/s
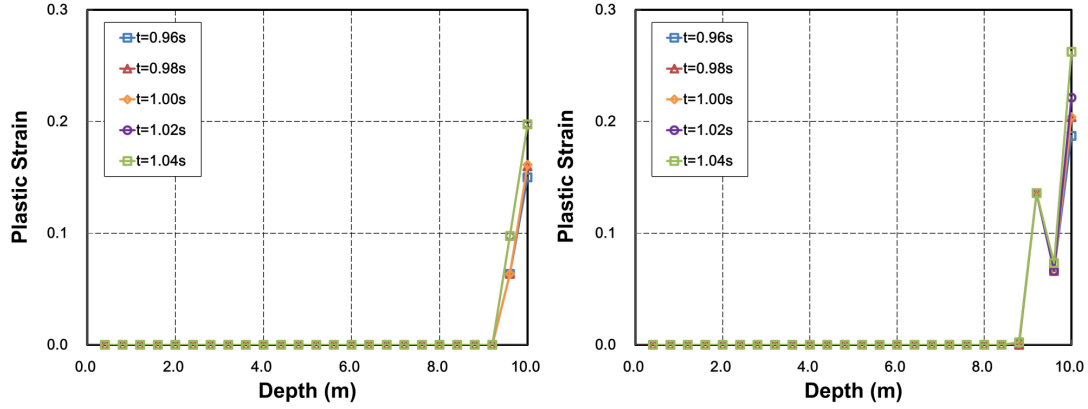
(a) Permeability change ($k_{perm} = 1.0 \times 10^{-2}$ m/s, $\sigma_y = 34$ MPa)

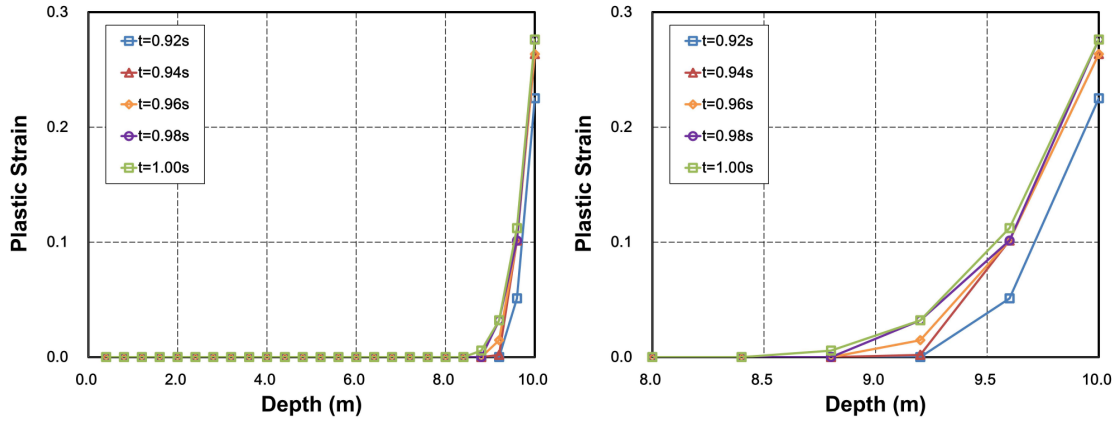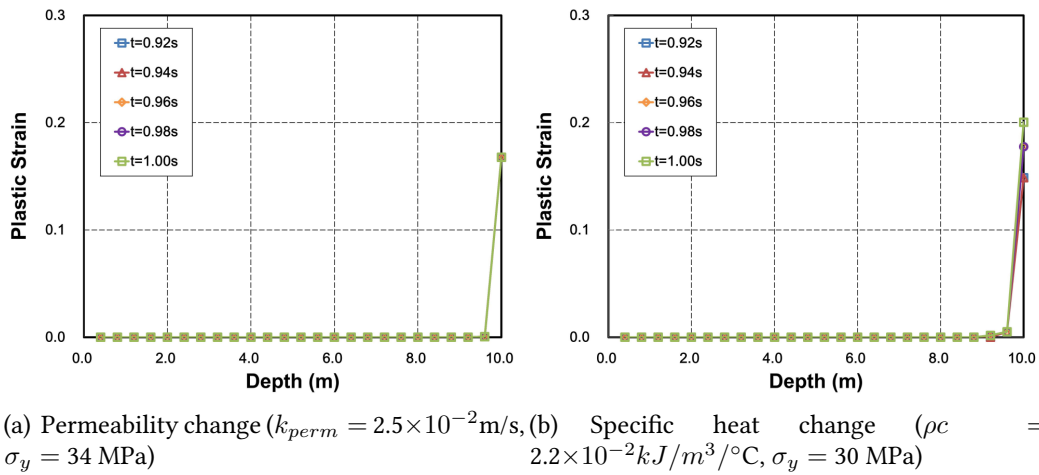(b) Specific heat change ($\rho c = 2.2 \times 10^{-2}$ kJ/m^3/°C, $\sigma_y = 30$ MPa)

Figure 4.11: Development of the localization zone under no wave propagation - the plastic strain stays the same depth along the time (Non-isothermal condition, $\kappa = 1.0$ kW/m/°C)

was selected to have enough internal length scale for stability. The thermal conductivity ($\kappa = 2.5 \times 10^{-3}$ kW/m/°C) and the specific heat ($\rho c = 4.5$ kJ/m^3/°C) were adopted from the previous study by Sun [19]. The one-dimensional domain were discretized by 10, 20, 25, 30 linear finite element of equal sizes to study mesh dependency. As shown in Figure 4.12 (a), the plastic strain distribution from the numerical simulations suggests mesh independence. In addition, Figure 4.12 (b) describes temperature field distribution of the numerical simulations for the non-isothermal condition. With the same material properties used in the mesh study, the domain with 25 elements is selected. We can see how the temperature changes with different thermal conductivities.

4.4 Conclusions

The one-dimensional wave propagation in a full saturated, thermo-sensitive porous medium has been analyzed. The stability analysis indicates that the governing equations of the thermo-hydro-mechanics system leads to a characteristic polynomial at least one order higher than the isothermal poromechanics counterpart. By applying the Routh-Hurwitz stability criterion to this higher-order characteristic polynomial, we determine
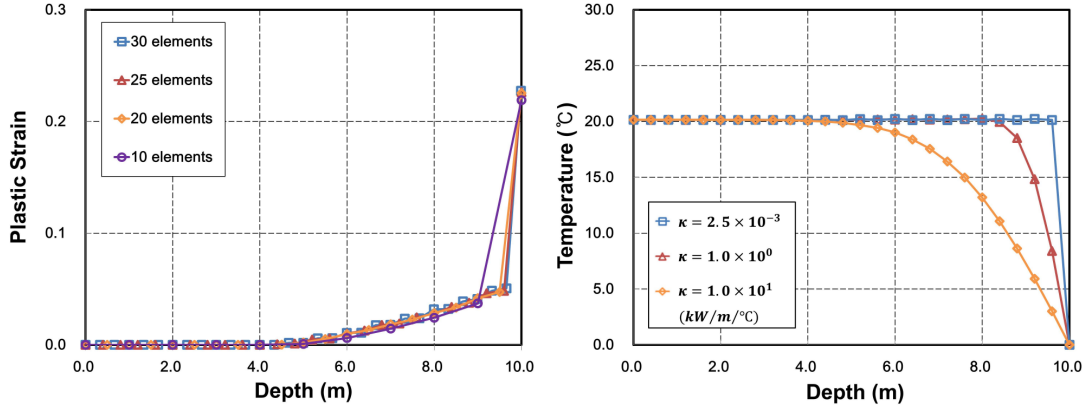
(a) Plastic strain along the bar under different (b) Temperature field results under different thermesh conditions ($\kappa = 2.5 \times 10^{-3}$kW/m/°C)) mal conductivities (with 25 elements)

Figure 4.12: Independence of the strain localization zone width under different mesh sizes, and limited changes of temperature field along the bar under various thermal conductivities (at $t = 1.0\ sec$ with $k_{perm} = 1.0 \times 10^{-10}$m/s, $\rho c = 4.5$kJ/m^3/°C)

that instability may occur if (1) strain softening occurs and/or (2) specific heat per mass is less than a critical value proportional to Biot's modulus and the square of the thermal expansion coefficient and (3) when both permeability and thermal conductivity are zero. Dispersion analysis on the THM system reveals that a dispersive wave may propagate in a fully saturated, thermo-sensitive system under certain limited conditions. Nevertheless, the internal length scale introduced by the thermo-hydro-mechanical coupling vanishes at the short wavelength limit. For the adiabatic limit case, we derive an explicit expression of the internal length scale as a function of permeability, specific heat, wavenumber and other material properties. The cutoff wavenumber is also identified. Our results indicate that there is a limited range of wavenumbers that allows dispersive waves to propagate at finite speeds.

Chapter 5

Numerical techniques and solution strategies for coupled multiphysics mechanisms in crystalline solids and geomaterials

In this chapter, Sections 5.2.1, 5.2.2, and 5.2.3 are reproduced from the published papers: Na and Sun [177]; Na and Sun [75].

5.1   Introduction

This chapter covers specific numerical issues, which can be potentially raised from the muliphysics problems, and how we resolve those topics in terms of numerical and physical aspects. Firstly, we focus on the stability of numerical solutions and the efficiency of computational calculations. Because the numerical system of multi-component problems are often constructed by the equal-order dimensional spaces for each component, the inf-sup condition is not satisfied in the limit cases. In addition, the system of equations has high condition number due to different physics. The stabilized procedure and preconditioning strategy associated with monolithic simulations are addressed to solve those numerical issues. We further introduce the operator-split scheme to resolve the multiphysics problem including fracture behavior. Next, we discuss the computational

methods to regularize the local constitutive law, which leads to pathological mesh dependence in strain localization problems. The scale dependence in multiphase materials is further addressed in terms of the plastic length scaled introduced by the nonlocal constitutive model. By leveraging that nonlocality, we cover the adaptive meshing strategy that updates the plastic internal variables based upon the concept of Lie algebra and configurational force.

5.2   Inf-sup, preconditioing, and operator-split

The lack of two-fold inf-sup condition is caused by the usage of equal-order finite dimensional space for displacement, liquid water pressure and temperature. This well-known effect has been intensively studied for poromechanics problems in the last few decades [16, 19, 43, 178, 263, 264]. Here, we adopt the stabilization procedure to overcome this numerical deficiency in the system of frozen porous media covered in Section 2. To ensure that the stabilization procedure we used leads to stable results, we introduce a new numerical test called weak two-fold inf-sup tests to check whether solution remains stable for arbitrary mesh size. We then address a system of equation with high condition number due to unknown variables with different physical features: displacement, pressure, temperature. Here we propose a possible solution to overcome this problem, which is a preconditioner specialized for the THM system to speed up the simulations. Lastly, the operator-split scheme, an alternative method of monolithic approach, for multiphysics problems associated with fracture is addressed, the relevant topic is covered in Section 3.

5.2.1   Spatial stability and two-fold inf-sup tests

In classical poromechanics FEM models that employ solid displacement and pore pressure as the prime variables, the interpolated pore pressure field is known to suffer from spurious oscillation in the undrained limit [24, 265] if displacement and pore pressure are

spanned by the same basis function. The cause of the problem is due to the lack of inf-sup condition [24, 43, 209]. Similar spurious oscillations have been addressed in THM problem with the equal-order finite element when the prime variables of the displacement, pore pressure and temperature were considered in a very fine temporal discretization or near the undrained limit [19, 252]. Previously, Liu et al. [252] introduced an interior-penalty procedure on the discrete Galerkin model of the thermo-hydro-mechanics problem in geometrically nonlinear range. On the other hand, Sun [19] analyzes the cause of the spurious oscillation of pore pressure and temperature and proposes a projection-based stabilization method for the finite-strain thermo-hydro-mechanical problem to eliminate the spurious modes in the pore pressure and temperature [266]. In this study, we adopt the polynomial projection scheme of Sun [19] to stabilize the THM problems, in which the inf-sup deficiency of equal-order finite element is counterbalanced using stabilization terms based on the weak two-fold inf-sup condition. Nevertheless, a systematical numerical procedure to test the validity of the stabilization procedure has not yet proposed.

Our starting point is the result from Howell and Walkington [267] which proves that saddle-point problems containing more than two solution fields require the two-fold inf-sup condition to maintain spatial stability [19, 178]. By considering the finite element model with a saddle point structure form: $(\boldsymbol{u}^h,\ p_{\mathrm{L}}^h,\ T^h) \in \boldsymbol{V}_{\boldsymbol{u}}^h \times V_{p_{\mathrm{L}}}^h \times V_T^h$, where $\boldsymbol{V}_{\boldsymbol{u}}^h$, $V_{p_{\mathrm{L}}}^h$ and V_T^h are the finite dimensional spaces chosen for displacement, liquid water pressure and temperature interpolations, the discrete two-fold inf-sup condition holds if and only if there exists a constant $C_0 > 0$ such that,

$$\sup_{\boldsymbol{w}^h \in \boldsymbol{V}_{\boldsymbol{u}}^h} \frac{\int_{\mathcal{B}} \left(a p_{\mathrm{L}}^h + b T^h \right) \nabla^{\boldsymbol{x}} \cdot \boldsymbol{w}^h dV}{\|\boldsymbol{w}^h\|_{\boldsymbol{V}_{\boldsymbol{u}}^h}} \geq C_0 \left(\|p_{\mathrm{L}}^h\|_{V_{p_{\mathrm{L}}}^h} + \|T^h\|_{V_T^h} \right)$$

$$\text{where, } (p_{\mathrm{L}}^h, T^h) \in V_{p_{\mathrm{L}}}^h \times V_T^h. \qquad (5.1)$$

Note that the coefficients of a and b are described by S_{L}, $S_{\mathrm{C}}(= 1 - S_{\mathrm{L}})$ and p_{C} which are functions of liquid water pressure and temperature fields (i.e., $a = \partial(S_{\mathrm{L}} p_{\mathrm{L}})/\partial p_{\mathrm{L}} +$

$\partial(S_C p_C)/\partial p_L$, $b = \partial(S_L p_L/\partial T) + \partial(S_C p_C)/\partial T)$; $\|\cdot\|_{\boldsymbol{V}_{\boldsymbol{u}}^h}$, $\|\cdot\|_{V_{p_L}^h}$ and $\|\cdot\|_{V_T^h}$ are the norms corresponding to the finite dimensional space $\boldsymbol{V}_{\boldsymbol{u}}^h$, $V_{p_L}^h$ and V_T^h. The same associated norms are equipped to the solution spaces and their corresponding test functions. We choose the norm $\|\cdot\|_{\boldsymbol{V}_{\boldsymbol{u}}^h} = \|\cdot\|_1$ and $\|\cdot\|_{V_{p_L}^h} = \|\cdot\|_{V_T^h} = \|\cdot\|_0$, where $\|\cdot\|_k$ indicates the standard Sobolev norm of order k, which leads to the relation, $C_0 \left(\|p_L^h\|_{V_{p_L}^h} + \|T^h\|_{V_T^h} \right) \geq C_0 \left(\|p_L^h + T^h\|_0 \right)$.

Adopting the same basis functions for displacement, liquid pore pressure, and temperature leads to a formulation that lacks the two-fold inf-sup condition as stated in (5.1). However, as pointed out in Sun [19], the spurious pressure and temperature oscillation due to the lack of two-fold inf-sup condition can be eliminated by introducing the additional gradient or projection terms that counterbalance the inf-sup deficiency. This study adopted the projection stabilization scheme to eliminate the spurious oscillations. Note that an analytical proof of the inf-sup condition for a particular choice of finite dimensional spaces can be difficult [268]. As an alternative, we introduce the usage of numerical inf-sup test [234, 264, 268–271] for analyzing the thermo-hydro-mechanical formulation. The underlying idea of this inf-sup test is to consider the liquid water pressure and temperature fields together as a product space and introduce proper norms for this product space. Following this step, one may solve a series of generalized eigenvalue problems of (5.2) corresponding to the inf-sup condition (cf. (5.1)) for a selected number of elements, that is,

$$\mathbf{G}^h \boldsymbol{V}^h = \lambda \mathbf{S}^h \boldsymbol{V}^h, \tag{5.2}$$

where λ_p is the smallest non-zero eigenvalue, in which $\sqrt{\lambda_p}$ corresponds to the inf-sup value; the matrices $\mathbf{G}^h$ and $\mathbf{S}^h$ are defined for a given finite element discretization, as detailed in reference Bathe [268] and Chapelle and Bathe [269]. To perform a two-fold inf-sup test for the product space, one may partition the Jacobian matrix of (2.73) such

that,

$$\begin{bmatrix} \mathbf{A} & \mathbf{B}_1 & \mathbf{D}_1 \\ \mathbf{B}_2 & \mathbf{C} & \mathbf{E}_1 \\ \mathbf{D}_2 & \mathbf{E}_2 & \mathbf{F} \end{bmatrix} \rightarrow \begin{bmatrix} \mathbf{A} & \mathbf{H}_1 \\ \mathbf{H}_2 & \mathbf{K} \end{bmatrix}, \tag{5.3}$$

$$\text{where } \mathbf{H}_1 = \begin{bmatrix} \mathbf{B}_1 & \mathbf{D}_1 \end{bmatrix}, \quad \mathbf{H}_2 = \begin{bmatrix} \mathbf{B}_2 \\ \mathbf{D}_2 \end{bmatrix}, \quad \text{and } \mathbf{K} = \begin{bmatrix} \mathbf{C} & \mathbf{E}_1 \\ \mathbf{E}_2 & \mathbf{F} \end{bmatrix}.$$

We limit our focus in a very fine temporal discretization in which the heat transfer and pore-fluid diffusion terms are both assumed to be minor. Note that this limit case leads the matrices $\mathbf{H}_1$ and $\mathbf{H}_2$ to be $\mathbf{H}_1 \approx \mathbf{H}_2^\mathsf{T} = \mathbf{H}$.

Following Chapelle and Bathe [269] and Bathe, Iosilevich, and Chapelle [270] and two-fold inf-sup test of Howell and Walkington [267] and Sun and Mota [234] based on (5.1) and (5.3), the matrices for the eigenvalue problem in (5.2) are represented as,

$$\mathbf{G}^h = \mathbf{H}^h \mathbf{K}^h (\mathbf{H}^h)^\mathsf{T} \quad \text{and} \quad (\boldsymbol{w}^h)^\mathsf{T} \mathbf{S}^h \boldsymbol{w}^h = \|\boldsymbol{w}^h\|_{\boldsymbol{V}_{\boldsymbol{u}}^h}^2, \tag{5.4}$$

where $\mathbf{H}^h$ and $\mathbf{K}^h$ are the expressions of $\mathbf{H}$ and $\mathbf{K}$ discretized by shape functions (2.72). Meanwhile, the expression of $\mathbf{G}^h$ depends on the choice of weighted norm equipped for the product space of the interpolated pore pressure and temperature. In our case, we follow the procedures depicted in Bathe, Iosilevich, and Chapelle [270], Bathe et al. [272], and Sun, Cai, and Choo [273] and simply use the condensed lower diagonal matrix $\mathbf{K}^h$ to form the weighted norms. It should be noted that this particular $\mathbf{G}^h$ is not the only valid choice. For instance, one may also replace $\mathbf{K}^h$ with its inverse in (5.4) such that the two-fold inf-sup test is directly related to the statically condensed system of equations as have done in Sun and Mota [234]. However, as pointed out in Chapelle and Bathe [269], a choice that involves inversed matrix may likely increase the computational cost for evaluating the inf-sup tests due to the fact that the inverse matrix is more dense and the inverse

operation can also be costly. $\mathbf{S}^h$, which is referred as the norm matrix in Chapelle and Bathe [269], is obtained from the linear operator that gives the norm $\|\cdot\|_{\mathbf{V}_u^h}$ following Bathe [268], in which $\|\boldsymbol{u}^h\|_1^2 = \int_{\mathcal{B}} \nabla^{\boldsymbol{x}} \boldsymbol{u} \cdot \nabla^{\boldsymbol{x}} \boldsymbol{u} dV$ (cf. Sun [19], Mira et al. [264], and Pantuso and Bathe [274]).

Note that the numerical inf-sup value is sensitive to the norms chosen to construct the inf-sup test. While the existence of the inf-sup value and hence the validity of the inf-sup condition can be proved by any equivalent norms, the actual choice of the norms used to construct the inf-sup test may affect the trend of the numerical inf-sup values upon mesh refinement [271, 272]. Here we select the problem of 1D thawing consolidation for the numerical inf-sup test. The problem description including boundary conditions can be found in Section 2.5.1. The number of elements with 4, 8, 16 and 32 are selected for the numerical inf-sup test (Fig. 5.1). The stabilized inf-sup value is bounded which indicates the test is passed (e.g. Mira et al. [264], Bathe [268], Bathe, Iosilevich, and Chapelle [270], and Bathe [271]).
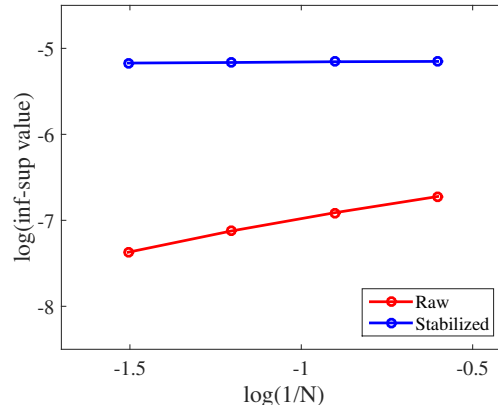
Figure 5.1: Inf-sup test of 1D thawing consolidation (the results from the number of elements with 4, 8, 16 and 32 are presented)

5.2.2 Pre-conditioner for three-field system

It is well acknowledged that the implicit monolithic solvers for mixed finite element may lead to ill-conditioning tangential matrix system [208, 275]. Since the residuals of the balance of mass, linear momentum and energy are all of different units, the eigenvalues and singular values of the block matrix system could be of several orders of difference and in different signs. Presumably, direct solvers such as Gaussian elimination may allow one to obtain incremental updates even when condition number of the tangent is high, provided that the condition number is still sufficiently small compared with the inverse of the machine error. Nevertheless, the direct solvers are often slower due to the significantly higher numbers of arithmetic operations. Another feasible possibility to resolve this issue is to design a proper pre-conditioner and then use it with an iterative solver. This approach is adopted in this study. The implementation of the preconditioner leverages the open source finite element library, `deal.II` (cf. Bangerth, Hartmann, and Kanschat [204] and Bangerth et al. [205]) interfaced with p4est mesh handling library [206], and algorithm libraries from the `Trilinos project` [207]. When the coupled thermo-hydro-mechanical (THM) model is solved in an implicit monolithic scheme, the nonlinear system of equations may leads to a three-by-three block-partitioned tangential matrix through a consistent linearization process (Section 2.4.2).

In this study, we extended the block-preconditioned Newton-Krylove solvers for originally designed for a $\boldsymbol{u}/p$ formulation by Dawson et al. [276] and White and Borja [208]. The underlying idea is to simply consider the space of the interpolated pore pressure and temperature fields as a product space and design a pre-conditioner such that,

$$\mathbf{P}^{-1}\mathbf{J}\boldsymbol{x} = \mathbf{P}^{-1}\boldsymbol{b}, \tag{5.5}$$

where $\mathbf{J}$ is the Jacobian; $\boldsymbol{x}$ is the solution fields; $\boldsymbol{b}$ is the residuals; $\mathbf{P}^{-1}$ is the preconditioner. The strategy of preconditioning is to choose $\mathbf{P} \approx \mathbf{L}$ such that $\mathbf{P}^{-1}\mathbf{J} \approx \mathbf{U}$ when a block LU

factorization of $\mathbf{J}$ is concerned as $\mathbf{J} = \mathbf{LU}$, in which the quality of this approximation determines how fast the Krylov solver converges [208]. In this study, we first express the 3 by 3 system of equations (2.73) into 2 by 2 system as written in (5.3). In this case, the block Schur complement with respect to $\mathbf{A}$ is $\mathbf{S} = \mathbf{K} - \mathbf{H}_2\mathbf{A}^{-1}\mathbf{H}_1$ (cf. Demmel, Higham, and Schreiber [277]). Therefore, the template using the "exact" preconditioner and its approximation can be described as,

$$
\mathbf{P}^{-1} = \begin{bmatrix} \mathbf{A}^{-1} & \mathbf{0} \\ \mathbf{S}^{-1}\mathbf{H}_2\mathbf{A}^{-1} & \mathbf{S}^{-1} \end{bmatrix} \approx \begin{bmatrix} \mathbf{P}_\mathbf{A}^{-1} & \mathbf{0} \\ \mathbf{P}_\mathbf{S}^{-1}\mathbf{H}_2\mathbf{P}_\mathbf{A}^{-1} & \mathbf{P}_\mathbf{S}^{-1} \end{bmatrix}. \tag{5.6}
$$

Note that the exact inverses $\mathbf{A}^{-1}$ and $\mathbf{S}^{-1}$ are too expensive to compute, which requires designing good approximations ($\mathbf{P}_\mathbf{A}^{-1}$ and $\mathbf{P}_\mathbf{S}^{-1}$). In particular, we extend the approximation of Schur complement ($\mathbf{S}$) for THM problem based on the hydro-mechanical systems [208] as,

$$
\mathbf{S}_\mathrm{M} = \mathbf{K}_D - \alpha\mathbf{M}, \tag{5.7}
$$

$$
\text{where} \quad \mathbf{M} = \begin{bmatrix} \mathbf{M}_{p_\mathrm{L}} & \mathbf{0} \\ \mathbf{0} & \mathbf{M}_T \end{bmatrix} \quad \text{with} \quad [\mathbf{M}_\pi]_e^{a,b} = \int_{\mathcal{B}} N_a N_b dV, \quad (\pi = p_\mathrm{L}, T).
$$

Here, we choose $\mathbf{K}_D$ with matrices at diagonal positions ($\mathbf{C}$ and $\mathbf{F}$) to simplify and improve the calculations based on physics point of view (assuming weak coupling between pressure and temperature) [204, 205, 208]. In addition, $\mathbf{M}$ is the extended mass matrix including liquid water pressure and temperature fields. The methods to estimate the optimal coefficient α and the approximation of $\mathbf{A}^{-1}$ and $\mathbf{S}^{-1}$ for the block Krylov solver in isothermal poromechanics problem can be found in White and Borja [208] and White, Castelletto, and Tchelepi [194]. Note that it is also possible to estimate an optimal choice of α for thermo-hydro-mechanical problems. In such a case, the parameter α should be different for each block to deliver the optimal performance. One feasible strategy can be found

Table 5.1: Residence norm (square root of the inner product of residual column vector) and the number of Krylov iterations at the selected Newton steps for comparison of pre-conditioning strategy (coarse mesh condition with the total degrees of freedom 120)

Newton Steps	No Preconditioning		Diagonal Preconditioning		Current Preconditioning	
	RHS norm	Krylov Iteration	RHS norm	Krylov Iteration	RHS norm	Krylov Iteration
Trial Step	5.9E-03	7839	5.9E-03	4	5.9E-03	4
Iteration 1	1.9E-01	2575	1.9E-01	4	1.9E-01	4
Iteration 5	1.1E-03	7335	1.1E-03	4	1.1E-03	4
Iteration 10	7.5E-10	6951	7.5E-10	4	7.5E-10	4
Solve time (s)	3.10		0.16		0.16	

in the interesting works done by White, Castelletto, and Tchelepi [194] and Kim [278], where the relationship of the operator-split solvers (fixed stress split [279]; adiabatic split [280]) can be exploited for the pre-conditioners. The improvement of preconditioning strategy for thermo-hydro-mechanical formulation will be considered in the future. Nevertheless, based on the evidences collected from the numerical experiments, even the simple preconditioning strategy in (5.6) has already provided significant improvement in efficiency for THM solvers. In these numerical tests, we adopt the thawing consolidation problem as a benchmark to evaluate the efficiency of the preconditioning strategy within the infinitesimal deformation range. The detailed problem descriptions are provided in Section 2.5.1. Due to the difference in scales of the tangential term with respect to the displacement (e.g. tangential stiffness), pore pressure (e.g. hydraulic conductivity) and temperature (e.g. thermal conductivity), the thawing consolidation may lead to a highly nonlinear problem whose consistent tangents can be very ill-conditioned (i.e. with a very high condition number).

To evaluate the efficiency of different preconditioning strategies, we first introduce a coarse mesh (the total number of unknowns is 120 with 72 degrees of freedoms for displacement, 24 for liquid water pressure and another 24 for the temperature fields) and solve the corresponding system of equations with and without applying the pre-conditioners. The number of iterations required to obtain the converged solution from the solver without any no-preconditioning strategy is compared against the counterparts

Table 5.2: Residence norm (square root of the inner product of residual column vector) and the number of Krylov iterations at the selected Newton steps for comparison of pre-conditioning strategy (refined mesh condition with the total degrees of freedom 420) – No preconditioning case does not yield converged solution within 50,000 iterations with the same tolerance (10^{-9})

Newton Steps	Diagonal Preconditioning		Current Preconditioning	
	RHS norm	Krylov Iteration	RHS norm	Krylov Iteration
Trial Step	1.6E-02	38	1.6E-02	13
Iteration 1	1.6E-01	19	1.6E-01	15
Iteration 5	1.9E-03	16	1.9E-03	13
Iteration 10	7.4E-10	17	7.4E-10	13
Solve time (s)	10.2		5.28	

in which two different preconditioning strategies are used (Table 5.1). For comparison purposes, in addition to the pre-conditioner introduced in (5.7), we implement a simpler block-diagonal pre-conditioner where each diagonal block is separately inverted and no Schur-complement approximation is introduced, which is one of the simplest approaches one might use in practice. The preconditioining strategy for the current study saves the calculation time by reducing the Krylov iterations. Regardless of whether a preconditioner is used, the norm of the residual obtained after each Newton iteration step is identical as expected. Although there is no significant difference between the diagonal and current preconditioning strategies, the number of Krylov iterations is significantly reduced in both cases – an indication that both pre-conditioners are effective for this simple problem.

To analyze how mesh refinement affects the performance of the pre-conditioners, we re-run the numerical experiments with a finer mesh (the total number of unknowns is 420 with 252 degrees of freedoms for displacement, 84 for liquid water pressure and another 84 for the temperature fields). In this case, the solver without any pre-conditioner does not yield converged solution within 50,000 iterations with the same tolerance (10^{-9}). However, the solvers equipped with either pre-conditioner is still able to deliver converged solution, as shown in Table 5.2. This result also indicates that the pre-conditioner in (5.7)

146

outperforms the simpler diagonal pre-conditioner. It requires less Krylov iterations in each Newton-Raphson step and is approximately 48% faster. Both numerical experiments indicate the importance of pre-conditioners on the solver performance.

5.2.3 Operator-split solution strategies

Due to nonlinearity and path-dependence nature of the proposed model, linearizing the system of equations is necessary if an implicit solver is used. In this work, the system of equations is multi-physical. As a result, this system of equations can be solved either in a monolithic or operator-split manner [193, 194]. As previously numerical experiments with single phase-field problems show that the operator splitting approach may potentially be more robust [125, 165], we propose a semi-split iterative strategy. In this procedure, the multiple phase fields are advanced followed by the thermo-mechanical solver, which updates the displacement and temperature fields together. These sub-systems are iteratively updated until all the residuals are below the tolerance.

In the proposed operator-split setting, the crack driving force $\mathcal{H}_i$ (3.50) is fixed while the multiple phase-fields are updated. As a result, the split multi-phase-field incremental problem becomes linear. The schematic of solution strategies is summarized as follows:

$$
\begin{bmatrix} \boldsymbol{u}_n \\ \theta_n \\ \underline{d}_n \end{bmatrix} \xrightarrow[\delta \underline{d}=0]{\mathcal{R}(\boldsymbol{u},\theta)=\mathbf{0}} \underbrace{\begin{bmatrix} \boldsymbol{u}_{n+1} \\ \theta_{n+1} \\ \underline{d}_n \end{bmatrix}}_{\text{Iterative solver}} \overbrace{\xrightarrow[\delta \boldsymbol{u}=0,\ \delta\theta=0]{\mathcal{R}(\underline{d})=\underline{0} \text{ with } \underline{\mathcal{H}}_{n+1}} \begin{bmatrix} \boldsymbol{u}_{n+1} \\ \theta_{n+1} \\ \underline{d}_{n+1} \end{bmatrix}}^{\text{Linear solver}},
\tag{5.8}
$$

where $\mathcal{R}(\boldsymbol{u},\theta)$ and $\mathcal{R}(\underline{d})$ are residuals expressed as follows:

$$
\mathcal{R}(\boldsymbol{u},\theta) :=
$$

$$
\begin{cases}
\displaystyle \int_{\mathcal{B}} \nabla \boldsymbol{\eta} : \boldsymbol{\sigma}_{n+1} dV - \int_{\partial \mathcal{B}} \boldsymbol{\eta} \cdot \bar{\boldsymbol{t}}_{n+1} d\Gamma, \\[2ex]
\displaystyle \int_{\mathcal{B}} \psi c_v \left(\frac{\theta_{n+1} - \theta_n}{\Delta t} \right) dV - \int_{\mathcal{B}} \psi \left[\sum_\alpha (\pi_n^\alpha \left(\frac{\gamma_n^\alpha - \gamma_{n-1}^\alpha}{\Delta t} \right) + g_n^\alpha \left(\frac{s_n^\alpha - s_{n-1}^\alpha}{\Delta t} \right) \right] dV \\[2ex]
\displaystyle - \int_{\mathcal{B}} \psi \left[3\alpha K \boldsymbol{I} : \left(\frac{\boldsymbol{\epsilon}_n^e - \boldsymbol{\epsilon}_{n-1}^e}{\Delta t} \right) \right] \theta_{n+1} dV + \int_{\mathcal{B}} \nabla \psi \cdot \kappa \nabla \theta_{n+1} dV - \int_{\partial \mathcal{B}} \psi \bar{q}_{n+1} d\Gamma,
\end{cases}
$$

$$
\tag{5.9}
$$

$$
\mathcal{R}(d_i) :=
$$

$$
\left\{ \int_{\mathcal{B}} \phi_i \left[2(1 - d_{i_{n+1}}) \mathcal{H}_{i_{n+1}} \right] dV + \int_{\mathcal{B}} \frac{G_c}{l} \left[\phi_i d_{i_{n+1}} + l^2 \nabla \phi_i \cdot \boldsymbol{\omega}_i \cdot \nabla d_{i_{n+1}} \right] dV. \tag{5.10}
$$

These equations are consistent with (3.73) to (3.75), in which the backward Euler method is used for time discretization for heat transfer. Under the iterative solver in (5.8), the solutions are advanced followed by Algorithm 3. This procedure requires the consistent

---

Algorithm 3 Solution strategies using iterative and linear solvers

---

Require: Compute $\boldsymbol{u}_{n+1}$, θ_{n+1}, and $\underline{d}_{n+1}$

1: Initialize: $k = 0$, $\boldsymbol{u}^k = \boldsymbol{u}_n$, $\theta^k = \theta_n$, and fix $\underline{d}_n$

2: **while** $\| \mathcal{R}(\boldsymbol{u}, \theta) \| \geq$ Tolerance **do**

3:     Compute $\Delta \boldsymbol{u}$, $\Delta \theta$:
$$
\delta \mathcal{R}(\boldsymbol{u}, \theta) \begin{bmatrix} \Delta \boldsymbol{u} \\ \Delta \theta \end{bmatrix} = -\mathcal{R}(\boldsymbol{u}, \theta)
$$

4:     Update $\boldsymbol{u}^{k+1}$, θ^{k+1}
$$
\begin{bmatrix} \boldsymbol{u}^{k+1} \\ \theta^{k+1} \end{bmatrix} = \begin{bmatrix} \boldsymbol{u}^k \\ \theta^k \end{bmatrix} + \begin{bmatrix} \Delta \boldsymbol{u} \\ \Delta \theta \end{bmatrix}
$$

5: **end while**

6: $\boldsymbol{u}_{n+1} \leftarrow \boldsymbol{u}^{k+1}$, $\theta_{n+1} \leftarrow \theta^{k+1}$

7: Update: $\underline{\mathcal{H}}_{n+1}$ using updated $\boldsymbol{u}_{n+1}$ and θ_{n+1}

8: Compute $\underline{d}_{n+1}$ by solving the linear problems of multiple phase-field variables

9: **end**

---

tangent $\delta \mathcal{R}$ of the operator-split sub-problem, which is described in the following section. To obtain the incremental updates of the multiple phase fields, the updated $\mathcal{H}_i$ from the displacement and temperature variables at time t_{n+1} is incorporated into the linear phase field solver. We then update the phase-field variables as in (5.8). To simplify the implementation, the temporal discretization of plastic dissipation and structural heating, i.e.,

the term $D_{\mathrm{mech}} - H_\theta$ in (3.38) is treated explicitly. As shown in previous work such as Wang and Sun [29, 30] and Wang and Sun [155], this semi-implicit approach can be effective if used properly. Finally, it should be noticed that one may choose other partition strategies to solve the same system of equations. For instance, the thermo-mechanical problem can also be solved using an isothermal or adiabatic approach. The exploration of different partition strategies and the construction of the proper pre-conditioners are important subjects but are out of the scope of this dissertation.

5.3 Nonlocality and adaptive mesh refinement

The nonlocal Cam-Clay model is presented associated with micromorphic settings. Starting from the critical state plasticity theory [281, 282], the regularization is achieved by considering global and local internal variables linked by penalty term in a modified hardening equation in the local constitutive model. The global and local internal variables are then resolved together via the modified Helmholtz equation which adopts a plastic length scale introducing size effect (e.g. Aldakheel [148], Forest [283], Miehe, Teichtmeister, and Aldakheel [284], and Miehe, Aldakheel, and Teichtmeister [285]). This numerical framework that connects the local and global internal variables may guide us to establish a new nonlocal constitutive model base upon the existing local plasticity model. By leveraging the nonlocal constitutive laws, we then develop adaptive mesh refinement to enhance computational efficiency based on configurational force and Lie algebra. Therefore, the adaptive mesh refinement near the critical regions (i.e. shear, compaction, and dilation bands in sand, clay, and rocks) is an efficient tool for the strain localization problems (cf. Ortiz and Quigley IV [286], Verfürth [287], and Schrefler, Secchi, and Simoni [288]), provided the regularized material responses are achieved based on a nonlocal model. Here our focus lies on how to properly perform the mesh refinement on problems involving history dependent materials (cf. Ortiz and Quigley IV [286]).

5.3.1 Micromorphic approach for nonlocal critical state plasticity

The local constitutive model for plasticity or damage under softening behavior exhibits the pathological mesh dependence in finite element implementations. In other words, the size of finite elements by spatial discretization controls the deformation localization zones. One of the approaches that can resolve this issue is to use the gradient plasticity model that constrains the width of localization zone by utilizing the plastic length scale, which influences the plastic dissipation. Here we construct this gradient plasticity model based upon the existing critical state plasticity law, the modified Cam-Clay [282], by leveraging the micromorphic regularization approach.

The main difference between the local and nonlocal modified Cam-Clay models lies in the hardening equation. In order to describe the nonlocal constitutive law, we start from the yield surface equation, that is, a two-invariant yield surface for plastic response based upon the effective stress ($\boldsymbol{\sigma}'$),

$$f_y = \frac{q^2}{M^2} + p'(p' - p'_c) = 0. \tag{5.11}$$

Here $p'_c < 0$ is a plastic internal variable determining the size of yield surface, that is known as the preconsolidation pressure. The mean normal stress p' and deviatoric stress q are defined by,

$$p' = \frac{1}{3}\operatorname{tr}(\boldsymbol{\sigma}'), \quad q = \sqrt{\frac{2}{3}} \parallel \boldsymbol{s} \parallel, \quad \boldsymbol{s} = \boldsymbol{\sigma}' - p'\boldsymbol{I}. \tag{5.12}$$

In this theory, the hardening law for the current model takes the form,

$$\dot{p}'_c = -\frac{\dot{\varepsilon}^p_v}{c_c - c_r} p'_c, \tag{5.13}$$

under the condition of $0 < c_r < c_c$, which accommodates the bilogarithmic relationship between the specific volume and the preconsolidation pressure. ϵ^p_v indicates the plastic

volumetric strain.

For the nonlocal constitutive model, we express the hardening equation as a residual form that is considered as an additional equation in the local nonlinear system. Base upon the given exact expression of the hardening parameter p'_c, we extend this relation to link the local internal variable ($\bar{\alpha} \equiv p'_c$) and the global micromorpihc variable (α). Introducing the penalty parameter [148] leads to the discrete hardening equation expressed as a residual form,

$$f_r = p'_c - p'_{c,old} \exp\left(\frac{\varepsilon_v^e - \varepsilon_v^{e\ \text{trial}}}{c_c - c_r}\right) + \epsilon_p(\bar{\alpha} - \alpha) = 0. \tag{5.14}$$

Here we note again that the local internal variable $\bar{\alpha}$ is equal to p'_c, which is linked to the global micromorphic variable α by the penalty parameter ϵ_p. The local nonlinear system of equations, therefore, is assembled by the local residual vector ($\boldsymbol{r}$) and the unknown vector ($\boldsymbol{x}$),

$$\boldsymbol{r} = \begin{Bmatrix} \varepsilon_v^e - \varepsilon_v^{e\ \text{trial}} + \Delta\lambda\partial_{p'}f \\ \varepsilon_s^e - \varepsilon_s^{e\ \text{trial}} + \Delta\lambda\partial_{q'}f \\ f_y \\ f_r \end{Bmatrix} ; \quad \boldsymbol{x} = \begin{Bmatrix} \varepsilon_v^e \\ \varepsilon_s^e \\ \Delta\lambda \\ p'_c \end{Bmatrix} ; \quad \boldsymbol{a} = \boldsymbol{r}'(\boldsymbol{x}), \tag{5.15}$$

which is solved by a local Newton's iteration approach. More details about the process of the return mapping algorithm and calculation of the Jacobian can be found from the previous works [54, 61].

With these two local and global internal variables in mind, the micromorphic regularization setting is constructed by formulating the modified Helmholtz equation,

$$\alpha - l_p^2\Delta\alpha = \bar{\alpha}. \tag{5.16}$$

This additional governing equation connects both the local internal variable $\bar{\alpha} = p'_c$ and

the micromorphic variable α associated with the plastic length scale l_p, which prevents mesh sensitivity of the materials under the strain localization phenomena. The associated Neumann boundary condition of the micromorphic equation is used in the form,

$$\nabla \alpha \cdot \boldsymbol{n} = 0 \ \text{ on } \ \partial \mathcal{B}. \tag{5.17}$$

By constructing the hardening relation in local plasticity model associated with the micromorphic regularization setting, we establish the nonlocal critical state plasticity model. In other words, this approach may shed light on easily establishing nonlocal models based upon the Cam-clay type constitutive laws.

This micromorphic setting can be combined with the existing governing equations. Associated with the u-p formulation for saturated porous media (e.g. White and Borja [209]), for example, the modified Helmholtz equation (5.16) is augmented as an additional governing equation. In this case, we may write the local forms of the balance equations as,

$$\nabla \cdot (\boldsymbol{\sigma}' - p\boldsymbol{I}) + \rho\boldsymbol{g} = \boldsymbol{0} \ \ \text{(Momentum Balance)}. \tag{5.18}$$

$$\nabla \cdot \dot{\boldsymbol{u}} + \nabla \cdot \left(-\frac{1}{\rho_f g} \boldsymbol{k} \cdot \nabla p \right) = 0 \ \ \text{(Mass Balance)}. \tag{5.19}$$

$$\alpha - l_p^2 \Delta \alpha = \bar{\alpha} \ \ \text{(Micromorphic Regularization)}. \tag{5.20}$$

Here, $\boldsymbol{\sigma}$ = effective Cauchy stress tensor, p = excess pore pressure, $\boldsymbol{I}$ = second-order unit tensor, $\boldsymbol{u}$ = displacement field for the solid matrix, ρ = density of the mixture in the saturating fluid, $\boldsymbol{g}$ = vector of gravity accelerations, $\boldsymbol{k}$ = tensor of hydraulic conductivities, ρ_f = density of the fluid phase, and $g = \parallel \boldsymbol{g} \parallel$.

The operator-split solution strategy (cf. Section 5.2.3) is adopted to solve the problem. To be specific, the momentum and mass balance equations are advanced monolithically followed by the micromorphic regularization equation. This approach simplifies the

Micromorphic Regularization

$$\alpha - l_p^2 \Delta\alpha = \bar{\alpha}$$

Global Iteration
(Eqns. 5.18 ~ 5.20)

Discrete Hardening Equation

$$p_c' - {p'}_{c,old}\exp\left(\frac{\varepsilon_v^e - \varepsilon_v^{e\;trial}}{c_c - c_r}\right) + \epsilon_p(\bar{\alpha} - \alpha) = 0$$

Local Iteration
(Eqn. 5.15)
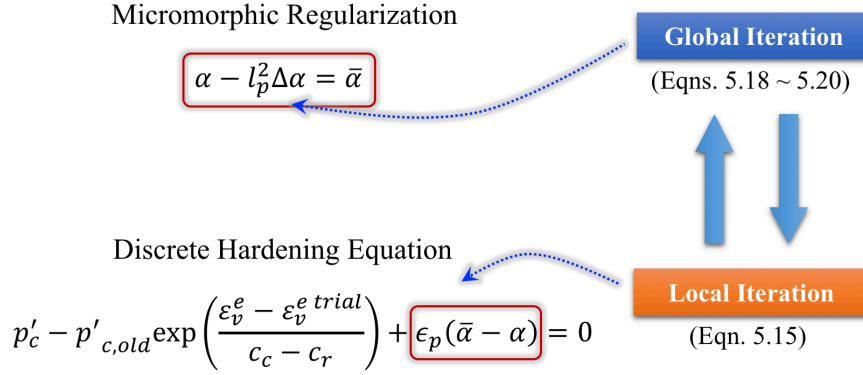
Figure 5.2: The conceptual illustration of the interaction between the local ($\bar{\alpha}$) and global (α) variables

derivation of the local Jacobian for Newton's iteration and the global consistent linearization procedure. Therefore, the finite element discretization of (5.18) and their linearization are straightforward because no couplings need to be constructed under the micromorphic setting. Note that the equal-order finite element approach is adopted, where we use the stabilization scheme to resolve inf-sup deficiency under undrained condition by White and Borja [209]. Figure 5.2 conceptually describes how the global and local iterations are connected.

5.3.2 Recovery of internal variables using Lie-group interpolation

We then leverage the nonlocal constitutive laws via adaptive mesh refinement to enhance computational efficiency. While increasing the number of degrees of freedom is an obvious remedy to improve the quality of finite element solutions (e.g. Díaz, Kikuchi, and Taylor [289]), this approach naturally demands the more computational resources and is inefficient to capture the localization of deformation. Furthermore, modeling strain localization with conventional finite element method often leads to pathological mesh dependence by strain softening (e.g. Needleman [226]). Therefore, the adaptive mesh refinement near the critical regions (i.e. shear, compaction, and dilation bands in sand, clay,

and rocks) is an efficient tool for the strain localization problems (cf. Ortiz and Quigley IV [286], Verfürth [287], and Schrefler, Secchi, and Simoni [288]), provided the regularized material responses are achieved based on a nonlocal model. Here our focus lies on how to properly perform the mesh refinement on problems involving history dependent materials (cf. Ortiz and Quigley IV [286]). In order to describe the adaptive meshing procedure, we address the three key components, that is, 1) mesh refinement criteria, 2) transfer of internal variables (i.e. tensor variables), and 3) reestablish of equilibrium.

The first key issue for an adaptive meshing scheme is the calculation of a suitable criteria for mesh refinement. This problem is closely related to how to identify the critical regions or singularities, such as strain localization and fracture, where the accuracy of finite element approximation is diminished. In this study, the adaptive meshing criterion is set the configurational force, or equally termed material force. We consider the case of small strains, the Newton-Eshelby stress ($\boldsymbol{\Sigma}$) is defined based upon the effective stress as [290],

$$\boldsymbol{\Sigma} := W\boldsymbol{I} - \boldsymbol{H}^{\mathrm{T}} \cdot \boldsymbol{\sigma}', \tag{5.21}$$

where $\boldsymbol{H}(\boldsymbol{u}) = \boldsymbol{u} \otimes \nabla_X$ and W is the strain energy density. The discrete configurational force is obtained [291, 292] as,

$$\boldsymbol{G}^I = \int_{\mathcal{B}_e} \boldsymbol{\Sigma} \cdot \boldsymbol{D} dV \tag{5.22}$$

Note that $\boldsymbol{D} = \nabla_X \lambda_a$ indicates the gradient of the test function. The discrete material forces are obtained from the existing solutions at the equilibrium state. In other words, the force calculation can be considered as a post-processing procedure. For adaptive mesh refinement, we can set the criteria by adopting the absolute value of $G^I = |\boldsymbol{G}^I|$, where $|\cdot|$ indicates L^2 norm of a vector.

To properly recover and update the internal variables, next, we compute the spectral decomposition of the tensor and obtain the logarithms of the rotation and stretch compo-

nent separately. In other words, we choose an internal variable, for example, the plastic strain, and construct the rotation tensor using the eigenvectors. The eigenvalues give rise to the stretch components. For the rotation tensor, we perform the logarithmic mapping that leads to a skew-symmetric tensor. The eigenvalues and each component of the skew-symmetric tensor are then projected onto a new mesh considered as a scalar value. The interpolated components of the skew-symmetric tensor are projected back to reconstruct the rotation tensor via the exponential mapping. The projected tensorial internal variables are then recovered based upon the reestablished eigenvalues and eigenvectors.

The logarithm of a rotation tensor can be computed using the explicit formulas [160, 293]. Firstly, the angle of rotation (θ) is obtained by,

$$\theta := \cos^{-1}\left[\frac{1}{2}(\operatorname{tr}\boldsymbol{R} - 1)\right], \quad \boldsymbol{R} \in SO(3), \quad \theta \in [0, \pi]. \tag{5.23}$$

Depending on the θ, the logarithm of the rotation is determined as follows,

$$\log \boldsymbol{R} = \begin{cases} \boldsymbol{0} & \text{if } \theta = 0, \\ \dfrac{\theta}{2\sin\theta}\left(\boldsymbol{R} - \boldsymbol{R}^{\mathrm{T}}\right) & \text{if } \theta \in (0, \pi), \\ \pm\,\pi\check{\boldsymbol{v}} & \text{if } \theta = 0, \end{cases} \tag{5.24}$$

Here $\check{\boldsymbol{v}}$ is the skew-symmetric tensor such that $\check{\boldsymbol{v}}\cdot\boldsymbol{u} \equiv \boldsymbol{v}\times\boldsymbol{u} \ \forall\boldsymbol{u} \in \mathbb{R}^3$, $\boldsymbol{v}$ is the eigenvector corresponding to the eigenvalue of 1 of $\boldsymbol{R}$, and the sign is selected according to continuity from the field in the neighborhood. The exponential map can be explicitly expressed likewise the logarithm [160, 293]. Assuming the $\boldsymbol{W} \in SO(3)$, we define the angle of rotation as follows,

$$\theta := \left(\frac{\boldsymbol{W} : \boldsymbol{W}}{2}\right)^{\frac{1}{2}}. \tag{5.25}$$

The exponential map for the skew-symmetric tensor $\boldsymbol{W}$ then is given by the following
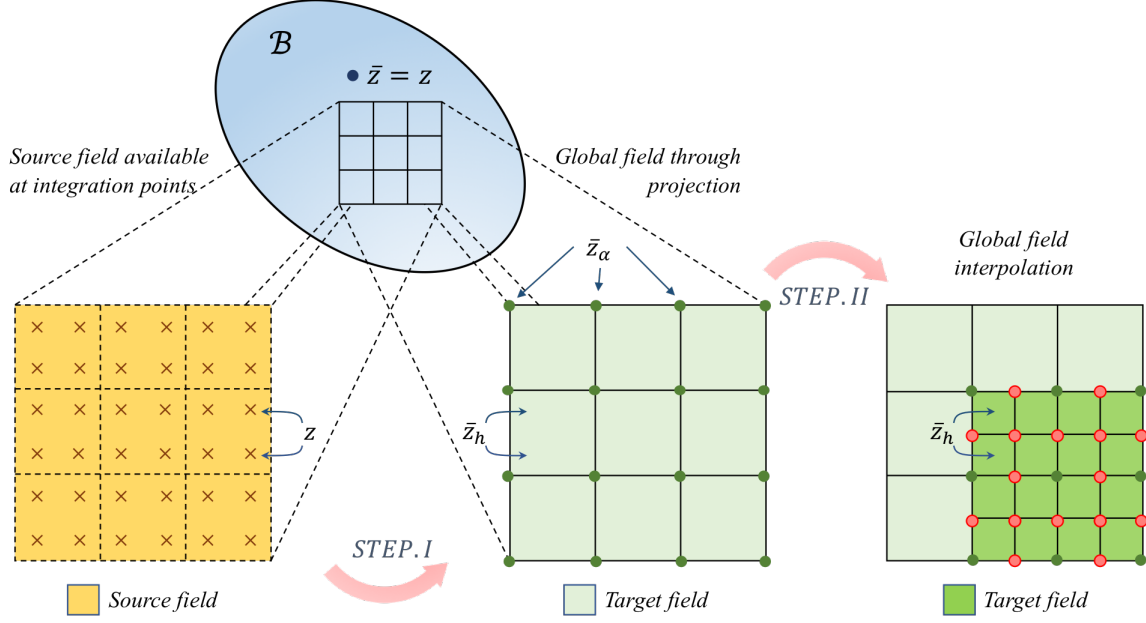
Figure 5.3: The projection of integration field z into the nodal values of the discrete target field $\bar{z}_h$ in the existing (STEP.I) and refined meshes (STEP.II)

expression,

$$
\exp \boldsymbol{W} = \begin{cases} \boldsymbol{I}, & \text{if } \theta = 0, \\ \boldsymbol{I} + \dfrac{\sin\theta}{\theta}\boldsymbol{W} + \dfrac{(1-\cos\theta)}{\theta^2}\boldsymbol{W}^2, & \text{if } \theta > 0, \end{cases} \tag{5.26}
$$

The projection of the components, the logarithms of the rotation and stretch components, are conducted using L_2 projection. As proved in Mota et al. [160], the projection of internal variables using L_2 is derived naturally based upon the variational approach. Furthermore, the global L_2 projection leads to smooth linear field, which is identical to the linear least squares regression of the nodal values of the original source field [160]. The recovery of target field $\bar{z}_h$ by nodal values $\bar{z}_\alpha$, the interpolation functions λ_α, and the

source field z can be expressed by,

$$\bar{z}_h(\boldsymbol{X}) := \lambda_\alpha(\boldsymbol{X})\bar{z}_\alpha$$

$$\bar{z}_h = \lambda_\alpha \left(\int_{\mathcal{B}} \lambda_\alpha \lambda_\beta \boldsymbol{I} dV \right)^{-1} \int_{\mathcal{B}} \lambda_\beta z dV. \tag{5.27}$$

For effective computational of the integrals, the interpolation functions λ_α and λ_β are adopted using the shape functions [160]. Figure 5.3 describes the concept of the projection procedure. The projection of scalar internal variables, therefore, is straight forward.

Lastly, the reestablishment of equilibrium then completes the adaptive mesh refinement process. Our strategy is to project either elastic or plastic strain tensor based upon the additive decomposition of the total strain ($\epsilon = \epsilon^e + \epsilon^p$). As the total strains are recovered by the symmetric gradient of the displacement fields, which are always nodal values, the projection of plastic strain tensors result in the elastic strain tensors and vice versa. To sum up, the mesh refinement process can be summarized as follows:

Algorithm 4 Establishment of equilibrium in adaptive meshing process
---
Require: Numerical simulation is converged to equilibrium at the numerical step n:
  1: Compute the magnitude of configurational forces and screening the mesh refinement criteria (post-processing in the step n)
  2: **if** the criteria is satisfied **then**
   a. refine the mesh for the elements satisfying the criteria
   b. project the internal variables
   c. interpolate them on to the new mesh
   d. construct the system of equations
   e. reestablish the equilibrium at the step n
  3: **else**
   no refinement process is triggered
  4: **end if**
  5: Move on to the next step $n + 1$

As an example of numerical simulations, we construct a boundary value problem which is a vertical cut depicted in Figure 5.4. To lead the strain softening behavior, the initial over consolidation ratio (OCR) parameter is set to 3.33. This example illustrates that the results of numerical simulation show consistent behavior under the different mesh

conditions constructed by the different number of refinement. In other words, we not only observe the mesh dependence is circumvented, but identify that adaptive meshing process is performed properly.
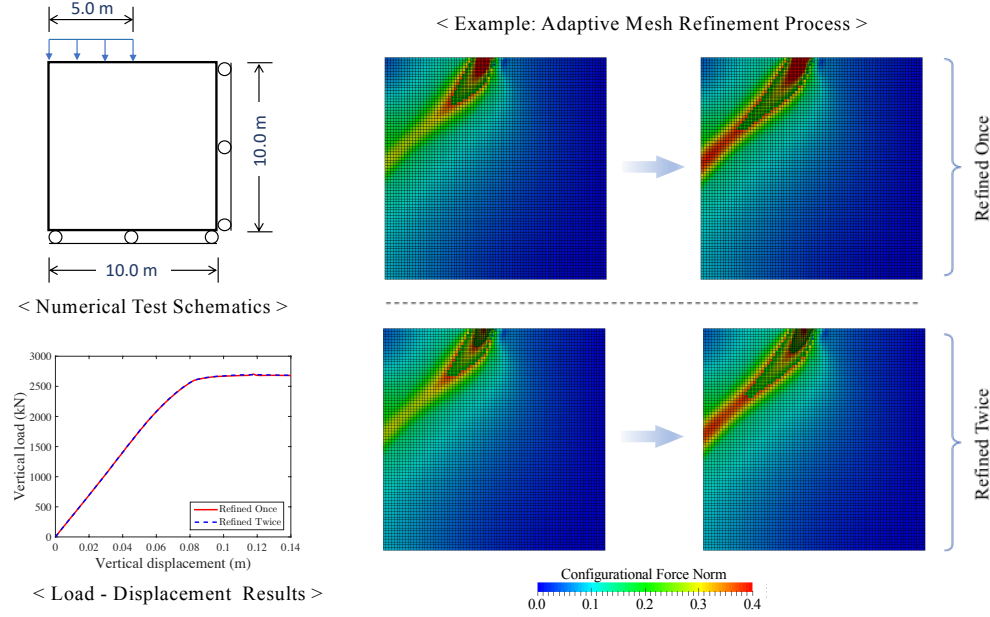
Figure 5.4: Numerical examples (vertical cut) that show the consistent results of the proposed numerical techniques under the different mesh refinement numbers: the same refinement criterion (L^2-norm of the configurational forces) is used

5.4 Conclusions

In this chapter, we address the potential numerical issues in the coupled multiphysics problem and the possible solutions to resolve those challenges. Firstly, the spurious oscillations in the liquid pressure and temperature fields are circumvented by the projection stabilization scheme associated with the weak inf-sup condition for freezing and thawing porous media at the finite deformation range. We then propose the preconditioner of the three-field thermo-hydro-mechanical system to enhance the computational efficiency, in which the performance of iterative solver, Krylov iterations, is improved. On a related is-

158

sue, the semi-implicit scheme to couple multi-field problems including damage behavior is also presented based upon the operator-split strategies. Finally, the nonlocal finite element approach associated with adaptive meshing technique is described. Our numerical methods indicate that the proposed methods are highly applicable to effectively capture the coupled thermo-hydro-mechanical-chemical behaviors including plasticity and fracture.

This page intentionally left blank.

Chapter 6

Closure

6.1 Scope and contribution

This dissertation explores theoretical and computational methods to analyze failure mechanics in geological materials associated with the coupled multiphysics processes. We develop a computational framework that incorporates the complicated physical and chemical mechanisms across different length scales by leveraging the finite element methods and corresponding constitutive laws.

In order to effectively characterize the materials, our research covers macroscopic and microscopic points of view that are selectively adopted depending on the application problems: the frozen soil is conceptualized as an effective medium; the components of rock salt are considered explicitly (e.g. gains, grain boundaries, brine inclusions, clay contents, etc.). Those features are materialized via mathematical formulations, where the governing equations are discretized and simulated based on the finite element counterparts.

In Chapter 2, the contribution on computational modeling of phase-transiting frozen porous media in macroscopic aspect begins with that, for the first time, we simulate and capture the thermo-hydro-mechanical responses of freezing and thawing soil in the finite deformation range. The mixture theory and pre-melting dynamics enable us to derive finite strain constitutive laws for the path-dependent solid, hydraulic and thermal constitutive responses. This work provides a feasible approach to model frozen porous media with

unfrozen water constituents and addresses some key theoretical and computational issues for capturing the essence of the path-dependent thermo-hydro-mechanical responses of porous media.

A cornerstone for modeling coupled thermo-hydro-mechanical-chemical behavior of polycrystalline rock salt is presented in Chapter 3. The main contribution is introducing the crystallographic information into modeling to account for the intrinsic anisotropy of salt coming from its microstructure. Our numerical framework provides numerical simulations that show qualitatively compatible physical behaviors of halite, such as rate dependence, brittle-ductile transition, anisotropic inelasticity and fracture, and thermal sensitive creep mechanism, by adopting the reduced number of material parameters. This result indicates the potential applicability of our approach for practical engineering applications, e.g., field scale problems for a geologic repository of the heat generating nuclear waste.

Subsequently, Chapter 4 describes a theoretical study for a saturated thermal sensitive porous medium, in which we investigate the coupled therm-hydro-mechanical effects on failure mechanism. Based upon the one-dimensional wave propagation setting, we evaluate the material and numerical stability of saturated porous media associated with strain softening under the non-isothermal condition. Our main contribution is evaluating the influence of thermal and hydraulic diffusivities on regularization effect and its limitation. This is analytically investigated by deriving the internal length scale as a function of permeability, specific heat, wavenumber, and other material properties

Lastly, in Chapter 5, we propose new remedies to address some major difficulties encountered in computational poromechanics problems and our strategies to resolve those issues. For monolithic mixed finite element method, we remedy the lack of two-fold inf-sup condition and improves the iterative solution scheme by proposing a preconditioning strategy for the nonlinear system of equations of the multi-component materials. Besides, we explore the semi-implicit approach that combines the monolithic and operator-split

solution strategies associated with multiphysics behavior including damage. The micromorphic approach for nonlocal critical state plasticity leveraged by adaptive meshing via Lie-algebra and configurational force further sheds light on robust computational methods for coupled multiphysics problems.

6.2   Future Perspective

This research has focused on the development, implementation, and application of a computational framework to investigate demanding challenges for resilient infrastructure systems associated with coupled multiphysics process. Although the presented numerical approaches are already capable of reproducing the coupled thermo-hydro-mechanical-chemical behavior for freezing soil or geological rock salt, there are further topics and issues that require extended development and consideration.

Regarding the frozen soil, the hysteresis loop of the freezing retention curve is often observed during the freezing and thawing cycles. This is further related to the growth of ice lens which can be associated with the existence of air and the void ratio of soil. The formation and dissipation of the ice lens, furthermore, not only influence the heaving behavior but also cause damage to the underground and the superstructure. Considering additional components of the frozen soil system with respect to fracture, dynamic behavior, and the brittle-ductile transition is a very exciting topic and possible extension of the current study.

For the rock salt, we may categorize the distinct feature of the material as follows: single crystals, clay contents, brine inclusions, and grain boundaries. While the first two components have been mainly focused on this thesis, brine inclusions and grain boundaries are essential components associated with the precipitation creep, dissolution-precipitation, pressure solution, etc. These characteristics can be also encapsulated by extending the phase-field method based upon Cahn-Hilliard equation that considers the

chemical potential functions of the rock salt. The key point lies in how to connect the chemical reaction, such as grain growth and pressure solution, to the mechanical deformation associated with the plastic or damage behavior. For a comprehensive description of rock salt, the more sophisticated and fundamental functional are needed.

Besides, combining different features based upon either homogenization theory or multi-scale approach is an integral part in analyzing geological materials like frozen soil and rock salt. The behavior of a representative volume element (RVE) with the proposed multiple grains, multiple components, and phase boundaries may be considered as a sub-scale model for field-scale geomaterials. The data-driven approach and off-line multiscale technique is a potential tool to be used to link microscopic responses to macroscopic scales. This systematic method enables us to have proper multiscale multiphysical computational models that capture coupled thermo-hydro-mechanical-chemical effects for fluid-infiltrating partially crystalline geological materials based on its microstructural information.

Finally, my future research application areas may include (1) modeling multi-physics processes in soil, rocks, and granular media under extreme climate events, (2) earth resource engineering and assessment of hazards caused by natural and/or induced seismicity, geologic CO_2 sequestration, and nuclear waste storage, (3) dynamics of deep-geosystems, coastal systems, and off-shore systems for energy production and resilient infrastructure, (4) analytical, experimental, and numerical study of soil-structure interactions, (5) data analytics and machine learning for geomaterial and geostructure characterizations, and (6) geomechanical simulations with multi-phase groundwater flow and reactive transport processes.

Bibliography

[1] A. Schofield and P. Wroth. *Critical state soil mechanics.* Vol. 310. McGraw-Hill London, 1968.

[2] Y. F. Dafalias. "An anisotropic critical state soil plasticity model." *Mechanics Research Communications* 13.6 (1986), pp. 341–347.

[3] M. A. Mooney, R. J. Finno, and M. G. Viggiani. "A unique critical state for sand?" *Journal of Geotechnical and Geoenvironmental Engineering* 124.11 (1998), pp. 1100–1108.

[4] J. M. Pestana and A. Whittle. "Compression model for cohesionless soils." *Géotechnique* 45.4 (1995), pp. 611–631.

[5] H. I. Ling et al. "Anisotropic elastoplastic bounding surface model for cohesive soils." *Journal of engineering mechanics* 128.7 (2002), pp. 748–758.

[6] S. A. Shoop and S. R. Bigl. "Moisture migration during freeze and thaw of unsaturated soils: modeling and large scale experiments." *Cold Regions Science and Technology* 25.1 (1997), pp. 33–45.

[7] O. Coussy. "Poromechanics of freezing materials." *Journal of the Mechanics and Physics of Solids* 53.8 (2005), pp. 1689–1718.

[8] A. W. Rempel, J. Wettlaufer, and M. G. Worster. "Premelting dynamics in a continuum model of frost heave." *Journal of Fluid Mechanics* 498 (2004), pp. 227–244.

[9] S. Shoop et al. "Mechanical behavior modeling of thaw-weakened soil." *Cold Regions Science and Technology* 52.2 (2008), pp. 191–206.

[10] D. Wisser et al. "Soil temperature response to 21st century global warming: the role of and some implications for peat carbon in thawing permafrost soils in North America." *Earth System Dynamics* 2.1 (2011), pp. 121–138.

[11] R. L. Michalowski and M. Zhu. "Frost heave modelling using porosity rate function." *International journal for numerical and analytical methods in geomechanics* 30.8 (2006), pp. 703–722.

[12] S. Nishimura et al. "THM-coupled finite element analysis of frozen soil: formulation and application." *Géotechnique* 59.3 (2009), pp. 159–171.

[13] H. L. Jessberger. "Theory and application of ground freezing in civil engineering." *Cold Regions Science and Technology* 3.1 (1980), pp. 3–27.

[14] J. M. McKenzie, C. I. Voss, and D. I. Siegel. "Groundwater flow with energy transport and water–ice phase change: numerical simulations, benchmarks, and application to freezing in peat bogs." *Advances in water resources* 30.4 (2007), pp. 966–983.

[15] O. Coussy and P. Monteiro. "Unsaturated poroelasticity for crystallization in pores." *Computers and Geotechnics* 34.4 (2007), pp. 279–290.

[16] A. Belotserkovets and J. Prévost. "Thermoporoelastic response of a fluid-saturated porous sphere: An analytical solution." *International Journal of Engineering Science* 49.12 (2011), pp. 1415–1423.

[17] M. Zhou and G. Meschke. "A three-phase thermo-hydro-mechanical finite element model for freezing soils." *International Journal for Numerical and Analytical Methods in Geomechanics* 37.18 (2013), pp. 3173–3193.

[18] M. Mikkola and J. Hartikainen. "Mathematical model of soil freezing and its numerical implementation." *International Journal for Numerical Methods in Engineering* 52.5-6 (2001), pp. 543–557.

[19] W. Sun. "A stabilized finite element formulation for monolithic thermo-hydro-mechanical simulations at finite strain." *International Journal for Numerical Methods in Engineering* 103.11 (2015), pp. 798–839.

[20] S. Na and W. Sun. "Wave propagation and strain localization in a fully saturated softening porous medium under the non-isothermal conditions." *International Journal for Numerical and Analytical Methods in Geomechanics* (2016).

[21] A. Gens. "Soil–environment interactions in geotechnical engineering." *Géotechnique* 60.1 (2010), pp. 3–74.

[22] J. Wettlaufer and M. G. Worster. "Premelting dynamics." *Annu. Rev. Fluid Mech.* 38 (2006), pp. 427–452.

[23] K. S. Henry. *A review of the thermodynamics of frost heave*. Tech. rep. DTIC Document, 2000.

[24] O. C. Zienkiewicz et al. *Computational geomechanics*. Wiley Chichester, 1999.

[25] W. Ehlers and J. Bluhm. *Porous media: theory, experiments and numerical applications.* Springer Science & Business Media, 2013.

[26] H. Wang. *Theory of linear poroelasticity with applications to geomechanics and hydrogeology.* Princeton University Press, 2000.

[27] L. Dormieux, D. Kondo, and F.-J. Ulm. *Microporomechanics.* John Wiley & Sons, 2006.

[28] K. Wang and W. Sun. "Anisotropy of a Tensorial Bishop's Coefficient for Wetted Granular Materials." *Journal of Engineering Mechanics* (2015), B4015004.

[29] K. Wang and W. Sun. "A semi-implicit discrete-continuum coupling method for porous media based on the effective stress principle at finite strain." *Computer Methods in Applied Mechanics and Engineering* 304 (2016), pp. 546–583.

[30] K. Wang and W. Sun. "A semi-implicit micropolar discrete-to-continuum method for granular materials." *Proceedings of European Congress on Computational Methods in Applied Science and Engineering, Papadrakakis M, Papadopoulos V, Stefanou G, Plevris V (eds.), June, Crete Island.* 2016, pp. 5–10.

[31] A. Bishop and G. Blight. "Some aspects of effective stress in saturated and partly saturated soils." *Géotechnique* 13.3 (1963), pp. 177–197.

[32] D. Fredlund and H. Rahardjo. *Soil mechanics for unsaturated soils.* John Wiley & Sons, 1993.

[33] M. Frémond and F. Maceri. *Mechanics, Models and Methods in Civil Engineering.* Vol. 61. Springer Science & Business Media, 2011.

[34] B. Schrefler. "The finite element method in soil consolidation." PhD thesis. University College of Swansea, 1984.

[35] K. O'Neill. "The physics of mathematical frost heave models: A review." *Cold Regions Science and Technology* 6.3 (1983), pp. 275–291.

[36] K. O'Neill and R. Miller. "Exploration of a rigid ice model of frost heave." *Water Resources Research* 21.3 (1985), pp. 281–296.

[37] M. M. Zhou. "Computational Simulation of Soil Freezing: Multiphase Modeling and Strength Upscaling." PhD thesis. Rubr University Bochum, 2013.

[38] L. Sanavia, B. Schrefler, and P. Steinmann. "A formulation for an unsaturated porous medium undergoing large inelastic strains." *Computational Mechanics* 28.2 (2002), pp. 137–151.

[39]   S. Diebels and W. Ehlers. "Dynamic analysis of a fully saturated porous medium accounting for geometrical and material nonlinearities." *International Journal for Numerical Methods in Engineering* 39.1 (1996), pp. 81–97.

[40]   J. Simo. "Numerical analysis and simulation of plasticity." *Handbook of Numerical Analysis* (1998), pp. 183–499.

[41]   W. Ehlers. "Foundations of multiphasic and porous materials." *Porous Media.* Springer, 2002, pp. 3–86.

[42]   L. Sanavia, F. Pesavento, and B. Schrefler. "Finite element analysis of non-isothermal multiphase geomaterials with application to strain localization simulation." *Computational Mechanics* 37.4 (2006), pp. 331–348.

[43]   W. Sun, J. T. Ostien, and A. G. Salinger. "A stabilized assumed deformation gradient finite element formulation for strongly coupled poromechanical simulations at finite strain." *International Journal for Numerical and Analytical Methods in Geomechanics* 37.16 (2013), pp. 2755–2788.

[44]   X. Song and R. I. Borja. "Mathematical framework for unsaturated flow in the finite deformation range." *International Journal for Numerical Methods in Engineering* 97.9 (2014), pp. 658–682.

[45]   J. Andrade and R. Borja. "Modeling deformation banding in dense and loose fluid-saturated sands." *Finite Elements in Analysis and Design* 43.5 (2007), pp. 361–383.

[46]   R. Michalowski. "A constitutive model of saturated soils for frost heave simulations." *Cold Regions Science and Technology* 22.1 (1993), pp. 47–63.

[47]   J. Simo and C. Miehe. "Associative coupled thermoplasticity at finite strains: formulation, numerical analysis and implementation." *Computer Methods in Applied Mechanics and Engineering* 98.1 (1992), pp. 41–104.

[48]   L. Goodrich. "An introductory review of numerical methods for ground thermal regime calculations." *Paper, Division of Building Research, National Research Council Canada* 1061 (1982), p. 32.

[49]   K. Hansson et al. "Water flow and heat transport in frozen soil." *Vadose Zone Journal* 3.2 (2004), pp. 693–704.

[50]   J. Côté and J.-M. Konrad. "A generalized thermal conductivity model for soils and construction materials." *Canadian Geotechnical Journal* 42.2 (2005), pp. 443–458.

[51]   G. Taylor and H. Quinney. "The latent energy remaining in a metal after cold working." *Proceedings of the Royal Society of London. Series A, Containing Papers of a Mathematical and Physical Character* 143.849 (1934), pp. 307–326.

[52]   L. Stainier and M. Ortiz. "Study and validation of a variational theory of thermo-mechanical coupling in finite visco-plasticity." *International Journal of Solids and Structures* 47.5 (2010), pp. 705–715.

[53]   M. Arriaga, C. McAuliffe, and H. Waisman. "Instability analysis of shear bands using the instantaneous growth-rate method." *International Journal of Impact Engineering* 87 (2016), pp. 156–168.

[54]   R. Borja and C. Tamagnini. "Cam-Clay plasticity Part III: Extension of the infinitesimal model to include finite strains." *Computer Methods in Applied Mechanics and Engineering* 155.1 (1998), pp. 73–95.

[55]   C. Callari, F. Auricchio, and E. Sacco. "A finite-strain Cam-clay model in the framework of multiplicative elasto-plasticity." *International Journal of Plasticity* 14.12 (1998), pp. 1155–1187.

[56]   D. Gallipoli et al. "An elasto-plastic model for unsaturated soil incorporating the effects of suction and degree of saturation on mechanical behaviour." *Géotechnique.* 53.1 (2003), pp. 123–136.

[57]   R. Nova, R. Castellanza, and C. Tamagnini. "A constitutive model for bonded geomaterials subject to mechanical and/or chemical degradation." *International Journal for Numerical and Analytical Methods in Geomechanics* 27.9 (2003), pp. 705–732.

[58]   C. Tamagnini, R. Castellanza, and R. Nova. "A generalized backward Euler algorithm for the numerical integration of an isotropic hardening elastoplastic model for mechanical and chemical degradation of bonded geomaterials." *International Journal for Numerical and Analytical Methods in Geomechanics* 26.10 (2002), pp. 963–1004.

[59]   A. Cuitino and M. Ortiz. "A material-independent method for extending stress update algorithms from small-strain plasticity to finite plasticity with multiplicative kinematics." *Engineering computations* 9.4 (1992), pp. 437–451.

[60]   E. A. de Souza Neto, D. Peric, and D. R. J. Owen. *Computational methods for plasticity: theory and applications.* John Wiley & Sons, 2011.

[61]   R. I. Borja. *Plasticity: modeling & computation.* Springer Science & Business Media, 2013.

[62] R. I. Borja. "On the mechanical energy and effective stress in saturated and unsaturated porous continua." *International Journal of Solids and Structures* 43.6 (2006), pp. 1764–1786.

[63] R. I. Borja, C. Tamagnini, and A. Amorosi. "Coupling plasticity and energy-conserving elasticity models for clays." *Journal of geotechnical and geoenvironmental engineering* 123.10 (1997), pp. 948–957.

[64] E. E. Alonso, A. Gens, and A. Josa. "A constitutive model for partially saturated soils." *Géotechnique* 40.3 (1990), pp. 405–430.

[65] R. Butterfield. "A natural compression law for soils (an advance on e-log p')." *Géotechnique* 29.4 (1979).

[66] K. Hashiguchi. "Elasto-plastic constitutive laws of granular materials, Constitutive Equations of Soils." *Proc. Spec. Session 9 of 9th Int. ICSMFE* (1977), pp. 73–82.

[67] K. Hashiguchi. "On the linear relations of v–ln p and ln v–ln p for isotropic consolidation of soils." *International Journal for Numerical and analytical Methods in Geomechanics* 19.5 (1995), pp. 367–376.

[68] R. Koopmans and R. Miller. "Soil freezing and soil water characteristic curves." *Soil Science Society of America Journal* 30.6 (1966), pp. 680–685.

[69] E. J. Spaans and J. M. Baker. "The soil freezing characteristic: Its measurement and similarity to the soil moisture characteristic." *Soil Science Society of America Journal* 60.1 (1996), pp. 13–19.

[70] M. T. Van Genuchten. "A closed-form equation for predicting the hydraulic conductivity of unsaturated soils." *Soil science society of America journal* 44.5 (1980), pp. 892–898.

[71] L. Luckner, M. T. Van Genuchten, and D. Nielsen. "A consistent set of parametric models for the two-phase flow of immiscible fluids in the subsurface." *Water Resources Research* 25.10 (1989), pp. 2187–2193.

[72] S. Grant. *Physical and chemical factors affecting contaminant hydrology in cold environments*. Tech. rep. DTIC Document, 2000.

[73] G. Holzapfel. *Nonlinear solid mechanics. A continuum approach for engineering*. West Sussex, England: John Wiley & Sons, Ltd, 2000.

[74] R. Borja and E. Alarcón. "A mathematical framework for finite strain elastoplastic consolidation Part 1: Balance laws, variational formulation, and linearization." *Computer Methods in Applied Mechanics and Engineering* 122.1 (1995), pp. 145–171.

[75]   S. Na and W. Sun. "Computational thermomechanics of crystalline rock, Part I: A combined multi-phase-field/crystal plasticity approach for single crystal simulations." *Computer Methods in Applied Mechanics and Engineering* (2018).

[76]   S. Zhang et al. "Analysis of frost heave mechanisms in a high-speed railway embankment." *Canadian Geotechnical Journal* 53.3 (2015), pp. 520–529.

[77]   X. Yao, J. Qi, and W. Wu. "Three dimensional analysis of large strain thaw consolidation in permafrost." *Acta geotechnica* 7.3 (2012), pp. 193–202.

[78]   C. Li, R. I. Borja, and R. A. Regueiro. "Dynamics of porous media at finite strain." *Computer methods in applied mechanics and engineering* 193.36 (2004), pp. 3837–3870.

[79]   D. Mottaghy and V. Rath. "Latent heat effects in subsurface heat transport modelling and their impact on palaeotemperature reconstructions." *Geophysical Journal International* 164.1 (2006), pp. 236–245.

[80]   D. Anderson, A. Tice, and H. McKim. "The unfrozen water and the apparent specific heat capacity of frozen soils." *North American contribution, Second international conference on Permafrost, Yakutsk, USSR., Washington D.C., National Academy of Science.* 1973, pp. 289–295.

[81]   H. Zhang, L. Sanavia, and B. Schrefler. "An internal length scale in dynamic strain localization of multiphase porous media." *Mechanics of Cohesive-frictional Materials* 4.5 (1999), pp. 443–460.

[82]   K. L. Kuhlman and B. Malama. *Brine flow in heated geologic salt (SAND2013-1944).* Tech. rep. Sandia National Labs., Albuquerque, NM (USA), 2013.

[83]   T. von Berlepsch and B. Haverkamp. "Salt as a host rock for the geological repository for nuclear waste." *Elements* 12.4 (2016), pp. 257–262.

[84]   A. Urquhart and S. Bauer. "Experimental determination of single-crystal halite thermal conductivity, diffusivity and specific heat from- 75 C to 300 C." *International Journal of Rock Mechanics and Mining Sciences* 78 (2015), pp. 350–352.

[85]   W. Bechthold et al. "Backfilling and sealing of underground repositories for radioactive waste in salt (BAMBUS-II Project)." *Commission of the European Communities, EUR* 20621 (2004).

[86]   K. Chan, S. Bodner, and D. Munson. "Recovery and healing of damage in WIPP salt." *International Journal of Damage Mechanics* 7.2 (1998), pp. 143–166.

[87]   F. D. Hansen and C. D. Leigh. *Salt disposal of heat-generating nuclear waste.* Sandia National Laboratories Albuquerque, NM, 2011.

[88]   R. Bradshaw and F. Sanchez. "Migration of brine cavities in rock salt." *Journal of Geophysical Research* 74.17 (1969), pp. 4209–4212.

[89]   E. Nowak and D. McTigue. *Interim results of brine transport studies in the Waste Isolation Pilot Plant (WIPP).* Tech. rep. Sandia National Labs., Albuquerque, NM (USA), 1987.

[90]   R. Beauheim et al. *Integrated modeling and experimental programs to predict brine and gas flow at the Waste Isolation Pilot Plant (No. SAND−94-0599C; CONF-941053−1).* Tech. rep. Sandia National Labs., Albuquerque, NM (United States), 1995.

[91]   Z. Schléder et al. "Solution-precipitation creep and fluid flow in halite: a case study of Zechstein (Z1) rocksalt from Neuhof salt mine (Germany)." *International Journal of Earth Sciences* 97.5 (2008), pp. 1045–1056.

[92]   F. Hansen et al. *Coupled Thermal-Hydrological-Mechanical Processes in Salt: Hot Granular Salt Consolidation, Constitutive Model and Micromechanics (SAND2012-9893P).* Tech. rep. Sandia National Labs., Albuquerque, NM (United States), 2012.

[93]   M. Guillope and J. Poirier. "Dynamic recrystallization during creep of single-crystalline halite: An experimental study." *Journal of Geophysical Research: Solid Earth* 84.B10 (1979), pp. 5557–5567.

[94]   N. L. Carter, F. D. Hansen, and P. E. Senseny. "Stress magnitudes in natural rock salt." *Journal of Geophysical Research: Solid Earth* 87.B11 (1982), pp. 9289–9300.

[95]   N. L. Carter and F. D. Hansen. "Creep of rocksalt." *Tectonophysics* 92.4 (1983), pp. 275–333.

[96]   J. L. Urai et al. "Weakening of rock salt by water during long-term creep." *Nature* 324.6097 (1986), pp. 554–557.

[97]   N. Carter et al. "Rheology of rocksalt." *Journal of Structural Geology* 15.9-10 (1993), pp. 1257–1271.

[98]   P. Senseny et al. "Mechanical behaviour of rock salt: phenomenology and micromechanisms." *International journal of rock mechanics and mining sciences & geomechanics abstracts.* Vol. 29. 4. Elsevier. 1992, pp. 363–378.

[99]   J. Urai et al. "Flow and transport properties of salt rocks." *Dynamics of Complex Intracontinental Basins: The Central European Basin System* (2008), pp. 277–290.

[100] F. D. Hansen et al. "Micromechanics of isochoric salt deformation." *48th US Rock Mechanics/Geomechanics Symposium.* American Rock Mechanics Association. 2014.

[101] D. E. Munson and P. Dawson. *Constitutive model for the low temperature creep of salt (with application to WIPP).* Tech. rep. Sandia National Labs., Albuquerque, NM (USA), 1979.

[102] K. Chan et al. "Constitutive representation of damage healing in WlPP salt." *The 35th US Symposium on Rock Mechanics (USRMS).* American Rock Mechanics Association. 1995.

[103] S. Miao, M. L. Wang, and H. L. Schreyer. "Constitutive models for healing of materials with application to compaction of crushed rock salt." *Journal of Engineering Mechanics* 121.10 (1995), pp. 1122–1129.

[104] D. Munson. "Constitutive model of creep in rock salt applied to underground room closure." *International Journal of Rock Mechanics and Mining Sciences* 34.2 (1997), pp. 233–247.

[105] M. Aubertin et al. "A rate-dependent model for the ductile behavior of salt rocks." *Canadian Geotechnical Journal* 36.4 (1999), pp. 660–674.

[106] S. Olivella and A. Gens. "A constitutive model for crushed salt." *International journal for numerical and analytical methods in geomechanics* 26.7 (2002), pp. 719–746.

[107] C. Zhu and C. Arson. "A model of damage and healing coupling halite thermo-mechanical behavior to microstructure evolution." *Geotechnical and Geological Engineering* 33.2 (2015), pp. 389–410.

[108] S. Broome et al. "Mechanical response and microprocesses of reconsolidating crushed salt at elevated temperature." *Rock Mechanics and Rock Engineering* 48.6 (2015), pp. 2615–2629.

[109] X. Shen, C Zhu, C Arson, et al. "Chemo-mechanical damage and healing of granular salt: micro-macro modeling." *50th US Rock Mechanics/Geomechanics Symposium.* American Rock Mechanics Association. 2016.

[110] S. Olivella et al. "Nonisothermal multiphase flow of brine and gas through saline media." *Transport in porous media* 15.3 (1994), pp. 271–293.

[111] S. Olivella et al. "Porosity variations in saline media caused by temperature gradients coupled to multiphase flow and dissolution/precipitation." *Transport in Porous Media* 25.1 (1996), pp. 1–25.

[112] S. Olivella et al. "Numerical formulation for a simulator (CODE_BRIGHT) for the coupled analysis of saline media." *Engineering computations* 13.7 (1996), pp. 87–112.

[113] S. Olivella and A. Gens. "Vapour transport in low permeability unsaturated soils with capillary effects." *Transport in Porous Media* 40.2 (2000), pp. 219–241.

[114] J. R. Rice. "Inelastic constitutive relations for solids: an internal-variable theory and its application to metal plasticity." *Journal of the Mechanics and Physics of Solids* 19.6 (1971), pp. 433–455.

[115] D. Peirce, R. Asaro, and A. Needleman. "An analysis of nonuniform and localized deformation in ductile single crystals." *Acta metallurgica* 30.6 (1982), pp. 1087–1119.

[116] K. Havner. *Finite plastic deformation of crystalline solids.* Cambridge University Press, 1992.

[117] M. E. Gurtin, E. Fried, and L. Anand. *The mechanics and thermodynamics of continua.* Cambridge University Press, 2010.

[118] A. M. Cuitino and M. Ortiz. "Computational modelling of single crystals." *Modelling and Simulation in Materials Science and Engineering* 1.3 (1993), p. 225.

[119] R. I. Borja and J. R. Wren. "Discrete micromechanics of elastoplastic crystals." *International Journal for Numerical Methods in Engineering* 36.22 (1993), pp. 3815–3840.

[120] L. Anand and M. Kothari. "A computational procedure for rate-independent crystal plasticity." *Journal of the Mechanics and Physics of Solids* 44.4 (1996), pp. 525–558.

[121] C. Miehe and J. Schröder. "A comparative study of stress update algorithms for rate-independent and rate-dependent crystal plasticity." *International Journal for Numerical Methods in Engineering* 50.2 (2001), pp. 273–298.

[122] R. I. Borja and H. Rahmani. "Computational aspects of elasto-plastic deformation in polycrystalline solids." *Journal of Applied Mechanics* 79.3 (2012), p. 031024.

[123] M. Tjioe and R. I. Borja. "On the pore-scale mechanisms leading to brittle and ductile deformation behavior of crystalline rocks." *International Journal for Numerical and Analytical Methods in Geomechanics* 39.11 (2015), pp. 1165–1187.

[124] C. Miehe, F. Welschinger, and M. Hofacker. "Thermodynamically consistent phase-field models of fracture: Variational principles and multi-field FE implementa-

tions." *International Journal for Numerical Methods in Engineering* 83.10 (2010), pp. 1273–1311.

[125] C. Miehe, M. Hofacker, and F. Welschinger. "A phase field model for rate-independent crack propagation: Robust algorithmic implementation based on operator splits." *Computer Methods in Applied Mechanics and Engineering* 199.45 (2010), pp. 2765–2778.

[126] J. Clayton and J Knap. "Phase field modeling of twinning in indentation of transparent crystals." *Modelling and Simulation in Materials Science and Engineering* 19.8 (2011), p. 085005.

[127] J. Clayton and J Knap. "Phase field modeling of directional fracture in anisotropic polycrystals." *Computational Materials Science* 98 (2015), pp. 158–169.

[128] S. Na et al. "Effects of spatial heterogeneity and material anisotropy on the fracture pattern and macroscopic effective toughness of Mancos Shale in Brazilian tests." *Journal of Geophysical Research: Solid Earth* (2017).

[129] O. Aslan et al. "Micromorphic approach to single crystal plasticity and damage." *International Journal of Engineering Science* 49.12 (2011), pp. 1311–1325.

[130] J. Clayton. "Deformation, fracture, and fragmentation in brittle geologic solids." *International Journal of Fracture* 163.1 (2010), pp. 151–172.

[131] M. Koslowski and M. Ortiz. "A multi-phase field model of planar dislocation networks." *Modelling and Simulation in Materials Science and Engineering* 12.6 (2004), p. 1087.

[132] T. Takaki et al. "Multi-phase-field simulations for dynamic recrystallization." *Computational Materials Science* 45.4 (2009), pp. 881–888.

[133] K. Oshima, T. Takaki, and M. Muramatsu. "Development of multi-phase-field crack model for crack propagation in polycrystal." *International Journal of Computational Materials Science and Engineering* 3.02 (2014), p. 1450009.

[134] T. T. Nguyen, J. Réthoré, and M.-C. Baietto. "Phase field modelling of anisotropic crack propagation." *European Journal of Mechanics-A/Solids* (2017).

[135] T. T. Nguyen et al. "Multi-phase-field modeling of anisotropic crack propagation for polycrystalline materials." *Computational Mechanics* (2017), pp. 1–26.

[136] I. Steinbach. "Phase-field models in materials science." *Modelling and simulation in materials science and engineering* 17.7 (2009), p. 073001.

[137]   B. Li et al. "Phase-field modeling and simulation of fracture in brittle materials with strongly anisotropic surface energy." *International Journal for Numerical Methods in Engineering* 102.3-4 (2015), pp. 711–727.

[138]   S. Teichtmeister et al. "Phase field modeling of fracture in anisotropic brittle solids." *International Journal of Non-Linear Mechanics* 97 (2017), pp. 1–21.

[139]   M. Ekh, R. Lillbacka, and K. Runesson. "A model framework for anisotropic damage coupled to crystal (visco) plasticity." *International Journal of Plasticity* 20.12 (2004), pp. 2143–2159.

[140]   R. de Borst and C. V. Verhoosel. "Gradient damage vs phase-field approaches for fracture: Similarities and differences." *Computer Methods in Applied Mechanics and Engineering* 312 (2016), pp. 78–94.

[141]   U. Lee, G. A. Lesieutre, and L. Fang. "Anisotropic damage mechanics based on strain energy equivalence and equivalent elliptical microcracks." *International Journal of Solids and Structures* 34.33-34 (1997), pp. 4377–4397.

[142]   J. Simo and J. Ju. "On continuum damage-elastoplasticity at finite strains." *Computational Mechanics* 5.5 (1989), pp. 375–400.

[143]   B. Budiansky and T. T. Wu. *Theoretical prediction of plastic strains of polycrystals.* Tech. rep. Havard University Cambridge Mass, 1961.

[144]   J. Williams. *Crystal Engineering: How Molecules Build Solids.* Morgan & Claypool Publishers, 2017.

[145]   C. B. Carter and M. G. Norton. *Ceramic materials: science and engineering.* Springer Science & Business Media, 2007.

[146]   W. D. Callister Jr and D. G. Rethwisch. *Fundamentals of materials science and engineering: an integrated approach.* John Wiley & Sons, 2012.

[147]   W. G. Moffat, G. W. Pearsall, and J. Wulff. *The structure and properties of materials. volume 1, structure.* Vol. 1. Wiley New York, 1964.

[148]   F. Aldakheel. "Micromorphic approach for gradient-extended thermo-elastic–plastic solids in the logarithmic strain space." *Continuum Mechanics and Thermodynamics* (2017), pp. 1–11.

[149]   C. Miehe et al. "Phase field modeling of fracture in multi-physics problems. Part II. Coupled brittle-to-ductile failure criteria and crack propagation in thermo-elastic–plastic solids." *Computer Methods in Applied Mechanics and Engineering* 294 (2015), pp. 486–522.

[150] L. Anand and M. E. Gurtin. "Thermal effects in the superelasticity of crystalline shape-memory materials." *Journal of the Mechanics and Physics of Solids* 51.6 (2003), pp. 1015–1058.

[151] J. Clayton. *Nonlinear mechanics of crystals*. Vol. 177. Springer Science & Business Media, 2010.

[152] F. Meissonnier, E. Busso, and N. O'Dowd. "Finite element implementation of a generalised non-local rate-dependent crystallographic formulation for finite strains." *International Journal of Plasticity* 17.4 (2001), pp. 601–640.

[153] B. Bourdin, G. A. Francfort, and J.-J. Marigo. "The variational approach to fracture." *Journal of elasticity* 91.1 (2008), pp. 5–148.

[154] B. Schmidt, F. Fraternali, and M. Ortiz. "Eigenfracture: an eigendeformation approach to variational fracture." *Multiscale Modeling & Simulation* 7.3 (2009), pp. 1237–1266.

[155] K. Wang and W. Sun. "A unified variational eigen-erosion framework for interacting brittle fractures and compaction bands in fluid-infiltrating porous media." *Computer Methods in Applied Mechanics and Engineering* 318 (2017), pp. 1–32.

[156] L. De Lorenzis, A. McBride, and B. Reddy. "Phase-field modelling of fracture in single crystal plasticity." *GAMM-Mitteilungen* 39.1 (2016), pp. 7–34.

[157] J. D. Bredehoeft et al. *Geologic disposal of high-level radioactive wastes: Earth-science perspectives*. US Department of the Interior, US Geological Survey, 1978.

[158] M. E. Gurtin. "Generalized Ginzburg-Landau and Cahn-Hilliard equations based on a microforce balance." *Physica D: Nonlinear Phenomena* 92.3-4 (1996), pp. 178–192.

[159] M. J. Borden. "Isogeometric analysis of phase-field models for dynamic brittle and ductile fracture." PhD thesis. 2012.

[160] A. Mota et al. "Lie-group interpolation and variational recovery for internal variables." *Computational Mechanics* (2013), pp. 1–19.

[161] Q. Yang, L. Stainier, and M. Ortiz. "A variational formulation of the coupled thermo-mechanical boundary-value problem for general dissipative solids." *Journal of the Mechanics and Physics of Solids* 54.2 (2006), pp. 401–424.

[162] R. Abeyaratne, K. Sang-Joo, and J. K. Knowles. "A one-dimensional continuum model for shape-memory alloys." *International journal of solids and structures* 31.16 (1994), pp. 2229–2249.

[163] V. Lubarda. "On thermodynamic potentials in linear thermoelasticity." *International Journal of Solids and Structures* 41.26 (2004), pp. 7377–7398.

[164] M. Peigney and J.-P. Seguin. "An incremental variational approach to coupled thermo-mechanical problems in anelastic solids. Application to shape-memory alloys." *International Journal of Solids and Structures* 50.24 (2013), pp. 4043–4054.

[165] T. Heister, M. F. Wheeler, and T. Wick. "A primal-dual active set method and predictor-corrector mesh adaptivity for computing fracture propagation using a phase-field approach." *Computer Methods in Applied Mechanics and Engineering* 290 (2015), pp. 466–495.

[166] M. Ambati, T. Gerasimov, and L. De Lorenzis. "Phase-field modeling of ductile fracture." *Computational Mechanics* 55.5 (2015), pp. 1017–1040.

[167] M. J. Borden et al. "A phase-field formulation for fracture in ductile materials: Finite deformation balance law derivation, plastic degradation, and stress triaxiality effects." *Computer Methods in Applied Mechanics and Engineering* 312 (2016), pp. 130–166.

[168] A. Bartels et al. "On the thermomechanical coupling in dissipative materials: a variational approach for generalized standard materials." *Journal of the Mechanics and Physics of Solids* 82 (2015), pp. 218–234.

[169] M. Canadija and J. Mosler. "On the thermomechanical coupling in finite strain plasticity theory with non-linear kinematic hardening by means of incremental energy minimization." *International Journal of Solids and Structures* 48.7 (2011), pp. 1120–1129.

[170] J. Lemaitre. "How to use damage mechanics." *Nuclear engineering and design* 80.2 (1984), pp. 233–245.

[171] J. Simo and J. Ju. "Strain-and stress-based continuum damage models—II. Computational aspects." *International journal of solids and structures* 23.7 (1987), pp. 841–869.

[172] J. Ju. "On energy-based coupled elastoplastic damage theories: constitutive modeling and computational aspects." *International Journal of Solids and structures* 25.7 (1989), pp. 803–833.

[173] R. de Borst, J. Pamin, and M. G. Geers. "On coupled gradient-dependent plasticity and damage theories with a view to localization analysis." *European Journal of Mechanics-A/Solids* 18.6 (1999), pp. 939–962.

[174] J. Choo and W. Sun. "Coupled phase-field and plasticity modeling of geological materials: From brittle fracture to ductile flow." *Computer Methods in Applied Mechanics and Engineering* (2017).

[175] O. Coussy. *Poromechanics*. John Wiley & Sons, 2004.

[176] W. Sun. "A unified method to predict diffuse and localized instabilities in sands." *Geomechanics and Geoengineering* 8.2 (2013), pp. 65–75.

[177] S. Na and W. Sun. "Computational thermo-hydro-mechanics for multiphase freezing and thawing porous media in the finite deformation range." *Computer Methods in Applied Mechanics and Engineering* 318 (2017), pp. 667–700.

[178] J. Choo and R. Borja. "Stabilized mixed finite elements for deformable porous media with double porosity." *Computer Methods in Applied Mechanics and Engineering* 293 (2015), pp. 131–154.

[179] J. Choo, J. A. White, and R. I. Borja. "Hydromechanical modeling of unsaturated flow in double porosity media." *International Journal of Geomechanics* 16.6 (2016), p. D4016002.

[180] J. P. Hirth and J. Lothe. *Theory of dislocations*. John Wiley & Sons, 1982.

[181] J. B. Wachtman, W. R. Cannon, and M. J. Matthewson. *Mechanical properties of ceramics*. John Wiley & Sons, 2009.

[182] M. A. Durand. "The temperature variation of the elastic moduli of NaCl, KCl and MgO." *Physical Review* 50.5 (1936), p. 449.

[183] R. A. Bartels and D. Schuele. "Pressure derivatives of the elastic constants of NaCl and KCl at 295 K and 195 K." *Journal of Physics and Chemistry of Solids* 26.3 (1965), pp. 537–549.

[184] F. Birch. "Finite strain isotherm and velocities for single-crystal and polycrystalline NaCl at high pressures and 300 K." *Journal of Geophysical Research: Solid Earth* 83.B3 (1978), pp. 1257–1268.

[185] W. C. Oliver and G. M. Pharr. "An improved technique for determining hardness and elastic modulus using load and displacement sensing indentation experiments." *Journal of materials research* 7.6 (1992), pp. 1564–1583.

[186] R. Asaro. "Crystal plasticity." *Journal of Applied Mechanics* 50.4b (1983), pp. 921–934.

[187] H. Amor, J.-J. Marigo, and C. Maurini. "Regularized formulation of the variational brittle fracture with unilateral contact: numerical experiments." *Journal of the Mechanics and Physics of Solids* 57.8 (2009), pp. 1209–1229.

[188] W. Qi and A. Bertram. "Anisotropic continuum damage modeling for single crystals at high temperatures." *International Journal of Plasticity* 15.11 (1999), pp. 1197–1215.

[189] W. R. Wawersik and D. H. Zeuch. *Creep and Creep Modeling of Three Domal Salts: A Comprehensive Update*. Vol. 84. 15755. Sandia National Laboratories, 1984.

[190] Y. Liu, W. Sun, and J. Fish. "Determining material parameters for critical state plasticity models based on multilevel extended digital database." *Journal of Applied Mechanics* 83.1 (2016), p. 011003.

[191] K. Wang et al. "Identifying material parameters for a micro-polar plasticity model via X-ray micro-CT images: lessons learned from the curve-fitting exercises." *International Journal for Multiscale Computational Engineering* (2016).

[192] J. C. Simo and T. J. Hughes. *Computational inelasticity*. Vol. 7. Springer Science & Business Media, 2006.

[193] J. Kim, H. A. Tchelepi, R. Juanes, et al. "Stability, accuracy and efficiency of sequential methods for coupled flow and geomechanics." *SPE reservoir simulation symposium*. Society of Petroleum Engineers. 2009.

[194] J. White, N. Castelletto, and H. Tchelepi. "Block-partitioned solvers for coupled poromechanics: A unified framework." *Computer Methods in Applied Mechanics and Engineering* 303 (2016), pp. 55–74.

[195] R. Pawlowski, E. Phipps, and A. Salinger. "Automating embedded analysis capabilities and managing software complexity in multiphysics simulation, Part I: Template-based generic programming." *Scientific Programming* 20.2 (2012), pp. 197–219.

[196] R. Pawlowski et al. "Automating embedded analysis capabilities and managing software complexity in multiphysics simulation, Part II: Application to partial differential equations." *Scientific Programming* 20.3 (2012), pp. 327–345.

[197] A. Salinger et al. "Albany: Using Component-Based Design to Develop a Flexible, Generic Multiphysics Analysis Code." *International Journal for Multiscale Computational Engineering* 14.4 (2016), pp. 415–438.

[198] K. Wang and W. Sun. "Data-Driven Discrete-Continuum Method for Partially Saturated Micro-Polar Porous Media." *Poromechanics VI*. 2017, pp. 571–578.

[199] D. Tromans and J. Meech. "Fracture toughness and surface energies of minerals: theoretical estimates for oxides, sulphides, silicates and halides." *Minerals Engineering* 15.12 (2002), pp. 1027–1041.

[200] T. Nguyen et al. "On the choice of parameters in the phase field method for simulating crack initiation with experimental validation." *International Journal of Fracture* 197.2 (2016), pp. 213–226.

[201] H. Wenk et al. "Texture development in halite: comparison of Taylor model and self-consistent theory." *Acta metallurgica* 37.7 (1989), pp. 2017–2029.

[202] A. Birch and H. Clark. "The thermal conductivity of rocks and its dependence upon temperature and composition." *American Journal of Science* 238.8 (1940), pp. 529–558.

[203] D. Smith. *Thermal conductivity of halite using a pulsed laser.* Tech. rep. Oak Ridge Y-12 Plant, TN (USA), 1976.

[204] W. Bangerth, R. Hartmann, and G. Kanschat. "deal. II—a general-purpose object-oriented finite element library." *ACM Transactions on Mathematical Software (TOMS)* 33.4 (2007), p. 24.

[205] W. Bangerth et al. "The deal. II library." *Version* 8 (2013), pp. 1–5.

[206] C. Burstedde, L. Wilcox, and O. Ghattas. "p4est: Scalable algorithms for parallel adaptive mesh refinement on forests of octrees." *SIAM Journal on Scientific Computing* 33.3 (2011), pp. 1103–1133.

[207] M. Heroux and J. Willenbring. "A new overview of the Trilinos project." *Scientific Programming* 20.2 (2012), pp. 83–88.

[208] J. White and R. Borja. "Block-preconditioned Newton–Krylov solvers for fully coupled flow and geomechanics." *Computational Geosciences* 15.4 (2011), pp. 647–659.

[209] J. White and R. Borja. "Stabilized low-order finite elements for coupled solid-deformation/fluid-diffusion and their application to fault zone transients." *Computer Methods in Applied Mechanics and Engineering* 197.49 (2008), pp. 4353–4366.

[210] R. I. Borja and J. Choo. "Cam-Clay plasticity, Part VIII: A constitutive framework for porous materials with evolving internal structure." *Computer Methods in Applied Mechanics and Engineering* 309 (2016), pp. 653–679.

[211] M. Rashid and S. Nemat-Nasser. "A constitutive algorithm for rate-dependent crystal plasticity." *Computer Methods in Applied Mechanics and Engineering* 94.2 (1992), pp. 201–228.

[212] M. S. Paterson and T.-f. Wong. *Experimental rock deformation-the brittle field.* Springer Science & Business Media, 2005.

[213] Y. Wei and L. Anand. "Grain-boundary sliding and separation in polycrystalline metals: application to nanocrystalline fcc metals." *Journal of the Mechanics and Physics of Solids* 52.11 (2004), pp. 2587–2616.

[214] K. H. Nam, I. H. Park, and S. H. Ko. "Patterning by controlled cracking." *Nature* 485.7397 (2012), p. 221.

[215] A. Nádai and A. Wahl. *Plasticity.* McGraw-Hill Book Company, inc., 1931.

[216] R. de Borst et al. *Non-linear finite element analysis of solids and structures.* John Wiley & Sons, 2012.

[217] Z. Bažant and B. Oh. "Crack band theory for fracture of concrete." *Matériaux et construction* 16.3 (1983), pp. 155–177.

[218] J. W. Rudnicki and J. Rice. "Conditions for the localization of deformation in pressure-sensitive dilatant materials." *Journal of the Mechanics and Physics of Solids* 23.6 (1975), pp. 371–394.

[219] J. Desrues and R. Chambon. "Shear band analysis for granular materials: the question of incremental non-linearity." *Ingenieur-Archiv* 59.3 (1989), pp. 187–196.

[220] W. Sun et al. "Connecting microstructural attributes and permeability from 3D tomographic images of in situ shear-enhanced compaction bands using multiscale computations." *Geophysical Research Letters* 38.10 (2011).

[221] W. Sun, J. E. Andrade, and J. W. Rudnicki. "Multiscale method for characterization of porous microstructures and their impact on macroscopic effective permeability." *International Journal for Numerical Methods in Engineering* 88.12 (2011), pp. 1260–1279.

[222] W. Sun. "A unified method to predict diffuse and localized instabilities in sands." *Geomechanics and Geoengineering* 8.2 (2013), pp. 65–75.

[223] J. Hadamard. *Propagation des ondes.* Chelsea Publishing Company, 1949.

[224] R. Hill. "Acceleration waves in solids." *Journal of the Mechanics and Physics of Solids* 10.1 (1962), pp. 1–16.

[225] J. Rice. "On the stability of dilatant hardening for saturated rock masses." *Journal of Geophysical Research* 80.11 (1975), pp. 1531–1536.

[226] A. Needleman. "Material rate dependence and mesh sensitivity in localization problems." *Computer methods in applied mechanics and engineering* 67.1 (1988), pp. 69–85.

[227] R. Hill. "A general theory of uniqueness and stability in elastic-plastic solids." *Journal of the Mechanics and Physics of Solids* 6.3 (1958), pp. 236–249.

[228] Z. Bažant and T. Belytschko. "Wave propagation in a strain-softening bar: exact solution." *Journal of Engineering Mechanics* 111.3 (1985), pp. 381–389.

[229] D. Lasry and T. Belytschko. "Localization limiters in transient problems." *International Journal of Solids and Structures* 24.6 (1988), pp. 581–597.

[230] K. Runesson, N. Ottosen, and P. Dunja. "Discontinuous bifurcations of elastic-plastic solutions at plane stress and plane strain." *International Journal of Plasticity* 7.1 (1991), pp. 99–121.

[231] L. J. Sluys. "Wave propagation, localisation and dispersion in softening solids." PhD thesis. Netherlands: Delft University of technology, 1992.

[232] L. Sluys, R De Borst, and H.-B. Mühlhaus. "Wave propagation, localization and dispersion in a gradient-dependent medium." *International Journal of Solids and Structures* 30.9 (1993), pp. 1153–1171.

[233] R. Borja. "Bifurcation of elastoplastic solids to shear band mode at finite strain." *Computer Methods in Applied Mechanics and Engineering* 191.46 (2002), pp. 5287–5314.

[234] W. Sun and A. Mota. "A multiscale overlapped coupling formulation for large-deformation strain localization." *Computational Mechanics* (2014), pp. 1–18.

[235] T. Belytschko et al. *Nonlinear finite elements for continua and structures.* John Wiley & Sons, 2013.

[236] A. C. Eringen. "On nonlocal plasticity." *International Journal of Engineering Science* 19.12 (1981), pp. 1461–1474.

[237] J. Fish, W. Chen, and G. Nagai. "Non-local dispersive model for wave propagation in heterogeneous media: one-dimensional case." *International Journal for Numerical Methods in Engineering* 54.3 (2002), pp. 331–346.

[238] J. Fish. *Practical multiscaling.* John Wiley & Sons, 2013.

[239] H. W. Zhang and B. A. Schrefler. "Gradient-dependent plasticity model and dynamic strain localisation analysis of saturated and partially saturated porous me-

dia: one dimensional model." *European Journal of Mechanics-A/Solids* 19.3 (2000), pp. 503–524.

[240]   B. Loret and J. Prevost. "Dynamic strain localization in fluid-saturated porous media." *Journal of Engineering Mechanics* 117.4 (1991), pp. 907–922.

[241]   B. Schrefler, C. Majorana, and L. Sanavia. "Shear band localization in saturated porous media." *Archives of Mechanics* 47.3 (1995), pp. 577–599.

[242]   B. Schrefler, L. Sanavia, and C. Majorana. "A multiphase medium model for localisation and postlocalisation simulation in geomaterials." *Mechanics of Cohesive-frictional Materials* 1.1 (1996), pp. 95–114.

[243]   A. Benallal and C. Comi. "On numerical analyses in the presence of unstable saturated porous materials." *International journal for numerical methods in engineering* 56.6 (2003), pp. 883–910.

[244]   M. A. Abellan and R. de Borst. "Wave propagation and localisation in a softening two-phase medium." *Computer Methods in Applied Mechanics and Engineering* 195.37 (2006), pp. 5011–5019.

[245]   D Adam and R Markiewicz. "Energy from earth-coupled structures, foundations, tunnels and sewers." *Géotechnique* 59.3 (2009), pp. 229–236.

[246]   C. Tsang, O. Stephansson, and J. Hudson. "A discussion of thermo–hydro–mechanical (THM) processes associated with nuclear waste repositories." *International Journal of Rock Mechanics and Mining Sciences* 37.1 (2000), pp. 397–402.

[247]   E. Veveakis, I. Vardoulakis, and G. Di Toro. "Thermoporomechanics of creeping landslides: The 1963 Vaiont slide, northern Italy." *Journal of Geophysical Research: Earth Surface (2003–2012)* 112.F3 (2007).

[248]   H. Zhang and B. Schrefler. "Particular aspects of internal length scales in strain localization analysis of multiphase porous materials." *Computer methods in applied mechanics and engineering* 193.27 (2004), pp. 2867–2884.

[249]   M. Biot. "Variational Lagrangian-thermodynamics of nonisothermal finite strain mechanics of porous solids and thermomolecular diffusion." *International Journal of Solids and Structures* 13.6 (1977), pp. 579–597.

[250]   D. McTigue. "Thermoelastic response of fluid-saturated porous rock." *Journal of Geophysical Research: Solid Earth (1978–2012)* 91 (1986), pp. 9533–9542.

[251]   A. Selvadurai and A. Suvorov. "Boundary heating of poro-elastic and poro-elasto-plastic spheres." *Proceedings of the Royal Society of London A: Mathematical, Physical and Engineering Sciences* 468.2145 (2012), pp. 2779–2806.

[252]   R. Liu et al. "Modeling of convection-dominated thermoporomechanics problems using incomplete interior penalty Galerkin method." *Computer Methods in Applied Mechanics and Engineering* 198.9 (2009), pp. 912–919.

[253]   E. J. Routh. *A treatise on the stability of a given state of motion: particularly steady motion.* Macmillan and Company, 1877.

[254]   A. Hurwitz. "Ueber die Bedingungen, unter welchen eine Gleichung nur Wurzeln mit negativen reellen Theilen besitzt." German. *Mathematische Annalen* 46.2 (1895), pp. 273–284. ISSN: 0025-5831.

[255]   A. Selvadurai and A. Suvorov. "Thermo-poromechanics of a fluid-filled cavity in a fluid-saturated geomaterial." *Proceedings of the Royal Society of London A: Mathematical, Physical and Engineering Sciences.* Vol. 470. 2163. The Royal Society. 2014, p. 20130634.

[256]   A. Benallal and C. Comi. "Material instabilities in inelastic saturated porous media under dynamic loadings." *International journal of solids and structures* 39.13 (2002), pp. 3693–3716.

[257]   M. Biot. "Theory of propagation of elastic waves in a fluid-saturated porous solid. I. Low-frequency range." *the Journal of the Acoustical Society of America* 28.2 (1956), pp. 168–178.

[258]   F. Simoes, J. Martins, and B. Loret. "Instabilities in elastic–plastic fluid-saturated porous media: harmonic wave versus acceleration wave analyses." *International journal of solids and structures* 36.9 (1999), pp. 1277–1295.

[259]   E. Rizzi and B. Loret. "Strain localization in fluid-saturated anisotropic elastic–plastic porous media." *International journal of engineering science* 37.2 (1999), pp. 235–251.

[260]   L. Sluys and R De Borst. "Wave propagation and localization in a rate-dependent cracked medium—model formulation and one-dimensional examples." *International Journal of Solids and Structures* 29.23 (1992), pp. 2945–2958.

[261]   N. H. Abel. "Beweis der Unmöglichkeit, algebraische Gleichungen von höheren Graden als dem vierten allgemein aufzulösen." *Journal für die reine und angewandte Mathematik* 1 (1826), pp. 65–84.

[262] C. H. Morales. "A Bolzano's theorem in the new millennium." *Nonlinear Analysis: Theory, Methods & Applications* 51.4 (2002), pp. 679–691.

[263] W. Sun, Q. Chen, and J. T. Ostien. "Modeling the hydro-mechanical responses of strip and circular punch loadings on water-saturated collapsible geomaterials." *Acta Geotechnica* (2013).

[264] P. Mira et al. "A new stabilized enhanced strain element with equal order of interpolation for soil consolidation problems." *Computer Methods in Applied Mechanics and Engineering* 192.37 (2003), pp. 4257–4277.

[265] R. W. Lewis and B. A. Schrefler. *The finite element method in the static and dynamic deformation and consolidation of porous media.* John Wiley, 1998.

[266] P. Bochev, C. Dohrmann, and M. Gunzburger. "Stabilization of low-order mixed finite elements for the Stokes equations." *SIAM Journal on Numerical Analysis* 44.1 (2006), pp. 82–101.

[267] J. S. Howell and N. J. Walkington. "Inf–sup conditions for twofold saddle point problems." *Numerische Mathematik* 118.4 (2011), pp. 663–693.

[268] K. Bathe. *Finite element procedures.* Klaus-Jurgen Bathe, 2006.

[269] D. Chapelle and K. Bathe. "The inf-sup test." *Computers & Structures* 47.4 (1993), pp. 537–545.

[270] K. Bathe, A. Iosilevich, and D. Chapelle. "An inf-sup test for shell finite elements." *Computers & Structures* 75.5 (2000), pp. 439–456.

[271] K. Bathe. "The inf–sup condition and its evaluation for mixed finite element methods." *Computers & Structures* 79.2 (2001), pp. 243–252.

[272] K. Bathe et al. "Inf–sup testing of upwind methods." *International Journal for Numerical Methods in Engineering* 48 (2000), pp. 745–760.

[273] W. Sun, Z. Cai, and J. Choo. "Mixed Arlequin method for multiscale poromechanics problems." *International Journal for Numerical Methods in Engineering* (2016).

[274] D. Pantuso and K. Bathe. "A four-node quadrilateral mixed-interpolated element for solids and fluids." *Mathematical Models and Methods in Applied Sciences* 5.8 (1995), pp. 1113–1128.

[275] M. Ferronato, G. Gambolati, and P. Teatini. "Ill-conditioning of finite element poroelasticity equations." *International Journal of Solids and Structures* 38.34 (2001), pp. 5995–6014.

[276] C. Dawson et al. "A parallel, implicit, cell-centered method for two-phase flow with a preconditioned Newton–Krylov solver." *Computational Geosciences* 1.3-4 (1997), pp. 215–249.

[277] J. Demmel, N. Higham, and R. Schreiber. "Stability of block LU factorization." *Numerical linear algebra with applications* 2.2 (1995), pp. 173–190.

[278] J. Kim. "Unconditionally Stable Sequential Schemes for Thermoporomechanics: Undrained-Adiabatic and Extended Fixed-Stress Splits." *SPE Reservoir Simulation Symposium.* Society of Petroleum Engineers. 2015.

[279] J. Kim, H. A. Tchelepi, and R. Juanes. "Stability, accuracy, and efficiency of sequential methods for coupled flow and geomechanics." *SPE Journal* 16.2 (2011), pp. 249–262.

[280] F. Armero and J. Simo. "A new unconditionally stable fractional step method for non-linear coupled thermomechanical problems." *International Journal for Numerical Methods in Engineering* 35.4 (1992), pp. 737–766.

[281] K. Roscoe and A. Schofield. "Mechanical behaviour of an idealized 'wet'clay." *Proc. 3rd Eur. Conf. Soil Mech. Wiesbaden, 1963.* Vol. 1. 1963, pp. 47–54.

[282] K. Roscoe and J. Burland. "On the generalized stress-strain behaviour of wet clay." *Engineering Plasticity.* Cambridge University Press, 1968.

[283] S. Forest. "Micromorphic approach for gradient elasticity, viscoplasticity, and damage." *Journal of Engineering Mechanics* 135.3 (2009), pp. 117–131.

[284] C. Miehe, S. Teichtmeister, and F. Aldakheel. "Phase-field modelling of ductile fracture: a variational gradient-extended plasticity-damage theory and its micromorphic regularization." *Phil. Trans. R. Soc. A* 374.2066 (2016), p. 20150170.

[285] C. Miehe, F. Aldakheel, and S. Teichtmeister. "Phase-field modeling of ductile fracture at finite strains: A robust variational-based numerical implementation of a gradient-extended theory by micromorphic regularization." *International Journal for Numerical Methods in Engineering* 111.9 (2017), pp. 816–863.

[286] M. Ortiz and J. Quigley IV. "Adaptive mesh refinement in strain localization problems." *Computer Methods in Applied Mechanics and Engineering* 90.1-3 (1991), pp. 781–804.

[287] R. Verfürth. "A posteriori error estimation and adaptive mesh-refinement techniques." *Journal of Computational and Applied Mathematics* 50.1-3 (1994), pp. 67–83.

[288] B. A. Schrefler, S. Secchi, and L. Simoni. "On adaptive refinement techniques in multi-field problems including cohesive fracture." *Computer methods in applied mechanics and engineering* 195.4-6 (2006), pp. 444–461.

[289] A. R. Díaz, N. Kikuchi, and J. E. Taylor. "A method of grid optimization for finite element methods." *Computer Methods in Applied Mechanics and Engineering* 41.1 (1983), pp. 29–45.

[290] P. Heintz et al. "Adaptive strategies and error control for computing material forces in fracture mechanics." *International Journal for numerical methods in Engineering* 60.7 (2004), pp. 1287–1299.

[291] A. Tabarraei and N. Sukumar. "Adaptive computations using material forces and residual-based error estimators on quadtree meshes." *Computer Methods in Applied Mechanics and Engineering* 196.25-28 (2007), pp. 2657–2680.

[292] R. Mueller, D. Gross, and G. Maugin. "Use of material forces in adaptive finite element methods." *Computational Mechanics* 33.6 (2004), pp. 421–434.

[293] F. C. Park and B. Ravani. "Smooth invariant interpolation of rotations." *ACM Transactions on Graphics (TOG)* 16.3 (1997), pp. 277–295.